Interactions between Dark Matter Substructure and Galaxies

Benjamin Joseph Lowing

Abstract

In this thesis we study how subhaloes evolve and interact in the central regions of galactic dark matter haloes in a ΛCDM universe. We examine the effect that subhalo impacts have on disc galaxies and what visible signatures they leave behind. We use the Aquarius simulations, a set of high resolution simulations of Milky Way mass haloes, as the basis of the work in this thesis. We summarise the main properties of these haloes and show that they are typical haloes for most characteristics.

We develop a method to approximate the potential of host haloes that helps us understand how subhaloes evolve in the tidal field of their host. Using a basis function expansion method, we show that it is possible to create a time-evolving density/potential approximation of the late growth of simulated N-body dark matter haloes, and that particle and subhalo orbits can be integrated in this realistic, time-varying halo potential approximation at much lower computational cost than the original simulations.

Using samples of subhaloes extracted from the Aquarius haloes, we estimate the disc heating caused by substructure bombardment using the Benson et al. (2004) semi-analytical model. A critical evaluation of the model, however, finds that there are problems with the original implementation, including a numerical factor, that call into question its validity. We then approach the same problem using high resolution N-body simulations of subhalo interactions with discs. We find that only the most massive of subhaloes appreciably affect stellar discs, heating and thickening them, and that the majority of any heating occurs at early times and happens quickly. However, the substructure bombardment since redshift one is negligible in most of the haloes, and in the haloes that do show significant heating it is caused by a single massive subhalo.

Interactions between Dark Matter Substructure and Galaxies

Benjamin Joseph Lowing

A thesis submitted to the University of Durham
in accordance with the regulations for
admittance to the Degree of Doctor of Philosophy.

Institute for Computational Cosmology
Department of Physics
University of Durham
September 2011

Contents

List of Figures

List of Tables

Declaration

The work described in this thesis was undertaken between 2007 and 2011 while the author was a research student under the supervision of Dr. Adrian R. Jenkins and Dr. Vincent R. Eke at the Institute for Computational Cosmology in the Department of Physics at the University of Durham. This work has not been submitted for any other degree at the University of Durham or any other university.

Parts of this work have appeared in the following paper:

- Lowing, Ben J.; Jenkins, Adrian R; Eke, Vincent R.; Frenk, Carlos S., 2011, MNRAS, **416**, 2697

All figures were produced by the author, except the following:

- Figure 1.1: V. Belokurov and The Sloan Digital Sky Survey Collaboration
- Figure 1.2: Holmberg, J., Nordström, B., and Andersen, J.: 2007, A&A **475**, 519
- Figure 1.3: Navarro, J. F., Abadi, M. G., Venn, K. A., Freeman, K. C., and Anguiano, B.: 2011, MNRAS **412**, 1203
- Figures 2.1, 2.14, 2.15, 2.16 & 2.17: Springel, V., Wang, J., Vogelsberger, M., Ludlow, A., Jenkins, A., Helmi, A., Navarro, J. F., Frenk, C. S., and White, S. D. M.: 2008, MNRAS **391**, 1685
- Figures 2.5, 2.6 & 2.7: Wang, J., Navarro, J. F., Frenk, C. S., White, S. D. M., Springel, V., Jenkins, A., Helmi, A., Ludlow, A., and Vogelsberger, M.: 2011, MNRAS **413**, 1373
- Figure 2.18: Boylan-Kolchin, M., Springel, V., White, S. D. M., Jenkins, A., and Lemson, G.: 2009, MNRAS **398**, 1150
- Figures 2.19, 2.20 & 2.21: Boylan-Kolchin, M., Springel, V., White, S. D. M., and Jenkins, A.: 2010, MNRAS **406**, 896

Details of where simulations were run, and by whom, is provided below:

- Aquarius Project: carried out by the Virgo Consortium at the Leibniz Computing Centre, Garching, Germany, at the Computing Centre of the Max-Planck-Society in Garching, at the Institute for Computational Cosmology in Durham, and on the STELLA supercomputer of the LOFAR experiment at the University of Groningen.
- Disc Simulations: run by the author on the COSMA supercomputer at the Institute for Computational Cosmology in Durham

Acknowledgements

My first and foremost thanks goes to my supervisors, Adrian Jenkins and Vincent Eke. Without their support and guidance this thesis would not exist. Special thanks to Adrian for his many suggestions and explanations, and to Vince for our long Friday afternoon discussions. I would also like to thank Carlos Frenk in his role as my unofficial supervisor. I always came away from our meetings much enthused and with many new ideas. I only wish I had time to try them all.

I would like to extend my thanks to the whole of the ICC and everyone there for creating such a productive and friendly environment. I have made many good friends during my postgraduate studies at the ICC and these last fours years would not have been half as enjoyable without them. Thanks to all to those I have shared offices with, but especially Owen Parry for never shouting at me when I frequently interrupted him with a trivial question. A special mention must be made of Lydia Heck for her amazing support, often going way beyond the call of duty and always ready to help, even when she is already busy with a million other tasks.

I must thank Peter Creasey, who has in turn been a useful sounding board, an agreeable flatmate and a very good friend. I would like to thank all my friends and family who have offered me support and understanding, even when they have little idea what I am doing.

Special thanks must go to Ann-Marie Einhaus for putting up with me, for proofreading my many drafts and for giving me unwavering encouragement, support and patience. Finally, I must thank my mother, who has not just supported me over the last four years but on my long journey to reach this point. She has always believed in me.

Chapter 1 | *Introduction*

In recent years huge advances have been made in our understanding of the Universe. We now have a successful model of the overall structure of the Universe, which provides a framework in which to further develop our knowledge of galaxy formation and evolution. However, there remains much further work to be done to get the details right. Any model of the Universe must work at all levels, and it is on the scales of galaxies and below that many challenges now remain. This thesis focuses on one such challenge, that of the evolution and interaction of substructure with galaxies. The effect that substructure has on galactic discs and the question of whether thin discs are compatible with ΛCDM, are topics that have long been discussed. We start by outlining the cosmological framework this work is set in, before giving some historical and observational background to place the rest of the thesis in context.

1.1 The ΛCDM Model

With the emergence of a concordance ΛCDM model there is confidence that we now have an understanding of the basic framework of the visible Universe and that the fundamental parameters are known to within a few percent. This concordance cosmology is so called as its parameters are derived from the result of several different observational datasets (Komatsu et al., 2011), including the cosmic microwave background (Spergel et al., 2003; Larson et al., 2011), galaxy clustering measurements (Allen et al., 2003; Mantz et al., 2010), and supernovae data (Knop et al., 2003; Kessler et al., 2009). The model is based on the idea of a flat universe with a cosmological constant, containing cold dark matter, which is expanding at an accelerating rate. Since general relativity relates the contents of the universe to the curvature of space-time, a flat universe must have a total energy density $\Omega_{\rm tot} = 1$. In the ΛCDM model, the majority of the energy density, ~ 73 percent, is taken up by dark energy. Dark matter accounts for another ~ 23 percent of the total energy density and the rest is divided between baryonic matter and radiation

(as well as possibly relic neutrinos).

The history of the Universe can be briefly described as having started just over 13.7 billion years ago at the Big Bang, followed shortly afterwards by a brief period of rapid exponential expansion known as inflation (Guth, 1981). Inflation solves a number of problems; mainly the horizon problem, i.e. why non-causally connected regions have such similar temperatures, and the flatness problems, i.e. why is the space-time curvature of the Universe so close to flat. Inflation also seeds the tiny fluctuations that go on to collapse and form the structure in the Universe.

Dark matter, the subject of this thesis, is a form of matter that interacts gravitationally but not via the electromagnetic force. This means it does not emit, absorb or scatter light and that it is dissipationless (i.e. cannot radiate energy away) and collisionless. It is usually taken to be cold, in that its intrinsic velocity was non-relativistic at the epoch of radiation-matter equality. Hot dark matter has been shown to be unable to reproduce the clustering of galaxies (White et al., 1983, 1984). The first hints that the Universe contains more matter than could be seen came when Zwicky (1933) inferred that the mass of massive galaxy clusters was far in excess of that of visible stars. Further signs came from Babcock (1939), who measured from the rotation of our neighbouring galaxy M31 (Andromeda) and found a steep increase in the mass-to-light ratio outwards. Both these measurements have been confirmed by modern observations and found to be universally true. Perhaps the strongest evidence that galaxies contain some dark massive component comes from gravitational lensing, the bending of light of background galaxies by the haloes of foreground galaxies. This allows the direct imaging of dark matter haloes. Provided that general relativity is correct, there is now no doubt there must exist some form of dark matter.

The nature of dark energy is even less well understood. Some of the best evidence for its existence comes from the expansion of the Universe. The expansion of the Universe was first observed by Edwin Hubble, when he noticed that galaxies seemed to be receding away from each other at a rate that was proportional to their separation (Hubble, 1929). Einstein in his earlier theoretical models had struggled to construct a model that was static, finally resorting to adding a cosmological constant Λ to balance against gravitational collapse. Upon discovering the observed expansion, this additional term was deemed no longer necessary, though it has made occasional reappearances for other

reasons. In 1998 observations of supernovae redshift-luminosity distance relation found that rather than, as long assumed, the rate of expansion of the Universe slowing down, the rate is in fact accelerating (Riess et al., 1998). The simplest explanation for this is a non-zero cosmological constant Λ, that represents some form of dark energy. Other more complicated forms of dark energy are also possible, see Frieman et al. (2008) for a review.

The small perturbations left by inflation grow to form galaxies and clusters. ΛCDM takes the initial conditions to be of the form of a Gaussian random field. Because the amplitude of these irregularities is small they can be treated accurately using linear perturbation theory. By linearising the equations of motion for a multi-component fluid in an expanding universe, the rate of growth as a function of scale can be accurately modelled. Once structures collapse beyond the linear regime, their continuing growth must be studied numerically. How this is done using simulations is outlined in §1.4. Since ΛCDM predicts that the amplitude of the density perturbations is largest on the smallest scales, it is the smallest scale perturbations that collapse first to form haloes. Larger structures are then built up hierarchically through successive mergers of smaller haloes (White and Rees, 1978; Frenk et al., 1985). This hierarchical build-up continues throughout a halo's life. Galaxy-sized dark matter haloes are expected to undergo occasional major mergers with mass ratios $\lesssim$ 1: 3, along with more frequent minor mergers of lower mass ratios $\lesssim$ 1: 10 (Stewart et al., 2008).

ΛCDM has proven incredibly successful at explaining the large-scale structure of the Universe, accurately predicting both the distribution of galaxies and the cosmic microwave background (CMB) angular power spectrum. The real challenge to the model now is whether it works as well on the smaller, galactic scales.

1.2 Dark Matter on Small Scales

Small-scale structure is very sensitive to the exact nature of dark matter and therefore currently provides some of the best ways to test the ΛCDM model. At sub-galactic scales the picture is often more complicated, since baryonic effects are as important as the gravitational physics. Nevertheless, there are several challenges that current galaxy formation models struggle to explain. It is as yet unknown whether these are simply due to a missing important baryonic ingredient in the models or whether they are simply funda-

mentally inconsistent with the ΛCDM paradigm.

During the hierarchical growth of haloes, small haloes frequently merge into more massive haloes. The earliest simulations failed to find any sign of these small haloes surviving within the larger halo (Katz and White, 1993; Summers et al., 1995). This so-called "overmerging" problem turned out to be the result of insufficient mass and force resolution (Moore, 2000). As resolution increased, simulations were able to resolve these accreted haloes as substructures that are not immediately destroyed but continue to survive for a considerable time as gravitationally bound subhaloes orbiting within the larger parent halo (Klypin et al., 1999; Moore et al., 1999a). It is these small subhaloes that are expected to host the visible satellite galaxies seen around the Milky Way and other external galaxies. Throughout this thesis, the terms subhaloes and substructure are used interchangeably.

With higher resolution the problem quickly became one of too many rather than too few substructures. Haloes are predicted to be to rich in substructure (Klypin et al., 1999), but the predicted existence of such a large population of subhaloes has been difficult to reconcile with the relatively few visible satellites observed in the Milky Way. Most subhaloes must not be hosting galaxies. Even though the Sloan Digital Sky Survey (SDSS; Adelman-McCarthy et al., 2008) has doubled the number of known dwarf spheroidal satellites in the recent past (Zucker et al., 2004; Martin et al., 2006; Belokurov et al., 2007; McConnachie et al., 2008), there is still a significant discrepancy between the models and the observations. This 'missing satellite' problem has proven to be one of the major challenges to ΛCDM. The question is whether these subhaloes exist and are dark - meaning they do not contain a visible galaxy - or whether they are absent and there is a problem with the cold dark matter model.

There are two possible solutions to this problem. The first is to modify the nature of dark matter to remove these small structures. One way this could occur is if dark matter is not cold but warm. Simulations with warm dark matter find that the free-streaming in the early universe erases the primordial fluctuations below a certain scale. The exact mass cut-off depends on the nature of the dark matter particle, but could be as large as $10^9 - 10^{10}\mathrm{M}_\odot$, removing exactly those subhaloes expected to host dwarf galaxies (Lovell et al., 2011a).

The other solution is to appeal to additional baryonic astrophysics to prevent stars

forming in small haloes. A combination of photoionization and supernovae feedback can suppress the formation of galaxies in low mass subhaloes, keeping the majority of them dark (Li et al., 2010; Macciò et al., 2010). The photoionization due to a cosmic reionizing background photo-evaporates gas in low-mass haloes, reducing the supply of baryons available for star formation. When stars do form, the feedback from supernovae reheats the cold gas and removes it completely from the shallow potential well of the smaller haloes, further decreasing the efficiency of star formation. The latter explanation is currently the most popular and is thought sufficient to solve the missing satellite problem, but there may well be even more subtle issues with subhaloes in ΛCDM.

Strigari et al. (2010) performed a detailed examination of whether the observed properties of five of the classical Milky Way satellites are consistent with the potentials of ΛCDM haloes. By comparing spherical models with isotropic velocity dispersion tensors to the observed, circularly averaged star counts, line-of-sight velocity dispersion profiles and line-of-sight velocity distributions, they were able to identify subhaloes within high-resolution N-body simulations for which the spherically averaged potentials were excellent fits in five galaxies. However, the circular velocities of the matching substructures were found to be low (10 to 30 kms^{-1}); they were not the largest subhaloes in the simulations. This problem was further highlighted when Boylan-Kolchin et al. (2011) looked at which subhaloes in simulations were most likely to host the Milky Way satellites. They discovered that there remains a population of massive subhaloes that are too dense to host any of the bright satellites of the Milky Way. They used kinematic measurements to estimate the dwarf satellites' masses $M_{1/2}$ and half-light radii, $R_{1/2}$ (Walker et al., 2009; Wolf et al., 2010). Small dwarfs are effectively dark matter dominated within $R_{1/2}$, so $M_{1/2}$ provides a good estimate of the enclosed dark matter mass. These measurements place constraints on the total subhalo mass and sizes, which can be used to eliminate the simulated dark matter subhalo candidates.

The ΛCDM galaxy formation models that were successful at preventing the formation of galaxies in small subhaloes and achieving the correct satellite luminosity function for the Milky Way, put the brightest satellites in the biggest/most concentrated subhaloes, in conflict with the Boylan-Kolchin et al. (2011) result. The current cold dark matter models are able to fulfil the satellite luminosity function, but seem not to put the satellite in the largest subhaloes as would be expected. If true, either the structure of sub-

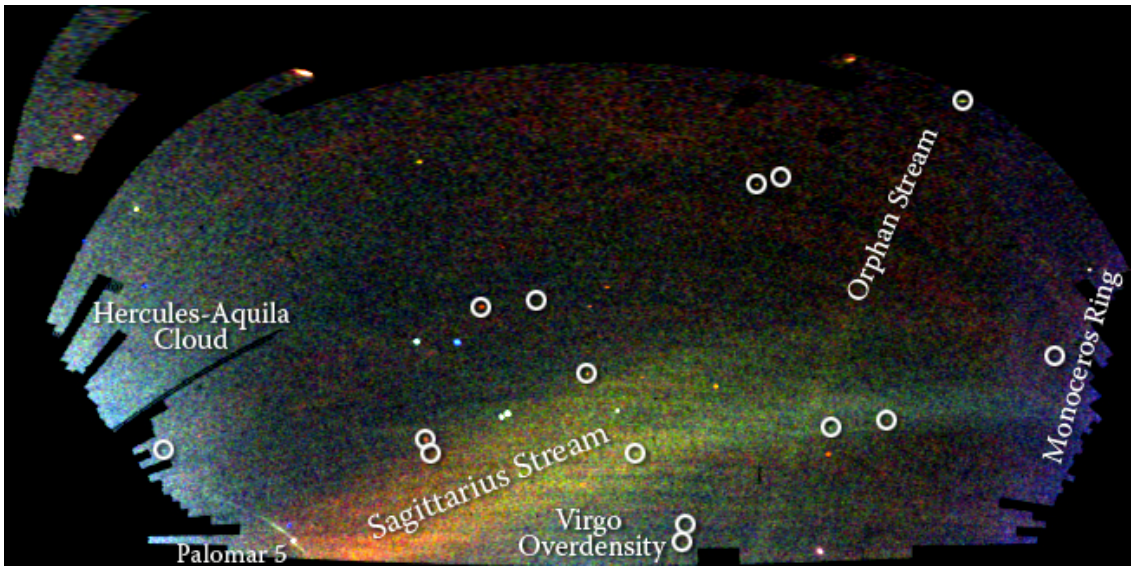

Figure 1.1: The field of streams - an SDSS map of stars in the outer regions of the Milky Way Galaxy, where the colour indicates the distance of the stars and the intensity the density of stars. Structures clearly visible in this image are the Sagittarius stream, the Orphan stream, the Monoceros Ring, as well as several faint dwarf galaxies and globular clusters. *Image courtesy V. Belokurov and The Sloan Digital Sky Survey Collaboration*.

haloes is wrong, or there must be some other reason these remain dark. One explanation for these discrepancies is if the presence of baryons in subhaloes affects their structure. It has long been proposed that the mass loss due to supernova-driven winds could turn dark matter cusps into cores (Navarro et al., 1996a; Pontzen and Governato, 2011).

In addition to the search for the subhaloes themselves, if a subhalo hosts a dwarf galaxy and is very heavily stripped, stars, as well as dark matter, are stripped and left behind in the form of stellar tidal streams. Such stellar streams have been clearly identified in observations. Fig. 1.1 shows what has come to be known as 'the field of streams'. By colouring an SDSS map of stars by their distance, Belokurov et al. (2006) discovered a large number of features in the outer regions of the Milky Way. In the lower half of the image, the Sagittarius Stream stretches from left to right, bifurcating into two distinct arms. Perpendicular to this is a thinner stream, known as the Orphan Stream, and on the far right of the image, a small section of the Monoceros Ring can be seen.

The stellar streams, in particular the extended Sagittarius stream that fully wraps around the Galaxy, can provide valuable information on the shape of the Milky Way

dark matter halo. The stream approximately traces the past orbit of its progenitor (Eyre and Binney, 2011), the Sagittarius Dwarf Elliptical galaxy, which is close to full tidal disruption. There has been extensive effort to produce a theoretical model that can reproduce the characteristics of the stream (Ibata et al., 2001; Helmi, 2004; Martínez-Delgado et al., 2004; Law et al., 2005; Fellhauer et al., 2006; Law et al., 2009; Peñarrubia et al., 2010). However, no one has yet succeeded in creating a model that can explain all the features. The stream's position on the sky suggests that the halo interior to the stream has an oblate or perhaps a nearly spherical shape (Ibata et al., 2001; Fellhauer et al., 2006), while the velocities imply a prolate shape (Helmi, 2004). In addition, a successful model must also explain the bifurcation in the stream. It is uncertain whether this bifurcation is due to the shape of the Milky Way dark matter halo (Fellhauer et al., 2006) or related to properties of the Sagittarius dwarf (Peñarrubia et al., 2010). This remains an active and unsolved area of research.

While dark matter subhaloes have not been directly observed, the dwarf galaxies they are believed to host both tell us a lot about the subhaloes themselves and provide information on the halo of the Milky Way. By attempting to match the predictions of current galaxy formation models for the satellites and streams with observations, we can test ΛCDM on the sub-galactic scale. The results so far seem to hint that there may be problems with the cold dark matter model.

1.3 Interactions of Subhaloes with the Galactic Discs

As well as searching for the direct observable features of subhaloes, there are other more indirect tests of ΛCDM. Dark matter subhaloes should be detectable through the signatures that they leave on the visible components of galaxies, particularly on galactic discs. The majority of stars in spiral galaxies reside in thin discs. Gravitational interactions with dark matter subhaloes should alter the orbits of these stars and should increase their random motions. The fact that thin discs survive in a ΛCDM universe allows us to put constraints on the amount of heating these subhaloes can effect, too much heating and thin discs cannot exist. Yet rare but dramatic encounters between subhaloes and discs have also been suggested as an explanation for the presence of the thick discs that are now found to be a ubiquitous feature of spiral galaxies. In this section the observable

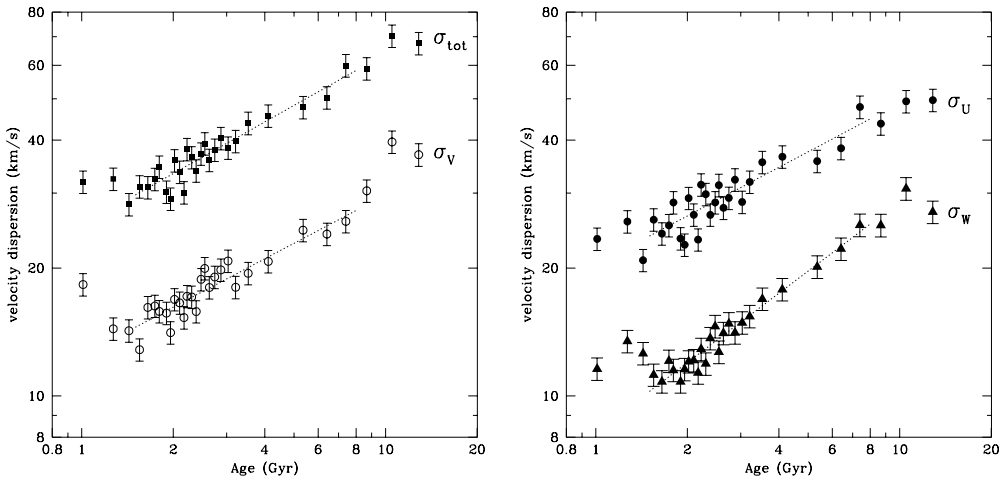

Figure 1.2: The age-velocity relation of stars in the solar neighbourhood from the Geneva-Copenhagen survey subsample. The components of the velocity dispersions are shown for the three directions: radially U, azimuthally V and vertically W, along with the total velocity dispersion. The lines show fitted power laws. *Figure 33 from Holmberg et al. (2007).*

evidence for these features of galactic discs is outlined and a comparison is made between the model of their formation by subhalo bombardment and alternative formation theories.

1.3.1 Disc heating

Young disc stars have been found to have low velocity dispersions, suggesting stars are born on nearly circular orbits. Stars form in giant molecular clouds, and these clouds tend to be found near the mid-plane, where the Milky Way gas disc is densest. Older stellar populations have larger dispersions (Wielen, 1977); some mechanism has 'heated' them from their initial cold state. Nordström et al. (2004) and the follow-up study of Holmberg et al. (2007) used the Geneva-Copenhagen survey of the solar neighbourhood to measure the local age-velocity dispersion of 4065 stars with ages between 1 and 10 Gyr. They find a smooth, general increase of the velocity dispersion with time in all three directions (see Fig. 1.2). The increase is well fitted by the power law $\sigma_i \propto t^{\alpha}$, with $\alpha = 0.38$ in the radial and azimuthal directions and $\alpha = 0.54$ in the vertical direction. This suggests that the disc has undergone continual heating over the past $\sim$10 Gyr.

By contrast, an earlier study by Quillen and Garnett (2001) found that heating of stars in the solar neighbourhood saturates at $\sim$ 3 Gyr, up until 9 Gyr, when there is a sudden increase in the velocity dispersion. They attributed the sudden increase as evidence of a minor merger that creates the thick disc. Though their work is based on a much smaller sample of only 189 nearby, slightly-evolved F and G dwarf stars from Edvardsson et al. (1993), their argument is further supported by Seabroke and Gilmore (2007). They showed that disc heating models that saturate after $\sim$ 4.5 Gyr are equally consistent with the Geneva-Copenhagen survey data. However, the recent analysis of Aumer and Binney (2009) excludes the scenario of Quillen and Garnett (2001), and though they do not completely rule out the Seabroke and Gilmore (2007) model of a later saturation, they still favour an exponential growth with values of α very similar to Holmberg et al. (2007).

Regardless of the exact form of the age-velocity dispersion relation, there is clear evidence that some process is heating the initially cold stars. The other alternative explanation to heating, that older stars were born with larger random speeds, is unattractive, since it would mean that the present low velocity dispersion era is special. There are various possible sources of continuous heating. These may be some internal, secular process such as heating by transient spiral arms in the disc (Barbanis and Woltjer, 1967; Sellwood and Carlberg, 1984) or scattering of stars by giant molecular clouds (GMCs) (Spitzer and Schwarzschild, 1951, 1953; Lacey, 1984), or may be due to the external influence of satellites and dark matter substructure disturbing or merging with the disc (Quinn and Goodman, 1986; Carlberg and Hartwick, 1989; Toth and Ostriker, 1992). Each of these processes has been studied in detail, but it is still unclear which are the dominant ones.

Long-lived spirals that grow and decay on long-time scales compared to the orbital and epicyclic periods of the stars do not change the star's energy or angular momentum, other than near resonances (Lynden-Bell and Kalnajs, 1972). For there to be significant heating by spiral waves they must be transient. Calculations of the expected heating by transient spirals gives a good fit to the observations and estimates of α using the Fokker-Planck equation (Jenkins and Binney, 1990; Jenkins, 1992), and numerical simulations (De Simone et al., 2004) vary between 0.25-0.5. However, the vertical oscillations of stars are little affected, so that the resulting vertical heating predicted is too low (Carlberg, 1987).

While spiral waves increase the random motions of stars, they do not lead to a more relaxed distribution function. Collisional processes, such as the scattering of stars from GMCs or black holes, accelerate the relaxation rate. Often the sites of star formation, GMCs have masses between $10^4 - 10^6 \mathrm{M}_\odot$ and are of the order of tens of parsecs in diameter. Spitzer and Schwarzschild (1951, 1953) first suggested that GMCs might be responsible for increasing the random velocities of disc stars. Lacey (1984) extended their work to three-dimensional discs and derived analytical expressions for the rate at which scattering by clouds increases the vertical and horizontal epicyclic energies of the stars. As stars pass a GMC they acquire a small amount of additional epicyclic motion. The result of many of these weak encounters is an overall perturbation of their velocities. The evolution of the distribution function of the random velocities is then determined by the diffusion equation. Estimates of the number density and masses of GMCs in the solar neighbourhood result in a heating that is too low compared to the observed rates, but this may be enhanced by the spiral wake induced in the stellar disc by the clouds (Julian and Toomre, 1966).

A problem with Lacey (1984) is that he concludes that scattering by GMCs alone would produce a vertical velocity dispersion, σ_z, that is intermediate between the radial, σ_R and the azimuthal, σ_ϕ, velocity dispersion in conflict with the observations. One plausible solution to this is a combination of the two mechanisms; scattering by spiral arms heats the disc and then GMCs redistribute velocities in the plane of the disc into vertical motion (Carlberg, 1987; Jenkins and Binney, 1990). However, Ida et al. (1993) claim that GMCs alone are able to produce the correct ratio σ_z/σ_R, provided the more distant scattering encounters are taken into account.

It has been proposed that if the Galactic dark halo were made up of massive compact halo objects (MACHOS), such as black holes they could be an external source of heating as they pass through the disc. Lacey and Ostriker (1985) calculated that the predicted heating by a population of $2 \times 10^6 \mathrm{M}_\odot$ black holes is consistent with the observed ratio of σ_z/σ_R, but that σ_z and σ_R both grow as $t^{0.5}$, when σ_R should be growing more slowly. Furthermore, black holes of this mass would destroy the discs of dwarf spiral galaxies (Friese et al., 1995). It is generally now regarded as unlikely that dark matter haloes are made up of MACHOS; however, the dark matter substructure of ΛCDM could have a similar effect.

Subhalo bombardment could be a major source of disc heating (Toth and Ostriker, 1992; Font et al., 2001; Benson et al., 2004; Kazantzidis et al., 2008). There is the general consensus that subhaloes can have an appreciable effect on discs, but that discs should survive in the ΛCDM cosmogony. The interactions between dark matter subhaloes and stellar discs are focused on in the second half of this thesis, in an attempt to gauge the heating that these encounters generate and discern whether this contributes significantly to the observed heating.

1.3.2 Thick disc formation

As well as being responsible for the age-velocity dispersion relation in the thin disc, minor mergers of subhaloes and satellites have been proposed as a potential formation mechanism of thick discs (Quinn et al., 1993; Mihos et al., 1995; Walker et al., 1996; Robin et al., 1996; Velazquez and White, 1999; Chen et al., 2001; Villalobos and Helmi, 2008). There is strong evidence to suggest that the Milky Way disc can be separated into two components; a younger thin disc containing the majority of the stars, and a sparser, older thick disc. The existence of a thick disc in the Milky Way was first discovered by Gilmore and Reid (1983), when they found that the vertical distribution of stars in the solar neighbourhood could not be fitted by a single exponential, but was best approximated by two exponential laws. For a long time it was unclear if the thick disc was truly a distinct component of the Milky Way, or if it was only an older, metal-poor extension of the thin disc, created by continuous vertical heating. Now it appears that the thick disc stars also have distinct chemical properties and thus are a separate population. Thick discs appear to be a common, if not ubiquitous, feature of spiral galaxies. They have been detected in S0 galaxies (Burstein, 1979) and many other spirals (Morrison et al., 1997; Dalcanton and Bernstein, 2002; Yoachim and Dalcanton, 2006; Elmegreen and Elmegreen, 2006).

The exact scale heights of the Milky Way thin and thick discs are uncertain and depend on the selection of stars used in the sample. The best fitted model to date, from the SDSS by Jurić et al. (2008) has a thin disc with an exponential scale height $h_z \simeq 300 \pm 60$ pc, a thick disc with scale height of $h_z \simeq 900 \pm 180$ pc, and a local thick-to-thin disc density normalisation of $\rho_{\rm thick}(R_\odot)/\rho_{\rm thin}(R_\odot) = 12\%$. The analysis of Carollo et al. (2010) of SDSS data obtained a smaller exponential scale height for the thick disc $h_z = 640$ pc, but did not treat the thick disc as strictly exponential, as is usually done. The significant

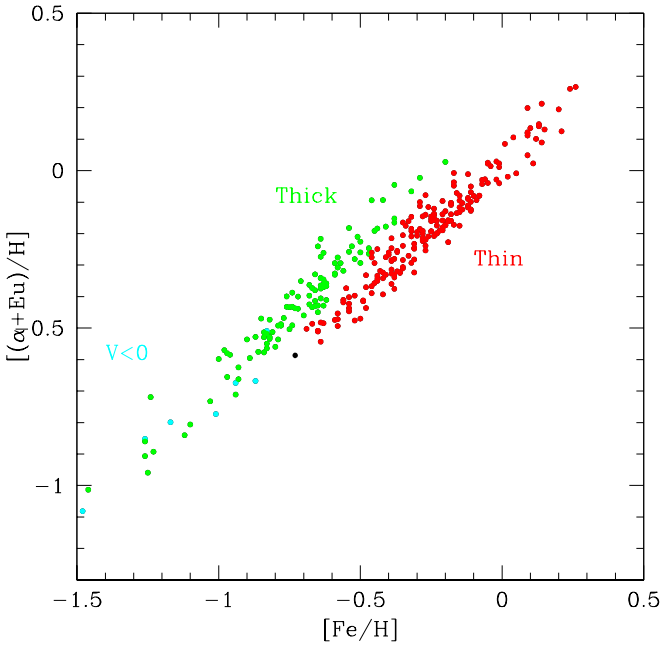

Figure 1.3: Iron abundance versus α elements abundance (plus the element Eu) for the Milky Way disc stars. Points in red represent the stars usually thought to belong to the thin disc. The blue points mark the stars usually associated with the thick disc. The cyan points are counterrotating stars unlikely to belong to either the thin or thick discs. *Figure 1 from Navarro et al. (2011).*

differences in measurements of the scale height of the thick disc may be a reflection of the fact that the vertical structure of the disc is more complicated than uniform scale height models allow. In addition to the structural differences, the thin disc has a small rotational lag with respect to the Sun of 12 kms^{-1}, while the thick disc a has a larger rotational lag anywhere between 20 kms^{-1} (Chiba and Beers, 2000) and 51 kms^{-1} (Soubiran et al., 2003).

The assignment of membership to either the thick disc or the thin disc for individual stars is often ambiguous. Observational studies have established that stars which are kinematically likely to belong to the thick disc are, on average, found to be older (8-12 Gyrs) than stars with kinematics typical of the thin disc ($<$ 10 Gyrs). Thick disc stars are also generally more metal poor, with an average metallicity of <[Fe/H]> $= -0.7$, compared to the thin disc stars which have an average metallicity of <[Fe/H]> $= -0.1 \sim 0.0$ (Gilmore and Wyse, 1985; Reddy et al., 2006; Bensby et al., 2007; Fuhrmann, 2008, 2011).

Unfortunately, both the age and metallicity distributions overlap and on their own cannot be used to discern the membership. However, when considering simultaneously both metallicity and α abundance, the points fall into two distinct populations, clearly evident in Fig. 1.3. These correlate very well with the traditional separation by kinematics, meaning that for a given metallicity the thick disc stars have higher abundances of α elements (Navarro et al., 2011). This chemical difference suggests the two components had different formation histories.

A popular model of the origin of the thick disc is through stars in an initially thin disc being dynamically heated to large scale heights by minor mergers (Quinn et al., 1993; Walker et al., 1996; Robin et al., 1996; Velazquez and White, 1999; Villalobos and Helmi, 2008). As encounters between discs and subhaloes increase the vertical random motions of the stars, they will also increase the thickness of the disc. An encounter between a massive satellite or subhalo and a thin disc at an early time could be responsible for the creation of the thick disc. The encounter would have to occur early in the disc's lifetime in order to allow enough time for the subsequent formation of a younger thin disc from the reformed gas of the merged satellite. This scenario does, however, require that there are no late large mergers, otherwise these would destroy the new thin disc. Since thin discs are prevalent in spiral galaxies, this puts constraints on the number of late mergers and the abundance of substructure within haloes, or limits the heating they can have and implies that some other mechanism formed the thick disc.

There are several other proposed scenarios for thick disc formation. Minor mergers rather than the heating of a thin disc could deposit stars from the smaller satellite galaxies to build up the thick disc through accretion (Abadi et al., 2003). Alternatively, the thick disc could be the result of gas-rich mergers during an early chaotic period (Brook et al., 2004), or a gas-rich initial disc that breaks into clumps through gravitational instabilities, which then scatter stars to high velocity dispersions (Bournaud et al., 2009). A recent model that requires no outside influences is based on the radial migration of stars. Sellwood and Binney (2002) showed that spiral waves can dramatically change the radial orbit of stars while not increasing their random motions. Stars can move considerable distances from their birthplaces but remain on circular orbits. As well as the morphological and kinematical properties of the thick disc, models based on this process claim to be able to reproduce many of its chemical properties (Schönrich and Binney, 2009), but

may find it difficult to explain the counter-rotating thick disc stars that are seen in some spiral galaxies.

Establishing which model can reproduce the metallically and chemical properties of the thick disc may be the best way to discern which of these mechanisms was responsible for the formation of the thick disc. Another way is to look at the distribution of orbital eccentricities of its stars, which is predicted to be different for each model (Sales et al., 2009). It of course may be a mixture of all these mechanisms that contributed to forming the thick disc.

1.3.3 Flares, Warps and Rings

The heating of galactic discs and the thin-thick disc decomposition that have been discussed so far are both global phenomena affecting the whole surface of the disc. It is possible that effects of subhaloes are more localised and that encounters with discs could be responsible for some of the morphological features seen in the Milky Way and other spiral galaxies. The outer regions ($R \gtrsim 12$ kpc) of both the Milky Way's stellar and gaseous discs are warped and flared (Alard, 2000; Momany et al., 2006). 21 cm line surveys of hydrogen in external galaxies revealed that of the order of 50 percent of disc galaxies have warped hydrogen discs (Bosma, 1978).

The SDSS discovered the Monoceros Ring, a coherent ringlike structure at low Galactic latitude spanning about $\sim 170^o$ in the sky (Newberg et al., 2002; Yanny et al., 2003), made up of low-metallicity stars at a distance of ~ 20 kpc. It has been proposed that the ring could be tidal debris stripped from a recently accreted satellite (Peñarrubia et al., 2005), or could be an extension of the stellar disc. The simulations of Kazantzidis et al. (2008) of interactions between a dissipationless N-body disc and accreting massive subhaloes resulted in a very similar feature created through the latter mechanism. Although they were not attempting to reproduce the Monoceros Ring, the structure that formed in their simulations closely matched both the spatial and kinematic measurements of the Monoceros Ring.

Interactions between subhaloes and galactic discs have been suggested to be responsible for all these features present in the Milky Way and other spiral galaxies; the increasing velocity dispersion of thin disc stars, the formation of a thick disc, and distinct morphological features such as flares and rings. Theoretical models have shown that

subhalo encounters are a plausible explanation in all these cases, provided there is a sufficient abundance of substructure at the centre of dark matter haloes. Since thick discs are such a ubiquitous feature, this will have to be proven to be the case for all haloes. A very valuable tool in the effort to solve this question are N-body simulations.

1.4 N-body Simulations

Once structures start to collapse, their growth quickly becomes non-linear and can no longer be predicted analytically. To follow the growth further, it must be modelled using numerical schemes. When modelling the growth of dark matter structure, it is only necessary to consider gravity, for which in the weak Newtonian limit the physics is well understood. The challenge is then to find efficient computational ways to solve problems with as much accuracy as possible.

On astrophysical scales dark matter acts like a continuous collisionless fluid, so that the 6-dimensional phase-space density of dark matter can be described using a distribution function (or DF) f, such that $f(\boldsymbol{x}, \boldsymbol{v}, t)d\boldsymbol{x}^3 d\boldsymbol{v}^3$ is the density of dark matter at time t at a position $\boldsymbol{x}$ and with velocity $\boldsymbol{v}$. By necessity $f \geq 0$ everywhere. The flow of the phase-space density is conserved and obeys

$$(\dot{\boldsymbol{x}}, \dot{\boldsymbol{v}}) = (\boldsymbol{v}, -\nabla\Phi), \tag{1.1}$$

where Φ is the gravitational potential. The gravitational potential and density are related by Poisson's equation

$$\nabla^2\Phi(\boldsymbol{x}, t) = 4\pi G\rho_{\rm tot}(\boldsymbol{x}, t), \tag{1.2}$$

with $\rho_{\rm tot}$ being the total density field.

A common way to follow the evolution of the continuous density field is to discretise it into particles, where each particle has a mass much larger than that expected for the physical dark matter. The N-body particles form a Monte Carlo sampling of the phase-space density distribution and the DF can then be viewed as a probability density where $f(\boldsymbol{x}, \boldsymbol{v}, t)d\boldsymbol{x}^3 d\boldsymbol{v}^3$ gives the probability that a particle is in the given phase-space volume centred on the position $\boldsymbol{x}$ and velocity $\boldsymbol{v}$. The equations of motion are given by equation 1.1 and are solved separately for each particle. On small scales the discrete nature of the N-body approximation introduces sampling shot noise, which is ideally minimised by using as many particles as computationally reasonable.

The usual procedure for evolving the density field is to solve Poisson's equation for a given distribution of particles. As gravity is long range and the potential at one point depends on the density at all other points, this is the most computationally intensive step, and various ways of solving Poisson's equation are discussed below. Using the resulting gravitational potential, the particle positions and velocities are advanced by integrating the equations of motion. In practice this is done by approximating the differentials as finite differences. The particles' new positions and velocities then define a new density field for which the entire process can be repeated.

1.4.1 Solving Poisson's Equation

The simplest way of constructing the potential is through direct summation (it is usually the gradient of the potential, the force, rather than the potential that is usually calculated, as it is this that is needed). The potential at particle i is the sum of the contributions from every other particle j

$$\Phi(\boldsymbol{x}_i) = -G \sum_{j \neq i} \frac{m_j}{\sqrt{|\boldsymbol{x}_i - \boldsymbol{x}_j|^2 + \epsilon^2}}. \tag{1.3}$$

In simulations, particles are treated as point masses, but to avoid introducing unphysical two-body effects such as scattering to large angles, an additional gravitational softening ϵ is usually included. For the potential of each N particles, the contribution from the other $N - 1$ particles needs to be calculated, making this an $\mathcal{O}(N^2)$ operation. Using direct summation quickly becomes computationally infeasible for even modest simulations.

There are various algorithms that through sacrificing some accuracy gain vast computational speed-ups. The N-body code GADGET, which is employed for all the simulations in this thesis, uses two such algorithms, generally one is used for the long range component of the force and the other for the short range component.

Particle-Mesh Algorithm

Particle-mesh (PM) methods (Klypin and Shandarin, 1983; White et al., 1983) involve assigning the density field to a regular grid using an interpolation scheme. There are various possible schemes to map the mass of each particle to a grid point (Hockney and Eastwood, 1988). The simplest is to assign all the mass of each particle to their nearest point. This scheme is rarely used, as it results in discontinuous force changes and

only samples the density crudely. GADGET uses the cloud-in-cell (CIC) method, which expands each particle into a cube of the same size as the grid spacing and splits the mass up over the nearest neighbours of each element of the cube. There are more complex schemes that involve splitting the mass over more cells and give smoother density fields, but these increase the computational cost and reduce the spatial resolution.

From the discretised density field ρ_{ijk}, where the subscripts label the grid cells, the potential can be found by convolution with a suitable Green's function $\mathcal{G}$. This can be quickly solved by taking advantage of the fact that in Fourier space a convolution becomes a simple product. The density field is Fourier transformed $\rho_{ijk} \rightarrow \hat{\rho}_{lmn}$, where the subscripts index the cell in $\boldsymbol{k}$-space, and multiplied by the transform of the Green's function, $\hat{\mathcal{G}}$. The result is transformed back to real space. Once the potential has been found on the grid, the gravitational field is calculated by finite differencing the potential. This is mapped back to the particles by the same interpolation scheme used in the particle-cell assignment.

PM methods are very fast, as the Fourier transformation steps are carried out by efficient FFTs. However, their resolution is limited by the spacing of the grid. On scales compared to the size of the grid cells the force they calculate is significantly smaller than that predicted by the Newtonian inverse force law. The dynamics of small objects therefore are wrong. Larger meshes can help alleviate this problem, but at the cost of dramatically increasing the memory requirements. One solution is to combine the PM method with direct summation for the short scales; Particle-Particle Particle-Mesh schemes, P^3M Efstathiou et al. (1985); Hockney and Eastwood (1988). However, objects tend to become highly clustered and the direct summation often ends up becoming dominant. Another solution is to subdivide the grid only in high density regions, this can be done in an adaptive way as the simulation is running (Couchman, 1991).

Tree codes

Tree codes organise the particles in the simulation into a hierarchical tree structure. The algorithm involves first building the tree and then repeatedly traversing it in order to calculate forces. An octree (Barnes and Hut, 1986) is the most commonly used system. A cube is placed round the entire simulation volume and divided into 8 equal size cubic subcells. If a subcell contains more than a given number of particles, it is again

subdivided in the same way into another 8 subcells. This process of subcell division is recursively repeated until every cell contains less than a specified number of particles. In this manner the levels of cells form a tree-like structure. The largest cube is known as the root node and the subcells are the branches. The final undivided cells are called leaf nodes. For each cell, the force due to the particles contained within it is calculated using a multipole expansion.

The force on a particle can now be found by traversing the tree. Starting from the root node, each subcell is checked to determine whether an opening criterion is met. The opening criterion used by GADGET is that for a cell containing mass, M, of side length, l, and at distance, r, is not opened if

$$\frac{GM}{r^2}\left(\frac{l}{r}\right)^2 \leq \alpha|\boldsymbol{a}|, \tag{1.4}$$

where α is a tolerance parameter that governs the accuracy and $|\boldsymbol{a}|$ is the magnitude of the acceleration of the particle at the previous time step. For cells which are not opened, their contribution is directly added to the accumulating force felt by the particle. When a cell is opened, its subcells are then considered and each tested against the opening criterion. The tree is recursively traversed downwards until all particles have contributed to the force. In this way distant particles are grouped together and contribute collectively through larger-scale nodes.

The contribution each cell makes to the force depends on the number of multipole moments that are included. Using more terms gives greater accuracy and allows use of a larger opening criterion, so that the tree does not need to be traversed as deeply. However, this is balanced against the increased memory requirements and computational cost of calculating the higher order moments. The original version of GADGET (Springel et al., 2001b) evaluated up to the quadrupole moment. Later versions only use the monopole term and instead walk deeper into the tree. The gravity calculation in the tree method scales as $\ln N$ for each particle, making the entire process an $\mathcal{O}(N \ln N)$ operation. GADGET can be used as a TreePM code; the potential is split into a long-range part calculated by the PM method and a short-range-part calculated by the tree. These two components combined give close to the exact force in a more efficient manner than using either methods for the entire range of scales (Springel, 2005).

A final method that can be suitable for certain types of simulations is to use a basis

function expansion, such as the self-consistent field method. A new application based on the principles of this method is discussed in chapter 3.

1.4.2 Finding Substructure

The output from a simulation is usually a set of instantaneous 'snapshots' that store the position and velocities of all the particles at specified times. However, it is often of more interest how the particles are organised into groups and bound haloes. There are various algorithms that can either be run on the fly or can post-process the snapshots to identity groups.

The friends-of-friends (FOF) algorithm (Davis et al., 1985) is used to connect particles that are close together into groups. The algorithm works by linking together particle pairs separated by less than some fraction b of the mean interparticle separation. The particles are linked associatively to build up larger groups. A linking length of $b = 0.2$ is commonly used. The properties of all FOF groups with at least 20 particles are stored in group catalogues, these usually include total mass, centre of mass and velocity.

FOF groups are made up of particles close together but not necessarily gravitationally bound. In order to find bound substructures, more complicated halo-finder algorithms are used. The one relied on in this thesis is the SUBFIND algorithm (Springel et al., 2001a). The SUBFIND algorithm looks for bound subhaloes within FOF groups. It uses an SPH estimate of the local dark matter density to locate density maxima and then continues to group together associated nearby particles until it reaches a saddle point in the density. For each set of candidates it then iteratively removes unbound particles. Each particle in the simulation can only be a member of at most one subhalo. If more than 20 particles remain, the particle group is catalogued as a subhalo. The algorithm works from the highest density maxima downwards, so is able to locate subhaloes within subhaloes. In addition to storing many of the same properties as for FOF groups, SUBFIND groups also store the position of minimum potential as given by the most bound particle, the halo spin, velocity dispersion, maximum circular velocity, and the radius where this occurs, as well as the radius containing half the mass.

Merger trees are used to track the subhaloes through the simulation (Lacey and Cole, 1993). They link together subhaloes between successive snapshots tracking all the subhaloes that merged to create each descendant. They allow the subhaloes' orbits and

structural evolution to be followed. Each subhalo is said to have only a single unique descendant, but can have multiple progenitors if several subhaloes merged to form it. Possible descendants are determined by finding all subhaloes in the snapshot S_{N+1} that contain at least one bound particle which was previously a member of the given subhalo at snapshot S_N. The subhalo with the highest weighted score based on the particles' binding energies from S_N is defined to be the descendant (Helly et al., 2003). The algorithm also checks the next snapshot S_{N+2}, in case the subhalo was temporarily lost in the immediate snapshot; this can occur when a subhalo passes near another more massive subhalo.

SUBFIND suffers from a number of issues in defining the exact membership of a subhalo. Since the algorithm only considers particles within a density saddle point, the number of particles assigned to a subhalo depends on the background density. Particles which may belong to the subhalo but are outside the saddle point will not be grouped into the subhalo. Therefore a subhalo located near the centre of a larger halo will often be found to have a considerably smaller mass than if it was isolated from any other haloes (Muldrew et al., 2011). In addition to this, the overall binding energy of subhaloes orbiting within a larger halo is affected by the position along the orbit within the host halo. This environmental dependence is not considered by SUBFIND, which leads to further underestimates of subhalo masses as they make pericentric passages.

1.5 Structure of this Thesis

In this thesis we explore the interactions of dark matter subhaloes on galactic scales. As we have outlined, at this level there are several discrepancies between the predictions of ΛCDM models of galaxy formation and observations of the satellites and streams around the Galaxy. We focus on that of interactions between subhaloes and galactic discs, as this is primarily a gravitational process related to perturbations of stellar orbits, and is less sensitive to the more complicated and possibly unknown baryonic physics. We aim to test whether subhaloes can have a visible effect on galactic discs, whether they are the main cause of disc heating, and whether the level of heating predicted in ΛCDM is consistent with the thinness of spiral galaxies.

We start by outlining the Aquarius project, a set of high-resolution N-body dark

matter simulations. These simulations of haloes provide the dataset that much of the work in this thesis is based on and so we spend some time detailing the properties of these haloes and examining whether they are a good representation of Milky Way like haloes. In chapter 3, we develop a method of approximating the potential of a simulated halo using a basis function expansion. This allows orbits to be integrated within an approximation of a realistic halo potential at much cheaper cost than the rerunning of a full N-body simulation. Using this technique, the orbits of subhaloes can be recovered in much greater detail than is stored in the limited outputs of the Aquarius simulations.

The second half of this thesis looks at the problem of encounters between dark matter subhaloes and galactic discs, with a particular focus on assessing the resulting disc heating. The Aquarius simulations are used to provide details of the expected frequency of interactions between subhaloes and discs and the expected parameters of such encounters. We first use the Benson et al. (2004) semi-analytical models of disc heating to gain understanding of the process and attempt to estimate the heating that could occur in haloes like the Aquarius haloes. However, problems with the model lead us to perform full high-resolution dissipationless N-body simulations of the same interactions in chapter 5. Using a simple N-body model disc galaxy we directly measure the disc heating in a cosmological context, as well as allowing us to test the validity of the Benson model.

Chapter 2

Aquarius Simulations

2.1 Introduction

In this chapter we take a detailed look at the haloes of the Aquarius project, a set of high-resolution dark matter only N-body simulations of Milky Way-like haloes. These simulations are used as the basis for much of this thesis. They have been the subject of multiple papers exploring various aspects of halo formation. We bring together the main results from a selection of these papers to provide an overview of the Aquarius haloes and set the context for the later work in this thesis. In addition, we present some new results on the convergence of halo shapes that further aid an understanding of the central regions of dark matter haloes.

For over 20 years simulations have been used in an attempt to comprehend the growth and structure of dark matter haloes (Frenk et al., 1988; Dubinski and Carlberg, 1991; Warren et al., 1992; Cole and Lacey, 1996; Ghigna et al., 1998; Moore et al., 1999a). They have revealed many important insights into the dark matter haloes in which galaxies form; that haloes are well described by universal density profiles, are triaxial in shape and are rich in substructure. The initial power spectrum of density fluctuations in the CDM cosmogony has power on all scales, and this affects the internal evolution of haloes on a wide range of scales. The quest to probe the structure and substructure of haloes in greater detail and at smaller scales has resulted in the running of ever higher resolution simulations. These higher-resolution simulations not only better resolve the small-scale structure but also allow us to check that the results truly converge and are not just the result of artificial numerical limitations (Power et al., 2003; Diemand et al., 2004).

Unfortunately, haloes cannot be studied in isolation. To ensure that all relevant factors, including those of environment, are considered when modelling their formation, they must be simulated in the full cosmological context. To this end the method of zoom simulations has been developed to allow resources to be concentrated on the objects of

interest while still including the surrounding large-scale structure (Navarro and White, 1994; Frenk et al., 1996). This technique involves initially running a lower resolution simulation from which to select the objects of further interest. The particles making up these objects are tracked back to the initial conditions to identify the regions in which they originated. These regions in the initial conditions are then resampled with a larger number of lower mass particles, with additional power introduced in the higher frequencies. When the simulation is rerun, the object evolves in a similar manner as before, but at higher resolution and with extra detail on small scales.

Dark matter only simulations, such as the Aquarius simulations, do not include baryons or any of their associated physics. This massively simplifies the problem, as the non-linear growth of dark matter structure is a well-posed problem, but means that the simulations do not provide a complete picture. On large scales, where gravity dominates, the difference is expected to be negligible, but on small-scales, particularly at the centre of haloes where galaxies reside, the addition of baryons can drastically change haloes (Gnedin et al., 2004; Mashchenko et al., 2006, 2008; Debattista et al., 2008; Abadi et al., 2010; Bett et al., 2010). It is still possible to learn a lot about dark matter structure as the coupling is weak, but all results must be interpreted with the caveat that actual galaxies may be very different.

There is particular interest in simulating haloes similar to that in which the Milky Way is believed to reside. Recent estimates for the mass of the Milky Way halo range from $1 \times 10^{12}\mathrm{M}_{\odot}$ to $3 \times 10^{12}\mathrm{M}_{\odot}$ (Wilkinson and Evans, 1999; Sakamoto et al., 2003; Battaglia et al., 2005; Dehnen et al., 2006; Xue et al., 2008; Li and White, 2008). Lately, there have been significant efforts to simulate haloes in this range, with the largest simulations to date having over one billion particles within the virial radius, with particle masses $\sim 1000\ \mathrm{M}_{\odot}$. These include the Via Lactea II (Diemand et al., 2008) and the GHALO_2 (Stadel et al., 2009) simulations. However, both are of only a single object. The Aquarius project takes the approach of simulating one halo at ultra-high resolution and then five others at slightly lower but still impressive resolution to provide an ensemble of haloes for us on which to study the process galaxy formation.

Name	$m_{\rm p}$ ($\rm M_\odot$)	ϵ (pc)	$N_{\rm hr}$	$N_{\rm lr}$
Aq-A-1	1.712×10^3	20.5	4,252,607,000	144,979,154
Aq-A-2	1.370×10^4	65.8	531,570,000	75,296,170
Aq-A-3	4.911×10^4	120.5	148,285,000	20,035,279
Aq-A-4	3.929×10^5	342.5	18,535,972	634,793
Aq-A-5	3.143×10^6	684.9	2,316,893	634,793
Aq-B-2	6.447×10^3	65.8	658,815,010	80,487,598
Aq-B-4	2.242×10^5	342.5	18,949,101	648,874
Aq-C-2	1.399×10^4	65.8	612,602,795	78,634,854
Aq-C-4	3.213×10^5	342.5	26,679,146	613,141
Aq-D-2	1.397×10^4	65.8	391,881,102	79,615,274
Aq-D-4	2.677×10^5	342.4	20,455,156	625,272
Aq-E-2	9.593×10^3	65.8	465,905,916	74,119,996
Aq-E-4	2.604×10^5	342.5	17,159,996	633,106
Aq-F-2	6.776×10^3	65.8	414,336,000	712,839
Aq-F-3	2.287×10^4	120.5	122,766,400	712,839

Table 2.1: Basic parameters of the six Aquarius haloes. $m_{\rm p}$ is the particle mass in the high-resolution region, ϵ is the Plummer-equivalent gravitational softening length, $N_{\rm hr}$ is the number of high-resolution particles in the simulation and $N_{\rm lr}$ the number of lower resolution, more massive surrounding particles.

2.2 Simulation Parameters

The Aquarius project (Springel et al., 2008) consists of six dark matter haloes of mass $\sim 10^{12} M_\odot$ simulated at multiple resolutions. The simulations use the standard ΛCDM cosmology with parameters chosen to be consistent with the results from the *WMAP* 1-year data (Spergel et al., 2003) and the 2dF Galaxy Redshift Survey data (Colless et al., 2001): matter density parameter, $\Omega_M = 0.25$; cosmological constant, $\Omega_\Lambda = 0.75$; power spectrum normalisation, $\sigma_8 = 0.9$; spectral index, $n_s = 1$; and Hubble parameter $h = 0.73$. The cosmology is the same as that used in the Millennium (Springel et al., 2005) and Millennium-II (Boylan-Kolchin et al., 2009) simulations. The six haloes were selected randomly from the set of all isolated $\sim 10^{12} M_\odot$ haloes from a lower resolution 900^3-particle parent simulation of a $100 h^{-1}$ Mpc box (Gao et al., 2008), where isolated means

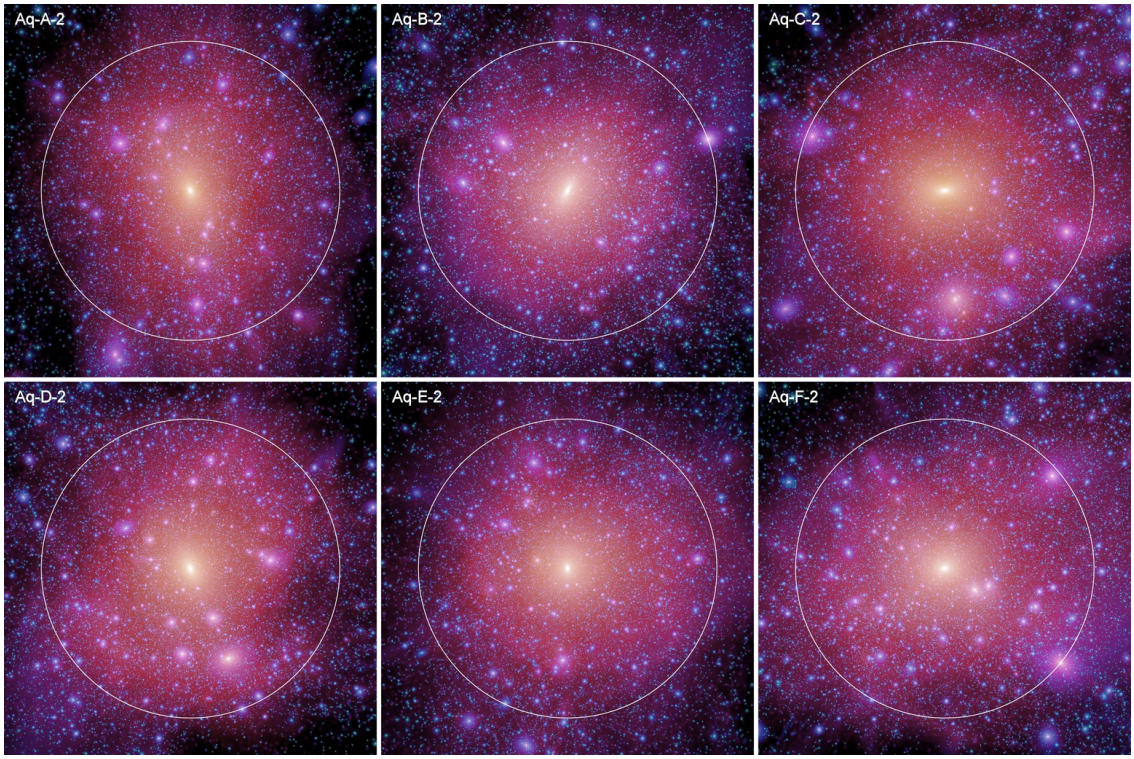

Figure 2.1: Projected dark matter density squared of the six level-2 Aquarius haloes. The circles mark the radius r_{50}, the radius enclosing a mean overdensity 50 times the critical value. The intensity of each pixel is proportional to the logarithm of the squared dark matter density projected along the line of sight and the colour encodes the mean dark matter velocity dispersion. *Figure 3 from Springel et al. (2008).*

that a halo had no neighbours exceeding half its mass within $1h^{-1}$ Mpc. This is a weak selection criterion, to ensure that the haloes were not members of any massive groups or clusters.

The six haloes are labelled 'Aq-A' through 'Aq-F'. Each halo has been resimulated at several resolutions in order to allow tests of numerical convergence. At each resolution the power spectrum and phases have been carefully replicated in order to ensure that the resolved structure is accurately replicated in all the runs. The different resolution levels are identified by the suffix 1-5, with level 1 being the highest resolution. Due to the computational cost only one halo, Aq-A, has been simulated at level 1 and has over 1.1 billion particles within the virial radius. All six haloes have been simulated at the level 2 resolution, with a particle mass $m_p \simeq 1.4 \times 10^4 \mathrm{M}_\odot$ and softening length $\epsilon \simeq 66$ pc; each has over 100 million particles within the virial radius. The numerical parameters

Name	M_{200} ($M_\odot$)	r_{200} (kpc)	$V_{\rm max}$ (kms^{-1})	$r_{\rm max}$ (kpc)	$c_{\rm NFW}$	$z_{\rm form}$
Aq-A-1	1.839×10^{12}	245.76	208.75	28.35	16.11	1.93
Aq-A-2	1.842×10^{12}	245.88	208.49	28.14	16.19	1.93
Aq-A-3	1.836×10^{12}	245.64	209.22	27.88	16.35	1.93
Aq-A-4	1.838×10^{12}	245.70	209.24	28.20	16.21	1.93
Aq-A-5	1.853×10^{12}	246.37	209.17	28.55	16.04	1.93
Aq-B-2	8.194×10^{11}	187.70	157.68	40.15	9.72	1.39
Aq-B-4	8.345×10^{11}	188.85	159.03	44.31	9.02	1.39
Aq-C-2	1.774×10^{12}	242.82	222.40	32.47	15.21	2.23
Aq-C-4	1.793×10^{12}	243.68	223.20	33.63	14.84	2.23
Aq-D-2	1.774×10^{12}	242.85	203.20	54.08	9.37	1.51
Aq-D-4	1.791×10^{12}	243.60	204.47	55.76	9.18	1.51
Aq-E-2	1.185×10^{12}	212.28	179.00	55.50	8.26	2.26
Aq-E-4	1.208×10^{12}	213.63	182.68	54.59	8.52	2.26
Aq-F-2	1.135×10^{12}	209.21	169.08	42.67	9.79	0.55
Aq-F-3	1.101×10^{12}	207.15	174.05	43.76	9.82	0.55

Table 2.2: Basic structural properties of the main haloes in the Aquarius simulations. r_{200} is the virial radius, defined as the radius enclosing a mean overdensity 200 times the critical value, M_{200} is the mass within the virial radius, $V_{\rm max}$ the maximum circular velocity, $r_{\rm max}$ is the radius where this maximum is reached, $c_{\rm NFW}$ is the concentration of an NFW profile fit to the halo. $z_{\rm form}$ gives the formation redshift of the halo, defined as the earliest epoch at which the M_{200} mass of the main halo progenitor exceeds half its final value.

for all the Aquarius simulations are given in Table 2.1. The projected dark matter density squared of the six haloes at level 2 resolution can be seen in Fig. 2.1. It is clear that the haloes are complex objects, rich in substructure. Throughout this thesis we primarily focus on the level 2 simulations, the highest available for all six haloes, with the lower resolution simulations occasionally used for testing convergence.

2.3 Main Halo Properties

The basic structural properties of the main haloes in the Aquarius simulations are listed in Table 2.2. The size and mass of dark matter haloes are usually defined by the region within which virial equilibrium holds, the virial mass M_Δ and the radius r_Δ. The bounded region is usually calculated based on the sphere which encloses a mean density $\Delta\rho_{\rm crit}$. There are several different choices of Δ used in the literature; the most common ones are a fixed overdensity $\Delta = 200$ (labelled r_{200} and M_{200}) (Navarro et al., 1996b), $\Delta \sim 178\,\Omega_m^{0.45}$ based on the spherical top-hat collapse model (labelled $r_{\rm vir}$ and $M_{\rm vir}$) (Eke et al., 1996; Bryan and Norman, 1998), and $\Delta = 200\,\Omega_m(z) = 50$, which gives a fixed overdensity relative to the background density (labelled r_{50} and M_{50}) and encompasses the largest radius. For a given halo $M_{200} < M_{\rm vir} < M_{50}$. We usually adopt r_{200} and M_{200} throughout this thesis unless otherwise noted. The other definitions are occasionally used when reviewing results from other authors. The virial masses of five of the six haloes lie within the possible range of the Milky Way, with halo Aq-B slightly below but still within the uncertainty of the lower estimates.

2.3.1 Density Profiles

It has been proposed that dark matter haloes are well fitted by a universal density profile (Navarro et al., 1996b, 1997, hereafter NFW). The NFW profile is given by

$$\rho(r) = \frac{\rho_s}{\left(\frac{r}{r_s}\right)\left(1+\frac{r}{r_s}\right)^2}, \tag{2.1}$$

where ρ_s and r_s are a characteristic density and radius. It has a broken power-law like form and asymptotes to a fixed power-law slope of -1 at the centre. The concentration is defined as $c_{\rm NFW} = r_{200}/r_s$.

In the central regions of simulated dark matter haloes the finite resolution of the simulations become important and the numerical noise due to the small particle numbers means that measurements of the halo properties become unreliable. The multiple levels of resolution for each halo allows quantitative estimates to be made of how close to the centre the haloes can be trusted. Power et al. (2003) proposed a "convergence radius" down to which the density profile of a simulation of a halo can be believed to some precision, usually chosen to be deviations of approximately 10 percent in the circular velocity

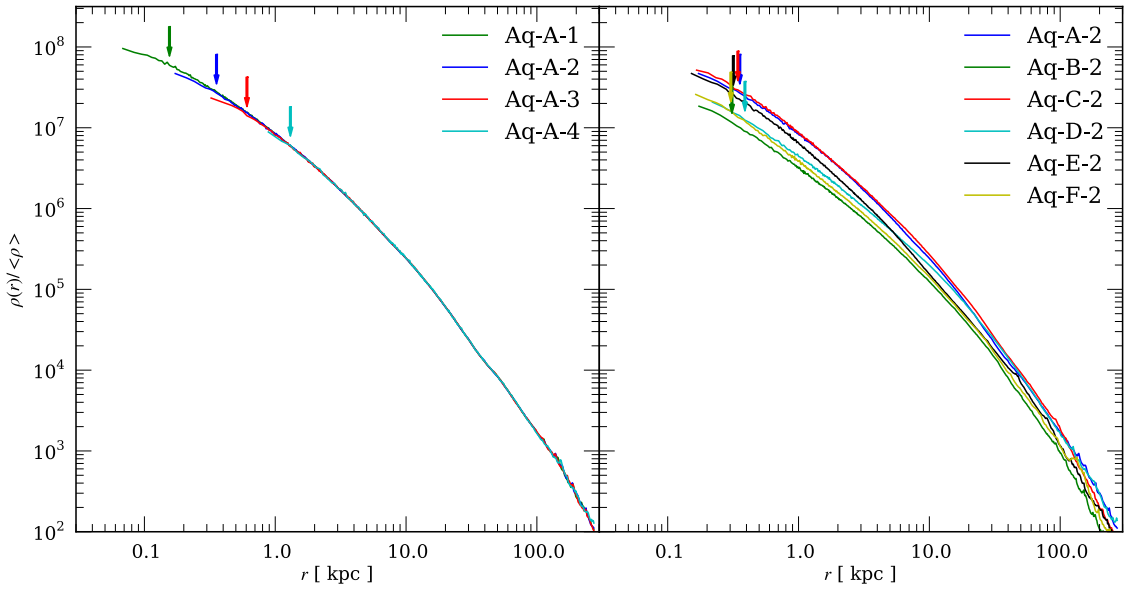

Figure 2.2: Spherically averaged density profiles of the main Aquarius haloes at $z = 0$. *Left panel:* density profile of the different resolutions of the Aq-A halo. *Right panel:* the density profiles of the level 2 resolution for all six haloes. The arrows mark the radii to which the profiles are expected to be converged according to the Power et al. (2003) resolution criteria.

profile. Below this, the mass profiles diverge due to systematic deviations which depend on the number of particles, and that scale roughly with the collisional "relaxation" time, $t_{\rm relax}$ (Binney and Tremaine, 2008). The relaxation time, κ, expressed in units of the circular orbit timescale at the virial radius, r_{200} can then be written as

$$\kappa(r) = t_{relax}/t_{circ}(r_{200}) = \frac{N}{8\ln N}\frac{r/V_c}{r_{200}/V_{200}} = \frac{\sqrt{200}}{8}\frac{N(r),}{\ln N(r)}\left(\frac{\bar{\rho}(r)}{\rho_{crit}}\right)^{-1/2} \tag{2.2}$$

where $N(r)$ is the number of particles within r and $\bar{\rho}(r)$ the mean density enclosed within a sphere of radius r. The convergence radius, with deviations of roughly 10 percent in the circular velocity profile, occurs where $\kappa \approx 1$. Stricter criteria require greater values of κ. Deviations of only 2.5 percent occur where $\kappa \approx 7$ (Navarro et al., 2010).

The spherically averaged density profiles of the main Aquarius haloes at $z = 0$ are plotted in Fig. 2.2. The arrows mark the convergence radii, $\kappa \approx 1$, for the different simulations. It can be seen that there is remarkable convergence between the different levels of the Aq-A halo, right down to the convergence radii, inside of which the profiles start to flatten out. This suggests that the results from the level-2 haloes that we use

throughout this thesis can be trusted down to 500 pc.

Previous simulations have lacked the resolution necessary to probe close enough to the centre to conclusively determine whether halo density profiles continue to follow an NFW form or whether they are better fitted by a profile without power-law asymptotic behaviour, such as the Einasto profile (Einasto, 1965; Navarro et al., 2004). It is only with such high-resolution simulations as the Aquarius or GHALO$_2$ (Stadel et al., 2009) simulations that these questions can be tackled. Fits to the Aquarius haloes' density profiles by Navarro et al. (2010) find that the haloes are better fitted by an Einasto profile. The Einasto profile has the form

$$\ln(\rho(r)/\rho_{-2}) = (-2/\alpha)[(r/r_{-2})^{\alpha} - 1], \tag{2.3}$$

where ρ_{-2} is the density when the logarithmic slope is -2, and r_{-2} the radius where this occurs. α is an additional free parameter, so it may not be surprising that this profile provides a better fit than an NFW. Navarro et al. (2010) show this to be still the case even for a fixed value of α = 0.157 and so conclude that an Einasto profile is their preferred model for a halo. This is consistent with their result that the smallest radius at which the slope of Aq-A-1 halo can still be trusted, it is shallower than -1. The level-2 resolution haloes also support this, suggesting inner slopes of -1 or shallower. The results from the GHALO$_2$ simulation agree with this conclusion. Stadel et al. (2009) found that the density profile of the GHALO$_2$ has an inner slope of -0.8 at 160 pc and is also very well fitted by an Einasto profile.

2.3.2 Velocity Dispersion

Measuring the mass profile of actual galaxies can only be done through indirect observations, either through galaxy-galaxy lensing which requires the stacking of a large number of galaxies (Treu and Koopmans, 2004; Gavazzi et al., 2007), or by using a dynamical tracer. For the Milky Way, convenient tracers of disc rotation such as stars and gas clouds only extend outwards to $\sim$ 20 kpc (Sofue et al., 2009). At greater distances statistical analysis of radial velocities must be used (Kochanek, 1996; Wilkinson and Evans, 1999; Sakamoto et al., 2003). Another way of estimating the Galaxy's mass profile is to use measurements of its radial velocity dispersion with spherical Jeans modelling (Gnedin et al., 2010). Based on 240 halo objects between 30 kpc and 50 kpc, Battaglia et al. (2005)

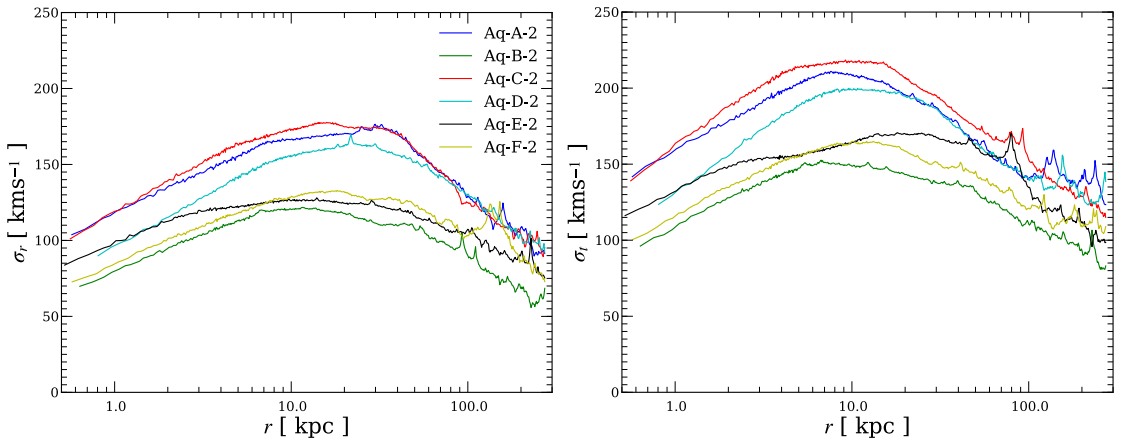

Figure 2.3: The velocity dispersion profiles of the level 2 main Aquarius haloes at $z = 0$. *Left panel:* the radial velocity dispersion. *Right panel:* the tangential velocity dispersion.

found that the radial velocity dispersion decreases from 120 kms^{-1} to 50 kms^{-1}. In contrast, Brown et al. (2010), using a spectroscopic sample of 910 distant halo stars from the Hypervelocity Star survey, found a slower decrease from 110 kms^{-1} at $R = 15$ to 85 kms^{-1} at 80 kpc. The radial velocity dispersion curves of the Aquarius haloes, plotted in Fig. 2.3, manifest the same trend. While the decrease in the Battaglia et al. (2005) result is considerably steeper than the radial velocity dispersion curves of any of the Aquarius haloes, the slope of the Brown et al. (2010) sample is consistent with the Aquarius haloes though slightly lower in value. The Aquarius curves are calculated by binning the simulation particles into radial shells and finding the velocity dispersion in the radial and tangential direction. The results are very similar for all the haloes and peak around 20 kpc before decreasing outwards.

The Aquarius tangential velocity dispersion curves have a similar shape to the radial ones but peak at smaller radii. Combining these two into a velocity anisotropy, defined as

$$\beta = 1 - \frac{\sigma_t^2}{2\sigma_r^2}, \tag{2.4}$$

allows us to assess the motion of material at each radii. The velocity anisotropy is shown in Fig. 2.4. The haloes all follow the same trends, they are isotopic near the centre and become increasingly dominated by radial dispersion further out. At even greater radii this radial dispersion declines, until near the virial radii they are once again isotopic. The large spikes in the curves are due to the coherent motions of particles bound in sub-

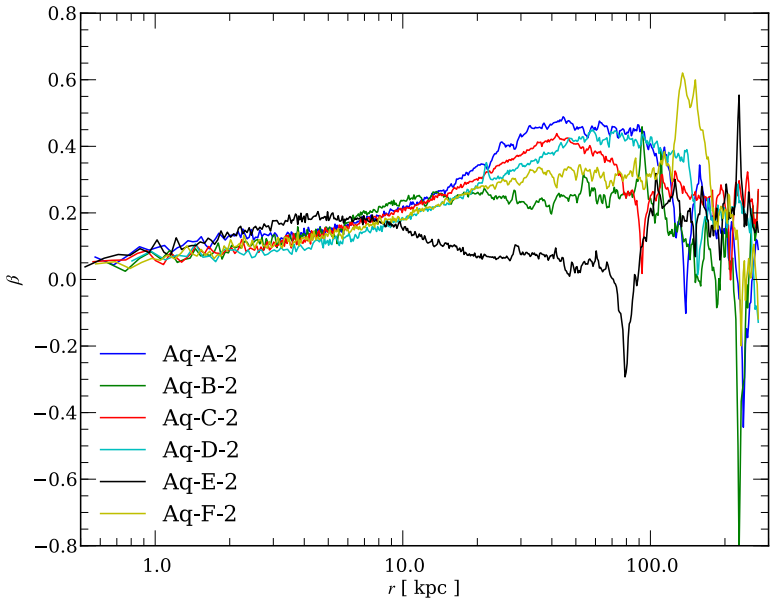

Figure 2.4: The velocity anisotropy of the main Aquarius haloes at $z = 0$ from the level-2 simulations.

structures. The shape of the curve is consistent with other pure dark matter simulations (Cole and Lacey, 1996), which have found that $\beta = 0$ at the centre and increases to 0.5 in the outer regions. The difference in the anisotropy of Aq-E is discussed later.

2.3.3 Mass assembly

As well as studying their final $z = 0$ properties, it is interesting to look at how the Aquarius haloes were built up. This has been done in detail by Wang et al. (2011) and we summarise their main conclusions here. The growth of the mass of the main friends-of-friends (FOF) progenitor of the six Aquarius haloes is shown in Fig. 2.5. To allow a direct comparison, the haloes are all normalised to have mass of one at $z = 0$. Any merger events with a mass ratio greater than $f_m = M_2/M_1 = 0.05$ are represented by vertical lines colour coded for each halo.

As listed in Table 2.2, the formation time of the haloes, defined as the redshift when the halo first reaches half its final mass, all lie in the range $z \sim 1.3 - 2.3$, except for Aq-F. The Aq-F halo is different in that it experiences a late time major merger with a mass ratio $f_m = 0.75$, followed quickly afterwards by a second smaller merger with $f_m = 0.31$. This makes it special in many ways as at the final time the halo is still recovering from these

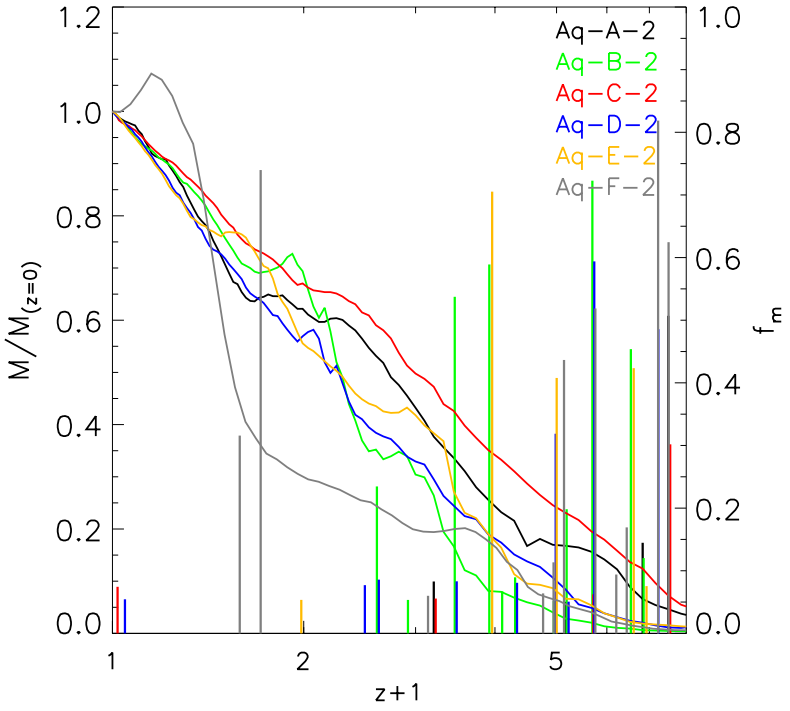

Figure 2.5: The evolution of the mass of the main FOF progenitor of the six Aquarius haloes in the level-2 simulations. The masses (left axis) have all been normalised to one at $z = 0$. The vertical lines represent the mass ratios (right axis) of major merger events the FOF groups experienced. *Figure 1 from Wang et al. (2011).*

events. The other five haloes have similar mass growth histories to each other but show more variation in their merger histories. Haloes Aq-A and Aq-C experience no major mergers after $z = 6$, while haloes Aq-B, Aq-D and Aq-E suffer from a variety of mergers between $z \sim 2 - 7$. At the end of this chapter we will compare the assembly histories of the Aquarius haloes against a bigger sample from a larger simulation to show that they span a diverse and representative range of assembly histories.

In the hierarchical model of formation haloes grow through repeated mergers of smaller haloes. This can be tested by looking at the manner in which the material at different radii originally entered the halo. Fig. 2.6 shows the fraction of the material in each radial spherical shell that was accreted through major mergers with mass ratios $\geq 10 : 1$, that came via minor mergers and that arrived via smooth accretion, namely accretion of those particles that were not a member of any FOF group immediately before they entered onto the main halo. It is clear that major mergers contribute most of the

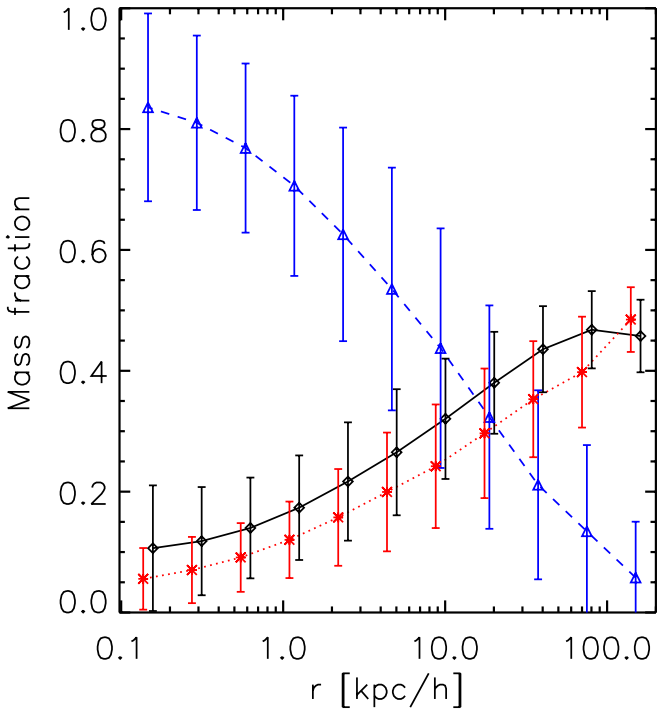

Figure 2.6: The origin of the particles at each radius at the final time $z = 0$. The blue triangles indicate that the particles entered the halo as part of a major merger, the red stars a minor merger and the black squares mean the particles were smoothly accreted. The symbols mark the average for all six haloes and the error bars the rms scatter. *Figure 7 from Wang et al. (2011).*

mass in the central regions. Over two-thirds of the particles within 1 h^{-1} kpc entered the halo as part of a major merger. However, typically less than 1 percent of the total mass of a halo is found in this region. The fraction from major mergers rapidly drops away from the centre. Outside of 10 h^{-1} kpc minor mergers and smooth accretion contribute equally and dominate over major mergers. Overall the total amount of material coming from major mergers ranges from 3 percent (Aq-A) to 26 percent (Aq-F). The universal fraction of material that is expected to accrete into haloes in a smooth manner is at least 10 percent (Angulo and White, 2010), but since simulations can only resolve down to a limited mass for substructure this fraction will be higher, around 30-40 per cent. This is exactly what is found in the level-2 Aquarius simulations.

The haloes grow in an inside-out fashion. Fig. 2.7 breaks down what fraction of mass in concentric radial shells is accreted in various redshift intervals. The cores of Aq-A

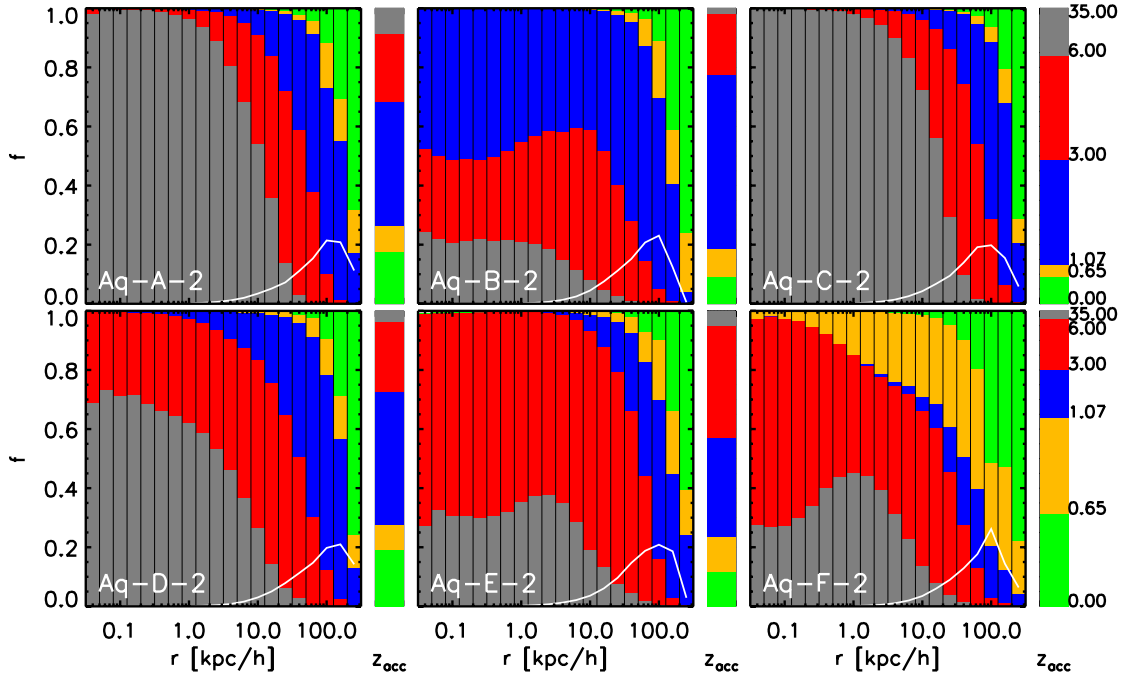

Figure 2.7: The fraction of mass in each spherical shell that is accreted in various redshift intervals is indicated by the proportion of the vertical bar each colour occupies. The white curve gives the fraction of the total mass in each shell, while the larger bars to the right show the fraction of the total mass accreted in each redshift interval. *Figure 4 from Wang et al. (2011).*

and Aq-C are already in place before $z = 6$. The particles in the cores of haloes Aq-D, Aq-E and Aq-F take slightly longer to be assembled, but are there by $z = 3$. Even the late major merger of Aq-F has little effect on the innermost core, instead depositing mass at 1 h^{-1} kpc outwards. Only halo Aq-B takes until $z = 1$ to be built. This is due to two major mergers that happen between $z = 1$ and $z = 3$ and bring in 50 percent of the mass. The haloes have onion-like growth, new material is added to the outer regions, while the centres are older and are less affected by what happens later. This reflects what has been previously found for substructure, subhaloes near the centre tend to have been accreted earlier, while recently accreted subhaloes tend to occupy the outer regions (Gao et al., 2004).

2.4 Halo Shape

The shape of the dark matter haloes is another important property that the Aquarius simulations offer a unique opportunity to study. Most analytical models of galaxy haloes treat the haloes as spherically symmetric objects. They describe quantities such as the density profile averaged over spherical shells. However, even from the earliest N-body simulations (Frenk et al., 1988; Dubinski and Carlberg, 1991; Warren et al., 1992; Cole and Lacey, 1996) it was known that dark matter haloes are more complicated than this. Haloes were found to be triaxial, with more prolate shapes near the centre and oblate shapes in the outer regions. Recent high-resolution simulations have yielded similar results (Allgood et al., 2006; Hayashi et al., 2007; Bett et al., 2007; Stadel et al., 2009). Mass accretion onto haloes is non-uniform; clumps tend to fall onto haloes from preferential directions, along filaments whose directions change with time (Tormen, 1997; Colberg et al., 1999; Aubert et al., 2004; Aubert and Pichon, 2007; Libeskind et al., 2011; Lovell et al., 2011b). The shapes of haloes reflect this complex growth history and tend to align along the direction of infall (Faltenbacher et al., 2005; Altay et al., 2006; Aragón-Calvo et al., 2007; Vera-Ciro et al., 2011).

Weak gravitational lensing has been proposed as a way of measuring the ellipticity of haloes (Natarajan and Refregier, 2000), though so far the galaxy-galaxy lensing shear signal has proven to be too weak from a single halo, and, when stacked, the anisotropic shear signal can be washed out (Bett, 2011). However, the eventual detection of dark matter halo ellipticity would offer a way to discriminate between alternative theories of structure formation. It is therefore important to know what ΛCDM predicts for halo shapes and to understand how this varies throughout a halo. While Vera-Ciro et al. (2011) have looked at how the shape of the Aquarius haloes correlates with the direction of infalling material, in this section we focus on the convergence of the shape between the different resolutions. The shape is a more complicated quantity than the spherically averaged density, so it is not obvious that we can expect it to continue to be converged as close to the centre as the density. The multiple resolutions of the same halo allow us to make a quantitative estimate of how close to the centre of a halo the shape can be trusted. The shape in the central regions of a halo is of particular interest because it has important implications for the alignment of galaxies.

2.4.1 Determining the Shape

The standard way of classifying the shape of haloes is to approximate them as a set of concentric ellipsoids of increasing semi-major axes. The ellipsoids are defined by three perpendicular axes and three axis lengths a, b and c, where $a \geq b \geq c$. The scale-independent axes ratios $s \equiv c/a$, $q \equiv b/a$ and $p \equiv c/b$ are often of more interest, as they give the shape of the ellipsoids independently of size. An ellipsoid with $a > b \approx c$ is classed as prolate, one with $a \approx b > c$ classed as oblate, and an ellipsoid with all three axis lengths different $a > b > c$ is triaxial. In addition to the axis ratios, the triaxiality parameter T, defined as

$$T = \frac{a^2 - b^2}{a^2 - c^2} = \frac{1 - q^2}{1 - s^2} \tag{2.5}$$

measures how oblate or prolate the ellipsoids are, with values close to one for prolate distributions and zero for purely oblate distributions (Franx et al., 1991).

There are various methods in the literature for measuring the shape of a halo. The most popular is to use an iterative technique to calculate a moment of inertia-like tensor for the material enclosed within a volume and diagonalise the tensor to find the ellipsoid with the equivalent moment of inertia (Warren et al., 1992; Allgood et al., 2006). All the particles within each given radius are used, so ellipsoids of different sizes are correlated with each other. Another method is to create isodensity surfaces and then fit these by ellipsoids (Jing and Suto, 2002; Vera-Ciro et al., 2011). The main difference between this and the previous method is that the ellipsoids of different radii are independent of each other and so are more sensitive to local variations in the shape. The final commonly applied method is to use the gravitational potential rather than the density and to fit ellipses to the isopotential contours computed on three orthogonal 2D planes (Springel et al., 2004; Hayashi et al., 2007). However, the potential here is intrinsically rounder than the density for the same density distribution.

A comparison of all the different methods finds that they all tend to give similar results for the shapes, particularly in the inner regions (Vera-Ciro et al., 2011), excepting as expected the gravitational potential, which gives a rounder shape. We choose to use the simplest method of Allgood et al. (2006) based on a moment of inertia like tensor to measure the shape of the Aquarius haloes. The moment of inertia is defined as

$$\boldsymbol{I}_{ij} \equiv \sum_{n \in V} \frac{m_n x_{i,n} x_{j,n}}{d_n^2} \tag{2.6}$$

where d_n is a distance weighting for nth particle, V is the set of particles in the volume of interest, $x_{i,n}$ is the ith component of the position of particle n, and m_n its mass. Note that this is slightly different to the usual definition of the inertia tensor. The square root of the eigenvalues of the tensor gives the axis lengths of the ellipsoid used to represent the halo, and the eigenvectors the principal axes. There are different choices for the distance weighting. It can either be set to $d_n^2 = 1$, so that the contribution from each particle depends on its distance from the centre or, as we choose to do, set as the elliptical distance in the eigenvector coordinate system, $d_n^2 = x_n^2 + y_n^2/q^2 + z_n^2/s^2$, so that the particles furthest away do not dominate the tensor. When the elliptical distance is used the tensor is known as the reduced moment of inertia tensor.

The axis ratios q and s have to be found iteratively. Initially, the reduced moment of inertia is calculated for all the particles within some spherical volume V, with radius r. Diagonalisation of this initial tensor finds an ellipsoid with axis ratios q and s. These are used to define a new elliptical volume, V, aligned along the principal axes of the previous tensor and with its longest axis kept fixed to the original radius r and other axes scaled by s and q. For this new volume the inertia tensor is computed from only the enclosed particles and diagonalised once again to find another ellipsoid. This procedure is iterated until it finally converges to a stable set of axis ratios. Occasionally the ellipsoid does not converge and collapses to an infinitely thin shape with zero volume. This is avoided by terminating the procedure after a maximum number of iterations and excluding any ellipsoids that reach this limit.

Fig. 2.8 shows a comparison of the axis ratios of the Aq-A-4 halo using variations on the algorithm. The top set of lines measures the axis ratio q and the lower set of lines the smaller axis ratio s. The solid black line represents the axis ratios for the inertia tensor when all particles within the volume are used, while the blue dashed line is when bound substructure as identified by SUBFIND is removed, so only the smooth halo component is considered. It seems that the presence of substructure only affects the measured axis ratios beyond 180 kpc, where it increases the noise. Also compared is the difference in using the reduced moment of inertia tensor with a constant distance weighting $d_n = 1$ as opposed to using the elliptical distance, $d_n^2 = x_n^2 + y_n^2/q^2 + z_n^2/s^2$. The unweighted axis ratios tend to be slightly larger as the effect from the central material with smaller axis ratios no longer contributes as much at greater radii. In all subsequent results we

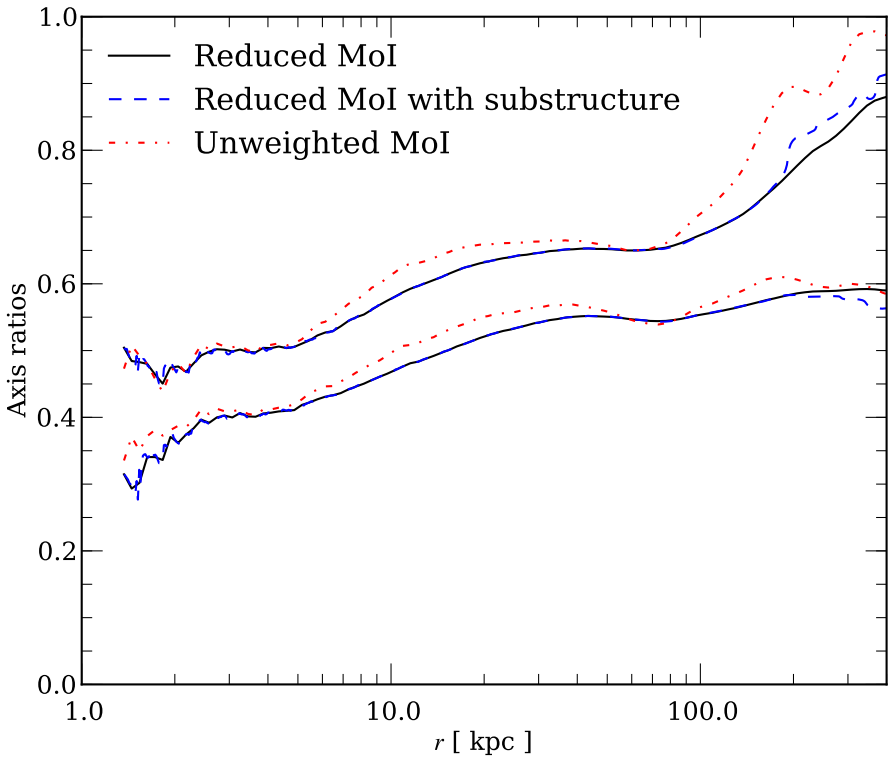

Figure 2.8: The axis ratios, $q \equiv b/a$ (top set of lines) and $s \equiv c/a$ (bottom set of lines) for the Aq-A-4 halo. The axis ratios have been calculated in three slightly different ways. The black solid line shows the results using the reduced moment of inertia tensor with the elliptical distance and with substructure removed. The blue dashed line is the reduced moment of inertia tensor including substructure and the red dash-dotted line is without substructures but using a constant distance weight $d_n = 1$ for all particles.

use the elliptical distance weighted reduced moment of inertia tensor with substructure removed.

2.4.2 Axis ratios and Orientations

The axis ratios and triaxiality for all six level-2 Aquarius haloes at $z = 0$ can be seen in Fig. 2.9. All the haloes follow the same trend of being very prolate in the inner regions $q \sim s \sim 0.4 - 0.6$ with axis ratios increasing outwards, to become oblate/triaxial near the virial radii. This is reflected in the triaxiality which decreases outwards. The radius at which the triaxiality changes from prolate to oblate varies considerably between the haloes. In one extreme, the triaxiality of Aq-D-2 does not significantly drop until very

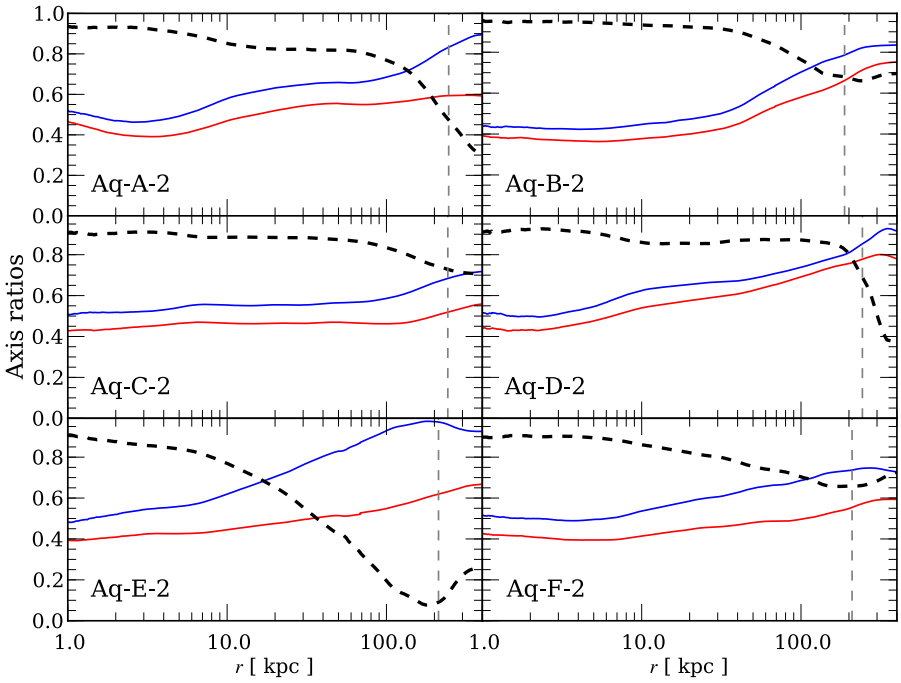

Figure 2.9: The axis ratios and triaxiality of the six level-2 main Aquarius haloes at $z = 0$ as a function of radius. The solid blue lines mark the axis ratio $q \equiv b/a$ and the red lines $s \equiv c/a$. The triaxiality parameter T is plotted as the black dashed lines. The vertical lines mark the virial radius, r_{200} of each halo.

close to the virial radius while at the other, the triaxiality of Aq-E-2 changes smoothly from 10 kpc outwards.

The haloes change in shape with radius, but, as can be seen in Fig. 2.10, the ellipsoids of different radii remain well aligned with each other. The two exceptions are the Aq-E-2 and Aq-D-2 haloes. It appears that whenever there is a rotation one of the axes remains in an almost fixed direction and the other two orthogonal axes can deviate about this axis. This occurs if the axis about which the orientation of the halo rotates is slightly aligned with any of the principal axes, then to first order the changes in the angles of the other two axes are the same.

Looking at the orientation of the Aq-E halo as a function of time reveals that the shape of the inner regions of the Aq-E halo is rotating. From at least $z = 1$ onwards the shape in the inner regions remains prolate, with $s \sim 0.43$ and $q \sim 0.67$ at 10 kpc, but it rotates about its semi-minor axis at a constant rate of one revolution every ~ 3 Gyr. We are able to follow the constant rotation for over 2.5 revolutions. While the inner

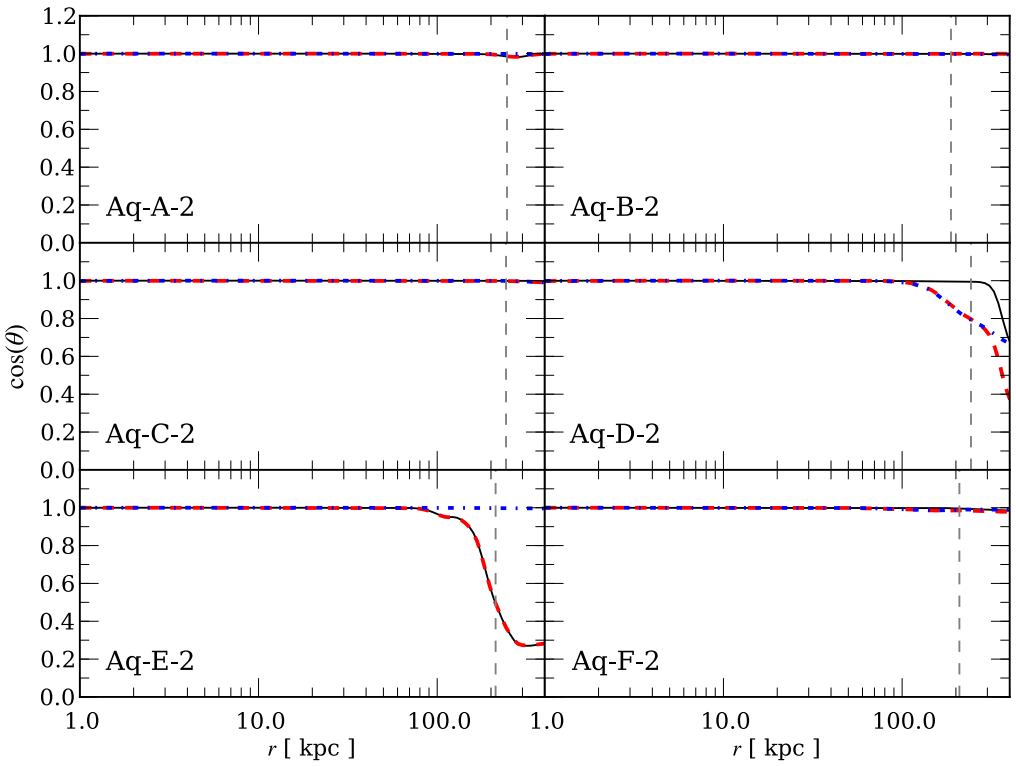

Figure 2.10: The cosine of the angle of orientation of the principal axes of the six level-2 main Aquarius haloes at $z = 0$, relative to their orientation at 10kpc. The black line is the angle of the semi-major axis, the red line the intermediate axis and the blue line the semi-minor axis. The virial radius of each halo is indicated by the vertical dashed lines.

regions are rotating, the outer regions are stationary, resulting in the misalignment of the ellipsoids in Fig. 2.10. The velocity anisotropy of the Aq-E halo (see Fig. 2.4) is different from all the other haloes, suggesting that there is an actual rotation of the material in the inner regions, rather than just the shape reacting to a density wave. Figure rotation has been previously observed in haloes, but for entire haloes and with a much slower angular velocity (Dubinski, 1992; Bailin and Steinmetz, 2004; Bryan and Cress, 2007).

The change in orientation of the Aq-D halo is not due to rotation but instead stems from a twisting of the shape due to a change in the direction of accretion as the halo is forming. At later times $t \gtrsim 7.5$ Gyrs the infall of material occurs along a secondary filament that is orientated perpendicular to the main filament (Vera-Ciro et al., 2011).

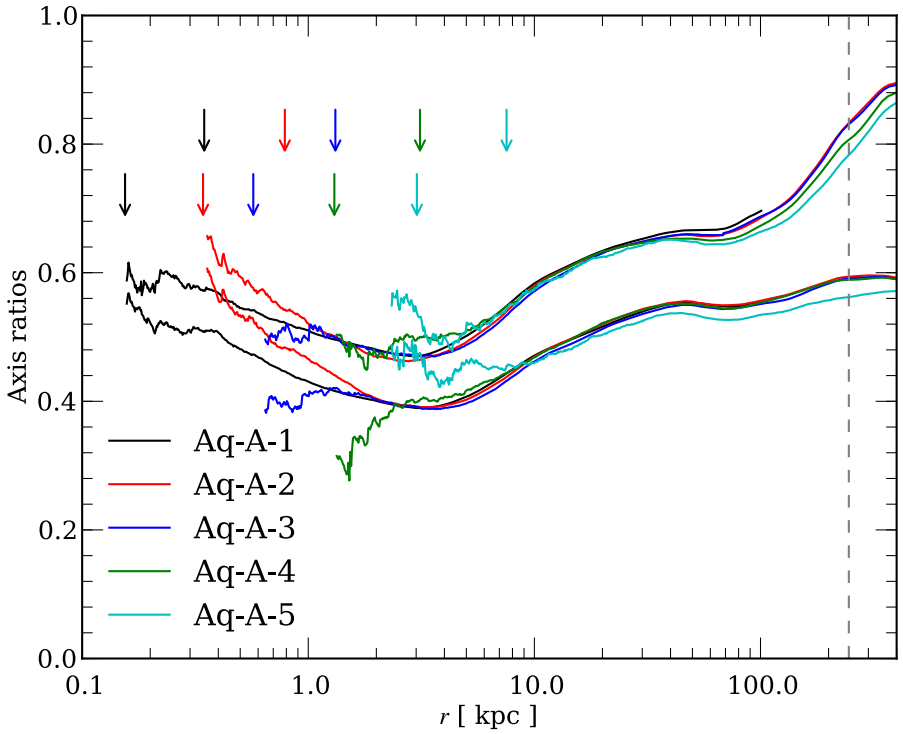

Figure 2.11: The axis ratios of the Aq-A halo resimulations. The top set of lines is the axis ratio $q \equiv b/a$ and the lower set $s \equiv c/a$. The arrows mark the Power et al. (2003) convergence radii for each resolution. The lower arrow corresponds to the $\kappa = 1$ and the upper arrows the $\kappa = 7$ radii.

2.4.3 Convergence

The density profiles of the Aquarius haloes have been shown to be converged down to the Power et al. (2003) $\kappa = 1$ convergence radii (see Fig. 2.2). In order to gauge the convergence of the shape, Fig. 2.11 compares the axis ratios of the Aq-A-1 – 5 simulations. Due to limitations of computational resources it has only been possible to calculate the shape of the Aq-A-1 resolution simulation including substructure. Since, as Fig. 2.8 shows, substructure only alters the results in the outer regions of the halo, we have restricted the results for Aq-A-1 to within 100 kpc, where they are expected to be identical to those without substructure.

In the outer regions all the simulations agree very well but near the centre the axis ratios diverge. The lower arrows mark the $\kappa = 1$ convergence radii and the upper arrows the stricter $\kappa = 7$ convergence radii. From the figure it appears that the axis ratios are

still well converged at the $\kappa = 7$ radii but not at the $\kappa = 1$ radii. In order to quantitatively assess the convergence of both the axis ratios and the orientation, we require a measure of the difference between the inertia tensors of the various resolutions. A comparison of just the axis ratios or directions can be sensitive to the exact shapes under consideration. For example, for near spherical distributions, slight differences in the tensors can result in axes pointing in very different directions when diagonalised, as they have no strong orientation. Instead we seek a measure that compares the complete moment of inertia tensors. We propose that the simplest metric for determining the difference between the reduced moment of inertia tensors $I_i(r)$ and $I_j(r)$ at the same radius, is

$$\Delta_{ij} = \sqrt{\frac{Tr((I_i - I_j)^2)}{\sqrt{Tr(I_i^2)Tr(I_j^2)}}}, \tag{2.7}$$

where $I_i(r)$ is the reduced moment of inertia tensor of the ellipsoid with semi-major axis r for resolution i. Due to the moment of inertia being symmetric, the $Tr((I_i - I_j)^2)$ is equivalent to taking the sum of the squares of the differences between all elements of the tensors. It is zero when the tensors agree and positive otherwise. The metric, Δ includes equal contributions from all elements of the inertia tensor and importantly has the property of being rotationally invariant, so does not depend on the coordinate system in which the shape is measured. The normalisation means the metric is independent of the absolute size of inertia tensors and allows the comparison as a function of radius.

The metric, Δ, between the reduced moment of inertia tensor of the highest resolution version of each halo and their level 4 versions is plotted in Fig. 2.12, the arrows marking the two convergence radii. Aq-A halo compares all the lower resolution (level 2 – 4) versions to the Aq-A-1 simulation. In nearly all cases the difference metric exhibits similar behaviour; at large radii the difference between the moment of inertias is small and approximately constant, but at some inner radius the metric difference rapidly increases. This suggests that at some inner radii the reduced moment of inertia of the same halo in different resolution simulations is no longer similar. The point of increase for the Aq-A haloes moves closer to the centre the higher the resolution of the simulation, and occurs at approximately the same radii at which the axis ratios in Fig. 2.11 begin to disagree. The difference metric Δ has the desired behaviour for a test of convergence and provides a quantitative way to compare moments of inertia. We can therefore define the shape to be converged whenever the difference metric Δ is below some threshold. We

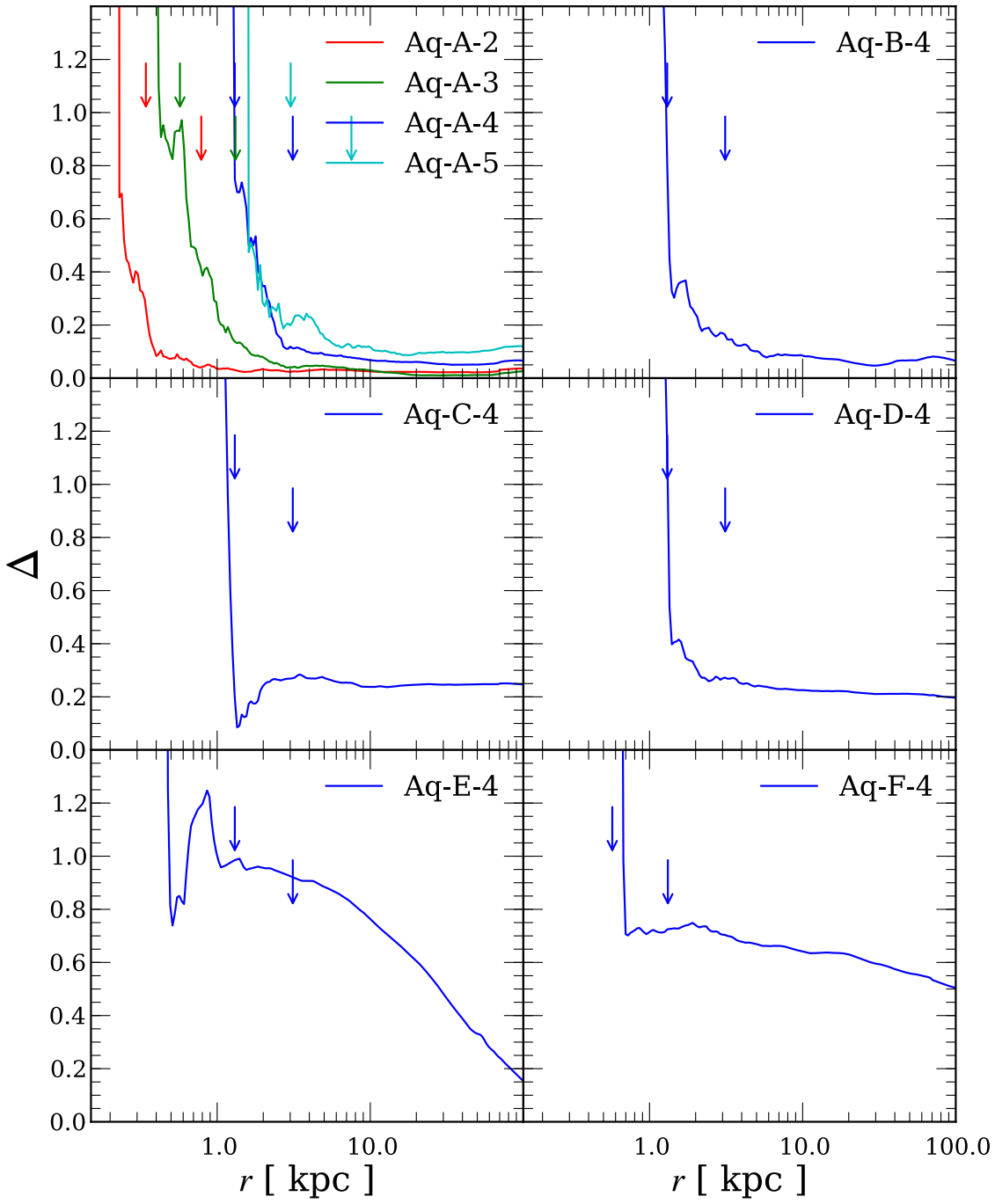

Figure 2.12: The difference metric, Δ (see text for definition), between the reduced moment of inertia tensor of the highest resolution of each of the Aquarius haloes and the level 4 realisations. For Aq-A the level 1 resolution simulation provides the baseline to which all the lower resolution versions are compared. For the other haloes level 2 is used as the baseline. The upper arrows mark the $\kappa = 1$ convergence radii and the lower arrows the $\kappa = 7$ convergence radii.

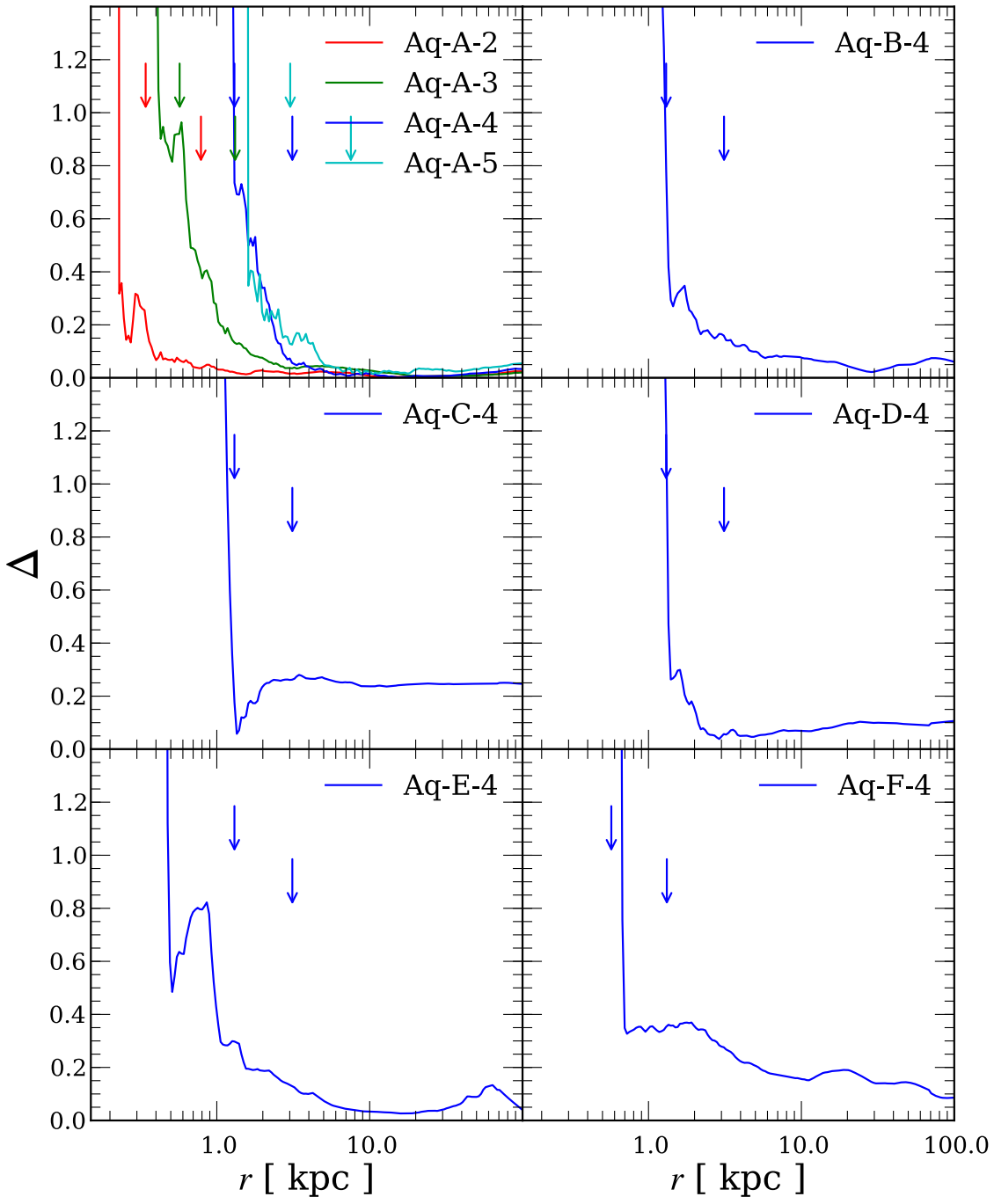

Figure 2.13: Same as Fig. 2.12, but the distance metric is based on the diagonalised form of the reduced moment of inertia.

choose to use the threshold of $\Delta = 0.4$, as for most haloes in the outer regions Δ lies beneath that level. In nearly all cases the divergence of the shape occurs within the $\kappa = 7$ convergence radius, but at radii greater than the $\kappa = 1$ convergence radii. This indicates that the shape of the haloes does not remain converged as close to the centre as the density profiles, but that the $\kappa = 7$ convergence radii provide a useful guide to how close to the centre the shape of simulated haloes can still be considered reliable.

The two exceptions whose reduced moments of inertias do not agree as well in the outer regions are haloes Aq-E and Aq-F. The difference in Aq-E is likely due to a timing issue, if the rotations of the inner regions are slightly out of phase between the resolutions then the orientations will not agree and the moment of inertias will be different. To account for differences in orientations of the haloes we also test the diagonalised forms in Fig. 2.13. The diagonalised form of the reduced moment of inertia removes the orientation information from the tensor and is just a test of agreement of the ellipsoid shapes at a given radius. In comparison with the complete tensor at radii $r \gtrsim 10$ kpc, Δ is smaller, indicating better agreement of shape in the outer regions. However, Δ still increases at the same inner radii as the complete tensor, indicating that the shape is no better converged near the centre. Haloes Aq-E and Aq-F both show better convergence in the outer regions, demonstrating that the different resolution versions have very similar shapes even if they do not have the same orientations.

On a final note, it must be remembered that the Aquarius haloes are from dark matter only simulations and that the presence of baryons in the central galaxy forming region will have an effect on the inner halo shapes. In full hydrodynamic simulations, the condensation of baryons at the centres of halos leads to axis ratios increasing and the shape changing from being prolate to being more spherical or even oblate (Kazantzidis et al., 2004a; Bailin and Steinmetz, 2005; Debattista et al., 2008; Abadi et al., 2010; Bett et al., 2010; Tissera et al., 2010; Kazantzidis et al., 2010). The convergence tests for the Aquarius haloes have demonstrated that while the shape does not remain as well converged quite as close to the centre as the spherical density profile does, for the level 2 simulations the shapes are reliable down to a few kpc.

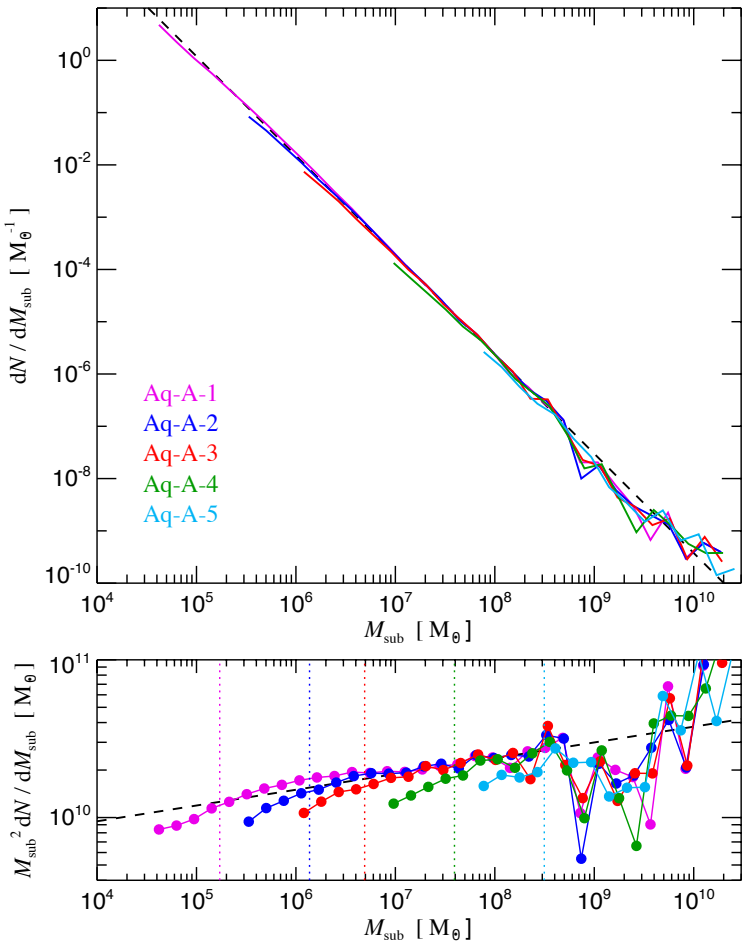

Figure 2.14: Differential subhalo abundance by mass in the different resolutions of the Aq-A halo within r_{50}. The bottom panel shows the same data multiplied by $M_{\rm sub}^2$ to compress the vertical dynamical range. The dashed lines show the power law $dN/dM \propto M^{-1.9}$. *Figure 6 from Springel et al. (2008).*

2.5 Subhaloes

Not only does the high resolution of the Aquarius simulation allow us to probe closer to the centre of the haloes, it also enables us to resolve smaller subhaloes down to lower masses than has previously been possible. In the highest resolution Aq-A-1 halo, nearly 300,000 bound subhaloes are identified within the virialized region and in some cases multiple levels of substructure within substructures can be seen. In this section we outline some results from Springel et al. (2008), who conducted a thorough study of the substructure present within the Aquarius haloes.

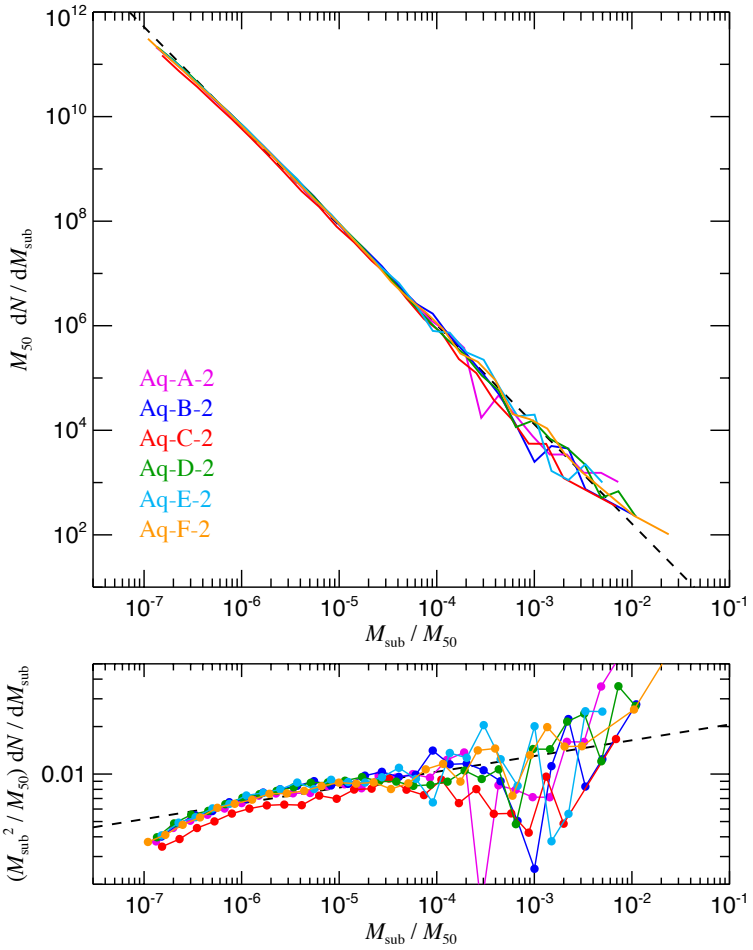

Figure 2.15: Differential subhalo abundance by mass in the different resolutions of the Aquarius haloes within r_{50}. The bottom panel shows the same data multiplied by $M_{\rm sub}^2$ to compress the vertical dynamical range. The dashed lines show the power law $dN/dM \propto M^{-1.9}$. *Figure 8 from Springel et al. (2008).*

In Fig. 2.14 the differential subhalo abundances by mass of the Aq-A halo is shown, with the different resolutions allowing a comparison of the convergence. The slope of the converged part of the function is best fitted by the power law $dN/dM \propto M^{-1.9}$. This is close to the $n = -2$ logarithmically divergent limit, which would have infinite mass in substructure and no smooth component. However, even in the $n = -2$ case this would be avoided due to a lower mass limit that should be set by the thermal free-streaming limit of dark matter. Depending on the dark matter candidate this should be around an Earth mass, at $\sim 10^{-6} \mathrm{M}_{\odot}$ (Green et al., 2004; Profumo et al., 2006). The total amount of mass within resolved subhaloes in the highest resolution Aq-A-1 simulation

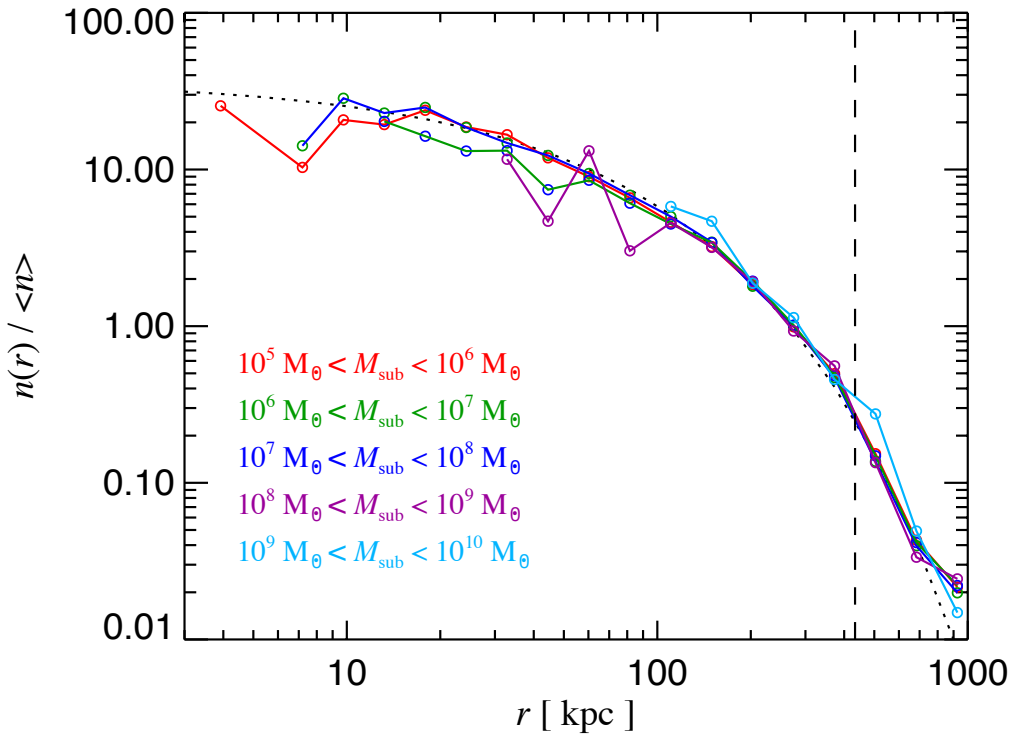

Figure 2.16: The number density of subhaloes as a function of radius for different subhalo mass ranges for the Aq-A-1 halo. The number density profiles of each of the five logarithmic mass ranges has been normalised to the mean number of subhaloes within r_{50} (vertical dashed line). *Figure 11 from Springel et al. (2008).*

is 13.2 percent within r_{50}. If the mass function continues to follow the slope of -1.9, then extrapolating from the minimum resolved mass down to the free-streaming limit predicts that the total fraction of mass in substructure is ~ 18 percent. This fraction falls to less than 3 percent when considering only substructure within 100 kpc of the halo centre. The inner regions of the halo must therefore be dominated by a smooth dark matter component and not by subhaloes.

The differential subhalo abundances by mass for all six level-2 Aquarius haloes are shown in Fig. 2.15. They are all very similar, with little scatter. Due to the lower resolution, there is less mass in resolved substructure in the Aq-A-2 halo than in the Aq-A-1 halo. The fraction of mass in resolved substructure in each halo is Aq-A-2 - 12.2 percent, Aq-B-2 - 10.5 percent, Aq-C-2 - 7.2 percent, Aq-D-2 - 13.1 percent, Aq-E-2 - 10.8 percent, and Aq-F-2 - 13.4 percent. These numbers are very similar to previous results for Galaxy-sized haloes (Stoehr et al., 2003).

A more surprising result is that the radial distribution of subhaloes throughout the main halo is the same independent of mass. This can be seen in Fig. 2.16, which shows the number density of subhaloes in five logarithmic mass ranges binned into radial shells. Each mass range is normalised by the mean number of subhaloes within r_{50}. The curves have remarkably similar shapes and are well fitted by an Einasto profile with $\alpha = 0.678$ and scale radius $r_{-2} = 199$ kpc. The total number of subhaloes of a given mass in each shell is greatest in the outer regions of the haloes, even though density of subhaloes is highest in the centre. This result for the mass independence of the spatial distribution of subhaloes, together with the power-law abundance, allows us to make predictions for the number of subhaloes in the central regions and is further considered in chapter 4 where we look at disc bombardment by subhaloes.

Finally, we examine the density profile of subhaloes in the different resolutions. In order to compare the density profiles of subhaloes between resolutions, it was necessary to match the same subhalo in the multiple simulations. The procedure, as described in Springel et al. (2008), was used to track the particles from a particular subhalo back to their initial conditions and then identify in the other resolutions the particles that started in the same spatial volume. Following these particles forward in time and seeing where they end up generates a set of possible subhalo matches. The subhalo containing the most tracked particles is said to be the counterpart of the original subhalo. The procedure works well and finds good agreement in the position of the subhaloes in the various simulations, with a mean absolute spatial offset ~ 30 kpc.

The spherically averaged density profiles of nine subhaloes from the Aq-A halo are shown in Fig. 2.17. Each one has been matched in the multiple resolutions and shows good convergence down to the $\kappa = 1$ convergence radii. Their inner regions inside of the truncation radius are better fitted by Einasto profiles, as was found for the main halo, even for a fixed value of α, than by NFW profiles or Moore profiles (Moore et al., 1999b). The truncation radius, or edge of a subhalo, is usually taken to be the tidal radius. This is where the gravitational tidal force from the main halo balances the force from the subhalo itself. Material beyond this radius is not bound to the subhalo and will be stripped away.

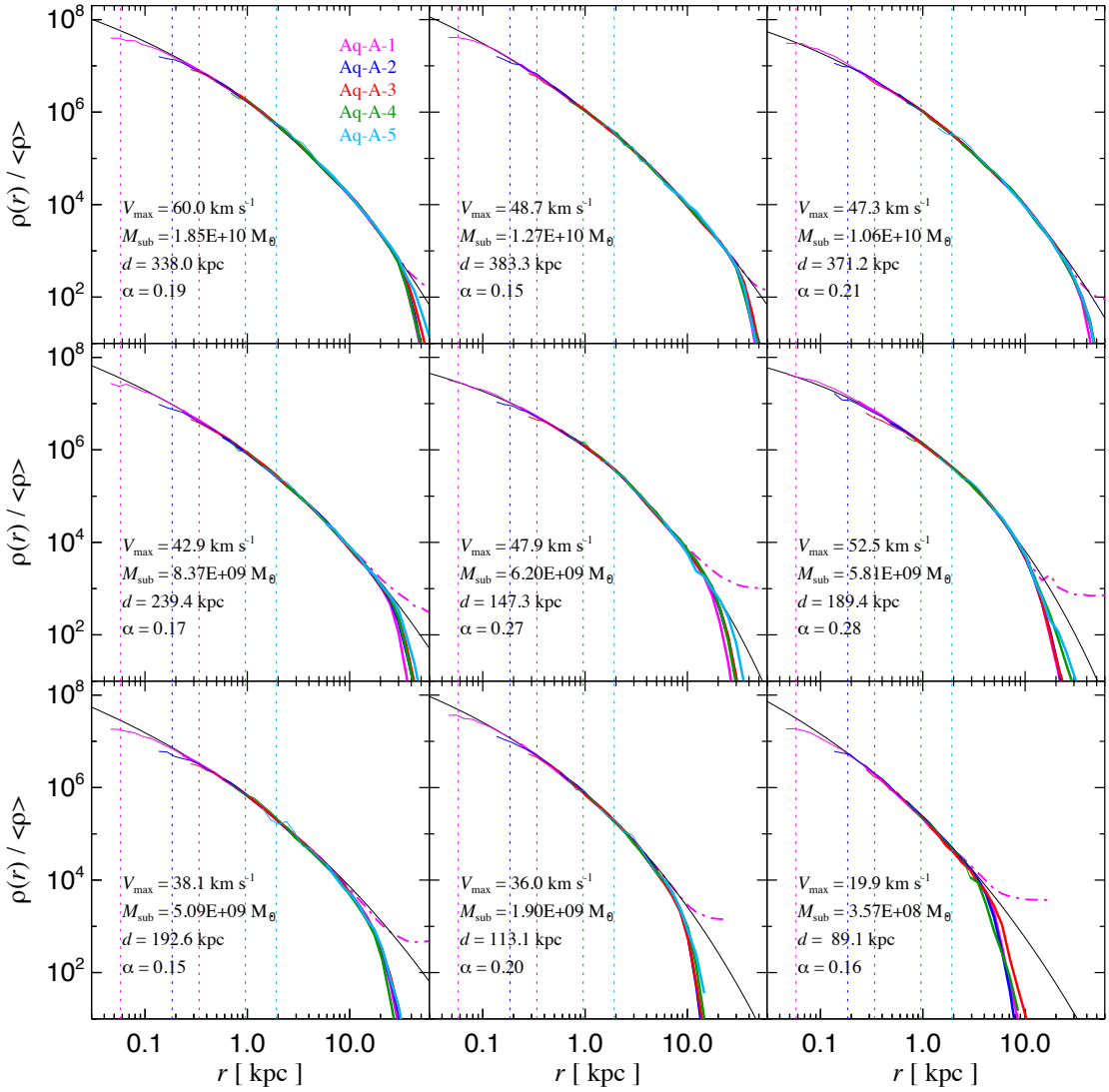

Figure 2.17: The spherically averaged density profile of nine subhaloes from the varying resolutions of the Aq-A simulations. Only the bound mass is included in the profiles, which are plotted as solid lines down to the Power et al. (2003) $\kappa = 1$ convergence radii. The dash-dotted purple lines are the density profile for the total mass, including unbound particles for each subhalo. In each panel the maximum circular velocity, $V_{\rm max}$, the total subhalo mass, $M_{\rm sub}$, and the distance, d, of the subhalo from the centre of the main halo are given. The thin black line shows the fit to an Einasto profile for each subhalo and the shape parameter α, which was allowed to vary freely, is also given. *Figure 22 from Springel et al. (2008).*

2.6 Haloes in a broader context

In order to put the results for the Aquarius haloes into a full cosmological context, it is necessary to ascertain how typical the Aquarius haloes are. Investing substantial computational resources into simulating haloes at increasingly high resolution is only useful if it is known that they are representative of the overall population. Through comparison with a large sample of Milky Way mass haloes from a larger volume but lower resolution simulation, it is possible to gauge where the Aquarius haloes lie in the distributions of various interesting properties, such as assembly history and subhalo content. The Millennium-II Simulation (MS-II; Boylan-Kolchin et al., 2009) is ideal for this task, as it was designed to allow investigation of the statistical properties of MW-mass haloes.

2.6.1 Millennium-II Simulation

The MS-II follows the evolution of $2160^3 \approx 10$ billion particles in a periodic box with side of length $L = 100h^{-1}$ Mpc, from redshift $z = 127$ to $z = 0$. Each particle has a mass $m_p = 6.9 \times 10^6 h^{-1}$ $M_\odot$ and Plummer-equivalent force softening of $\epsilon = 1h^{-1}$ kpc that was kept constant in comoving units. The resolution is sufficient to give approximately 100,000 particles per Milky-Way-like halo and resolve ~ 10 subhaloes per host. The cosmology is the same as used for the Aquarius simulations. The MS-II was run with GADGET-3 and took approximately 1.4 million CPU hours, with 2.77×10^{13} force calculations over 22,142 simulation time-steps.

During the simulation, at each of the 68 output times, dark matter haloes containing at least 20 particles were identified using the friends-of-friends (FOF) algorithm with a linking length of b = 0.2. There are 1.17×10^7 FOF groups present at $z = 0$, with just over 60% of all particles a member of some FOF group. The FOF groups were post-processed with SUBFIND to identify bound substructures. Any objects with at least 20 particles were deemed to be physical subhaloes. Each FOF group generally contains a single dominant subhalo that contains most of the mass in the group. This dominant subhalo corresponds to the large main haloes that have been frequently referred to during the analysis of the Aquarius haloes. The smaller, non-dominant subhaloes are the satellites or substructures that have been discussed at length.

The simulation from which the Aquarius haloes were originally selected is a lower

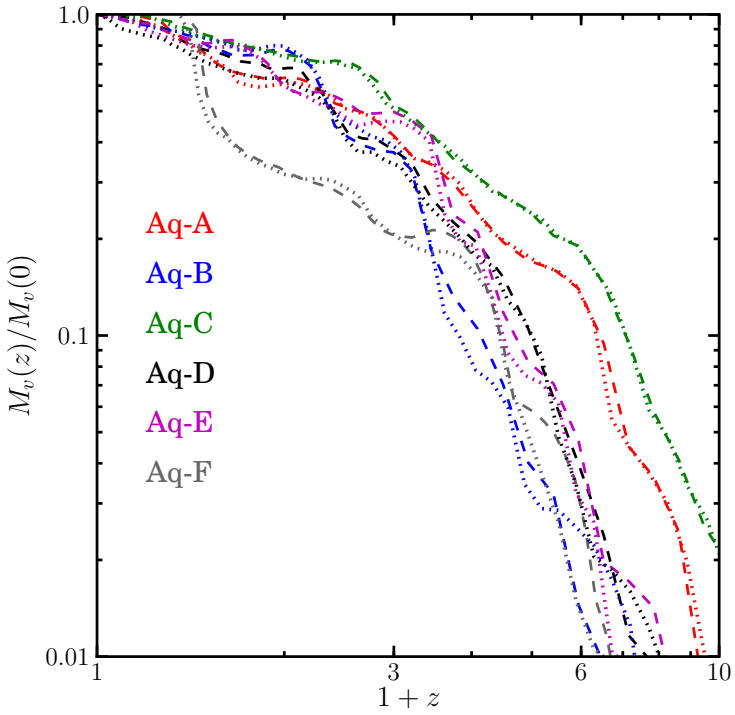

Figure 2.18: Mass accretion histories for the six level 2 resolution Aquarius haloes (dashed lines), compared to the histories of the same haloes in the MS-II (dotted lines). *Figure 13 from Boylan-Kolchin et al. (2009).*

resolution version of the MS-II, therefore the Aquarius haloes are present in the MS-II. Boylan-Kolchin et al. (2009) checked the values of their virial mass, $V_{\rm max}$ and $r_{\rm max}$, and found an agreement of within 10% between the two simulations. The mass accretion histories, as can be seen in Fig. 2.18, are also very well reproduced. The close match of these quantities demonstrates the remarkable convergence between the haloes in the MS-II and the one thousand times higher resolution Aquarius simulations.

Boylan-Kolchin et al. (2010) perform a detailed comparison between the Aquarius haloes and all the similar Milky Way mass haloes in the MS-II. Their main results are outlined in the next few subsections. They selected all haloes in the mass range in which the mass of the Milky Way's dark matter halo is thought to lie of $10^{11.5} \leq M_{\rm vir}/[h^{-1}M_\odot] \leq 10^{12.5}$ from the redshift zero output of the MS-II. The resulting 7642 haloes are then used as the basis for the comparison with the Aquarius haloes. The virial radii and masses used in this section are given in terms of $r_{\rm vir}$, rather than the usual r_{200}.

2.6.2 Main Halo Properties

The mass assembly history of the entire sample is shown in the top panel of Fig. 2.19. The dotted line shows the median and the grey regions mark the $\pm 1\sigma$ regions. While all the haloes' masses are normalised to unity at $z = 0$, the scatter in $M(z)/M(z = 0)$ grows quickly with redshift, reaching at $z = 4$ a factor of 4 in the 1σ spread. Overplotted on this are the mass assembly histories of the Aquarius haloes measured from the MS-II. The Aquarius haloes span the entire range of assembly histories. The Aq-A and Aq-C haloes form early, while Aq-B forms late but catches up by $z = 2$. The Aq-D and Aq-E haloes follow the medium history closely. Aq-F is an exception, as previously discussed. It has a lower than normal mass for most of its history until close to $z = 0$, when it experiences the late major merger that rapidly boosts its mass.

As a halo's boundaries are defined by an enclosed overdensity compared to the background density, the virial mass of a halo can increase with time simply due to the expansion of the universe lowering the critical density, even when no physical accretion is occurring. A better way to characterise the growth in the central regions is to use the maximum circular velocity, $V_{\rm max}$. The maximum circular velocity for a Milky Way mass halo typically occurs at a radius, $r_{\rm max}$, that is about one sixth the virial radius, therefore providing a much better idea of the changes occurring in the centre than the virial mass often does. The evolution of the sample is shown in the lower panel of Fig. 2.19.

The growth of $V_{\rm max}^2$ is very similar to the mass assembly history, and the Aquarius haloes have qualitatively similar evolutions in both, but with a larger scatter in the former. In addition, $V_{\rm max}^2$ flattens out at an earlier redshift than the mass assembly. This reflects the inside-out nature of the growth of haloes, verifying that the inner regions are in place earlier. For haloes Aq-A - E, $V_{\rm max}^2$ is flat from $z = 2$ onwards, suggesting that from this point in time the haloes have stable central potentials that should be conducive to disc galaxy formation. Aq-F is again the exception and it can be seen that its late major merger causes significant disruption even to the central regions.

The distribution of the concentrations and spins of the haloes from the sample is plotted in Fig. 2.20. Rather than calculate the concentrations in the usual manner by fitting a profile to each halo, Boylan-Kolchin et al. (2010) estimate them by assuming that each halo is well fitted by an NFW, so that $r_{\rm max} = 2.16 r_{-2}$ and so define the concentration as $c = 2.16 r_{\rm vir}/r_{\rm max}$. This is much quicker than fitting a profile to every halo, as $r_{\rm max}$ is

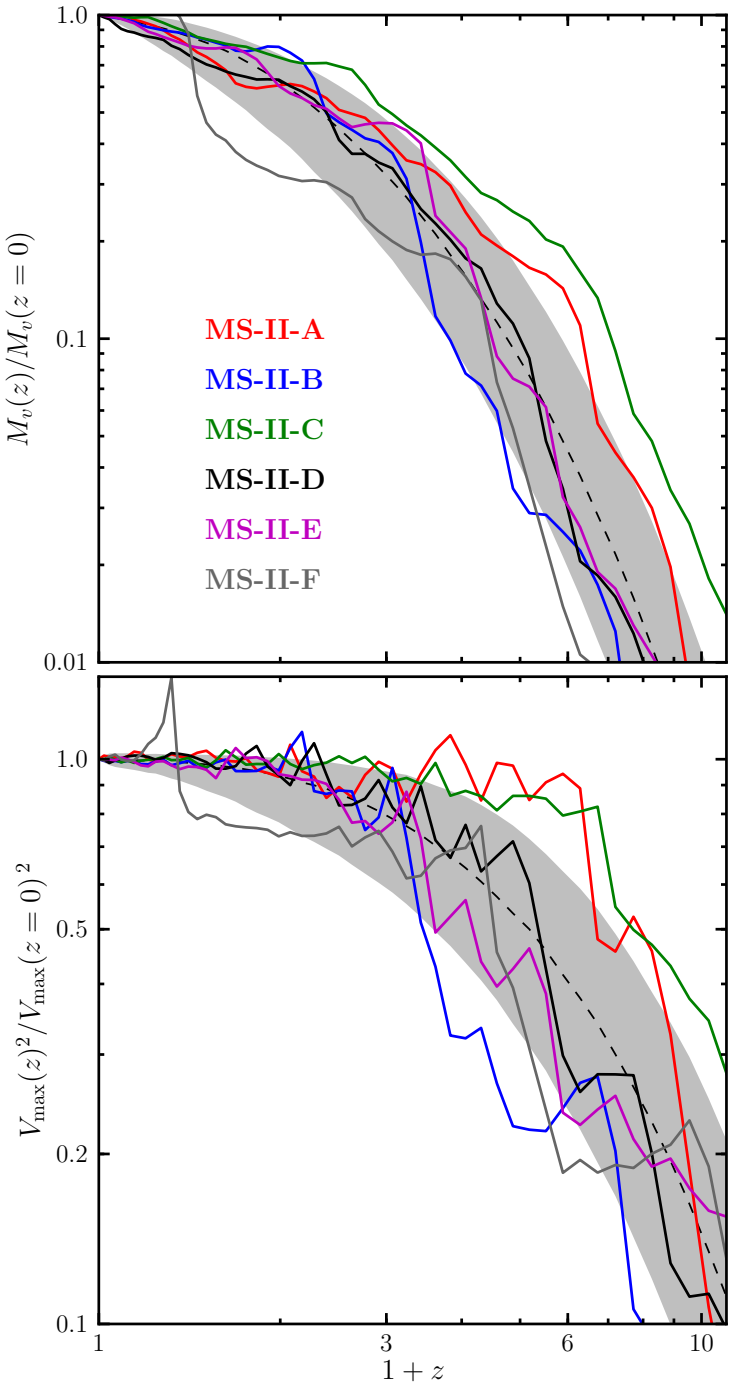

Figure 2.19: *Top panel:* the mass assembly history of the sample of Milky Way mass haloes in the MS-II. The black dashed line marks the median and the shaded grey regions mark $\pm 1\sigma$ for the distribution. The solid colour lines show the mass assembly histories of the Aquarius haloes measured from the MS-II. *Bottom panel:* The growth in $V_{\rm max}$ for the same sample plotted in the same manner as above. *Figure 2 from Boylan-Kolchin et al. (2010).*

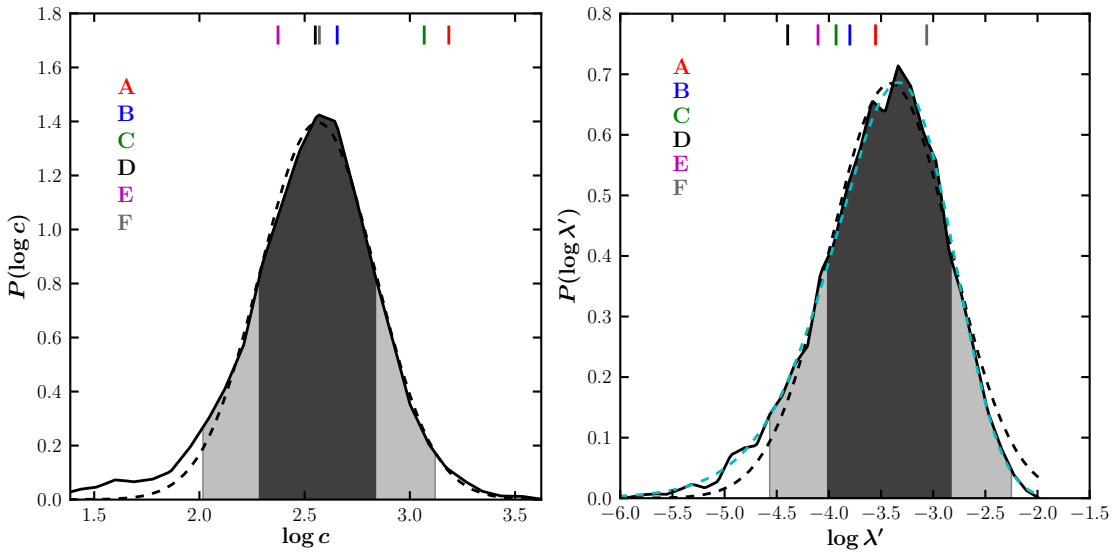

Figure 2.20: The distribution of the concentrations (left panel) and spins (right panel) of the Milky Way mass haloes in the MS-II. The dark regions shade the $\pm 1\sigma$ range, and the light the $\pm 2\sigma$ range. The values for the six Aquarius main haloes are marked by the vertical coloured line. *Figures 3 and 4 from Boylan-Kolchin et al. (2010).*

calculated by SUBFIND. The distribution of $\log_e c$ is well fitted by a normal distribution with $\langle \log_e c \rangle = 2.56$ and $\sigma_{\log_e c} = 0.272$, with a slight excess at low concentrations due to unrelaxed haloes (Neto et al., 2007). The values of the concentrations of the Aquarius haloes are marked by the vertical lines. Haloes Aq-A and Aq-C have higher concentrations reflecting their earlier formation. There is a weak relation between formation time and concentration, as at earlier times the universe is denser when they decoupled from the background expansion. The other haloes all lie near the peak of the distribution.

The modified spin parameter (Bullock et al., 2001) of a halo is defined as

$$\lambda' = \frac{1}{\sqrt{2}} \frac{j}{V_{\rm vir} r_{\rm vir}} \tag{2.8}$$

where j is the specific angular momentum of a halo. The spin parameter provides a measure of the amount of coherent rotation in a system compared to random motions. It is often assumed that the angular momentum content of a galaxy is related to the spin of the dark matter halo (e.g. Mo et al., 1998). The best fitting log-normal distribution to the MS-II sample spins has $\langle \log \lambda' \rangle = -3.41$ and $\sigma_{\log \lambda'} = 0.580$. The Aquarius haloes Aq-A – E all lie below the median and halo Aq-F is the only one with a higher spin parameter, typical of a recent major merger. It was checked that the isolation criterion used for the

Aquarius halo selection did not bias the spin parameters, as the spin distributions of isolated and non-isolated samples were statistically identical. There does not seem to be a reason for the low spin of the haloes other than misfortune.

2.6.3 Subhalo Abundance

As looked at in §2.5, the differential subhalo mass function for the Aquarius haloes follows a power law with slope -1.9. Due to the lower resolution, the subhalo mass function constructed from the MS-II haloes does not probe as far down the mass scale, but instead has sufficient statistics to constrain the higher mass end. In the intermediate mass range, where the MS-II sample overlaps with results from the Aquarius haloes, the subhalo mass function has the same form of a power law, with a very similar slope. At higher masses beyond the range sampled by the Aquarius haloes, the subhalo mass function has an exponential cut-off.

In the second half of this thesis the expected encounters between subhaloes in the Aquarius haloes and galactic discs are studied in great detail. It is therefore useful to know how the abundance of subhaloes in the very central regions of the Aquarius haloes compare to the overall distribution. One way of doing this is to look at mergers within the central regions of MS-II Milky Way mass haloes. In this case a merger is defined to have occurred once a subhalo can no longer be identified as a bound structure within the main halo. The size of the merger, μ, is defined as the ratio of the mass of the subhalo when it was first accreted into the main halo to the mass of the main halo at $z = 0$. For mergers of the largest subhaloes in the MS-II the median distance from the centre is about 15 h^{-1} kpc, and for 80 percent (90 percent) of the cases, the separation is less than 30 (50) h^{-1} kpc. Thus, the size of the largest merger in a halo provides a rough guide to the size of the largest encounter a disc may experience.

The cumulative probability of a halo having experienced a merger with $\mu > M_{\rm acc}/M_{\rm vir,0}$ can be seen in Fig. 2.21. As well as just the largest merger, the probabilities for the second, third, fourth and fifth largest are also given. It can be seen that only 50 percent of haloes experience a merger with $M_{\rm acc} > 0.1M_{\rm vir,0}$ and only 10 percent have two mergers of greater than this size. Overall, 90 percent of haloes have experienced a merger with $M_{\rm acc} > 0.03M_{\rm vir,0}$ since $z = 2$. It must be remembered that the mass of the subhalo is the mass upon accretion. By the time the subhalo reaches the central regions, the subhalo

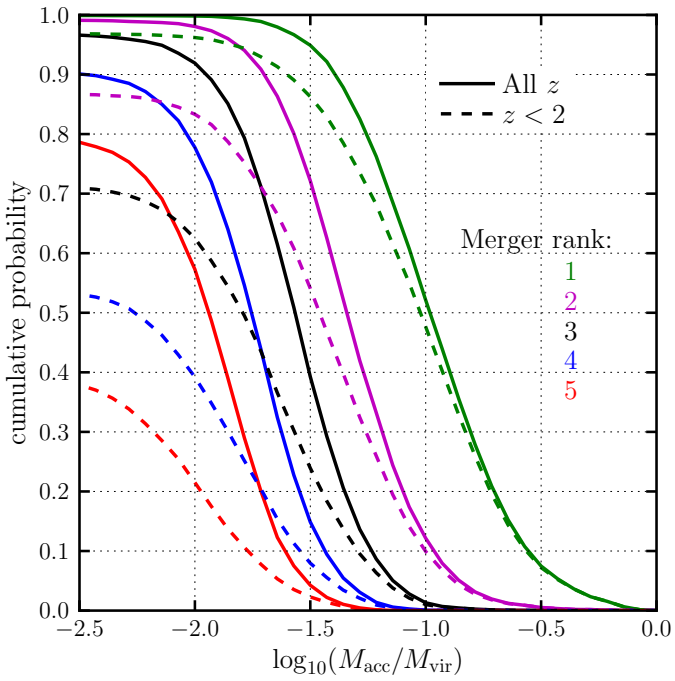

Figure 2.21: The cumulative probability of a halo having experienced a merger with $\mu > M_{\rm acc}/M_{\rm vir,0}$, for the first, second, third, fourth and fifth largest central merger. The solid lines show the probability over a halo's entire lifetime, while the dashed lines give the probability since $z = 2$. The different colours correspond to the different ranks as given in the legend. *Figure 14 from Boylan-Kolchin et al. (2010).*

will have already been stripped of most of its mass, often having just 1 percent of the mass on accretion left by the time of actually merging. Based on this information it is impossible to predict the mass subhaloes are likely to have when they might encounter a disc but still allows a useful comparison of the Aquarius haloes with the overall distribution.

The most massive mergers since $z = 2$ in the Aquarius haloes have ratios 0.033, 0.078, 0.028, 0.030, 0.033 and 0.259, respectively. Haloes Aq-A, Aq-C, Aq-D and Aq-E therefore are in the quietest ~ 15 percent, while halo Aq-B lies close to the median value so is fairly typical. The major merger of Aq-F situates it in the most active 10 percent. The fact that five out of the six haloes lie near the edges of the distribution may be a concern when, in the latter half of the thesis, we attempt to estimate the disc heating for the substructure of the Aquarius haloes. However, it is not clear that the size of the most massive merger is indicative of the expected numbers of disc-subhalo interactions, especially as it will be

the redshift range $z = 1$ to $z = 0$ that is of interest.

2.7 Conclusions

As we have seen in this chapter, the Aquarius haloes, while all selected to have Milky Way like mass, vary greatly in their properties. The haloes have many features in common; they are all best fitted by an Einasto density profile, have similar velocity dispersions, and their differential subhalo abundances follow the same power law, but each halo stands out in a different way. There is almost certainly no such thing as a halo which is average in every property; each forms in a different environment with its own unique formation history.

The Aq-A and Aq-C haloes form earlier than typical haloes, resulting in their having higher concentrations and having their cores in place already by $z = 6$. Halo Aq-B is the smallest mass of the six haloes, but is most typical based on the size of the most massive subhalo merger since $z = 2$. Halo Aq-D tracks the median formation history and has a concentration very close to the median, but its spin lies in the tail of the distribution. The Aq-E halo appears less anomalous, closely following median mass assembly history, but a more detailed examination of the central shape finds the inner regions are undergoing a constant rotation about its semi-minor axis, even though for the halo overall it has a lower than average spin. The Aq-F halo is unique in that it experiences a late major merger and is still in the stage of recovering from this at $z = 0$, which influences many of its final properties, making it the most unlikely to be a host of a Milky Way like galaxy.

The Aquarius haloes were not specially selected, other than to have Milky Way-like mass and to not be a member of any large groups or clusters. It is fortunate that the haloes span such a wide range of properties, and it is this diversity, coupled with the high resolution of the simulations, that makes them the ideal sample for studying the behaviour of dark matter on small scales.

Chapter 3

Halo Expansion (HEX) Technique

3.1 Introduction

Simulations are a powerful tool and have allowed us to gain insight into the non-linear stages of halo growth. However, investigating the structure and substructure of halos requires simulations of ever increasing resolution and ever increasing computational expense. Even the state-of-the-art Aquarius simulations, with a resolution of $\sim 10^3 M_\odot$, have a number of limitations. Firstly, only a few examples have been calculated so far; secondly, their resolution is still below that required to follow the evolution of the smallest subhaloes, including those that host the ultrafaint dwarfs of the Milky Way; finally, they neglect the effects of baryons in the evolution of the main halo and its subhaloes.

One way of avoiding the high cost of full simulations is by introducing approximations. A commonly used one is to assume a static analytical potential to represent the halo and then perform a live simulation of just the small-scale component of interest. Computational resources can then be targeted at that component and large numbers of resimulations performed. This method has been applied to a wide range of problems such as the orbits and evolution of subhaloes (Taylor and Babul, 2001; Zentner and Bullock, 2003; Peñarrubia and Benson, 2005), the build-up of galactic stellar haloes (Bullock and Johnston, 2005), the formation of streams (Peñarrubia et al., 2006), or the disruption and heating of disks (Benson et al., 2004).

Using an analytical potential allows the parameters of the dark matter halo to be varied in a way that cannot be done in full N-body simulations. The major shortcoming of this approach is that representing the halo with a simple analytical potential is unrealistic. Although recent studies have assumed slightly more complicated forms for the

potential, such as axisymmetric NFW profiles (Peñarrubia et al., 2006) or triaxial NFW profiles (Law et al., 2009), they fail to include a realistic time evolution, as haloes grow in stages through mergers, or to account for changes in triaxiality with radius (Hayashi et al., 2007) and time.

In this chapter, we present a more advanced approach for representing the potential of a halo using a series expansion. Our approach is based on the formulation of the self-consistent field (SCF) method (Clutton-Brock, 1973; Hernquist and Ostriker, 1992). The SCF method involves describing a density field as a series expansion and then using this to self-consistently evolve the field. This is usually done by representing the density field as an N-body particle sampling and integrating the orbits of the particles in the series expansion potential. Previous work has used this method to perform N-body simulations (Weinberg, 1996, 1999) and recently it has been applied by Choi et al. (2009) to simulate the potential of subhaloes. SCF codes (also known as expansion codes) have the advantage of being efficient, of scaling linearly with the number of particles, and of suppressing small-scale noise. It is desirable that the lowest order radial basis function resembles the system of interest so that a large number of terms are not required just to describe the basic density distribution. This can be avoided if one tailors the basis functions to the system by numerically solving the Sturm-Liouville equation for the particular density distribution (Weinberg 1999). We have not done this in this work; instead, for simplicity we employ a radial basis function set based on the common simple analytical Hernquist halo profile (Hernquist, 1990).

Rather than using the SCF method for the purpose of performing a complete simulation, we use just the series expansion part of the technique to approximate a precomputed evolving density field, in this case a dark matter halo. This halo expansion (HEX) method offers us the means to create realistic approximations of an existing time-varying halo, which can then be employed for resimulations. Our approach has the distinct advantage of providing a much more realistic description of a halo potential than a simple static analytical form, while still being inexpensive. The starting-point is a full N-body simulation. A set of coefficients is calculated that describes the halo with a chosen set of basis functions. Subsequently, an estimate of the halo density or potential at any point in space can be obtained by evaluating the appropriately weighted sum of the basis functions at that point. In addition, by calculating multiple independent sets of

coefficients at various times in the halo's history and interpolating between the sets we can describe the halo at any time during this period.

There is a wide range of possible applications of this method. It allows us to create approximations of very expensive halo simulations and then replay them at will. It can be used to study the evolving internal environment of the haloes or for the purpose of placing new objects into the simulations and observing behaviour as if they had been present in the original simulation. Problems to which it is ideally suited include: the orbits and stripping of subhaloes, the response of a light disk to the changing halo potential, the shape and precession of tidal streams, and the dynamics of satellite galaxies. In this chapter, we focus on the first of these applications. Comparing orbits within a halo approximated by a series expansion to orbits calculated from the N-body halo serves as a demonstration of the method and provides a test of the accuracy of the approximation.

Limitations of our halo expansion technique include the lack of back reaction of the halo potential when new components are added. For example, if a model of a baryon disk is introduced, the associated reduction of the triaxiality at the centre of the dark matter halo (Debattista et al., 2008; Abadi et al., 2010; Bett et al., 2010) cannot be included in the expansion approximation. At present, the method does not treat the effect of dynamical friction on objects orbiting within the halo. Although this can, in principle, be implemented in the method, Boylan-Kolchin et al. (2008) find that, for subhalo-to-halo mass ratios less than 0.1 the decay of the subhalo orbit due to dynamical friction over a few Gyrs is small.

The first part of this chapter describes the theory behind the expansion technique and how it has been applied to generate a representation of the density and potential of a simulated dark matter halo. Section 3.5 quantifies how well the approximation succeeds in recreating the orbits of both single particles and subhaloes. The latter part of the section carries out a comparison between the evolution of subhaloes in a full simulation and in the approximated potential. In Section 3.6, we use the expansion method for adding a new subhalo into the halo and finally, in Section 3.7, we summarise our conclusions.

3.2 Basis Function Series Expansions

The self-consistent field (SCF) method was originally devised by Ostriker and Mark (1968), where it was used to find the equilibrium structure of rapidly rotating stars. Clutton-Brock (1972, 1973) applied the SCF method to computational stellar dynamics, to model the potential of simple galaxies. Hernquist and Ostriker (1992) (hereafter HO) further developed the technique and it is upon their formulation that we base this work. The idea of the SCF technique is to expand the density and potential in a set of basis functions. The coefficients for the density can be found by summing over the particle distribution of a simulation. The corresponding coefficients for the potential are then obtained through solving Poisson's equation. Differentiation of the potential series gives the acceleration, which can then be used to self-consistently evolve the particles. We adopt the SCF method for creating a series expansion for an N-body distribution, but not to move the particles; instead, we are interested in the expansion itself.

We perform our expansion in spherical polar coordinates with r the radial distance, θ the polar angle and ϕ the azimuthal angle. We start by considering the density and potential written as the biorthogonal series

$$\rho(r,\theta,\phi) = \sum_{nlm} A_{nlm}\rho_{nlm}(r,\theta,\phi), \tag{3.1}$$

$$\Phi(r,\theta,\phi) = \sum_{nlm} A_{nlm}\Phi_{nlm}(r,\theta,\phi), \tag{3.2}$$

where $\rho_{nlm}(r,\theta,\phi)$ and $\Phi_{nlm}(r,\theta,\phi)$ are the basis functions labelled by n,l,m. A pair of biorthogonal series are defined by the property that

$$\int \rho(\boldsymbol{r})_{nlm}\Phi(\boldsymbol{r})_{n'l'm'}d\boldsymbol{r} = \delta_{nn'}\delta_{ll'}\delta_{mm'}. \tag{3.3}$$

If the individual basis function series are not orthogonal then it is necessary to use a pair of biorthogonal series instead. When taking the overlap of the density with the potential basis functions, the biorthogonality property ensures that each coefficient only depends on a single potential basis function and that there is no contribution to it from any of the other basis functions. The basis functions are chosen so that each pair of terms are a solution to Poisson's equation

$$\nabla^2\Phi_{nlm}(r,\theta,\phi) = 4\pi G\rho_{nlm}(r,\theta,\phi), \tag{3.4}$$

with G the universal gravitational constant.

While we have a free choice of basis functions, it is desirable that lowest order terms be a good approximation to the system being modelled. This reduces the need to expand to high order to obtain a good fit. We have adopted basis functions from HO, where radial basis functions are based on the Hernquist profile. A Hernquist profile is a reasonable fit to a dark matter halo, having an appropriate slope of r^{-1} at small radii but differing from the standard NFW form in its behaviour at large radii. For near spherical distributions it is natural to expand in spherical coordinates and use spherical harmonics. Equations (3.1) and (3.2) then become

$$\rho(r,\theta,\phi) = \sum_{nlm} A_{nlm}\rho_{nl}(r)Y_{lm}(\theta,\phi), \tag{3.5}$$

$$\Phi(r,\theta,\phi) = \sum_{nlm} A_{nlm}\Phi_{nl}(r)Y_{lm}(\theta,\phi), \tag{3.6}$$

where $Y_{lm}(\theta,\phi)$ are the usual spherical harmonics. The zeroth order radial basis function is just the Hernquist profile

$$\rho_{00} = \frac{1}{2\pi}\frac{1}{r}\frac{1}{(1+r)^3}, \tag{3.7}$$

with potential

$$\Phi_{00} = -\frac{1}{1+r}, \tag{3.8}$$

when written in dimensionless units where $G = 1$ and the scalelength in the Hernquist form, $a = 1$. For $n = 0$, the higher order l terms are chosen to be analogous to the usual multipole expansion in that they should behave asymptotically as $r \to \infty$, and that $\Phi_{0l} \sim r^l$ near the origin. To construct terms with $n \neq 0$, an additional radial function, $W_{nl}(\xi)$, is included, the form of which is found by inserting it into Poisson's equation. The transformation

$$\xi = \frac{r-1}{r+1}, \tag{3.9}$$

maps r from the semi-infinite range to a finite interval and simplifies the following expressions. Following the derivation from HO, the final full set of potential and density basis functions are found to be

$$\rho_{nl}(r) = \frac{K_{nl}}{2\pi}\frac{r^l}{r(1+r)^{2l+3}}C_n^{(2l+3/2)}(\xi)\sqrt{4\pi}, \tag{3.10}$$

and

$$\Phi_{nl}(r) = -\frac{r^l}{(1+r)^{2l+1}}C_n^{(2l+3/2)}(\xi)\sqrt{4\pi}, \tag{3.11}$$

where

$$K_{nl} = \tfrac{1}{2}n(n+4l+3) + (l+1)(2l+1), \tag{3.12}$$

and $C_n^{(2l+3/2)}(\xi)$ are the ultraspherical polynomials (Abramowitz and Stegun, 1964). The expansions can then be rewritten in purely real quantities as

$$\begin{aligned}\rho(r,\theta,\phi) = &\sum_{l=0}^{\infty}\sum_{m=0}^{l}\sum_{n=0}^{\infty} N_{lm}(\theta)\rho_{nl}(r)[S_{nlm}\cos m\phi \\ &+ T_{nlm}\sin m\phi], \end{aligned}\tag{3.13}$$

$$\begin{aligned}\Phi(r,\theta,\phi) = &\sum_{l=0}^{\infty}\sum_{m=0}^{l}\sum_{n=0}^{\infty} N_{lm}(\theta)\Phi_{nl}(r)[S_{nlm}\cos m\phi \\ &+ T_{nlm}\sin m\phi]. \end{aligned}\tag{3.14}$$

where $N_{lm}(\theta)$ are the normalised associated Legendre polynomials, given by

$$N_{lm}(\theta) = \sqrt{\frac{(2l+1)}{4\pi}\frac{(l-m)!}{(l+m)!}}P_l^m(\cos\theta) \tag{3.15}$$

For a known density profile the expansion coefficients S_{nlm} can easily be obtained by multiplying both sides of equation (3.13) by $[N_{lm}(\theta)\Phi_{nl}(r)\cos\phi]$ and integrating over all space, or T_{nlm} can be obtained by multiplying equation (3.13) by $[N_{lm}(\theta)\Phi_{nl}(r)\sin\phi]$ and integrating. This needs to be modified for N-body simulations where the density field is represented by discrete particles. In this case the integration over space becomes a sum over the particles, each weighted by its mass. Then the expansion coefficients are

$$\begin{pmatrix} S_{nlm} \\ T_{nlm} \end{pmatrix} = (2-\delta_{m0})\tilde{A}_{nl}\sum_k m_k\Phi_{nl}(r_k)N_{lm}(\theta_k)\begin{pmatrix}\cos m\phi_k \\ \sin m\phi_k\end{pmatrix}, \tag{3.16}$$

where

$$\tilde{A}_{nl} = -\frac{2^{8l+6}}{4\pi K_{nl}}\frac{n!(n+2l+\frac{3}{2})[\Gamma(2l+\frac{3}{2})]^2}{\Gamma(n+4l+3)}, \tag{3.17}$$

and r_k is the position of each particle and m_k its mass.

Once the coefficients are calculated, they can be used to evaluate equation (3.14) and find the potential at any location in space. Accelerations are obtained by differentiating the potential. By taking the gradient of equation (3.14), the accelerations can be written

in spherical coordinates as

$$a_r(r,\theta,\phi) = -\sum_{l=0}^{\infty}\sum_{m=0}^{l}\sum_{n=0}^{\infty} N_{lm}(\theta)\frac{d}{dr}\Phi_{nl}(r) \\ [S_{nlm}\cos m\phi + T_{nlm}\sin m\phi], \tag{3.18}$$

$$a_\theta(r,\theta,\phi) = -\frac{1}{r}\sum_{l=0}^{\infty}\sum_{m=0}^{l}\sum_{n=0}^{\infty} \frac{dN_{lm}(\theta)}{d\theta}\Phi_{nl}(r) \\ [S_{nlm}\cos m\phi + T_{nlm}\sin m\phi], \tag{3.19}$$

$$a_\phi(r,\theta,\phi) = -\frac{1}{r}\sum_{l=0}^{\infty}\sum_{m=0}^{l}\sum_{n=0}^{\infty} \frac{mN_{lm}(\theta)}{\sin\theta}\Phi_{nl}(r) \\ [T_{nlm}\cos m\phi - S_{nlm}\sin m\phi]. \tag{3.20}$$

Both the radial and spherical harmonic basis sets are complete, so when summed from $n = 0 \to \infty$ and $l = 0 \to \infty$ the expansion converges to the exact distribution, although non-uniformly near discontinuities. However, in practice the expansions are truncated at some high order term, $n_{\max}$ and $l_{\max}$. Truncated to a finite number of terms, equations (3.13) and (3.14) become

$$\rho(r,\theta,\phi) = \sum_{n=0}^{n_{\max}}\sum_{l=0}^{l_{\max}}\sum_{m=0}^{l} N_{lm}(\theta)\rho_{nl}(r)[S_{nlm}\cos m\phi \\ + T_{nlm}\sin m\phi], \tag{3.21}$$

$$\Phi(r,\theta,\phi) = \sum_{n=0}^{n_{\max}}\sum_{l=0}^{l_{\max}}\sum_{m=0}^{l} N_{lm}(\theta)\Phi_{nl}(r)[S_{nlm}\cos m\phi \\ + T_{nlm}\sin m\phi], \tag{3.22}$$

with the number of terms determining the accuracy to which the expansions reproduce the actual density distribution.

3.3 Implementation of the HEX Algorithm

This algorithm is ideally suited to parallel computation. Each processor can independently calculate the coefficients for disjointed subsets of particles. A final summation collects together the contributions from each processor to generate the coefficients for the complete particle set. This ease of parallelism, coupled with the algorithm being of $\mathcal{O}(n)$ in the number of particles means, it is ideally suited for use on huge datasets. Due

to the parallel nature of GADGET each output from simulations is usually split into several files of roughly equal size. This makes it very easy to divide the computation of the coefficients for a snapshot between multiple processors, by assigning each processor its own set of files. Carrying out the division in this manner imposes the restrictions that to ensure equal workload the number of processors must be a divisor of the total number of files and that the maximum number of processors that can be employed is equal to the number of files. However, it avoids the need for more complicated schemes for dividing the data.

We have implemented the algorithm in C++, using the standard Message Passing Interface (MPI) for communication. The standard mathematical functions used within the basis functions are evaluated by the GNU Scientific Library (GSL) (Galassi et al., 2003). The performance of the implementation has been tested and as expected is linear as a function of the number of particles. For $n_{\max} = l_{\max} = 20$, excluding initialisation and loading, the code takes $\sim 1.9\times10^{-4}$s per particle. The total run time is approximately independent of the number of processors; there is some imbalance as the snapshots are not always split over files in a completely random manner.

The algorithm is to leading order $\mathcal{O}(n_{\max}l_{\max}^2)$ for the number of basis terms included in the expansion and can quickly become computationally expensive if too many higher order terms are included. The GSL library uses recursion relations to calculate the spherical harmonics and the ultraspherical polynominals, so calculating the highest order basis function also returns the lower order ones. The run time as a function of number of basis functions for 10^5 particles can be seen in Fig. 3.1. $l_{\max}$ is kept equal to $n_{\max}$ in order to maintain approximately equal spatial resolution in both the radial and angular directions. For small numbers of basis functions the run time is dominated by other parts of the code so does not follow the predicted cubic relationship. Once the expansion includes more than $n_{\max} = l_{\max} = 15$ terms, the performance is close to the expected $\mathcal{O}(n_{\max}l_{\max}^2)$ behaviour.

3.4 Considerations in Application to Simulations

The Aquarius project haloes are ideally suited for testing the HEX technique due to their high-resolution and large number of outputs saved at regular times. We have applied

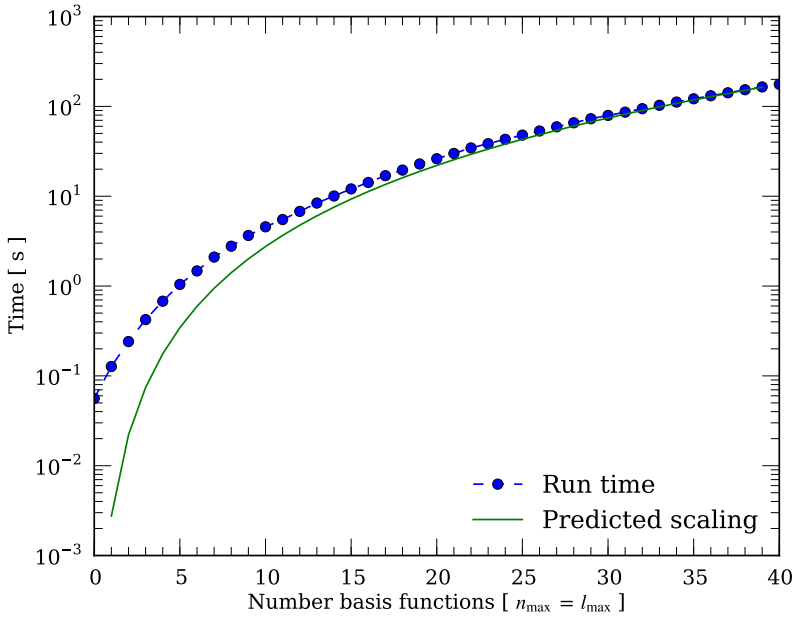

Figure 3.1: Time taken to calculate coefficients of 10^5 particles as a function of the number of basis functions included in the expansion. We keep $n_{\max} = l_{\max}$ as is usually the case in order to maintain equal spatial resolution in both directions. The blue line shows the measured performance and the green line the expected scaling.

the expansion technique to two different resolution versions of the Aquarius A halo. The majority of this work is based on the higher resolution Aq-A-2 version, while the lower resolution Aq-A-4 simulation is used to check for convergence. There is a factor of 28 difference in the mass resolution of the two versions, with excellent convergence found between them. The Aq-A-2 simulation has a total of 1024 outputs, while the Aq-A-4 has only 128. For this work we have restricted ourselves to the same 128 outputs from both versions, giving one approximately every 155 Myrs at late times.

To apply the HEX technique to a dark matter halo from the Aquarius simulation, we expand about the potential minimum, as identified by SUBFIND by the most bound particle. A summation over all particles is performed, once for each halo, to yield a set of coefficients that describe the halo by the given basis functions. We limit the expansions to a small number of terms, resulting in a set of coefficients much smaller in comparison to the number of dark matter particles in the halo. This truncation of the series smooths the density and removes small-scale detail.

Only particles within 1.3 virial radii of the halo centre are included in the coefficient

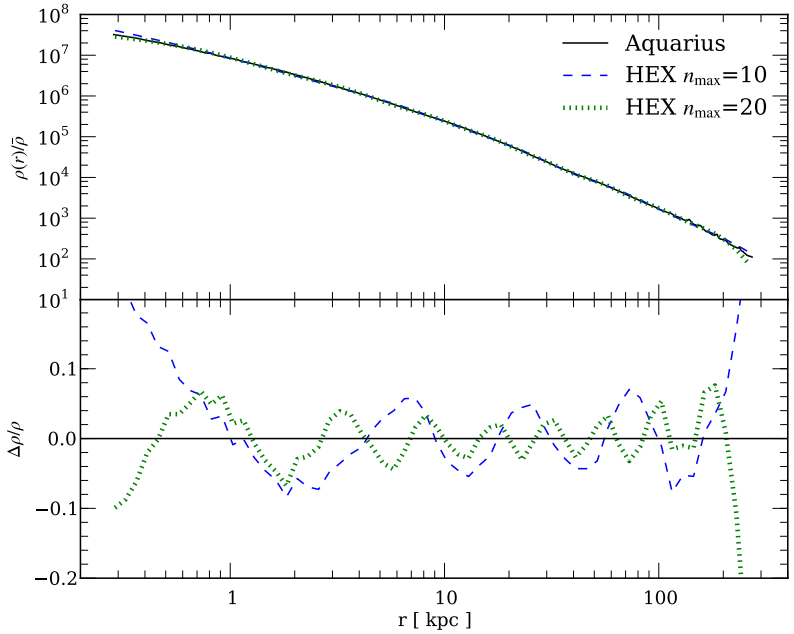

Figure 3.2: *Upper panel:* Spherically averaged density profiles $\rho(r)$ of the main Aq-A-2 halo. The solid line is the profile of the actual halo from the simulation, while the dotted and dashed lines are the profiles from the expansion with $n_{\rm max} = 10$ and $n_{\rm max} = 20$ respectively. *Bottom panel:* Residuals of the density profile fits, $\Delta\rho/\rho \equiv (\rho_{HEX} - \rho_{halo})/\rho_{halo}$, where ρ_{halo} is the true halo density and ρ_{HEX} denotes the HEX approximated density.

summation. At greater distances, the distribution of material is more irregular and not well fitted by spherical basis functions. While the use of a hard cut-off at the boundary imposes a discontinuity in the density profile there, we find this not to be a problem. We have tested with larger as well as soft boundaries and find the exact choice makes little difference to our results. We choose to use a hard boundary for simplicity.

Fig. 3.2 shows the comparison of the density profile of the main halo from the Aq-A-2 simulation, obtained by binning the simulation particles into spherical shells, with its approximation by the HEX method. The lower panel shows the residuals between the model and the data. It can be seen that over the radial range 1-100 kpc, using just eleven radial basis functions, $n_{\rm max} = 10$, the RMS deviation of the residuals is 4.2%, decreasing to 2.6% when twice the number of radial terms, $n_{\rm max} = 20$, are included. Even using just a few radial basis functions, the expansion achieves a fit to within a few percent of the spherically averaged density profile of the halo, over a range where the radial density

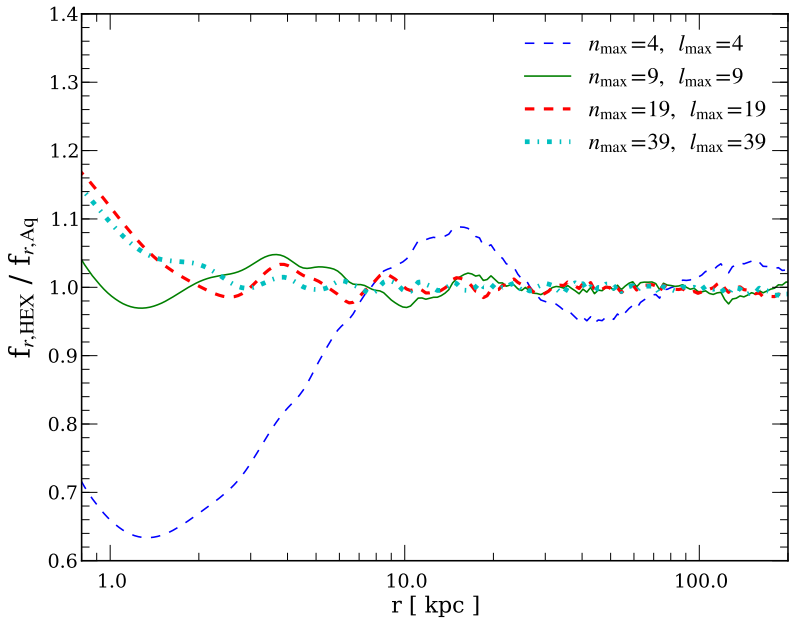

Figure 3.3: Radial component of the force calculated from the HEX approximation truncated at differing $n_{\max}$ divided by the actual force calculated directly from the Aq-A-4 simulation.

varies by over six orders of magnitude.

3.4.1 Order of Expansion

The accuracy of the approximation of the halo depends on the number of terms included in the expansion, the use of more terms allows smaller spatial features to be resolved. The spatial resolution approximately scales inversely proportional to $n_{\max}$ and $l^2_{\max}$. The effect on the force of including more terms in the expansion can be seen in Fig. 3.3. Here, the radial component of the force for $n_{\max} = l_{\max} = 4, 9, 19, 39$ is compared to the force as calculated directly from the original N-body simulation.

In the central region of the haloes the radial force estimated from the expansion differs from that calculated in the simulations. The closer to the centre, the larger the disagreement. This divergence is due to the density of the simulated halo having a logarithmic slope shallower than -1, while the lowest order Hernquist basis function has a cusp at the centre with a slope of -1 and is not a good fit there. Excluding the centre from the comparison and considering the region between 5 and 100 kpc, it is found that doubling both $n_{\max}$ and $l_{\max}$ from five to ten terms results in a big improvement, with

the fractional RMS deviation falling from 4.8% to 1.3%. Doubling the number of terms again gives further gains, with expansions using 20 and 40 terms resulting in fractional RMS deviations of 0.83% and 0.46% respectively.

As the expansion is taken to increasingly higher orders, the contribution of individual terms declines. Higher order terms resolve smaller scale structure, and eventually the very high order terms model only the shot noise from the discrete particle nature of the simulation. Following Weinberg (1996), we take the signal-to-noise on a coefficient as $S/N \equiv [S_{nlm}^2/\mathrm{var}(S_{nlm})]^{1/2}$, where the variance can be estimated by considering the computation of the coefficients as a Monte Carlo integration. Signal-to-noise of less than one indicates that the particle distribution does not provide significant information on the value of that coefficient. We find that terms even as high order as $n_{\max} = l_{\max} = 20$ enjoy low levels of noise and contribute to resolving the halo structure. This is not surprising as the Aq-A-2 has over 100 million particles within the virial radius, while an expansion with $n_{\max} = l_{\max} = 20$ only contains 8000 terms.

Gravity is a long-range force dominated by the large-scale distribution of material. The force on an object is therefore determined primarily by the overall distribution of mass, and resolving nearby small-scale fluctuations does not substantially improve the radial force estimate. Going to higher expansion orders is thus unnecessary, as long as we employ sufficient terms to resolve the large-scale structure. Additional terms do not provide much gain. A force accuracy of less than 1% can be achieved using $n_{\max} = l_{\max} = 20$, and is sufficient for most purposes. We use expansions to this order in the rest of this chapter.

3.4.2 Choosing the Scalelength

The adopted set of basis functions contains a single free parameter corresponding to the scalelength, a, of their underlying Hernquist profile. This scalelength needs to be predetermined and chosen so that the lowest order basis function is a good fit to the halo. We find that the accuracy of the expansion when approximating the force is fairly insensitive to the exact choice of scalelength. Examination of the RMS deviation in the radial force as a function of scalelength shows that very small scalelengths give bad fits to the profile, but any scalelength larger than 10 kpc is acceptable, with a minimum RMS deviation at 33 kpc. As we have already seen, the lowest order basis function is not

a good fit to the halo at the origin due to a mismatch in central slopes. Reducing the scalelength does not help this.

The basis functions are primarily constrained by the region where the number of particles per radial interval is a maximum. This occurs where the logarithmic slope of the density profile is -2, which is at the scalelength for an NFW profile and at half the scalelength for a Hernquist profile. It is in this region that we desire the lowest order basis functions to fit well in order to minimise the number of terms needed in the expansion. The Aquarius A halo is very well fitted at $z = 0$ by an NFW profile with a scalelength of 15.3 kpc. It is therefore unsurprising that the optimum scalelength for the best fit by the lowest order Hernquist basis function is found to be 33 kpc, approximately twice the best fit NFW scalelength. Using this value obtains an average RMS deviation in the radial force between 5 and 100 kpc of 0.53%, with the force correct to within 3% down to 2 kpc. In the rest of the chapter we use a scalelength of 33 kpc when modelling this halo.

3.4.3 Frame of Reference

We perform the expansion in a frame moving with the halo. Haloes are accelerated by surrounding large-scale structure. In the simulation this results in the halo having a peculiar velocity of several hundred kilometres per second, a velocity comparable to the relative motion of material within it. We wish to transform into a frame in which we can treat the halo as stationary. This will allow us to follow the relative motion of objects within a halo, such as the orbit of particles, and neglect the halo's movement through space in their equation of motion and not need to take into account the position or the velocity of the halo at intermediate times. Because of the halo's finite extent, this frame is not strictly an inertial frame, but is accelerating due to the gravitational effects of distant large-scale material. Since material within the halo experiences the same acceleration, this is only important if there are significant differential tidal forces over the scale of the halo, but this is not the case; the long-range tidal force, calculated by direct summation from distant material is less than 1% the magnitude of the internal halo force within 100 kpc of the halo centre and can be safely ignored.

In order to transform into a stationary halo frame we must define an origin that moves with the halo and remove the halo velocity. The origin of the halo frame is cho-

sen as the halo potential minimum, $\boldsymbol{x}_{pm}$. This is a well defined point that follows a smooth path. The choice of the halo velocity to use for the transformation to a stationary frame is not obvious. We need to use the instantaneous halo velocity to make the correct transformation rather than the average velocity, which we could simply obtain from the motion of the potential minimum. A sensible choice is to look at the net motion of the material surrounding the potential minimum. We obtain a centre of mass velocity that corresponds to the potential minimum's velocity by selecting all particles within some bounding radius, R, of the halo centre. The velocity is then

$$\boldsymbol{v}_c = \frac{\sum_i m_i \boldsymbol{v}_i}{\sum_i m_i} \tag{3.23}$$

where i is all the particles that have $|\boldsymbol{x}_i - \boldsymbol{x}_{pm}| \leq R$. Restricting ourselves to just the inner region, where the halo is almost static, we find that the exact choice of R makes little difference to the centre of mass velocity. Varying R between 1 and 20 kpc alters the velocity by less than a kilometre per second. Including the entire halo gives a centre of mass velocity some 20 kms^{-1} different from that of the inner regions. We therefore choose to use the centre of mass velocity of the particles within 5% of the virial radius, which for Aq-A-2 is $R = 12$ kpc at $z = 0$.

To show that this is a valid choice we compare the orbits of particles integrated within the expansion to the orbits the same particles took within the original simulation. The next section describes this in detail. We find that for each subset of particles there is an optimal choice of velocity for the halo frame in which to integrate particle orbits in order to match their equivalent orbits from the Aquarius simulation. This velocity can be found through a minimisation scheme, in which we attempt to minimise the difference in their final position compared to their position in the original simulation. While the optimum velocity depends on the set of particles considered, it only varies within a few kilometres per second between cases, suggesting that the motion of the inner regions of the halo is almost uniform. A slight difference in motion throughout the halo is the cause of the small spread and allows us to define a window of several kilometres per second in which we find that any choice of velocity for the halo frame works satisfactorily. Choosing a different velocity within this window changes the path of the orbital integration by only a percent or two.

Not only does this show that an approximately stationary frame does exist, we also find that the centre of mass velocity that we chose earlier lies within this window. This

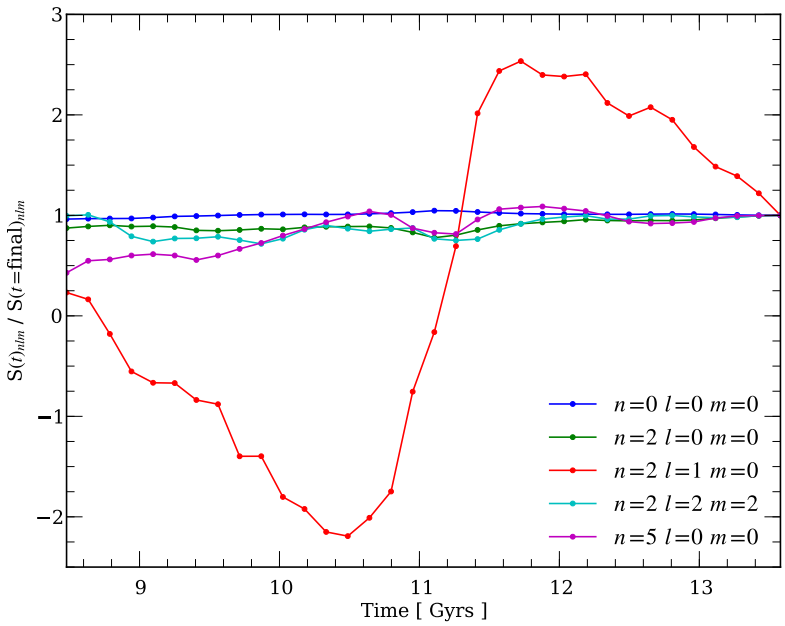

Figure 3.4: The variation of low order coefficients as a function of time for the last 5 Gyrs of the Aq-A-2 halo evolution.

is true for the Aquarius A, B and C haloes and demonstrates this to be a valid choice for the halo frame, especially as it can be easily determined in advance, whereas the optimum velocity for a particular case can only be located retrospectively. The resulting procedure for placing objects within the expansion approximation frame is to find their initial position relative to the halo potential minimum at the start time and their initial velocity with respect to the defined halo velocity, $\boldsymbol{v}_c$. The motion of the objects can then be followed totally within this frame and there is no need to further consider the overall motion of the halo.

3.4.4 Time Variation

Due to the fact that such a large amount of data is generated, the output of N-body simulations is usually recorded only at a few snapshots. Between these snapshots information on the exact evolution of the halo is lost. However, it is usually sufficient to use simple interpolation to approximate it. The expansion technique is ideal for this because at each snapshot a new set of coefficients are calculated to describe the halo at that time. An approximation to the state of the halo at any intermediate time can be recovered by linearly interpolating the coefficient of each basis function between the directly preceding

and following snapshots.

Fig. 3.4 illustrates the variation in a selection of low order coefficients over the last 5 Gyrs of the Aq-A-2 halo's growth, with a time resolution set by the snapshot spacing of 155 Myrs. The coefficient of the lowest order basis function varies very little, initially showing a slight increase until 11 Gyrs, followed by a slight decline. The variation corresponds to the slight fluctuation in mass of the inner $\sim$100 kpc of the halo. The higher order coefficients have greater variation. The fluctuations on short timescales, of the order of the time spacing of the snapshots, are generally small, while the larger, more important variations, such as the oscillation in the $n = 2$, $l = 1$, $m = 0$ coefficient, occur on longer timescales. The time spacing we use is sufficient to capture large-scale changes in halo structure. Smaller quicker changes, such as those from substructure, may be missed, but this does not matter as these are not spatially resolved by the expansion anyway.

3.5 Tests with the Aquarius Haloes

Once we have obtained a time-varying set of coefficients for a halo expansion approximation of an Aquarius halo potential and density, it is straightforward to use this to integrate orbits of test particles within the evolving halo potential. In order to test the accuracy of the HEX method, we examine how closely we can reproduce the properties of existing objects already present in the Aquarius simulations along their orbits. Based on the findings of the previous section we use a potential expansion including terms up to order $n_{\max} = 20$ and $l_{\max} = 20$, with a fixed scalelength of 33 kpc and summed over all particles within 340 kpc of the halo centre, to approximate Aq-A-2 halo. A set of coefficients is generated for each snapshot, approximately every 155 Myrs.

3.5.1 Integrating Particle Orbits

Ideally, if the potential is approximated accurately, test particles placed in the evolving halo potential will behave in the same manner as particles in the original simulation. This should be the case as long as the particles are not bound to any subhalo, since we are not attempting to resolve this level of detail. Therefore, by setting up a test particle with initial conditions matching the instantaneous state of a simulation particle and inte-

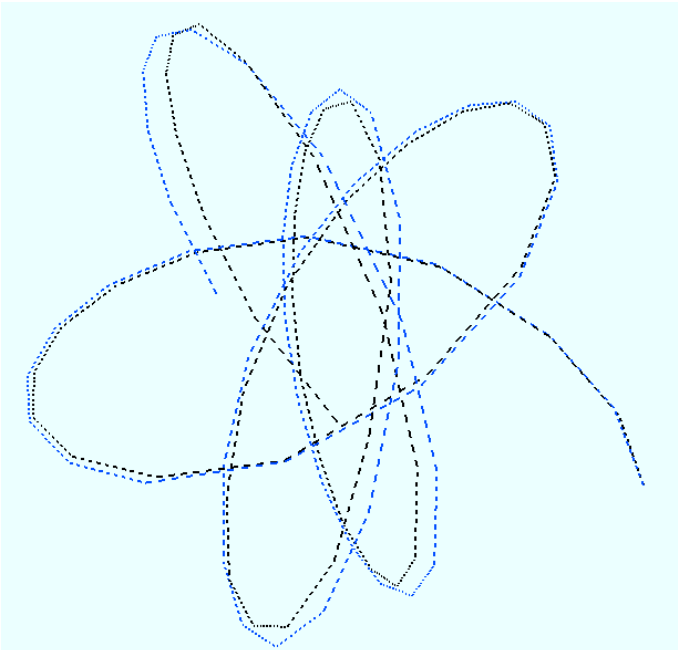

Figure 3.5: The orbit of a single particle in the Aq-A-4 simulation. The blue line shows the result of using the HEX approximation. The black line shows the actual path of the same particle followed through the Aquarius simulation. The particle positions were recorded only at limited points which have been joined by straight lines. Both paths start from the same point on the right and are integrated for 1 Gyr.

grating the orbit within the HEX approximation, a comparison can be made between the path that the simulation particle actually followed and the one recreated using the HEX method. Differences in the orbital path or properties provide a guide to the accuracy of the HEX approximation.

Fig. 3.5 shows an example of an orbit that is particularly well reproduced. The orbit of the particle extracted from the Aq-A-4 simulation is compared with one integrated for 1 Gyr in the HEX potential. The recreated orbit closely matches the actual particle path, though it slightly diverges over time. By the end of the integration there is some displacement between the final positions. While the orbit shape is well reproduced, the progress of the particles along their orbits is slightly out of phase. This discrepancy was introduced during the 3rd apocentre passage, when the resimulated particle took a slightly wider orbit so that it subsequently lags behind the actual particle. An increasing divergence in paths is not unexpected as once a particle has even slightly different phase

space coordinates it will subsequently follow an increasingly different orbit. The energy of the two particles is matched to within 1.3% throughout the entire orbit.

Once paths start to diverge, the particles will travel through different parts of the halo and it is therefore unsurprising that the properties of the original and recreated orbits become increasingly uncorrelated. It is more interesting to consider the properties of the particles over short time periods while the paths are still very similar. We do this for a set of 100 particles, randomly selected from the Aq-A-2 simulation from within 140 kpc of the halo centre at a redshift $z = 0.5$. We extract their orbits over 5 Gyrs by finding their positions through 33 successive snapshots.

In order to compare the acceleration of these particles in the HEX approximation to the acceleration they experienced in the original GADGET simulation, we must remove the overall halo acceleration from the GADGET values. This is necessary as the integration in the HEX approximation is performed in the moving halo frame. The linear component of the overall halo acceleration is easy to remove and shows up as a systematic offset in the accelerations between the two cases. Calculating the mean acceleration difference in the final $z = 0$ snapshot finds a clear offset of 18.2 kms^{-1} Gyr^{-1}. Once this component is removed we find a close match in the accelerations, with a median acceleration difference of 1.2% for the 100 particles over 33 snapshots.

A comparison between the HEX approximation and a direct N-body force summation of the same material included in the HEX expansion gives a slightly better agreement for the median force differences of 0.9%. The differences between this N-body summation and the GADGET force arise from a combination of the higher order acceleration components not being removed, possible errors in the force calculated by GADGET, which come from a TreePM method that is also an approximation, and the fact that the box containing the simulation is treated as periodic by GADGET. Regardless of these slight differences, both the comparison with GADGET calculated force and the direct summation demonstrate that there is in general an average force/acceleration error of approximately 1% for the HEX approximation. In certain situations there can be much larger errors; in one case we find a difference of 90%, when a particle comes within 500 pc of a large subhalo. Differences of this size are expected for the HEX potential near subhaloes, since such subhaloes are not well resolved in the approximation.

Integrating the orbits of the test particle set over the short time period between snap-

shots allows us to measure the distance between the final positions and the actual particle positions in the Aquarius simulation. The integration is done by treating the particles as non-interacting and placing them at the same initial position and with the appropriate relative velocity, and using a simple drift-kick-drift leapfrog integrator with a fixed time step of 1 Myr. By using the difference in forces at the snapshot times as an estimate for the average force error, we are able to calculate the expected divergence of orbits between snapshots and compare this to the divergence obtained from the HEX integration. Over the short time scale between snapshots of ~ 155 Myrs the displacements are small, usually a few hundred pcs. We find that the error in the displacement of the integrated paths are consistent with the estimated error.

Energy Changes

Examining how well the HEX approximation reproduces the integrals of the motion can be more indicative of differences in orbits than looking at the differences in final position. Position is an instantaneous phase space coordinate that rapidly varies along an orbit, and absolute differences in position are dependent on a particle's current radial distance from the halo centre. In contrast, energy, although not an integral of the motion since the potential is time-varying, changes slowly along the orbit. In a spherical potential, angular momentum would also be an integral of the motion. However, the Aquarius haloes are strongly triaxial, particularly in the centre, so contain a significant number of box type orbits (Binney and Tremaine, 1987). For these orbits the angular momentum varies rapidly over very short time-scales, which makes a comparison between the Aquarius simulation and the orbits integrated in the HEX approximation less useful. In this section we therefore only consider energy.

By again integrating the particle orbits between snapshot times in the HEX approximation we can obtain a change in the orbital energy for each particle. We have checked that the change in energy is equal to the integral of the time variation of the potential along the path to within 1%. Using a smaller step size has a negligible effect on our results, confirming that the changes in energy are not due to the numerical integration. Fig. 3.6 shows the correlation between the changes in the particles' energy in the Aquarius simulation compared to their energy change in the integrated HEX potential. There is a clear correlation between the two cases, with a Pearson correlation coefficient of

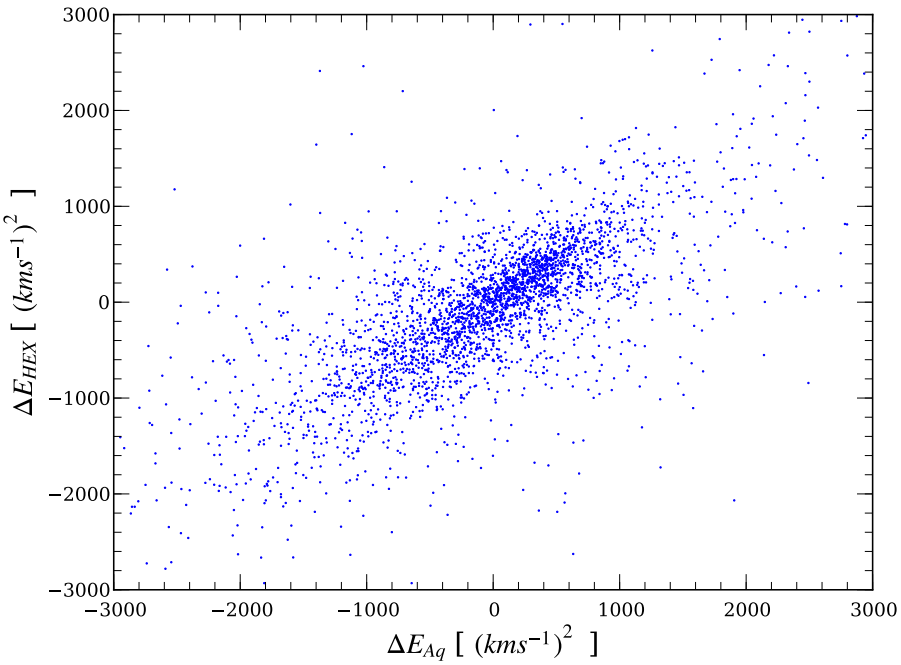

Figure 3.6: Energy change for selected particles between snapshots in the Aquarius simulation compared to energy change for the same particles when their orbits are integrated over the same period in an HEX approximation of the Aq-A-2 halo.

0.75. The HEX approximation does well at reproducing energy changes even though the particles may not follow exactly the same paths. As well as path differences the linear interpolation between coefficients will give a different variation in the potential at intermediate times; however, this does not seem to be important.

Encounters

Some of the test particles' orbits are significantly different to their Aquarius counterparts; they initially follow the Aquarius orbits but suddenly diverge and take very different paths. This occurs primarily for particles with low angular momentum on nearly radial orbits. The pericentric passages of these orbits are very close to the centre of the halo. As the particles approach the centre, the separation distance between the reconstructed orbits and the Aquarius paths becomes of the same scale as the pericentric distance. The large relative path separation results in the paths having substantially different approach angles and substantially different impact parameters, even in some cases passing opposite sides of the centre. Since the centre is very strongly triaxial, the change in the

angular momentum during the encounter with the non-spherical centre is sensitive to the direction of the incoming objects and will cause the pairs of particles to be diverted in radically different directions.

As well as the centre, which is responsible for the majority of these divergences, encounters with subhaloes can have a similar effect. Particles can either be deflected by subhaloes or become bound to them. To properly resolve a subhalo 1 kpc in size and 50 kpc from the centre would require at least an expansion with $n_{\max} = 150$ and $l_{\max} = 150$, over 3 million terms.

Population Distribution

Even though individual orbits integrated in the HEX approximation may not always match their counterparts, the overall distributions of the energy and the magnitude of the angular momentum are well reproduced. This can be seen in Fig. 3.7, the distributions of total energies of 10,000 randomly selected test particles and Fig. 3.8, the distribution of the magnitude of the orbital angular moment. Both figures include the initial distributions and the final distributions from both the original Aquarius simulation and HEX resimulation over 5 Gyrs.

The final energy distributions are very similar. A Kolmogorov-Smirnov (K-S) test gives a probability of 0.24 that the energy distributions are drawn from the same parent distribution. Therefore, the null hypothesis that the energy distributions of the orbits from the Aquarius simulation and HEX resimulation are the same is not rejected at a statistically significant level. There is equally good agreement for the angular momentum, with a 0.42 K-S test probability. The very similar distributions suggest that while individual orbits may not be exactly reproduced, there is no systematic difference in orbits integrated in the HEX approximation and those found in the Aquarius simulation. There is, however, a significant difference between the final and initial distributions, with a K-S test probability of less than 1.3×10^{-12} that the samples of orbital energies are drawn from the same distribution. The halo is accreting new material and evolving over the period of consideration, changing the overall distributions of energy. The fact that we match the final simulation distribution using the HEX approximation clearly demonstrates that the method correctly reproduces this evolution.

Focusing on orbits confined near to the centre of the parent halo we find an even

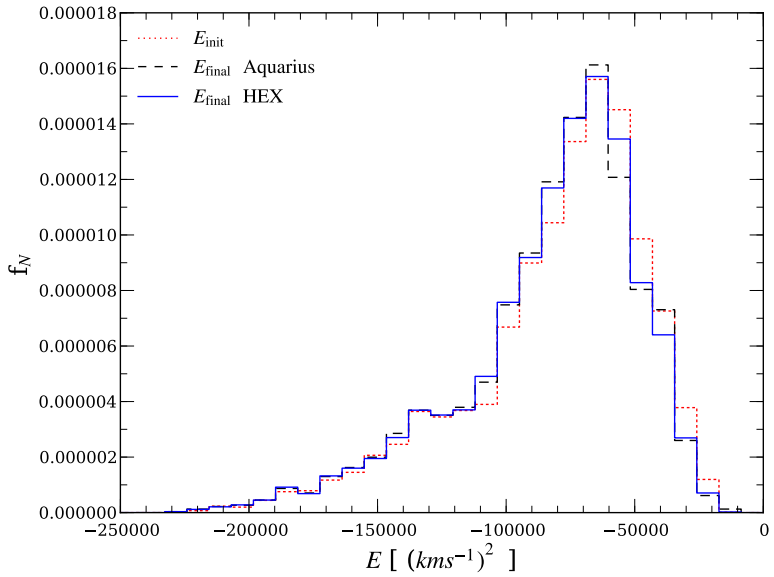

Figure 3.7: The distribution of the total energies of the 10,000 test particles. The dotted line shows the initial energy distribution, while the dashed line is the distribution of their energies in the simulations after 5 Gyrs. The solid line is the energy distribution in the HEX resimulation.

better match than for ones with larger apocentric distances. This is a consequence of both the fact that the basis functions used in the HEX approximation have lower spatial resolution at larger radii and thus structure is not resolved as clearly in the outer regions, and the fact that the halo is dynamically older and more stable towards the centre. Restricting our attention to particles confined to a region near the centre of between 3 kpc and 20 kpc, where the HEX expansion is very successful, selects particles on near circular orbits. When we consider the energy and angular momentum distributions for these orbits, we find that there is little evolution in the distributions, with significant K-S probability of 0.14 for energy and 0.76 for angular momentum, that the population properties of the initial and final simulations have not changed. There is also very good agreement between the HEX and the simulation distributions, 0.97 for energy and 0.37 for angular momentum. Orbits in this region are of particular interest when considering galactic disks.

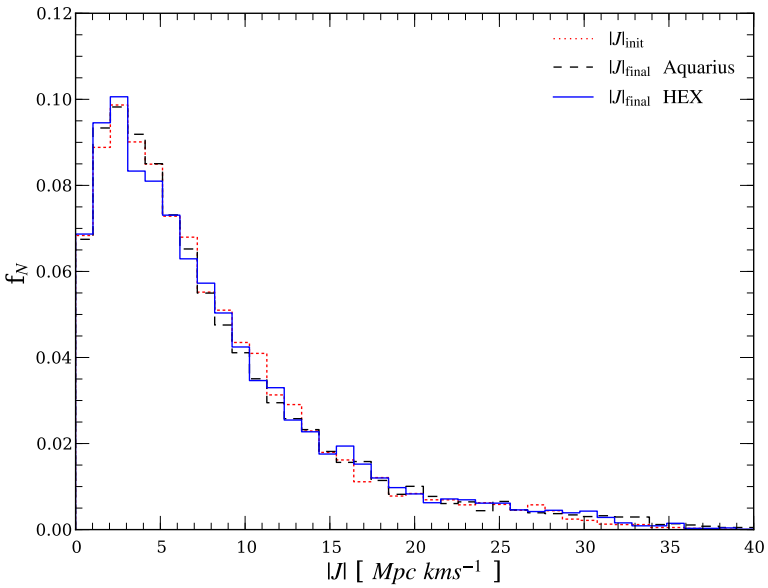

Figure 3.8: The distribution of the magnitude of the angular momentum of the 10,000 test particles. The dotted line shows the initial distribution, while the dashed line is the distribution in the Aquarius simulations after 5 Gyrs. The solid line is the distribution in the HEX resimulation.

3.5.2 Subhaloes

Having studied the orbits of individual particles, we now turn our attention to the dynamics and evolution of subhaloes. These are large, gravitationally bound, extended bodies undergoing tidal evolution as they orbit within the parent halo. We compare the orbits of subhaloes resimulated within different halo expansion potentials, treating the subhaloes as extended objects, to the orbits of subhaloes from the Aquarius simulation. To model a subhalo as an extended body, we select the subhalo from the Aquarius simulation and identify all the particles that SUBFIND assigns to it. The same particles are extracted from subsequent snapshots and SUBFIND is run on just this particle set to calculate those that are still gravitationally bound. This results in a complete orbital path and record of the subhalo's evolutionary history. The resimulation of the subhaloes is done using a version of GADGET modified to allow additional HEX external potentials. The subhaloes are composed of multiple particles allowed to interact gravitationally. From the Aq-A-2 simulation we selected all 1507 subhaloes with 100 or more particles that are within 90 kpc of the centre of the parent halo at $z = 0.5$. Their orbits and evolution are

then integrated for 5 Gyrs in the HEX potential.

The contribution to the potential from a subhalo needs to be removed from the halo expansion that is used to resimulate its orbit. Not excluding the self-contribution would lead to a double counting of the subhalo, because the gravitational effects of the subhalo are already included in the potential expansion. The double counting would generate an unrealistic self-attraction to the resimulated counterpart. Since the coefficients are just linear sums, it is easy to remove the contribution from the subhalo by separately calculating the coefficients of just the subhalo particles from the original simulation and subtracting them from the total coefficients. This does not remove the entire presence of the subhalo from the HEX approximation, as the halo response (i.e the dynamical friction wake) is still part of the expansion. While a resimulated subhalo closely follows the same orbit as in the original simulation, the wake can be an additional source of drag. However, an estimate of the dynamical friction on a subhalo based on the Chandrasekhar model (Chandrasekhar, 1943) shows that it is negligible for the majority of subhaloes and only really important for the most massive ones.

By contrast there can be no new halo response to the subhaloes in the resimulation, due to the fixed nature of the expansion; therefore there is no direct dynamical friction on the subhaloes. This is a potential limitation of the HEX technique, but if necessary dynamical friction could be added to the equation of motion. To do so would require an estimate of a subhalo's size and mass, information that is not easily available until the simulation is post-processed by SUBFIND or unless some subhalo evolutionary model is assumed. Since the majority of our samples are small subhaloes of mass $\sim 10^6 M_\odot$, dynamical friction from both effects can therefore be discounted as a significant source of error in reproducing subhalo orbits.

The success of recreating orbits of subhaloes resimulated within a full HEX approximation is similar to that of single particles; most orbits are very well matched while others are not. We find that there is minimal difference between the orbits of subhaloes when treated as point masses and when treated as extended bodies. Over 99% of subhaloes have a difference of less than 10% (82% less than 1%) in their final energy when treated as point mass rather than as an extended object, and over 90% have a difference of less than 10% (43% less than 1%) in their final radial distance from the centre. This suggests that the extended nature of the subhalo has a minor effect on its motion,

even though mass is being continuously stripped from the subhalo, forming leading and trailing streams.

Those cases where the Aquarius subhalo orbits and the resimulated orbits dramatically differ are again the result of encounter events. Subhaloes encounter the centre of the parent halo in the same way as particles, and any slight differences in the orbits are greatly amplified during the pericentric passage. However, as well as the passages near the centre, subhalo encounters are found to be more frequent than for single particles. When two subhaloes strongly interact, the orbit of at least one of the pair can be completely changed. In particular, a large subhalo merging into the parent halo will scatter any small subhaloes it passes as it falls in. These subhalo-subhalo interactions are not well reproduced in the subhalo simulations using the HEX approximation since, while contributions to the potential from subhaloes are included, these are not well enough resolved with the number of basis functions we use to model them. Instead, the potential from subhaloes is blurred out.

Evolution

As subhaloes orbit within their parent halo they are tidally stripped and shocked, losing mass and decreasing in size. Exactly how subhaloes evolve and their final fate is a problem that has been extensively studied (Peñarrubia and Benson, 2005; Angulo et al., 2009). We resimulate subhaloes in three different potential expansions corresponding to differing levels of sophistication. The simplest is a fixed, spherically symmetric Hernquist potential, an example of an analytical potential that is commonly used to represent dark matter haloes in simulations (Adams and Bloch, 2005; Bullock and Johnston, 2005). The second is a HEX potential that includes only radial basis functions to obtain the correct radial mass distribution, but with no information about the shape of the halo. The final potential is a full HEX potential including both radial and angular terms. We use the three different potentials in order to assess the difference between the evolution of subhaloes using the commonly employed method with a static simple potential and the effect of using a full time-varying triaxial approximation.

The parameters for the Hernquist potential are chosen so that it matches the lowest order basis function from the expansion of the halo at $z = 0$. It has a scalelength of 33 kpc and a total mass of $2 \times 10^{12} M_{\odot}$. This is a good fit to the halo at the final time but

overestimates the mass at earlier times. The second potential (HEX_R), using only radial terms, has $n_{\max} = 20$ and $l_{\max} = 0$, with a scalelength of 33 kpc, and has time-varying coefficients. The full potential (HEX_{20}) uses the default parameters, so it has $n_{\max} = 20$ and $l_{\max} = 20$, is also time-varying, and has a scalelength of 33 kpc. Again, we exclude the contribution to the HEX potential from the resimulated subhaloes.

We start by focusing on a single subhalo to illustrate the technique in more detail. This subhalo has been selected from the Aq-A-2 simulation and contains 13120 particles, with a total mass of $1.8 \times 10^8 M_\odot$. The subhalo was selected at redshift $z = 0.5$, and resimulated for 5 Gyrs, with output snapshots every 155 Myrs. It is compared to the same subhalo extracted at the same times from the Aq-A-2 simulation.

Fig. 3.9 shows the radial distance of the subhalo from the centre of the potential and three main structural properties that describe the state of a subhalo: the mass, the maximum circular velocity and the half-mass radius. The properties of the subhaloes in the two simplest methods, the Hernquist potential and the HEX_R, immediately diverge from that of the Aquarius simulation, as a consequence of the fact that they follow different orbits, as may be seen in the top panel. These different orbits cause the subhalo to experience different tidal stripping and, at pericentre, different amounts of tidal shocking, resulting in incorrect estimates of the structural properties. In the HEX_{20} resimulation, the subhalo follows an orbit very closely matching the actual subhalo's orbit for the first 2.5 Gyrs, until, following the first pericentric passage, the orbits begin to diverge. Subsequently, the Aquarius subhalo reaches a greater apocentric distance and falls back in slightly later. Following this, near the halo centre, the small differences in the paths are sufficiently large that during the second passage the HEX_{20} resimulated subhalo and the original Aquarius subhalo pass the centre on opposite sides and depart in different radial directions.

During the initial period, while the orbit of the subhalo in the HEX_{20} resimulation closely follows the fiducial Aquarius orbit, the subhalo properties, the mass, half-mass radius and maximum circular velocity, are reproduced extremely well. The subhalo is stripped and distorted in the same manner as in the Aquarius simulation. The subhalo continuously loses mass as it orbits within the parent halo, with sudden and large decreases during pericentric passages. Similarly, the maximum circular velocity, which is determined by the mass in the inner regions of the subhalo, is unaffected as mass is

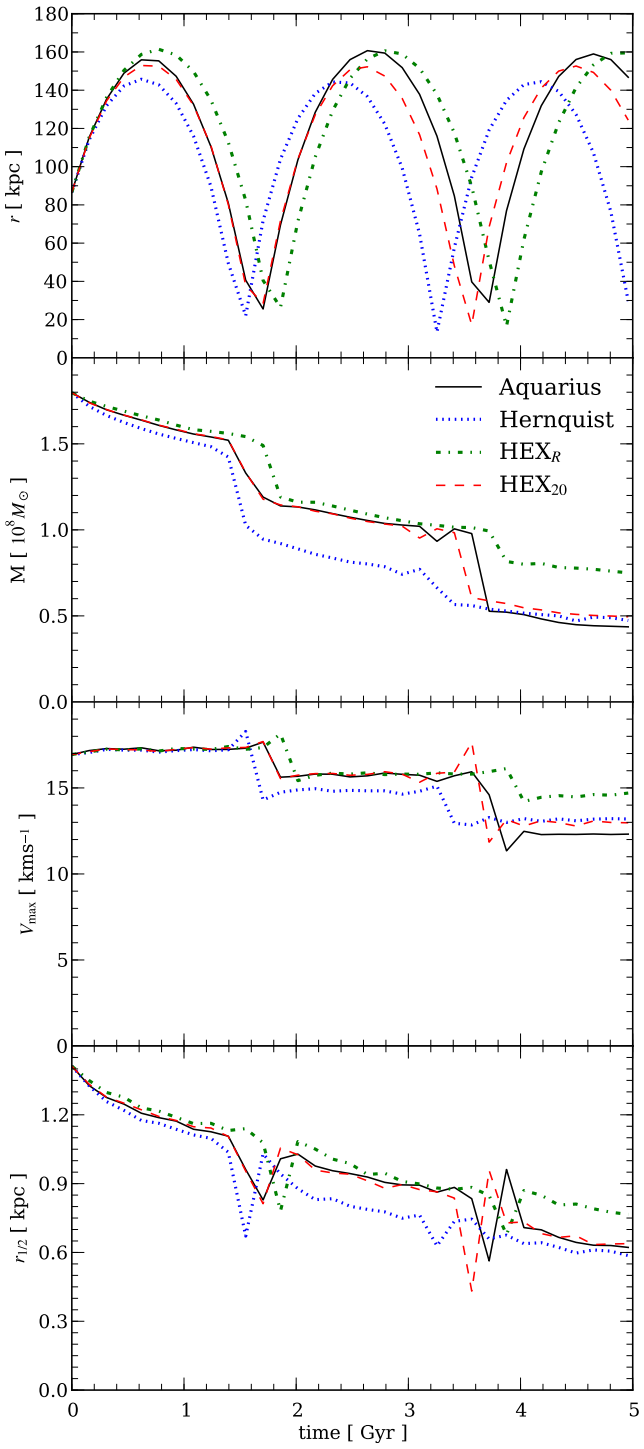

Figure 3.9: Comparison between the properties of different versions of the same subhalo. The full Aquarius Aq-A-2 simulation is represented by the black line. The other lines show resimulations of the subhalo in three differing potentials. *Upper panel:* the distance of the subhalo from the centre of the parent halo. *Upper middle panel:* the mass of the subhalo. *Lower middle panel:* the maximum circular velocity. *Bottom panel:* the half-mass radius.

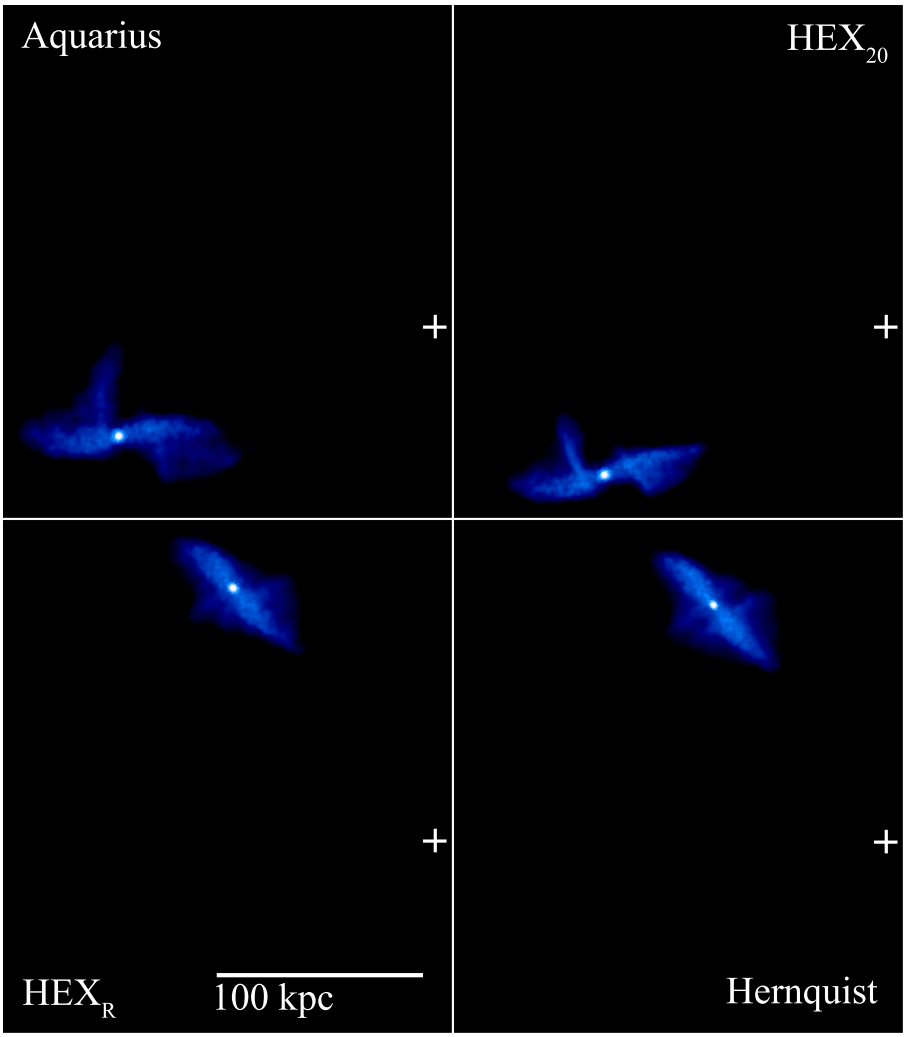

Figure 3.10: A projection of the smoothed density of a single subhalo resimulated in various different potential approximations at the subhalo's second apocentre. The subhalo reaches second apocentre at different times in the resimulations. The cross marks the centre of the parent halo in each case. *Upper left panel:* the subhalo at 2.6 Gyrs in the original Aquarius simulation. *Upper right panel:* the subhalo at 2.6 Gyrs in the full HEX_{20} potential *Lower left panel:* the subhalo at 2.8 Gyrs in the HEX_R potential. *Lower right panel:* at 2.3 Gyrs in a static Hernquist potential.

stripped from the outer edge. It is only when the subhalo makes a close approach to the parent halo centre and is tidally shocked and subject to maximum tidal stripping that the internal structure of the subhalo is notably changed. This behaviour is seen both in the Aquarius simulation and the HEX_{20} resimulation and indicates that the important gravitational mechanisms - tidal stripping and shocking, responsible for the evolution of a subhalo - are equivalently modelled by the full HEX potential as they are in the full simulation.

An instantaneous picture of the subhalo during its second apocentre can be seen in Fig. 3.10. Rather than comparing the subhalo at the same time, it is fairer to compare it at the same position along the orbit as this removes any difference in orbital phase. The resimulated subhalo in the HEX_{20} potential is strikingly similar to the original Aquarius subhalo. It is close to the correct position at the correct time and has very similar tidal tails. This similarity includes the small perpendicular protrusion to the left of the subhalo, which is a result of the end of the trailing tidal tail being broken off during the apocentric turn-around. In contrast, there is little resemblance between the subhalo in either the Hernquist or the HEX_R resimulation and the Aquarius original, though there is a strong resemblance between the two simulations. Both potentials are spherical, confining the subhalo to orbit in a plane, and thus the two potentials generate similarly shaped orbits. However, there is a large phase difference between the two. The Hernquist subhalo reaches the second apocentre 290 Myrs before the Aquarius subhalo, while the HEX_R reaches second apocentre 140 Myrs after the Aquarius subhalo.

The final values of the mass, maximum circular velocity and half-mass radius, are similar in the Hernquist and HEX_{20} resimulations, but this is more a coincidence than the result of the subhalo having the correct evolution in the Hernquist potential. While not completely correct, the evolution of the subhalo is much closer to the real case when the full HEX potential is used than when the simplified potentials are used. This suggests that both the radial mass distribution and the angular shape of the halo are important for reproducing correct orbits, which is a prerequisite to achieve similar evolution.

Population Evolution

To assess whether the evolutionary mechanisms on subhaloes are the same even though the orbits may not exactly match, we now consider a population of subhaloes and look at

the statistical match between a set of Aquarius reference subhaloes and resimulations of them in the three potentials. From the Aq-A-2 simulation we again use the set of selected subhaloes with 100 or more particles that are within 90 kpc of the centre of the parent halo at $z = 0.5$. The particles belonging to these subhaloes are then tracked forward in time to follow the subhaloes' evolution in the full simulation.

Fig. 3.11 shows the population distribution of the three main structural properties of subhaloes: the mass, the half-mass radius, and the maximum circular velocity. The distribution of the ratios of the final to the initial property has been used to remove the influence of the property distribution and allow an easier comparison of the actual evolution that the subhaloes undergo during 5 Gyrs. The distribution of mass ratios shows how much stripping the subhaloes experience. Nearly all subhaloes in the Aquarius simulation lose mass over the 5 Gyrs, but a small fraction gain mass. The gain in mass can be explained by inter-subhalo mergers, where two or more subhaloes join to form a larger subhalo. The HEX resimulations and the Aquarius simulation have the same small fraction of subhaloes undergoing this mass increase; they have similar distributions of mass ratios, with the same wide spread and a peak that occurs at 0.65. Only the Hernquist potential shows significant difference.

Similarly, the half-mass radius distribution is well matched by the resimulations, except again by the Hernquist potential, which is slightly shifted to smaller sizes. Even though subhaloes generally lose mass, a small proportion grow in size. This can occur when a subhalo passes pericentre and is tidally shocked by the rapidly changing potential field, thus increasing its internal energy and resulting in an increase in size. This occurs in both the Aquarius simulations and HEX resimulations. The maximum circular velocity distribution is very slightly smaller in all the resimulations, with the largest discrepancy again for the Hernquist population. The primary reasons why the results from the Hernquist resimulation are so different from the other two are the assumption of a static potential of fixed mass throughout the whole simulation, which overestimates the actual mass of the Aquarius halo at early times, and the fact that a Hernquist potential gives the incorrect tidal radius for subhaloes. The tidal radius is the distance from the centre of a subhalo at which the gravitational tidal pull from the parent halo is equal to the pull from the subhalo itself. Material outside of this radius is stripped from the subhalo and becomes part of the parent halo. We find that the Hernquist potential leads

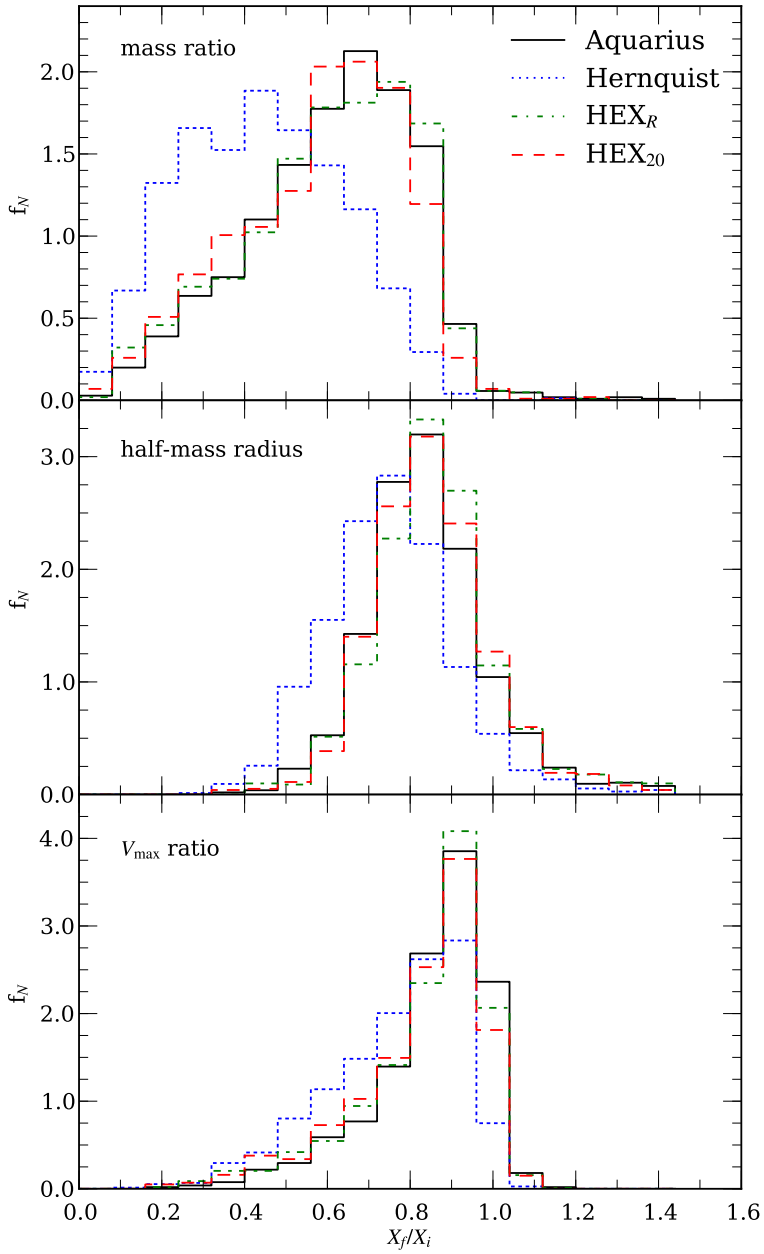

Figure 3.11: The distribution of X final over X initial for a selected Aquarius subhalo population for three different physical properties. The black line shows the actual distribution that occurred in the original Aquarius simulation, while the other colours correspond to the different resimulations. For each subhalo, the ratio is the given property at $z = 0$ compared to its initial value at $z = 0.5$. *Upper panel:* the distribution of final to initial mass ratios. *Middle panel:* the distribution of final to initial half-mass radii. *Bottom panel:* the distribution of final to initial maximum circular velocities.

to an underestimation of the tidal radius for subhaloes that are between 30 and 200 kpc from the centre of the parent halo and to overestimates outside this range. The subhaloes therefore experience a different rate of stripping over the course of their orbits than they do in the original simulation and the other cases.

Since the HEX$_R$ potential achieves an equally good match to the Aquarius simulation as the full HEX potential that also includes the angular terms, we conclude that the shape of the potential is unimportant for reproducing the structural evolution of the subhalo population in a statistical sense; only the radial mass distribution needs to be correctly reproduced. The stripping of mass from a subhalo is controlled by the tidal radius of the subhalo, so reproducing this property correctly ensures the correct overall evolution. This can be done by matching the radial mass distribution, which is easily achieved with a small number of basis functions. In order to obtain similar evolution on an individual subhalo basis, the orbits need to be well matched, which does require the angular distribution and the full HEX approximation.

3.6 Application - Increasing Subhalo Resolution

Having shown that the orbits, as well as the subhalo evolution, are similar in a HEX approximation and in the original simulation, we now demonstrate how the HEX technique can be used to go beyond the original simulation. The introduction of new objects into the halo that were not present in the original simulation allows us to investigate the reaction of these objects as if they had evolved in a cosmologically realistic potential. They are unable to induce a back reaction on the halo, but the method is appropriate for studying light objects that would have had little effect on the halo. This can be achieved at a much lower cost than re-running a complete simulation and is more realistic than assuming a fixed analytical profile, such as a Hernquist profile.

We now illustrate the technique of placing new, additional subhaloes into the potential and simulating them at much higher resolution. As a test, a subhalo is constructed to be similar to the subhaloes found in the simulations, with an NFW density profile

$$\rho(r) = \frac{\rho_0}{\left(\frac{r}{r_s}\right)\left(1+\frac{r}{r_s}\right)^2}, \tag{3.24}$$

with $\rho_0 = 8 \times 10^7 M_\odot \mathrm{kpc}^{-3}$ and $r_s = 0.27$ kpc, and an isotropic velocity distribution.

The subhalo is injected into the HEX potential approximation of the Aq-A-2 halo. To create equilibrium N-body halo realisations, we have used the algorithm described in Kazantzidis et al. (2004b) based on sampling the phase-space distribution function to generate the subhalo. This procedure is described in Appendix A. Since the mass of an object with an NFW profile does not converge with radius, we truncate the subhalo at the virial radius using an exponential cut-off with a decay length set to ten times the virial radius. This ensures the subhalo has a finite mass.

We generate the initial subhalo at two resolutions. The first, lower resolution version consists of 6000 particles with masses of $1.4 \times 10^4 M_\odot$, the same particle mass as the Aq-A-2 simulation. The second version contains 10^6 particles, a resolution 170 times higher, with individual particles masses of just $82 M_\odot$. Since the subhalo is small, with a SUBFIND mass of $5 \times 10^7 M_\odot$, the absence of dynamical friction should not be significant. The subhalo is placed 190 kpc from the halo centre, approximately at the virial radius of the parent halo, where it will be just entering into the main halo and will not yet have been significantly stripped. The subhalo is simulated from $z = 0.5$ for 5 Gyrs.

The orbits of the two different resolution versions of the subhalo are virtually identical. This is not unexpected, as we have already found that subhaloes orbit as point masses regardless of their extended nature. The changes in the properties of the subhalo over the 5 Gyr simulation are shown in Fig. 3.12. Here we compare the evolution of the mass, maximum circular velocity and half-mass radius between the low and high resolution simulations. While both realisations of the subhalo are sampled from identical NFW profiles, the initial SUBFIND mass is slightly higher for the low resolution version. Later mass estimates agree, suggesting that in both cases the subhalo was stripped to the same tidal radius, and the same material was lost regardless of whether SUBFIND had initially associated it with the subhalo or not.

The maximum circular velocities again are very slightly different, but the higher resolution version has a smoother evolution since it is less affected by noise from the discrete particle nature of the subhalo. The half-mass radius has the same initial discrepancy as the mass, but again agrees at later times, with both versions undergoing the same compression of the subhalo during the first pericentric passage. Overall there is excellent convergence between the two resolutions and it is clearly demonstrated that the structural evolution is independent of the resolution of the subhalo as expected.

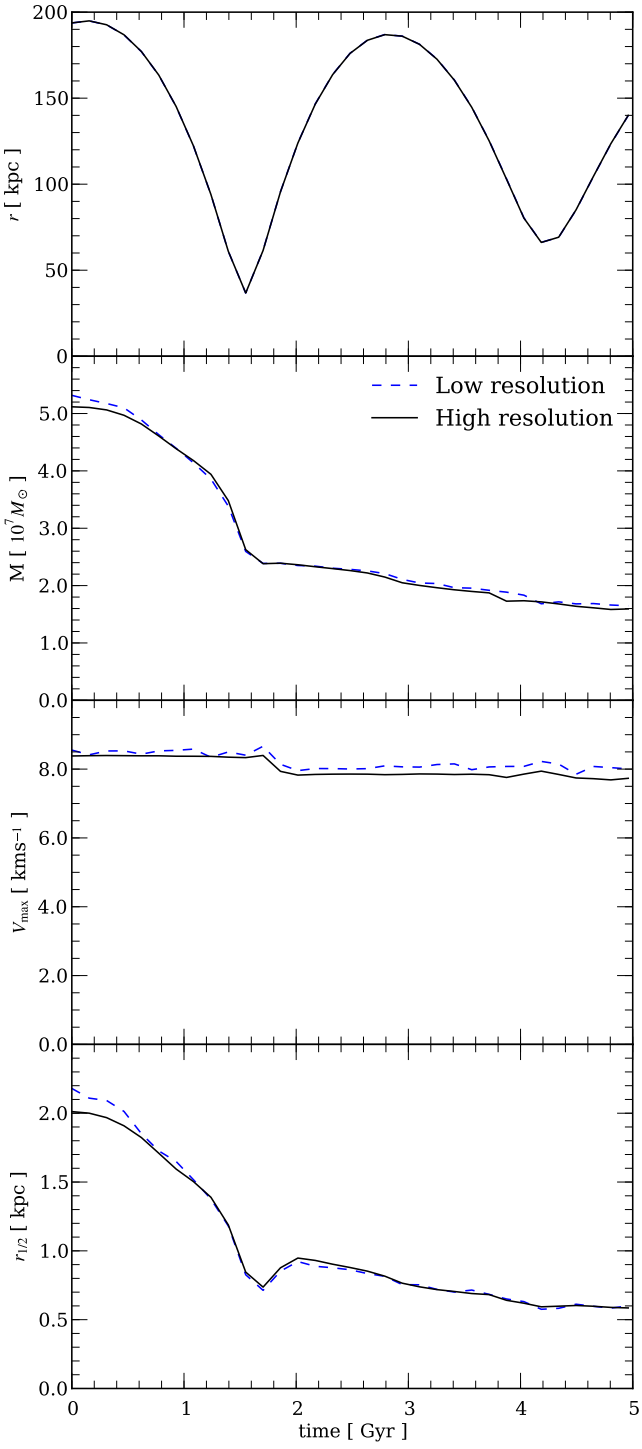

Figure 3.12: Comparison between the properties given by SUBFIND for a subhalo simulated for 5 Gyrs at two resolutions in the HEX potential. *Upper panel:* the distance of the subhalo from the centre of the parent halo. *Upper middle panel:* the mass of the subhalo. *Lower middle panel:* the maximum circular velocity. *Bottom panel:* the half-mass radius.

Apart from studying the subhalo we can compare the fate of the material that is stripped from it and forms streams. There is both a leading stream and a trailing stream, containing material that is no longer bound to the subhalo but continues to follow similar orbits. These streams match in the high and low resolution simulations, but are much clearer and can be traced much further in the high resolution version. Sections of the streams containing a few tens of particles in the low resolution version are now populated with thousands of particles in the high resolution simulation. Features that had been only hinted at are clearly defined in the high resolution simulation. Especially clear are the caustics of the streams, which can be seen in Fig. 3.13. Another feature that is not resolved in the low resolution simulation but is clearly visible in the high resolution version is the bifurcation into two separate arms of the leading tidal tail, the one above the subhalo in Fig. 3.13.

The HEX method allows us to simulate a subhalo at different resolutions, with clear convergence between the two cases we have examined. By focusing computing resources on just the subhalo and using an approximation to the potential of the larger parent halo, we have been able to reach an unprecedentedly high resolution, using a particle mass of a few tens of solar masses and resolving tidal streams much further and in a much sharper way than has been previously achieved. The low resolution simulation required only 15 cpu hours[1] and the high resolution subhalo only 2700 cpu hours. This is small compared to the Aquarius A level 2 simulation, which has equivalent resolution to the low resolution subhalo and which took of the order $\sim 150,000$ cpu hours over the same time interval. While a full simulation may include thousands of subhaloes, we have demonstrated that it is possible to vary the parameters and rerun multiple versions of a single subhalo in a small fraction of the time.

3.7 Conclusions

We have demonstrated the power of using the halo expansion method to approximate a dark matter halo. While much work has previously been carried out using expansion methods as part of the SCF technique to calculate the force in an N-body simulation, this is the first time that such an expansion technique has been applied to describe an

[1] On a 2.2 GHz AMD Opteron (AMD Opteron 175)

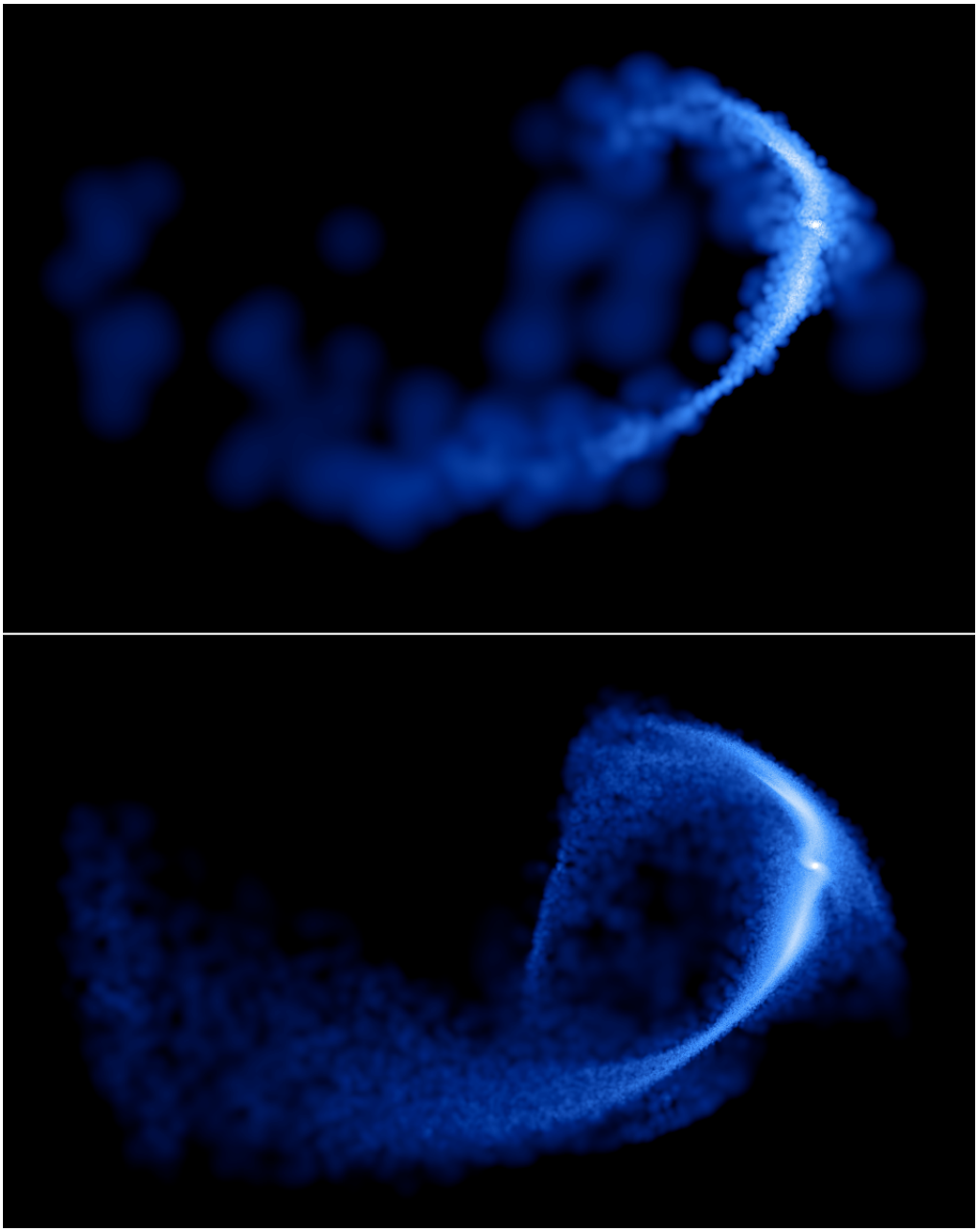

Figure 3.13: The smoothed density of the resimulated subhalo after 5 Gyrs at $z = 0$ using the HEX potential. *Upper picture:* the low resolution realisation subhalo containing 6000 particles. *Lower picture:* the high resolution realisation subhalo containing 10^6 particles.

already simulated dark matter halo. Using a small number of basis functions, the HEX technique offers a way to approximate the time-evolving potential. A set of coefficients can be calculated once from the simulation and then serve as a realistic approximation of a halo. It is simple to integrate orbits within the HEX potential approximation and, as a first test, we focused on particle and subhalo orbits.

Using the HEX method to represent a dark matter halo, however, has some limitations. The potential is fixed and unable to react to objects within it. New elements placed in the simulation, such as additional subhaloes, cannot modify the halo potential. This could be especially problematic when considering galaxies and the adiabatic contraction that the presence of baryons is expected to produce. The second major limitation is the lack of dynamical friction that should be present in the equations of motion. Subhaloes orbiting within the expansion are missing the effect of this force that would make their orbits decay. While it is possible to add in dynamical friction analytically, this requires assuming a model of subhalo evolution to estimate the mass and size of the subhalo.

Through application of the HEX method to a halo simulated by the N-body code GADGET, we have demonstrated that:

- A HEX potential of a dark matter halo can approximate the halo well enough to recover the radial component of the force to within 1 percent using only a few radial basis functions.

- It is possible to integrate orbits within the expansions and to reproduce overall population trends. For individual orbits the degree of success is varied. However, it must be remembered that GADGET dynamics are not necessarily numerically perfect and therefore differences are to be expected. For orbits that are near circular and stay within the central 20 kpc of the halo we can accurately follow their path over several dynamical timescales.

- Without dynamical friction, subhaloes follow orbits close to those of point masses. Their extended nature and tidal streams have little or no effect on their orbits. The orbits of subhaloes are not simple planar orbits but involve complicated changes in orientation and are strongly affected by encounters with the halo centre and other subhaloes.

- The method can reproduce the structural evolution of individual subhaloes. To ob-

tain similar evolution for a particular subhalo we need to match its orbit, which requires a full potential expansion. To match the correct overall population evolution we do not need the full expansion, but require only the radial terms to obtain the correct radial mass distribution. Not including the angular terms greatly speeds up the force evaluation.

We have been able to introduce new objects, such as subhaloes, into the HEX potential; we find an evolution consistent with that which would have taken place if the subhaloes had been present in the original Aquarius simulation. The technique allows us to simulate subhaloes with much higher resolution than in the original simulation and to resolve features in the tidally stripped streams in great detail.

While the HEX technique has some limitations, it offers a powerful way of improving current models of galaxy formation. The standard simple, spherically symmetric profiles often used to represent the dark matter halo when modelling dynamical processes involving orbits miss important effects related to the triaxiality of haloes and the evolution of the potential. In order to build more realistic models it is necessary, as we have shown, to use more sophisticated representations of dark matter haloes such as the ones the HEX technique offers. There is a large number of possible applications for this technique and we have briefly explored only a few of these in this chapter.

In the next two chapters we will explore the interactions between subhaloes and discs. Experiments of using the HEX technique to reconstruct the orbits between outputs of the subhaloes taken from the Aquarius simulations were not particularly successful. As demonstrated in this chapter, the technique does not reproduce the exact orbits, and it is therefore easier to use simple interpolation for this purpose. Even though much of this chapter has focused on attempting to reproduce the behaviour of objects from the simulations, this was purely to validate the technique and demonstrate that a HEX potential can generate behaviour with properties consistent with the simulations it approximates. The real power of the HEX technique is for understanding the behaviour of new objects that were not in the original simulations in realistic potentials in a controlled manner; such as the evolution of streams. This is not looked at in this thesis but is future work that we intend to explore and is discussed further in chapter 6.

Chapter 4

Disc Heating by Subhaloes

4.1 Introduction

In this chapter we use an analytical model to estimate the heating of galactic discs by substructure bombardment. The term disc heating was originally used to refer to the gradual and continuous increase in the velocity dispersion of stars in the Galactic disc, suggested by the age-velocity dispersion relation observed in the local neighbourhood (Nordström et al., 2004; Holmberg et al., 2007). Subhaloes (Quinn and Goodman, 1986; Carlberg and Hartwick, 1989; Toth and Ostriker, 1992), along with giant molecular clouds (Spitzer and Schwarzschild, 1951, 1953; Lacey, 1984), MACHOs (Lacey and Ostriker, 1985; Friese et al., 1995) and transient spiral waves (Barbanis and Woltjer, 1967; Sellwood and Carlberg, 1984) have all been regarded as possible candidates that, through gravitational interactions, might be responsible for the heating of disc stars. However, exactly what fraction of the observed heating each of these mechanisms contributes is still uncertain. It is thought that subhalo interactions should have notable effects on discs, but whether they are one of the dominant mechanisms responsible for increasing the random stellar motions is unknown.

It has been proposed that rather than the slow gentle heating needed to explain the age-velocity relation, interactions with massive subhaloes may generate sudden and much greater heating, which could explain the existence of thick discs. Thick discs have been observed in the Milky Way (Gilmore and Reid, 1983) and many other external galaxies (Morrison et al., 1997; Dalcanton and Bernstein, 2002; Yoachim and Dalcanton, 2006; Elmegreen and Elmegreen, 2006), and it is postulated that they might have been formed by some mechanism that dramatically increased the scale-height of an initially

thin disc. Both types of disc heating are considered in this chapter and we attempt to discern whether late time subhalo bombardment generates either gentle heating consistent with the age-velocity dispersion relation, or rapid dramatic heating needed to form a thick disc.

We focus on the late time heating of the disc from $z = 1$ to $z = 0$. Interactions between subhaloes and discs are much more complicated at earlier times when the formation and growth of the disc must also be considered (Fall and Efstathiou, 1980; Mo et al., 1998). To properly model the growth of a disc requires including a full treatment of the gas accretion and star formation (White, 2009; Burkert, 2009; Brooks, 2010). Instead, we use a simple pre-formed, fixed size disc to focus on the dynamical effects that the purely gravitational interactions have on stellar orbits, and restrict the problem to low redshifts, where a fixed size disc is a reasonable approximation.

To calculate the heating of a disc by substructure bombardment requires two elements: an estimate of the abundance of subhaloes in the central regions, and a model for the amount of heating each subhalo generates. In order to obtain realistic populations of subhaloes from cosmological haloes, the abundance of subhaloes can be directly measured from simulations, such as the Aquarius simulations. From the impulse heating approximation (Binney and Tremaine, 2008), the tidal effects of a subhalo population scale as $dE/dt \propto \int n(M_{sub}) M_{sub}^2 dM_{sub}$, where $n(M_{sub})$ is the number density of subhaloes and M_{sub} is the subhalo mass (White, 2000). Since $n(M_{sub}) \propto M^{-1.9}$ (Springel et al., 2008), the heating will be dominated by the most massive but rare subhaloes and there will be significant variation from disc to disc. Thus it is mainly these massive subhaloes that we will focus on.

4.1.1 Previous Work

The problem of estimating the heating of the disc by subhalo bombardment has been tackled in several different ways. One approach has been to use analytical models based on the energy transferred from the subhaloes as they spiral inwards to the vertical motions of the disc. Toth and Ostriker (1992) first proposed a model in which subhaloes are on circular orbits and slowly lose energy as they spiral inwards due to dynamical friction. The dynamical friction from the disc scatters the orbits of the stars within the disc, increasing their random motions, with 25 percent found to be deposited in motions

in the z-direction and 75 percent in planar motions. Their model led them to conclude that the resultant disc heating from subhalo bombardment was too high to be compatible with the observed thinness and coldness of discs in spiral galaxies, and that the Milky Way disc could not have undergone a merger of mass ratio 1:10 or larger in the last ~ 10 Gyr; a problem for the model of the hierarchical build-up of galaxies. However, they used a $\Omega = 1$ CDM cosmogony, where the build-up of structure is more rapid.

Further problems were soon identified with the Toth and Ostriker (1992) analytical estimates, indicating that the heating rate was somewhat too high (Huang and Carlberg, 1997; Velazquez and White, 1999). The first of these problems is that the merger rate was too high. Navarro et al. (1994) showed in cosmological simulations that many of the subhaloes accreted onto a halo do not survive to merge with the central galaxy. Secondly the model used circular orbits, whereas recent work (Hopkins et al., 2008) using more realistic subhalo orbits found instead that heating rates are nonlinear in mass, so the heating is dominated by the more stochastic, rare, low mass ratio mergers. The third issue was that the model used the simplification of local deposition of the subhalo's orbital energy. If instead it is the large-scale, disc bending waves (Sellwood et al., 1998) that are most important, then energy can be deposited some distance from the point of impact of the satellite. The net heating from a tightly bound subhalo can still be substantial, but only for subhaloes that are not tidally disrupted before they are able to excite bending waves.

The other main approach has been to use simulations of a galaxy model, comprised of a halo, disc and bulge, and introduce subhaloes that are allowed to fall into the centre to interact with the disc. However, early simulations contained as many problematic assumptions as the Toth and Ostriker (1992) model. Subhaloes were modelled as rigid point masses (Quinn et al., 1993; Sellwood et al., 1998; Ardi et al., 2003), or on circular orbits (Quinn et al., 1993; Walker et al., 1996; Huang and Carlberg, 1997), and/or using a smooth, fixed halo potential (Quinn and Goodman, 1986; Quinn et al., 1993; Ardi et al., 2003). Recent simulations now benefit from the availability of sufficient computational power to avoid these assumptions and model subhalo-disc encounters in a fully self-consistent manner, using multicomponent disc galaxy models treated in a full N-body way.

Modern simulations take the form of one out of two types, those that consist of en-

counters of single subhaloes with discs, and those that employ large ensembles of dark matter subhaloes, usually motivated from larger cosmological simulations, to measure the cumulative effect on a disc. The single encounter simulations usually follow the merger of a massive substructure, some significant fraction of the disc mass, in an effort to observe the major response of the disc. Using a subhalo with 10-20 percent of the mass of the disc, Villalobos and Helmi (2008) were able to form a thick disc with characteristics similar, both in morphology and in kinematics, to those observed. Purcell et al. (2009) on the other hand showed that the interaction with a subhalo three times the mass of a disc completely destroyed it.

While these simulations suggest that massive subhaloes can have a significant effect on some discs, the question remains whether subhaloes of these masses are common in the central regions of haloes. Font et al. (2001) were among the first to run simulations of disc bombardment using a large number of subhaloes with a realistic mass function derived from high-resolution cosmological simulations. While their simulations saw little heating, they used the population of subhaloes at $z = 0$, which has been shown to have vastly different properties to the population at earlier times (Zentner and Bullock, 2003; Gao et al., 2004). Kazantzidis et al. (2008) and Read et al. (2008) followed similar approaches, but looked at the population of subhaloes over an extended period, and both found that an average Milky Way-sized halo contains several subhaloes sufficiently massive to account for the formation of thick discs.

In this chapter we will focus on using an analytical model to measure the effect that subhaloes have on discs. For this purpose, we employ the Benson et al. (2004) semi-analytical model to estimate the heating. The model is based on similar principles to the original Toth and Ostriker (1992) model but takes a semi-analytical approach of integrating the orbits of subhaloes and using a dynamical evolution model to evaluate their mass loss as they fall in. We apply the semi-analytical heating model to populations of subhaloes selected from the Aquarius haloes. However, the Aquarius haloes are dark matter only simulations and lack the baryons that affect the very centres of haloes. For this reason in the next chapter we take the same selection of subhaloes at the point they start to fall in to the central 50 kpc, while they are still in the region where we believe the halo to be dark matter dominated, and perform new N-body simulations of their subsequent evolution in a multi-component galaxy. In this manner we can both test the

heating model on the simulations and compare the difference made by the inclusion of a galaxy on the heating estimate.

4.2 Central Subhalo Abundance in Aquarius Haloes

Cosmological simulations provide the best way to obtain estimates of the populations of subhaloes present in the central regions of Milky Way-mass haloes. Realistic parameters for the spatial and temporal distributions of substructure are a vital part of any estimate of the heating they may induce in discs. The number of massive subhaloes that pass within ~ 20 kpc of the centre of the host halo and the times of these passages can easily be extracted from simulations. The SUBFIND outputs and associated merger trees of the Aquarius simulations allow us to identify and track subhaloes as they pass close to the centres of the haloes. The level 2 Aquarius simulations are ideal for this as they have high enough resolution for subhaloes of the relevant masses to be well resolved and have frequent enough outputs for tracking the orbits with sufficient accuracy. Since the question is about bombardment of galactic discs, the last of the Aquarius haloes, Aq-F, has not been included. The two major mergers at late times ($z \sim 0.6$) that the halo undergoes render it unlikely to host a disc galaxy at $z = 0$, and consequently we only use Aquarius haloes A–E.

To gain an idea of how the abundance of subhaloes varies in time, the cumulative mass function of all subhaloes within 20 kpc of the centre of the five Aquarius haloes has been plotted in Fig. 4.1 for three redshifts, $z = 1$, $z = 0.5$, and $z = 0$. In all five haloes the abundance of subhaloes decreases by a factor of ~ 3 between $z = 1$ and $z = 0$. Due to the small number of subhaloes, the slope of the mass function is not well constrained, but appears similar in all five haloes and is consistent with the relation $n(> M) \propto M^{-0.9}$ measured for the entire population of subhaloes in the Aquarius A simulation (Springel et al., 2008). The slope does not show notable evolution with time, implying that the rate of subhalo depletion is the same for all masses.

There is considerable variation in the normalisation of the mass function between the five haloes. Aq-B and Aq-D have over ~ 70 subhaloes with masses greater than $10^6 \mathrm{M}_\odot$ at $z = 0$ compared to Aq-C, which has less than half this number. Haloes Aq-A and Aq-E lie intermediate between the two. Yet it is the largest subhaloes, where the mass

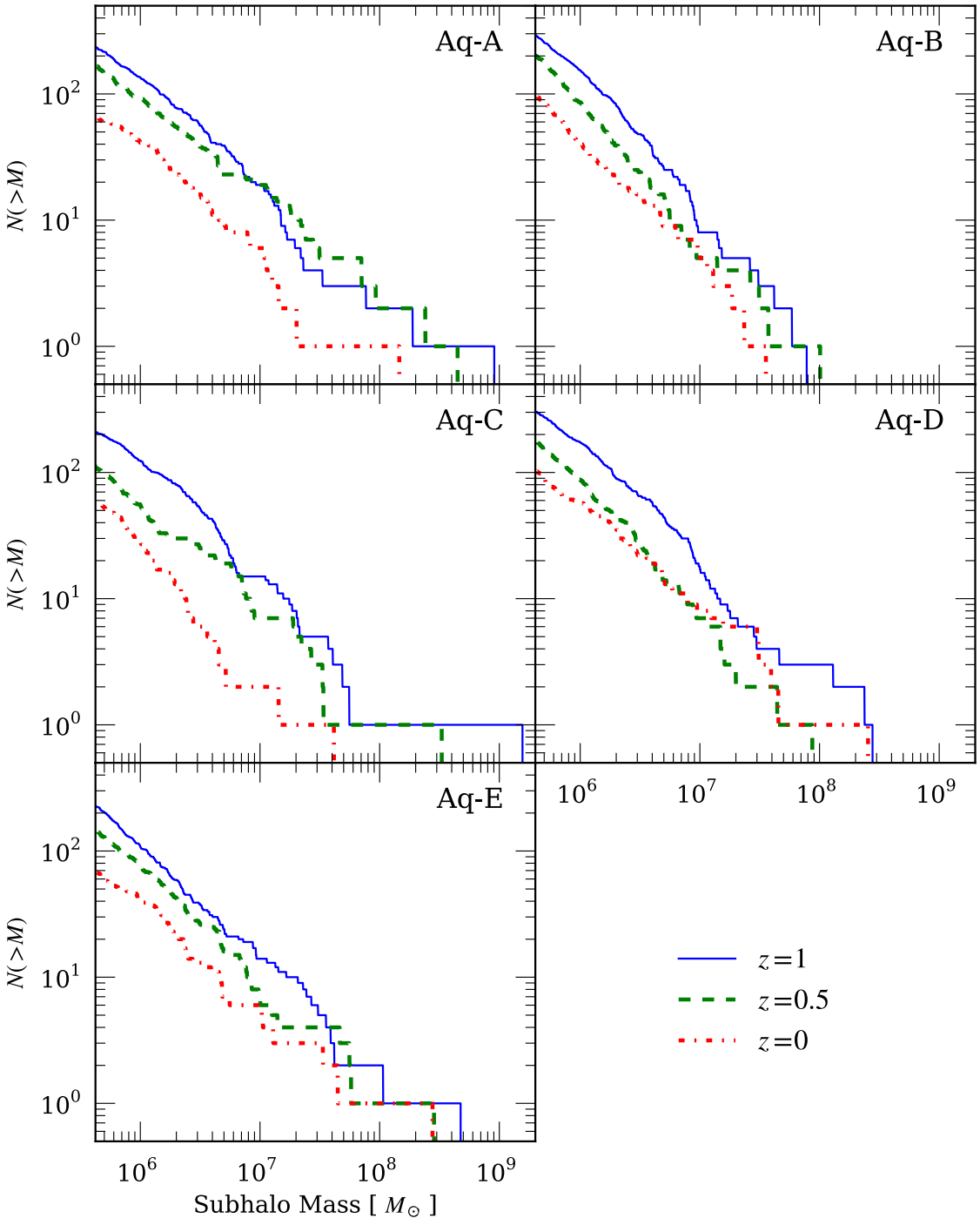

Figure 4.1: Cumulative mass functions of the subhaloes within 20 kpc of the halo centre at redshifts of $z = 1$ (blue solid line), $z = 0.5$ (green dashed line), and $z = 0$ (red dot-dashed line) for the five level 2 main Aquarius haloes.

function is stochastically sampled, that are of the greatest importance for heating. The mass of the largest subhalo varies widely between the haloes and over time. Subhaloes of these masses are so rare that there is no clear correlation between their number and the overall abundance. In order to gain an idea of the numbers of massive objects we therefore consider all subhaloes that enter the central regions over an extended period rather than looking at the instantaneous populations.

Fig. 4.2 shows the pericentric distance versus the mass at pericentre for all subhaloes that have come within 20 kpc of their host halo's centre between $z = 1$ and $z = 0$. The output of the Aquarius simulations are only saved at a fixed number of times, and subhaloes can complete large fractions of an orbit between outputs. In order to get an accurate estimate of their distance of closest approach, the path of the subhaloes during these periods must be reconstructed. Attempts to use the HEX technique to approximate the potential of the main halo and integrate the subhalo orbits within it, as described in chapter 3, failed in a number of important cases. The paths of subhaloes that pass very close, within 1 kpc, of the parent halo centre were often incorrectly reproduced. Instead, interpolation using cubic splines proved to be quicker, simpler and more robust than integrating the orbits within a HEX potential approximation. The paths recreated using splines are not constrained to be completely physical, but the error in positions along the path is small compared to the uncertainty in the subhalo masses.

The SUBFIND mass of the subhaloes is available for each output time of the Aquarius simulations. To accurately determine the mass of a subhalo at intermediate points would require a full evolution and stripping model. As this is outside the scope of the current work we use linear interpolation of the mass between outputs for simplicity. However, it is a general problem that halo finders relying on just the configuration space information struggle to recover the properties of subhaloes located close to the centres of haloes and can show an artificial radial dependence for the mass (Knebe et al., 2011). As subhaloes pass through the centre of a host halo they are tidally stripped and their mass drops rapidly. After the central passage, halo finders often see an unexpected, unphysical rise in the mass. In the case of SUBFIND this problem occurs because it looks for overdensities by finding saddle points in the mass density profile, so the particles identified as belonging to a subhalo depend on the background density. As a subhalo approaches the centre of the host halo and the background density increases, fewer particles are assigned to it.

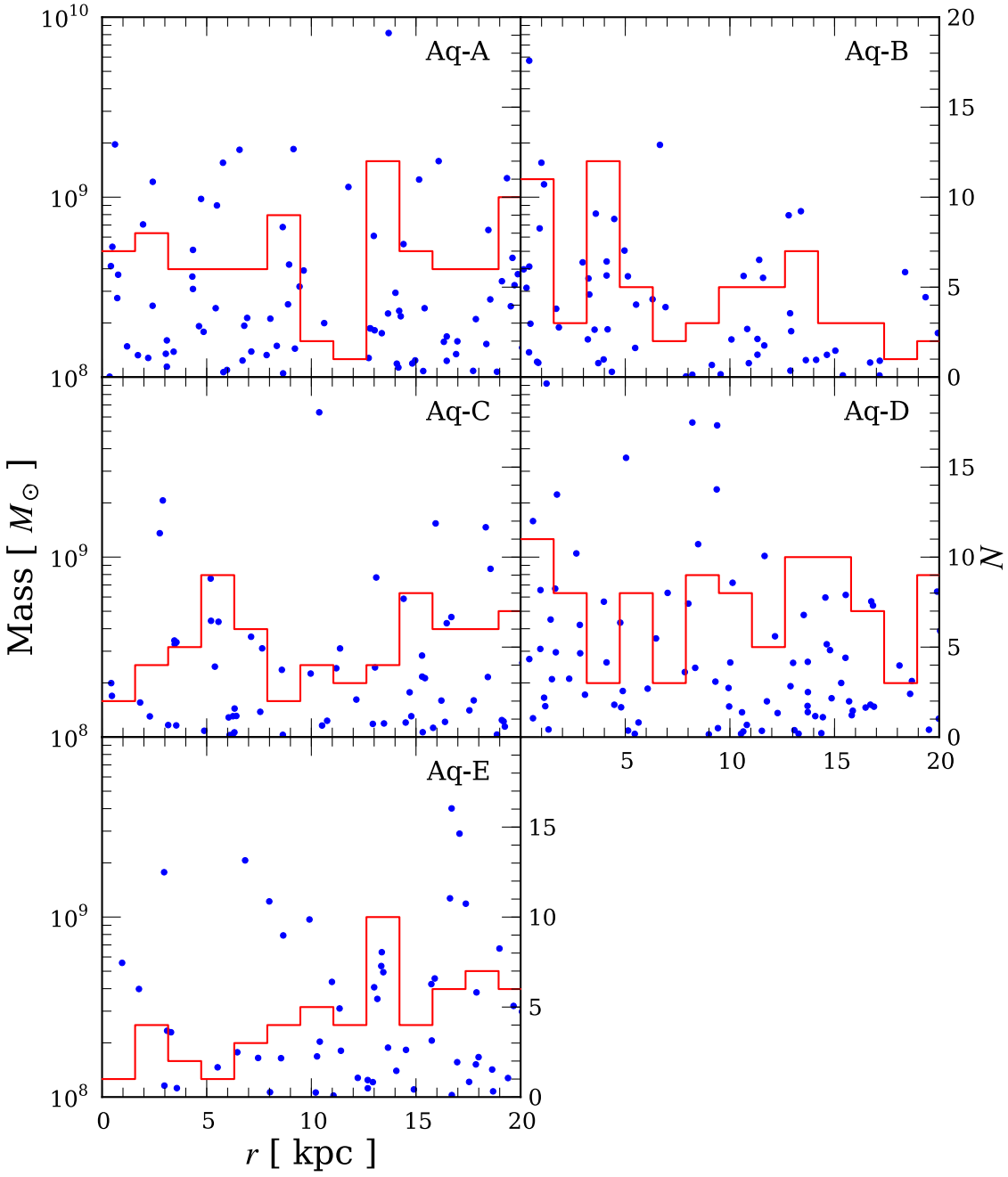

Figure 4.2: The SUBFIND mass at pericentre of the subhaloes that come within 20 kpc of the centre of each of the level 2 Aquarius haloes during the period from $z = 1$ to $z = 0$. The blue dots indicate both the mass and distance of each subhalo at pericentre, while the red histogram shows the number of subhaloes with mass $> 10^8 \mathrm{M}_\odot$ at pericentre binned by radius.

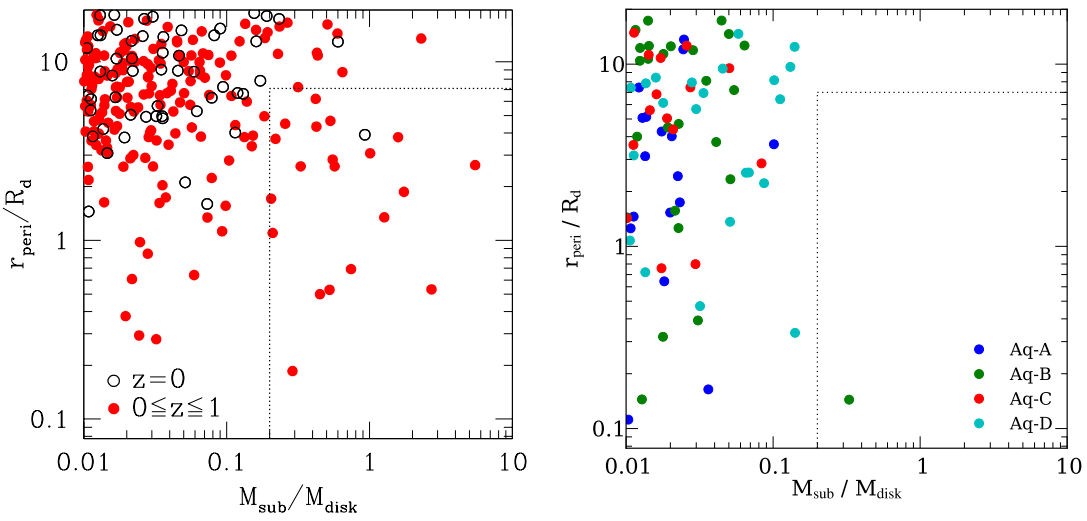

Figure 4.3: A comparison with Kazantzidis et al. (2009) for subhaloes within the centres of Milky-Way-like haloes. For each subhalo, the mass as it passes through the scaled 50 kpc boundary is plotted against its subsequent pericentric distance. The left panel shows the results from four of the simulations of Kazantzidis et al. (2009), while the right panel depicts the results from the four Aquarius haloes Aq-A - D. The radius and mass are presented in terms of the disc used by Kazantzidis et al. (2009), which has a mass, $M_{disc} = 3.53 \times 10^{10} M_{\odot}$, and radial scale length, $R_{disc} = 2.82$ kpc. The dotted region marks a 'danger zone' defined in Kazantzidis et al. (2009) as those subhaloes that come close enough, and are large enough, to do significant damage to a disc.

As the subhalo moves away again the set of candidate particles for belonging to the subhalo expands and its measured mass increases again (Muldrew et al., 2011). To minimise the problem, any output where a subhalo has a mass smaller than both the previous and subsequent outputs is removed from our interpolation.

The same object may appear multiple times in Fig. 4.2, as it makes subsequent pericentric passages, but will be much reduced in mass each time. From Fig. 4.2 it is clear that the mass of the most massive subhaloes is much greater than was seen in the instantaneous populations, but such objects are rare, with only one or two present in each halo over the entire period. These are the subhaloes that are expected to dominate the disc heating. The number of objects within each pericentric interval, shown by the red histogram, appears to be independent of radius.

The central abundance of substructure in the Aquarius haloes is considerably lower

than found in previous work. Fig. 4.3 shows a direct comparison between the simulations used for measuring disc heating by Kazantzidis et al. (2008, 2009) and the Aquarius haloes. Kazantzidis et al. (2009) similarly used high-resolution cosmological simulations of haloes to measure the central abundance. After scaling the simulations to a common virial mass $M_{\rm vir} = 7.35 \times 10^{11} {\rm M}_{\odot}$ and radius $r_{\rm vir} = 244.5$ kpc, they identified all infalling subhaloes as they crossed 50 kpc for the first time between $z = 1$ and $z = 0$. The masses correspond to the mass at the output time nearest to crossing the infall boundary and the pericentric distance is calculated from the orbit of a test particle in a static NFW potential whose properties match the host halo at the time of infall. The distances and masses are expressed in terms of units of a disc with mass $M_{\rm disc} = 3.53 \times 10^{10} {\rm M}_{\odot}$, and radial scale length $R_{\rm disc} = 2.82$ kpc. To facilitate a comparison we have followed the same procedure, scaling the Aquarius haloes in the same manner, but have used the actual distance of the first pericentre after crossing the boundary.

There are many more massive subhaloes in Kazantzidis et al. (2009) than in the Aquarius haloes, especially within the dotted region which Kazantzidis et al. (2009) define as the 'danger zone'. Subhaloes within this region are massive enough ($M_{\rm sub} \geq 0.2 M_{\rm disc}$), and pass close enough to the centre $r_{\rm peri} \leq 20$ kpc, to substantially perturb a central disc. There is only one subhalo that meets these criteria in the Aquarius simulations, as opposed to 20 in the other simulations. The effects on a disc by substructure bombardment will consequently be much greater in the latter simulations. One explanation for this difference is suggested by the fact that the most massive subhalo in the Kazantzidis et al. (2009) simulations has a mass $\sim 2.1 \times 10^{11} {\rm M}_{\odot} = 6 M_{\rm disc}$, almost 30 percent of the total host halo mass. An accretion of a subhalo this massive would be a major merger; even the second and third most massive subhaloes are large enough to have arrived in major mergers. This contrasts with the five Aquarius haloes, which have not experienced any major mergers at late times. The major mergers in the Kazantzidis et al. (2009) simulations may be a sign of a higher overall accretion activity.

4.2.1 Subhalo Selection

Having studied the abundance of subhaloes in the central 20 kpc of the Aquarius haloes, we can now select the set of subhaloes that are expected to be responsible for the majority of the late time heating. We first scale the five Aquarius haloes to a common size to have

Halo	Number subhaloes	Largest Subhalo
Aq-A	16	$6.42 \times 10^9 \mathrm{M}_\odot$
Aq-B	14	$2.26 \times 10^{10} \mathrm{M}_\odot$
Aq-C	8	$5.80 \times 10^9 \mathrm{M}_\odot$
Aq-D	13	$1.04 \times 10^{10} \mathrm{M}_\odot$
Aq-E	9	$9.83 \times 10^9 \mathrm{M}_\odot$

Table 4.1: Number of subhaloes with a mass greater than $4 \times 10^8 \mathrm{M}_\odot$ as they first pass in through $r_{\rm in} = 50$ kpc at any time after $z = 1$, along with the mass of the largest subhalo. These are the subhaloes that will be important for disc heating in the five Aquarius haloes. The Aquarius haloes have been scaled to a common size to allow direct comparison.

the same virial mass $M_{200} = 1.3 \times 10^{10} \mathrm{M}_\odot$ and virial radius $r_{200} = 220$ kpc, to allow a more direct comparison between haloes. These values are chosen to be typical of a spiral galaxy and are explained further in §4.4.1. Subhaloes are selected based on their infall mass as they pass the infall radius $r_{\rm in} = 50$ kpc from the host halo centre.

The mass of a subhalo near pericentre is not necessarily a good guide to the size of interactions between the subhalo and the disc. Subhaloes lose a lot of mass at pericentre, where they are shocked and tidal stripping is at its maximum. While the stripped mass is no longer bound to the subhalo, it is still associated with it, in that it will still be moving along very similar orbits and will also pass through the disc and contribute to the heating effect. Selecting subhaloes at $r_{\rm in} = 50$ kpc therefore avoids missing those subhaloes that have small masses at pericentre but large amounts of unbound material still associated with them. Only subhaloes that come within 20 kpc of the halo centre are considered. Imposing a lower mass limit of $4 \times 10^8 \mathrm{M}_\odot$ restricts the selection to the few most massive subhaloes that are predicted to be most important for heating. The number of subhaloes that meet these criteria for each of the Aquarius haloes is listed in Table 4.1.

There is a large variation in the number and masses of the substructures that come within 20 kpc of the centre of the five haloes. Figure 4.4 shows the distribution of masses and the times of the selected substructures as they enter the infall boundary. The lower virial mass of the Aq-B main halo compared to the other Aquarius haloes (see Table 2.2) means that after scaling it contains the most massive subhalo $\sim 2 \times 10^{10} \mathrm{M}_\odot$, twice

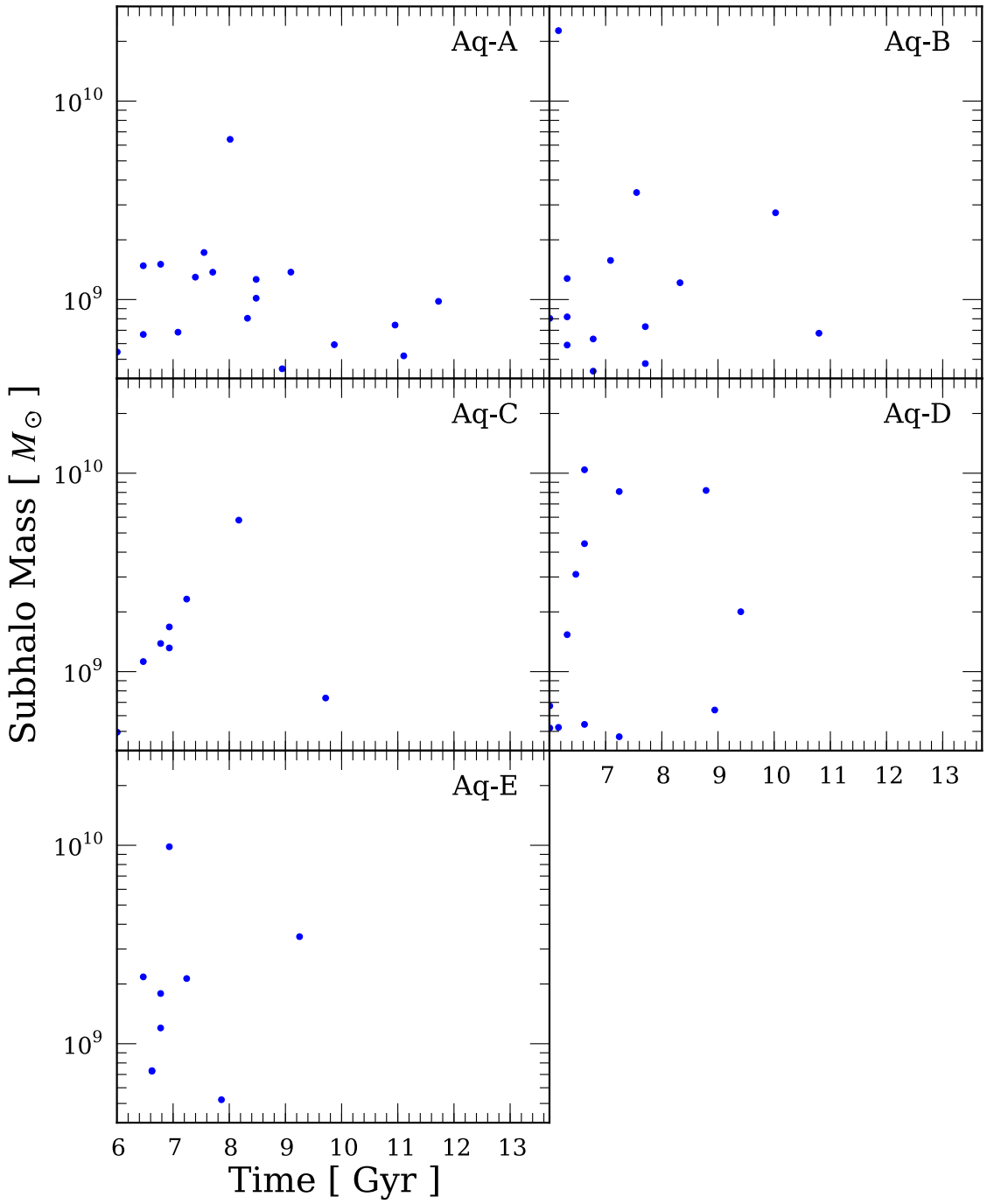

Figure 4.4: The time and SUBFIND mass of substructures as they first cross the scaled $r_{\rm in} = 50$ kpc boundary since $z = 1$, as they fall towards the centre of their parent halo. For the five Aquarius haloes, all substructures with a mass greater than $4 \times 10^8 {\rm M}_\odot$ and which come within 20 kpc of the centre of the halo are plotted.

as large as any other subhalo in the simulations. In contrast, Aq-A and Aq-C have no substructures with a mass greater than $1 \times 10^{10}\mathrm{M}_{\odot}$ and only a single one each with a mass greater than $3 \times 10^{9}\mathrm{M}_{\odot}$. The mass of the largest subhalo in each case is also given in Table 4.1. The majority of the subhaloes tend to enter the central regions at early times, with four out of the five haloes having none enter in the last 2-3 Gyrs before $z = 0$.

For the selected sample of subhaloes it is possible to calculate where their orbits would impact a disc. Following the orbits of the selected subhaloes we can find the point where they pass through a hypothetical disc plane. A hypothetical disc plane can be defined in the Aquarius haloes by the plane aligned perpendicular to the minor axis of the moment of inertia tensor of the material in the inner 20 kpc region of the haloes. This is a reasonable choice of orientation for a disc in a triaxial dark matter halo, as it is the lowest energy stable axis of rotation for a rigid disc. The positions of the intersections are marked by circles in Fig. 4.5, the colour of the circle represents the impact time, and the size of the circle is the linearly interpolated SUBFIND mass of the subhalo. There is considerable variation between the haloes. Haloes Aq-B and Aq-D are intersected very close to the centre of the disc by large impacts, while haloes Aq-C and Aq-E have much quieter histories. Halo Aq-A is intermediate between the two.

The results from Boylan-Kolchin et al. (2010) for the most massive merger since $z = 2$ (see §2.6.3) found that in the context of the Milky Way mass haloes in the MS-II simulation the Aquarius haloes Aq-A, Aq-C, Aq-D and Aq-E lie near the 10 percent most quiescent haloes and only halo Aq-B is typical. This partially correlates with the disc bombardment histories of the haloes. Halo Aq-B is the most active, while haloes Aq-A, Aq-C and Aq-E are much quieter, but halo Aq-D also suffers several large impacts. The most massive merger is therefore not necessarily a good guide to subhalo activity in the centre of haloes.

4.3 Benson Semi-Analytical Model of Disc Heating

To evaluate the heating that subhaloes would have caused to a galactic disc had one been present within the Aquarius haloes, we apply the Benson et al. (2004) semi-analytical model (hereafter known as the Benson model) to the sets of subhaloes selected in the previous section. The model estimates the increase in the vertical height of a disc due

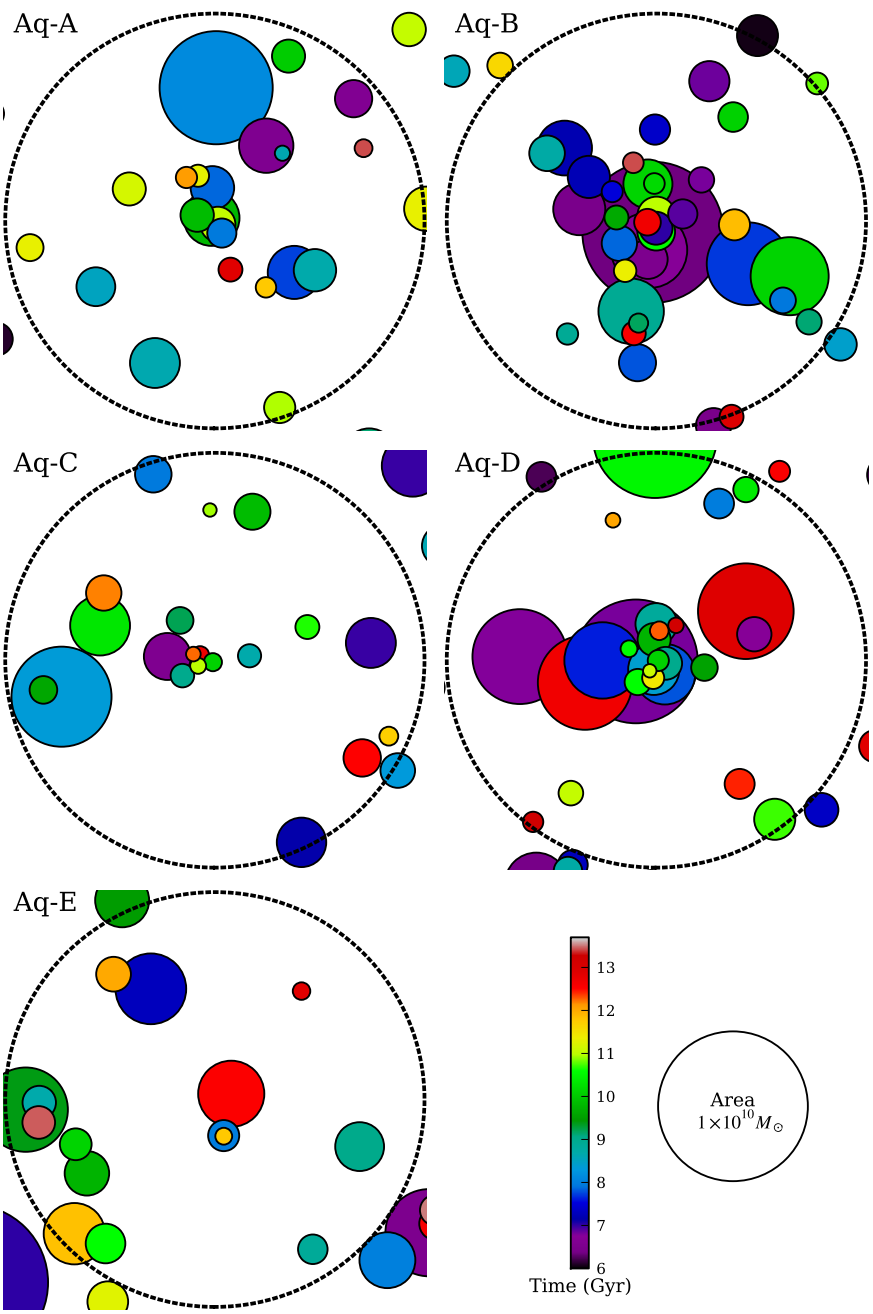

Figure 4.5: The locations of the intersection of subhalo orbits with the hypothetical disc planes in the Aquarius simulations. The circles mark the point of intersection on the disc. The colour of the circles represents the time of intersection and the area the mass estimated from its SUBFIND mass. The large dashed circle marks the 20 kpc radius defined to be the boundary of the disc. In order to calculate the exact point of intersection, the orbit of the subhaloes between outputs is reconstructed through interpolation, as explained in the text.

to the additional energy gained from subhaloes as they experience dynamical friction against the disc. The full model uses an improved version of the Benson et al. (2002) dynamical evolution model to calculate the orbit of subhaloes and the mass loss through tidal stripping, and a disc heating model to calculate the amount of energy transferred from the orbital motion of each subhalo into the disc. Since subhalo information from actual simulations is being used, which includes both orbits and the evolution of the subhalo properties, it is only the latter part of the Benson model that will be employed in this work. We start by outlining the basic model before going into greater detail for the individual concepts as they apply to a subhalo-disc interaction.

4.3.1 Model Outline

As subhaloes orbit within a dark matter halo they experience dynamical friction against both the halo and the galaxy. The dynamical friction between the disc and the subhalo scatters stars in the disc, increasing their random motion and injecting energy. The rate at which the subhalo injects energy into the disc is

$$P = -\boldsymbol{F}_{\rm df} \cdot \boldsymbol{v}_{\rm sub}, \tag{4.1}$$

where $\boldsymbol{F}_{\rm df}$ is the dynamical friction exerted by the disc and $\boldsymbol{v}_{\rm sub}$ is the velocity of the subhalo relative to the disc motion at the point of impact. The subhalo loses orbital energy and spirals inwards towards the centre of the halo. The disc gains kinetic energy, of which some fraction goes into increasing the vertical motions of stars. The rate at which the vertical energy of the disc increases is given as

$$\dot{E}_z = -\epsilon_z \boldsymbol{F}_{\rm df} \cdot \boldsymbol{v}_{\rm sub}, \tag{4.2}$$

where ϵ_z is an efficiency factor that determines what proportion of the energy goes into the vertical direction. Integrating along the orbit of a subhalo yields the total amount of vertical energy input into the disc during the encounter. The kinetic energy is quickly mixed between kinetic and potential energy as the disc moves into a new equilibrium configuration with a larger scale-height. A simple disc model relates the total vertical energy of the disc to its scale-height.

Disc

The galactic disc is modelled as an exponential disc with scale-length R_d and constant scale-height H_d over the entire surface of the disc. The density distribution of the disc is

$$\rho_d(r,z) = \frac{M_d}{4\pi R_d^2 H_d} \exp\left(-\frac{r}{R_d}\right) \mathrm{sech}^2\left(\frac{z}{H_d}\right), \tag{4.3}$$

where M_d is the total mass of the disc. The disc is treated as having an anisotropic velocity dispersion. The square of the radial velocity dispersion is taken to be proportional to the surface density

$$\sigma_R^2(r) = \sigma_{R_0}^2 \exp\left(-\frac{r}{R_d}\right), \tag{4.4}$$

(Lewis and Freeman, 1989), and the normalisation, fixed by requiring that the disc has a Toomre Q-parameter of 1.5 at its half mass radius, is

$$\sigma_{R_0} = \frac{0.232\,Q}{\kappa(r_{\frac{1}{2}M})} \frac{GM_d}{R_d^2}. \tag{4.5}$$

The azimuthal velocity dispersion is determined by the epicyclic approximation and is

$$\sigma_\phi^2(r) = \frac{\kappa^2(r)}{4\Omega^2(r)} \sigma_R^2(r), \tag{4.6}$$

where $\kappa^2(r) = r\frac{d\Omega^2}{dr} + 4\Omega^2$ is the epicycle frequency and $\Omega(r)$ the orbital frequency of the disc based on the total mass enclosed at each radius.

Using the thin disc approximation, in which the scale-height of the disc is always taken to be small compared to the radial extent, so that the disc can be treated as an infinite plane, and assuming that when energy is injected into the disc it quickly returns to virial equilibrium in the vertical direction, the scale-height of the disc can be related to its total vertical energy as

$$E_z = \frac{3}{16} M_d V_d^2 h + \frac{\pi^2}{12} V_d^2 h^2 R_d \int_0^\infty \frac{M_h(<r)}{r^2} e^{-\frac{r}{R_d}} dr, \tag{4.7}$$

and to the vertical kinetic energy as

$$T_z = \frac{1}{16} M_d V_d^2 h + \frac{\pi^2}{24} V_d^2 h^2 R_d \int_0^\infty \frac{M_h(<r)}{r^2} e^{-\frac{r}{R_d}} dr, \tag{4.8}$$

where $h = H_d/R_d$, $M_h(<r)$ is the mass of the halo within r, and $V_d = \sqrt{GM_d/R_d}$. The first term is due to the disc's self-gravitational energy and the second to the disc/halo interaction. Using this model the vertical energy of the disc is determined by its initial

scale-height. Extra energy input into the disc increases its scale-height. From the vertical energy we can also obtain the velocity dispersion in the vertical direction as

$$\sigma_z^2(r) = \pi G \Sigma_d(r) H_d + \frac{\pi^2}{12} \frac{G M_h(< r) H_d^2}{r^3}. \tag{4.9}$$

The Benson model keeps the disc mass, scale-length and surface velocity dispersions fixed in time. Only the vertical energy and thus vertical thickness are allowed to vary as energy is gained from subhalo encounters.

Dynamical Friction against a Disc

The dynamical friction from the disc is treated using the Chandrasekhar approximation (Chandrasekhar, 1943). The classical definition of dynamical friction is that it is the retarding force a massive body experiences as it moves through a homogeneous sea of smaller particles. The gravitational interactions between the massive body and the smaller particles with mass m and number density n, cause the small particles to be accelerated, and to gain momentum and kinetic energy. In return the massive body is slowed and loses momentum and kinetic energy. This definition is not strictly applicable to the subhalo-disc system and has to be modified to take the nature of the disc into account.

The rate at which the massive body of mass, $M(\gg m)$, is decelerated is given by

$$\frac{d\boldsymbol{v}_M}{dt} = -2\pi \ln(1+\Lambda^2) G^2 \rho M \int f(\boldsymbol{v}_m) \frac{(\boldsymbol{v}_m - \boldsymbol{v}_M)}{|\boldsymbol{v}_m - \boldsymbol{v}_M|^3} d^3\boldsymbol{v}_m, \tag{4.10}$$

where $\rho = nm$ is the density and $f(\boldsymbol{v}_n)$ the distribution of the velocities of the sea of particles. $\ln \Lambda$ is the Coulomb logarithm and is the result of an integration over all possible impact parameters, b. For a point mass the lower integration limit is taken to be zero, so $\Lambda = b_{\max} V_0^2 / GM$, where V_0 is the typical relative velocity between the massive object and the smaller bodies. For an extended body the lower integration limit is replaced by $b_{\min}$ so the effective Λ is

$$\Lambda_{\text{eff}} = \left(\frac{1+\Lambda^2}{1 + [b_{\min}/b_{\max}]^2 \Lambda^2} - 1 \right)^{1/2}. \tag{4.11}$$

For subhaloes we take $b_{\min}$ to be their half-mass radius, slightly different to the original Benson model, which uses half their tidal radius instead. The half-mass radius proves to be a better estimate of subhalo size, particularly at large radii, where the tidal radius can be noticeably larger and is often much greater than the size of a subhalo.

The choice for the maximum impact parameter, $b_{\max}$, is less clear. Since we use the logarithm of Λ, the value need only be correct to an order of magnitude. The maximum impact parameter $b_{\max}$ when considering a disc varies depending on the angle of intersection. For a subhalo interacting with the disc at an angle θ to the normal of the disc and some angle ψ in the surface of the disc, Λ in direction ψ is

$$\Lambda = \frac{3R_d h' V_0^2}{GM}, \tag{4.12}$$

where $h' = (\cos^2\psi + [\cos^2\theta + h^2\sin^2\theta]\sin^2\psi)^{1/2}$. Putting this together with the expression for an extended subhalo we get

$$(1+\Lambda)^2_{\text{eff}} = \frac{1+\Lambda^2}{1+(b_{\min}\Lambda/3R_d h')^2}. \tag{4.13}$$

The effective Λ for the whole disc is found by averaging over all ψ

$$\left\langle \frac{1}{2}\ln(1+\Lambda^2)_{\text{eff}} \right\rangle = \frac{1}{4\pi}\int_0^{2\pi} \ln(1+\Lambda^2)_{\text{eff}} d\psi, \tag{4.14}$$

and has to be solved numerically.

An expression for the dynamical friction of a system of particles with a uniform density distribution and Gaussian velocity distribution with dispersion $\sigma_\perp$ in one direction and $\sigma_\parallel$ in the other two was given in Binney (1977). Benson et al. (2004) generalise this to the case where the velocity dispersions are different in all three directions. The dynamical friction is then

$$\begin{aligned} \boldsymbol{F}_{\text{df}} &= \sqrt{2\pi}\ln(1+\Lambda^2)\rho G^2 M^2 \frac{\sqrt{(1-e_\phi^2)(1-e_{\text{z}}^2)}}{\sigma_{\text{R}}\sigma_\phi\sigma_{\text{z}}} \\ &\quad \times (B_{\text{R}} v_{\text{R}}\hat{\mathbf{e}}_{\text{R}} + B_\phi v_\phi \hat{\mathbf{e}}_\phi + B_{\text{z}} v_{\text{z}}\hat{\mathbf{e}}_{\text{z}}) \end{aligned} \tag{4.15}$$

where ρ is the background density, M the mass of the orbiting object, $(v_{\text{R}}, v_\phi, v_{\text{z}})$ is the relative velocity vector of object and background particles, $\hat{\mathbf{e}}_{\text{R}}$, $\hat{\mathbf{e}}_\phi$, $\hat{\mathbf{e}}_{\text{z}}$ are the basis vectors

of the cylindrical polar coordinate system. The coefficients B are given by,

$$B_{\mathrm{R}} = \int_0^\infty \frac{\mathrm{d}q}{[(1+q)^3(1-e_\phi^2+q)(1-e_{\mathrm{z}}^2+q)]^{1/2}} \times \exp\left(-\frac{1}{2}\left[\frac{v_{\mathrm{R}}^2/\sigma_{\mathrm{R}}^2}{(1+q)} + \frac{v_\phi^2/\sigma_{\mathrm{R}}^2}{(1-e_\phi^2+q)} + \frac{v_{\mathrm{z}}^2/\sigma_{\mathrm{R}}^2}{(1-e_{\mathrm{z}}^2+q)}\right]\right), \tag{4.16}$$

$$B_\phi = \int_0^\infty \frac{\mathrm{d}q}{[(1+q)(1-e_\phi^2+q)^3(1-e_{\mathrm{z}}^2+q)]^{1/2}} \times \exp\left(-\frac{1}{2}\left[\frac{v_{\mathrm{R}}^2/\sigma_{\mathrm{R}}^2}{(1+q)} + \frac{v_\phi^2/\sigma_{\mathrm{R}}^2}{(1-e_\phi^2+q)} + \frac{v_{\mathrm{z}}^2/\sigma_{\mathrm{R}}^2}{(1-e_{\mathrm{z}}^2+q)}\right]\right), \tag{4.17}$$

$$B_{\mathrm{z}} = \int_0^\infty \frac{\mathrm{d}q}{[(1+q)(1-e_\phi^2+q)(1-e_{\mathrm{z}}^2+q)^3]^{1/2}} \times \exp\left(-\frac{1}{2}\left[\frac{v_{\mathrm{R}}^2/\sigma_{\mathrm{R}}^2}{(1+q)} + \frac{v_\phi^2/\sigma_{\mathrm{R}}^2}{(1-e_\phi^2+q)} + \frac{v_{\mathrm{z}}^2/\sigma_{\mathrm{R}}^2}{(1-e_{\mathrm{z}}^2+q)}\right]\right), \tag{4.18}$$

where $1-e_\phi^2 = \sigma_\phi^2/\sigma_{\mathrm{R}}^2$ and $1-e_{\mathrm{z}}^2 = \sigma_{\mathrm{z}}^2/\sigma_{\mathrm{R}}^2$.

Efficiency

The final element needed is an expression for the efficiency factor ϵ_z. This is a result of considering how the scattering of the particles in the dynamical friction process changes the energy in different directions. Benson et al. (2004) use the expression for the change in velocity of a single particle from Binney and Tremaine (2008) and integrate over the whole particle distribution to obtain

$$\epsilon_z = \frac{2\Lambda^2\cos^2\theta + ((1+\Lambda^2)\ln(1+\Lambda^2) - \Lambda^2)(1-\cos\theta)}{2(1+\Lambda^2)\ln(1+\Lambda^2)}, \tag{4.19}$$

which takes values $0 \leq \epsilon_z \leq 1$ as required.

These elements together form the heating model. At each time step the dynamical friction force on the subhalo from the disc is calculated. The vertical disc energy is increased by the corresponding energy injected into the disc and the new scale-height found. On the next time step this process is repeated with the disc in its new state.

4.3.2 Implementation

A new implementation of the Benson model was created for this work. To facilitate testing our implementation of the model, the author, Andrew Benson, of Benson et al. (2004) kindly supplied us with a version of the original code from the paper. However, attempts

to verify our new implementation against the original version yielded discrepant results. Detailed investigations revealed several issues with the original implementation that led to overestimates of the subhalo heating. This is a problem for the supposed agreement with the set of test case simulations used to justify the model. We will briefly outline the test cases against which both versions were run and describe the problems with the Benson implementation. Using our new implementation we will present revised figures for the heating in these cases and discuss the implications for the model.

Benson et al. (2004) used modified versions of the simulations from Velazquez and White (1999) to test and calibrate their model. The Velazquez and White (1999) simulations consist of 15 scenarios of a single subhalo-disc encounter with a range of orbital parameters. They found that the resulting thickening and heating of the disc differed depending on whether the subhalo orbit was prograde or retrograde, but in both cases an encounter with a massive subhalo (10-20 percent $M_{\rm disc}$) heated but did not destroy the disc. For their tests Benson et al. (2004) slightly modified the form of the subhaloes, as the original central densities and velocity dispersions given by Velazquez and White (1999) were not consistent with the assumed concentration parameters, and so the subhaloes seemed too weakly bound. Each simulation consists of a disc galaxy with a bulge embedded in a dark matter halo, plus a subhalo. Density profiles and the number of particles are listed in Table 4.2, while the orbital parameters of the subhalo for the different scenarios is listed in Table 4.3.

Benson et al. (2004) ran the simulations using GADGET and used the change in vertical kinetic energy as a measurement of the heating of the disc over a four gigayear period. This is easily obtained from the outputs of the simulations by summing the kinetic energy of the disc particles in a direction perpendicular to the surface of a disc. While simulations are useful for providing a baseline against which to test models, they are not without problems themselves. One of the biggest problems is that discs in simulations can heat up due to numerical relaxation even without the presence of any perturber subhaloes. In a simulation of the evolution of a disc without subhaloes, the vertical kinetic energy increased from $5.7 \times 10^{13}\mathrm{M}_{\odot}$ km^{2}s^{-2} at $t = 0$ to $6.4 \times 10^{13}\mathrm{M}_{\odot}$ km^{2}s^{-2} at $t = 4$ Gyr , a change of $\Delta T_z = 7.0 \times 10^{12}\mathrm{M}_{\odot}$ km^{2}s^{-2}. The amount of numerical heating is a function of resolution. Due to the low resolution, the increase in the disc energy in the Benson et al. (2004) simulations is comparable to the heating caused by the subhaloes

Component	Density Profile	Parameters	Number of Particles
Halo	$\rho_{\rm h}(r) = \frac{M_{\rm h}\alpha}{2\pi^{3/2}r_{\rm cut}} \frac{\exp(-r^2/r_{\rm cut}^2)}{r^2+\gamma^2}$	$M_{\rm h} = 7.84 \times 10^{11} M_\odot$	687008
		$\gamma = 3.5$kpc	
		$r_{\rm cut} = 84$kpc	
		$\alpha = 1.076$	
Disc	$\rho_{\rm d}(R,z) = \frac{M_{\rm d}}{4\pi R_{\rm d}^2 H_{\rm d}} \exp(-R/R_{\rm d})\mathrm{sech}^2(z/H_{\rm d})$	$M_{\rm d} = 5.6 \times 10^{10} M_\odot$	163840
		$R_{\rm d} = 3.5$kpc	
		$H_{\rm d} = 700$pc	
Bulge	$\rho_{\rm b}(r) = \frac{M_{\rm b}}{2\pi} \frac{a}{r(a+r)^3}$	$M_{\rm b} = 1.87 \times 10^{10} M_\odot$	16384
		$a = 525$pc	
Satellite S1	King Model	$M_{\rm s} = 5.60 \times 10^9 M_\odot$	32768
		$r_{\rm c} = 1$kpc	
		$c = 0.8$	
Satellite S2	King Model	$M_{\rm s} = 5.60 \times 10^9 M_\odot$	32768
		$r_{\rm c} = 500$pc	
		$c = 1.1$	
Satellite S3	King Model	$M_{\rm s} = 1.12 \times 10^{10} M_\odot$	32768
		$r_{\rm c} = 875$pc	
		$c = 1.0$	

Table 4.2: Properties of the galaxy and subhalo models used in the Benson et al. (2004) test N-body simulations. The density profile for the disc is given in cylindrical polar coordinates (R, z) and the other components in spherical coordinates (r). The subhaloes are all described by King models (King, 1966). For these, we specify the core radius, $r_{\rm c}$, and the concentration $c = \log_{10} r_{\rm t}/r_{\rm c}$ where $r_{\rm t}$ is the tidal radius of the satellite.

in many of the test cases. Benson et al. (2004) do not seem to view this as a problem. However, we have repeated their fiducial simulation and found that the amount of numerical heating is highly variable between realisations. The change in the vertical kinetic energy for two different realisations is plotted in Fig. 4.6. The energy increases at a gradual and approximately linear rate in both cases, but one disc has a 7 percent increase ($\Delta T_z = 3.7 \times 10^{12} \mathrm{M}_\odot$ km^{2}s^{-2}), and the other twice that amount with a 13 percent increase ($\Delta T_z = 7.0 \times 10^{12} \mathrm{M}_\odot$ km^{2}s^{-2}). It is therefore questionable whether the heating by a subhalo can be taken as simply the difference between the value of the vertical kinetic energy from the simulation with subhaloes and the one without.

The comparison of the Benson analytical model to their simulations is not just a test of the heating calculation but also a test of the dynamical evolution model used to integrate the orbit of the subhalo and to calculate the mass stripping. Since it is only the

Model	Subhalo	$\theta_{\rm i}$	$\epsilon_{\rm J}$	$r_{\rm a}$/kpc
G1S1	S1	$45°$	0.33	59.0
G1S2	S1	$0°$	0.55	55.0
G1S3	S1	$45°$	0.55	55.0
G1S4	S1	$90°$	0.55	55.0
G1S5	S1	$135°$	0.55	55.0
G1S6	S1	$180°$	0.55	55.0
G1S7	S1	$0°$	0.82	46.5
G1S8	S1	$45°$	0.82	46.5
G1S9	S2	$0°$	0.55	55.0
G1S10	S2	$45°$	0.55	55.0
G1S11	S2	$90°$	0.55	55.0
G1S12	S2	$135°$	0.55	55.0
G1S13	S2	$180°$	0.55	55.0
G1S14	S3	$45°$	0.55	55.0
G1S15	S3	$135°$	0.55	55.0

Table 4.3: Properties and initial orbital parameters of the subhaloes in the N-body simulations. Column 2 specifies the subhalo model used (as defined in Table 4.2). Column 3 lists $\theta_{\rm i}$, the angle between the initial angular momentum vector of the subhalo and that of the disk. Column 4 lists the circularity of the subhalo's initial orbit, $\epsilon_{\rm J}$, while column 5 lists the initial radial position of the satellite (which is the apocentre of its orbit), $r_{\rm a}$.

heating calculation that is required, we assume the dynamical evolution model is correct and use the orbits it produces in order to remove it as a variable from the comparison. The results from our new implementation compared with the Benson original implementation can be seen in Table 4.4, along with the values from the simulations. From the original implementation it was claimed that the Benson model successfully reproduced the N-body heating rates to within a factor of 3 and usually underestimated it. Unfortunately the values from our new implementation are a further factor of 2-3 lower, pointing to an even greater difference between the model and simulations.

An example from the G1S3 test case can be seen in Fig. 4.7. The top line is the increase in the vertical kinetic energy of the disc from the Benson implementation and the lower line from our implementation. Both have sharp increases whenever the subhalo

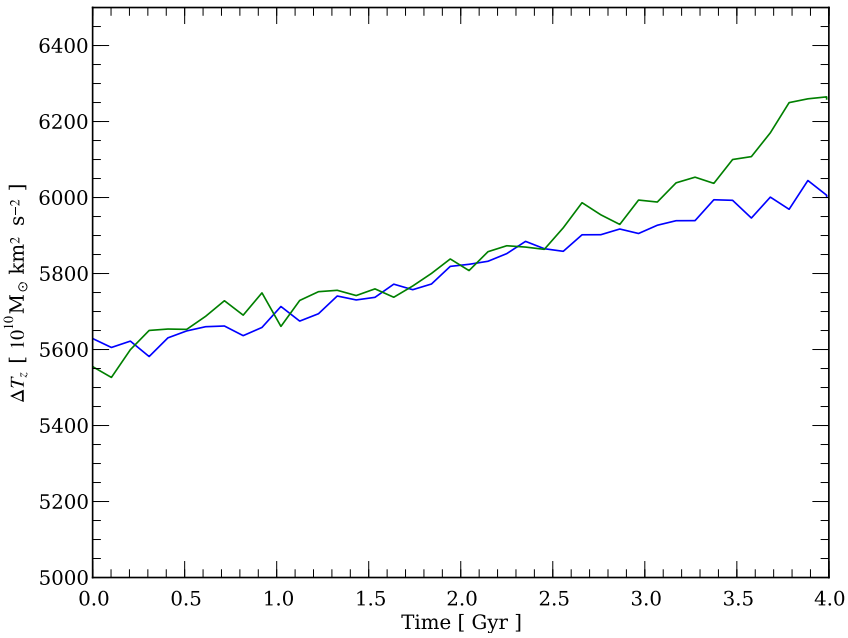

Figure 4.6: The increase in the vertical kinetic energy of the disc in the Benson fiducial simulation for two different realisations.

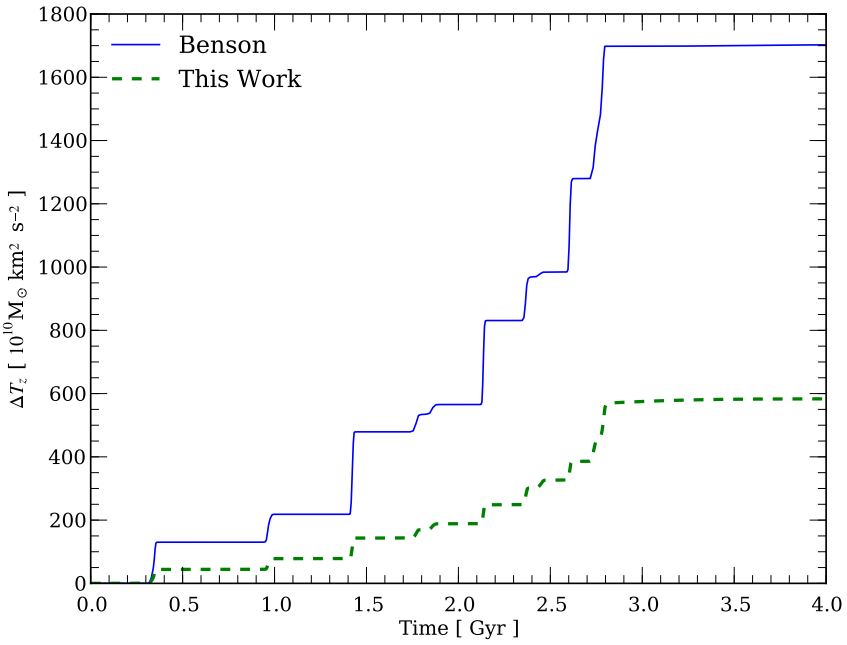

Figure 4.7: The increase in the vertical kinetic energy of the Benson test case G1S3, in which a disc suffers successive encounters with a subhalo. The blue line shows the results from the original Benson implementation, while the dashed green line represents our corrected implementation of the same model.

Model	N-body	Benson	This Work
G1S1	1010 (18%)	1330 (25%)	422 (8%)
G1S2	3420 (60%)	2570 (49%)	653 (12%)
G1S3	2380 (42%)	1840 (35%)	583 (11%)
G1S4	1010 (18%)	290 (5%)	166 (3%)
G1S5	570 (10%)	320 (6%)	233 (4%)
G1S6	900 (16%)	1770 (33%)	1235 (22%)
G1S7	4430 (77%)	560 (11%)	105 (2%)
G1S8	3240 (57%)	960 (18%)	458 (8%)
G1S9	3070 (54%)	2720 (51%)	735 (14%)
G1S10	5880 (103%)	2440 (46%)	1017 (19%)
G1S11	3630 (63%)	1140 (22%)	689 (13%)
G1S12	2290 (40%)	1310 (25%)	903 (16%)
G1S13	3500 (61%)	5070 (96%)	3799 (69%)
G1S14	8730 (153%)	5210 (98%)	2646 (48%)
G1S15	3740 (65%)	4380 (83%)	4096 (75%)

Table 4.4: Comparison of the results for the heating of a stellar disc from the Benson N-body simulations, the Benson implementation of the analytical disc heating model and our new implementation of the model. The heating is quantified by the increase in the additional vertical kinetic energy of the disc generated by interaction with a subhalo for the 15 test cases, and given in terms of the absolute increase, in units of $10^{10}\mathrm{M}_{\odot}\mathrm{km}^{2}\mathrm{s}^{-2}$, and as a percentage of the initial disc vertical kinetic energy (values in parentheses).

.

passes through the disc. However, the size of the steps is much smaller in our new implementation. After careful study to understand these differences, three major bugs were found in the code of the Benson implementation. These were:

- an additional factor of 2 was present in the formula for the dynamical friction, which spuriously doubles the rate at which power is put into the disc,
- the angle θ in the efficiency factor used the absolute subhalo velocity vector rather than the subhalo-disk relative velocity vector,
- the circular velocity curve of the disc is calculated incorrectly and is discontinuous at a point.

The first issue is the primary reason for the overestimation of the heating by the original implementation. The third issue also tends to boost the heating, as it gives an overly large relative velocity vector between the subhalo and disc, which increases the rate at which energy is transferred into the disc. Fixing these problems in our implementation results in a much smaller prediction for the amount of heating by subhaloes.

Due to the issues discovered in the original implementation, the results of the tests published for the heating model in the Benson et al. (2004) paper are wrong. The claimed reproduction of N-body heating rates as verification for the accuracy of the model is false. This does not necessarily imply that the model does not predict subhalo heating, only that it has not been proven to do so. Using a new implementation on the same tests we have found a much lower heating rate, almost an order of magnitude less than that measured in the test simulations. However, the reliability of the simulations themselves is also in question. The simulations are too low resolution for accurate measurement of the disc heating. A direct comparison between the Benson analytical model and the Benson test simulations is therefore insufficient to evaluate the model. We return to the issue of numerical disc heating in simulations in the next chapter, where we will be in a position to conclusively test the model.

4.4 Applying the Benson Model to the Aquarius Haloes

At this point we will assume that the Benson model can predict the heating of stellar discs by dark matter substructures and apply the model to the samples of subhaloes

Component	Parameter	Value
Halo	M_{200}	$1.3 \times 10^{12} M_{\odot}$
	r_{200}	220 kpc
	c	12.2
Disc	M_{total}	$4 \times 10^{10} M_{\odot}$
	r_d	3 kpc
	z_d	400 pc
	Q	2
Bulge	M_{total}	$1 \times 10^{10} M_{\odot}$
	r_b	0.8 kpc

Table 4.5: Parameters of our disc galaxy model. The galaxy is comprised of an NFW dark matter halo, a Hernquist bulge and an exponential disc.

selected from the Aquarius simulations.

4.4.1 Standardised Galaxy Model

In order to directly compare the heating in the five haloes, we set up a common galaxy model and scale the haloes and subhaloes to it. The galaxy is comprised of an NFW dark matter halo, a Hernquist bulge and an exponential disc. The Aquarius haloes at $z = 0$ are well described by NFW profiles with a range of concentrations c, virial masses M_{200} and radii r_{200} (see Table 2.2). The halo of the common galaxy model is taken to be an NFW profile with parameters selected to lie in the middle of the range of Aquarius values. The parameters for the disc and bulge components were chosen to resemble a typical disc galaxy and are specified in Table 4.5. The disc is aligned perpendicular to the minor axis of the material in the inner 10 kpc of the haloes.

4.4.2 Results

The disc as initially set up has a thickness of 400 pc and a vertical kinetic energy of $T_z = 2.292 \times 10^{13} \mathrm{M}_{\odot} \mathrm{km}^2 \mathrm{s}^{-2}$. After bombardment by the five subhalo samples the absolute and relative increases in the energy and thickness are given in Table 4.6. We present energies in the same units as Benson et al. (2004) for ease of comparison. There is a huge variation in the amount of heating that occurs for the five subhalo samples, with

Halo	ΔT_z [$10^{10}\mathrm{M}_\odot\mathrm{km}^2\mathrm{s}^{-2}$]	ΔH_z [pc]
Aq-A	55.9 (2%)	8 (2%)
Aq-B	1011.6 (44%)	144 (36%)
Aq-C	18.9 (1%)	3 (1%)
Aq-D	140.3 (6%)	21 (5%)
Aq-E	36.3 (2%)	5 (1%)

Table 4.6: The increase in the vertical kinetic energy and the thickness of the discs when bombarded by the subhalo samples from the Aquarius simulations. The changes are given in terms of the absolute increases and as a percentage of the initial energy and thickness (values in parentheses).

an increase 50 times larger in the vertical energy from the Aq-B subhalo sample than the Aq-C subhaloes. There is a negligible heating of the disc for the subhaloes from haloes Aq-A, Aq-C and Aq-E. How the vertical kinetic energy varies as a function of time can be seen in Fig. 4.8. The subhaloes interact with the disc for only brief periods, and during the impacts the energy increases rapidly.

It is possible to match many of the heating events to the intersections seen in Fig. 4.5. The very large increase for Aq-B stems from the impact of the most massive subhalo. Similarly, the first rise in the energy for halo Aq-D can be associated with the largest subhalo impact of that halo, and the two late large impacts that Aq-D experiences correspond to two tiny rises at $t = 12.6$ Gyr and $t = 12.9$ Gyr, but the subhaloes pass 8 kpc and 10 kpc from the centre so are not very effective at heating the disc. However, there are rises in the energy which do not obviously correspond to massive subhalo interactions. The second largest rise in halo Aq-B and the largest rise in Aq-A occur from less massive subhaloes hitting very close to the centre of the disc. For the assumed exponential disc the stellar velocity dispersions and disc surface density grow large towards the centre and result in an extremely strong dynamical frictional force on the subhalo. This illustrates what is probably the biggest flaw of the Benson model. The values used to calculate the dynamical friction are based on the properties of the disc at the point of impact. However, the subhaloes are often kiloparsecs in radius, a significant fraction of the disc size. It is almost certainly erroneous to model the dynamical friction over the

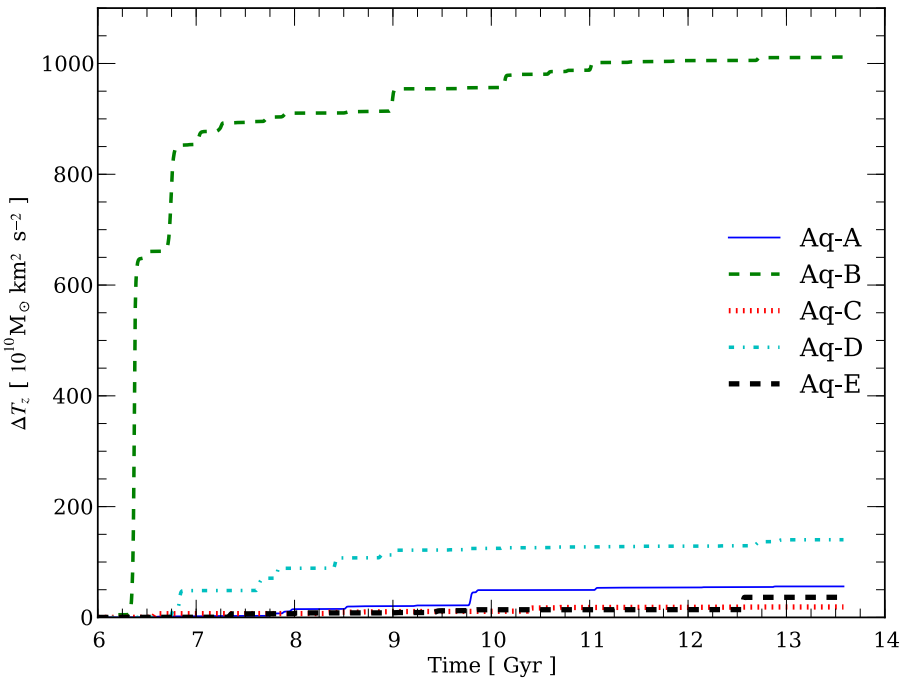

Figure 4.8: The predicted increase in the vertical kinetic energy of a disc due to substructure bombardment. The disc suffers a succession of encounters with the selected Aquarius subhaloes, gaining energy each time.

entire subhalo as if it is passing through a uniform medium as determined by the disc properties at one point. Instead, the disc properties vary significantly over the subhalo. This is especially true for impacts close to the centre, where a small change in position results in a very different dynamical friction force calculated by the model. Unfortunately, without this assumption the model becomes intractable.

The increase in the vertical energy can be converted into the change in the thickness of the disc using equation (4.8). The height of the disc increases in a very similar way to the vertical kinetic energy, so only one halo generates appreciable thickening of the disc.

4.5 Conclusions

The massive subhaloes that dominate the heating lie in the very tail of the distribution of substructures, where it is very sparsely sampled. They are extreme, rare objects with only a few present in each halo over the entire period between $z = 1$ and $z = 0$. With such small number statistics the overall abundance of substructure does not provide a

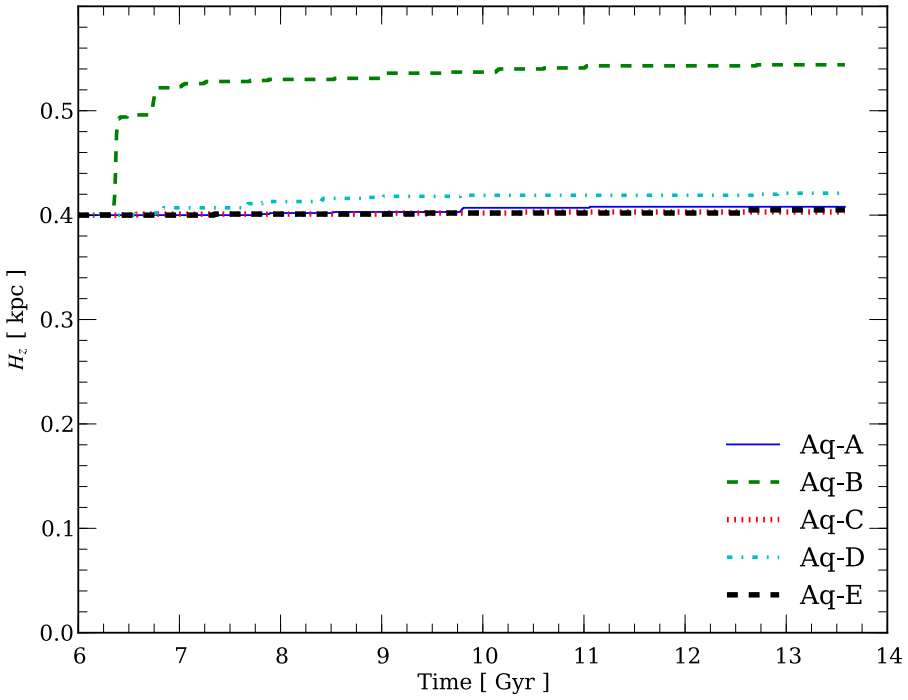

Figure 4.9: The change in the thickness of the disc predicted by the Benson model when bombarded by our subhalo samples from the five Aquarius simulations.

good guide to the number of objects expected. The mass of the largest subhalo in each of the five Aquarius haloes as measured at infall varies by a factor of five.

Given that the mass of a subhalo changes so drastically and rapidly during each pericentric passage, yet material stripped off can still be associated with it, it is more logical to select subhaloes at infall, before they have reached the centre of the halo. Doing so has the additional advantage of choosing the subhaloes at a distance where the selection is less sensitive to the lack of baryons that alter the very central regions of haloes. Choosing subhaloes with masses greater than $4 \times 10^8 \mathrm{M}_\odot$ that fall in after $z = 1$ results in a small selection of subhaloes from each of the Aquarius haloes. Haloes Aq-B and Aq-D contain the largest subhaloes with masses $\sim 1 \times 10^{10} \mathrm{M}_\odot$. Following the orbits of these subhaloes, it is possible to calculate where they would intersect a hypothetical disc plane.

To estimate the heating the subhalo samples generate we have used the Benson et al. (2004) semi-analytical model of disc heating. The authors of this model claim that it is able to approximately reproduce the heating measured in a set of N-body simulations. However, a review of their simulations found they were too low resolution to reliably

measure the actual heating that occurred above the noise of numerical heating. In addition, the original implementation contained a number of bugs that led it to overestimate the heating predicted by the model. Our new implementation predicts 2-3 times less heating in the same cases.

Applying the Benson model to the subhaloes of the Aquarius simulation allows us to estimate the disc heating that would have occurred in the five haloes. Only in one of the haloes, Aq-B, is there a significant amount of heating. In three there is almost none and in Aq-D a small amount. While the amount of heating in Aq-B halo is still not sufficient to create the Milky Way thick disc, it is nevertheless significant. At earlier times, when the substructure abundance was higher, it is conceivable that there might have been a sufficiently massive interaction or a large enough number of impacts to form the thick disc. The rapid, stochastic heating the Benson model predicts is more in line with thick disc formation than the heating needed to reproduce the age-velocity dispersion relation, though this may be an artefact of the model's assumption of an instantaneous return to virial equilibrium for the disc. In addition, thick discs are a common feature of observed galaxies (Gilmore and Reid, 1983; Morrison et al., 1997; Dalcanton and Bernstein, 2002; Yoachim and Dalcanton, 2006; Elmegreen and Elmegreen, 2006), but there is significant heating in only one of the five Aquarius haloes.

The Benson model itself is based on some questionable assumptions. The authors discuss a few of the simplifications in the paper, including the issue of whether using the Chandrasekhar approximation of dynamical friction is valid for this problem. In our view it is not, the subhaloes are comparable in size to the disc and thus it is inaccurate to be modelling the disc that the subhalo passes through as a uniform medium. Encounters between discs and subhaloes are complex interactions and while analytical models may capture the essential physics, the calculation of the quantities is non-trivial and huge simplifications are required. Therefore in the next chapter we tackle the same problem using N-body simulations to assess the effects subhaloes have on discs. We will apply the Benson model to these high resolutions as our concluding test of its validity.

Chapter 5

Simulations of Disc-Subhalo Encounters

5.1 Introduction

In the last chapter we looked at the Benson et al. (2004) semi-analytical model of disc heating in an attempt to estimate the heating that would be generated by populations of substructures selected from the Aquarius simulations. In this chapter we tackle the same problem using N-body simulations. These have the advantage of being able to measure the heating directly from the simulation outputs and of allowing an examination of the broader effects subhaloes have on discs, including the morphological features they can induce. Simulations have been extensively used to tackle this problem (Dubinski et al., 2008; Villalobos and Helmi, 2008; Kazantzidis et al., 2008; Read et al., 2008; Kazantzidis et al., 2009; Purcell et al., 2009) and there is the general consensus that discs can survive in the a ΛCDM cosmogony, but that subhaloes can have an appreciable effect on discs, contributing significantly to the heating and thickening. The heating is dominated by the most massive dark matter subhaloes, and as we have seen, it is a rather stochastic process, depending on the merger history of each individual galaxy's dark matter halo and the orbital properties of those massive substructures.

Simulations have clearly demonstrated that sufficiently massive substructures can substantially alter a stellar disc. Villalobos and Helmi (2008) performed a series of simulations of a single large subhalo of 10-20 percent of the host mass merging into the disc. Despite the massive size of the subhaloes the discs were not destroyed, but instead were found to form thick discs whose kinematic characteristics were consistent with observations. Their simulations were relatively low resolution, but this was not a problem as their purpose was to provoke large responses in the discs. This agreed with the conclu-

sions of Purcell et al. (2009), who performed similar but higher resolution simulations of the interaction between a massive subhalo and a disc and also found that the thin disc did not survive. The initially thin disc was transformed into a structure that was roughly three times as thick and more than twice as kinematically hot.

The question is, then, how common these large interactions are. Dubinski et al. (2008) bombarded an N-body model of M31 with 100 subhaloes over a 10 Gyr period. They generated a subhalo population whose properties reflect cosmological numerical predictions for the subhalo mass function, radial distribution and tidal radii. Rather than using the King model (King, 1966) that many of the previous studies had employed (Huang and Carlberg, 1997; Velazquez and White, 1999; Benson et al., 2004), they used an NFW profile for the perturbing subhaloes. The NFW profile is cuspy rather than cored, which makes the subhaloes more robust to tidal interactions than the King model and thus able to do more damage to the disc. Nevertheless, they found the vertical disc heating to be small despite many interactions, although the subhaloes did excite spiral structure and in some cases a bar instability. By contrast, Read et al. (2008) used cosmological simulations to assess the frequency of subhalo-disc encounter events and found that the average Milky Way-sized galaxy has three subhaloes with $v_{\rm max} \geq 80$ km s^{-1}. Their simulations based on these statistics found they heated the thin disc sufficiently to produce a thick disc.

Yet these studies have tended to follow the same approach in setting up a disc-bulge galaxy within a dark matter halo and performing dissipationless N-body simulations, and thus suffer from the same potential flaws. One of the main questionable assumptions they all make is for the structure of the subhaloes, either assuming an NFW profile if the subhaloes are introduced into the simulations out near the parent halo virial radius (Dubinski et al., 2008; Villalobos and Helmi, 2008), or using a more truncated profile if placed closer to the centre (Read et al., 2008).

The only simulations that have avoided this are the work of Kazantzidis et al. (2008, 2009). They measured the substructure abundance from four cosmological simulations of four galaxy-sized dark matter haloes and found that their typical halo had one object more massive than a disc cross within the central 20 kpc since $z = 1$, along with five objects more massive than 20 percent of the disc. From one of the simulations they selected all the subhaloes with $0.2M_{\rm disc} \leq M_{\rm sub} \leq M_{\rm disc}$ to obtain a set of six subhaloes

with masses in the range $\sim (0.7-2)\times 10^{10}\mathrm{M}_{\odot}$. These were then used in their controlled numerical experiments. The experiments involved introducing the subhaloes into their simulations of repeated encounters with an initially thin disc and observing the morphological and dynamical effects. Unlike previous work, Kazantzidis et al. (2008) actually measured the density profiles of the subhaloes and fitted a multi-parameter density profile law to them, so that they could generate N-body realisation for the simulations.

In their first paper, Kazantzidis et al. (2008), looked at the morphological features excited in the disc and found that the accretion events produced several distinctive morphological signatures, including long-lived, low surface brightness, ringlike features in the outskirts; significant flares; bars; and faint filamentary structures above the disc plane. Their second paper (Kazantzidis et al., 2009) looked at the dynamical effects. The disc experienced considerable thickening and heating at all radii, prominent flaring at the outer edges and lopsidedness as well as substantial tilting. They concluded that subhalo-disc interactions of the kind expected in ΛCDM models could induce morphological features in galactic discs that are similar to those being discovered in the Milky Way, M31, and other disc galaxies, and that they play a significant role in setting the structure of disc galaxies and driving galaxy evolution.

Another way to study disc galaxies is through hydrodynamical simulations. However, in the past it has proven extremely difficult to form disc galaxies in cosmological hydrodynamical simulations. Galaxies in the early simulations suffered from an excessive loss of angular momentum and, as a result, were too small (Navarro and Benz, 1991; Navarro and White, 1994; Navarro et al., 1995). Better treatment of feedback (Thacker and Couchman, 2001; Stinson et al., 2006; Governato et al., 2007) and higher resolution (Mayer et al., 2008; Sales et al., 2010; Keres et al., 2011) have partly alleviated the problem, however, it remains difficult to form completely bulgeless galaxies. Part of the problem is that it is still uncertain which physical processes are the most important and how the exact prescriptions used in the model affect the structure of the final galaxy. Even now the highest resolution simulations are still barely able to resolve the thin disc and thus do not yet probe the scales needed to understand disc heating. Given these problems we believe that the best way to tackle the question of disc heating remains the use of dissipationless N-body simulations.

We adopt the dissipationless approach and employ a similar technique as Kazantzidis

et al. (2008, 2009), but go one step further. Using the subhalo samples selected in § 4.2.1, we perform high resolution simulations of their encounters with a disc. However, rather than making any assumptions about the density profiles or velocity dispersions of subhaloes, we extract actual subhaloes from the Aquarius simulations and place them directly into our model. As seen in § 4.2, the Aquarius haloes are more quiescent than the Kazantzidis haloes, so we expect smaller changes to the discs and less heating.

5.2 Methodology

The same samples of subhaloes as selected from the Aquarius simulation in § 4.2.1 are placed into a simple disc galaxy model and simulated for 8.6 Gyr in order for us to observe the dynamical effects they have on a galactic disc.

5.2.1 Disc Galaxy Model

We construct an N-body galaxy model containing a dark matter halo, a bulge and a stellar disc using the publicly available MKGALAXY code. This is based on the method of McMillan and Dehnen (2007), which uses a general recipe for creating multicomponent equilibrium galaxy models. Other methods have the disadvantage that while they construct the individual components to fit the desired parameters, the combined models often do not match the required form or are not quite in equilibrium. The McMillan and Dehnen (2007) method avoids this by growing the disc adiabatically within the N-body halo.

The same standardised galaxy model as described in § 4.4.1 is employed in the simulations; it again allows a direct comparison between heating in the five haloes and has the advantage that the same galaxy model can be used in all the simulations. The halo profile is modified slightly from a pure NFW profile by multiplication with a truncation function, in order to limit the spatial extent of the halo and ensure it has a finite mass. The truncation function employed by the MKGALAXY code is

$$T(r) = \frac{2}{\mathrm{sech}\,(r/r_t) + \cosh(r/r_t)}, \tag{5.1}$$

where r_t is set to the virial radius $r_{200} = 220$ kpc. It is designed to have little effect within r_t but to cut off the halo at large radii. The generated halo has a total mass of $1.8 \times 10^{12}\mathrm{M}_{\odot}$, of which 72 percent lies within the virial radius.

Since the majority of the mass is in the halo, in order to focus the computational efforts on the disc and avoid expending unnecessary efforts on the halo, we use five times heavier halo particles than disc particles. Our galaxy model contains $N_d = 10^6$ particles in the disc, $N_h = 9 \times 10^6$ in the halo, and $N_b = 2.5 \times 10^5$ particles in the bulge, and uses a gravitational softening of $\epsilon = 35$ pc for the disc and bulge and $\epsilon = 78$ pc for the particles in the dark matter halo. We denote this as our level 2 resolution. This mass and force resolution is adequate to resolve the vertical structure of a thin stellar disc, yet running the simulations is of a low enough computational expense to allow repeated simulations of multiple haloes. In addition, in order to test convergence we have also run two sets of simulations at a higher resolution (level 3) with five times the number of particles in each component, and at a lower resolution (level 1) with one fifth the number of particles.

The stellar disc is axisymmetric with an exponential radial profile and a vertical distribution of disc stars is described by a sech^2 function. It is constructed to have a constant Toomre parameter (Toomre, 1964) of $Q = 2$ over the whole surface of the disc, indicating that the model is stable against local nonaxisymmetric instabilities. It is desirable that the disc is stable from developing spiral instabilities too easily, otherwise even minor interactions with substructures trigger the formation of bars and spiral arms (Dubinski et al., 2008), which can act as an additional mechanism to heat and redistribute energy within the disc (Minchev and Quillen, 2006; Saha et al., 2010).

The disc galaxy model has been evolved in isolation for 9 Gyrs to check its stability against the formation of spiral structure and to measure the extent of the artificial heating of the disc due to numerical relaxation. During this period the disc stayed stable, with no major instabilities evident. The change in the thickness of the disc as a function of radius and time for the three levels can be seen in Fig. 5.1. In this case the thickness measured as the root mean squared (rms) vertical height of the disc. To calculate the thickness as a function of radius, the surface of the disc is split into concentric annuli and then each annulus split into multiple cells. The root mean squared vertical displacement about the mean height of the particles is calculated for each individual cell. The cells are then binned by radius to give the mean rms thickness. The advantage of this method of splitting the disc into cells first, as opposed to simply binning the particles directly into radial bins, is that for each cell the thickness is calculated relative to its local mean and

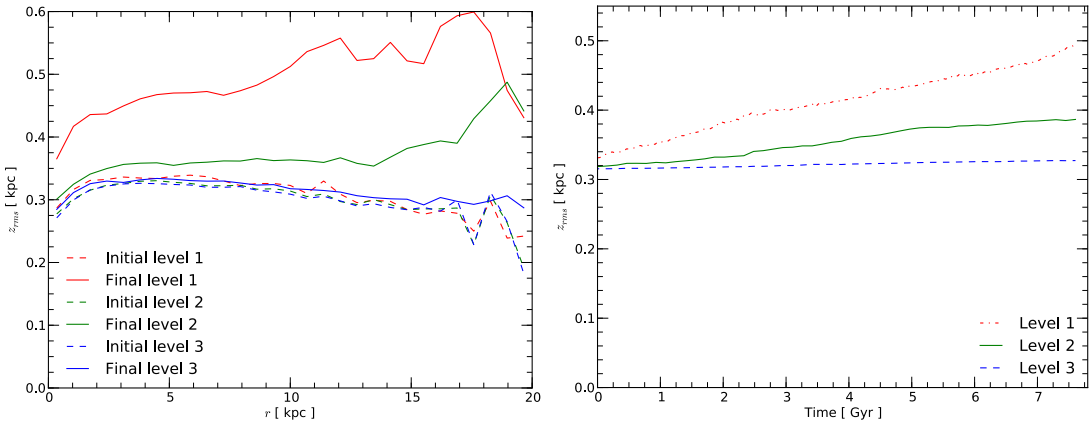

Figure 5.1: The change in the root mean squared vertical thickness of the disc due to numerical heating, for our 3 resolution isolated disc simulations. *Left panel:* the thickness of the disc as a function of radius. The dashed lines show the initial thickness of the disc and the solid lines show the final thickness. *Right panel:* the growth in the overall thickness over time.

avoids confusing warping of the disc as thickening. As expected the numerical heating is greater the fewer the number of disc particles, with increases of 52%, 22% and 3% for the level 1, 2 and 3 models respectively.

5.2.2 Subhalo Models

A common method used to construct N-body models of subhaloes has been to assume a density profile and sample the corresponding distribution function to generate self-consistent realisations. The density profile is often chosen to be something simple such as a Hernquist profile (Hernquist, 1990) or King model, or alternatively, as in Kazantzidis et al. (2008), is specified by fitting a multi-parameter density profile law to actual subhaloes from cosmological simulations. The issue with this latter approach is that it restricts the forms of the subhaloes generated to simple spherical equilibrium objects.

As subhaloes orbit within their parent halo, their masses are reduced by tidal stripping (Hayashi et al., 2003). Mass is removed from the outside of the halo, sharply truncating their profiles (Kazantzidis et al., 2004c). As the subhaloes undergo pericentric passages the shocking they suffer affects the central regions and can cause them to be substantially different from a cuspy $\rho(r) \propto r^{-1}$ profile. From the Aquarius simulations we have found that there are large variations in the forms of the selected subhaloes and

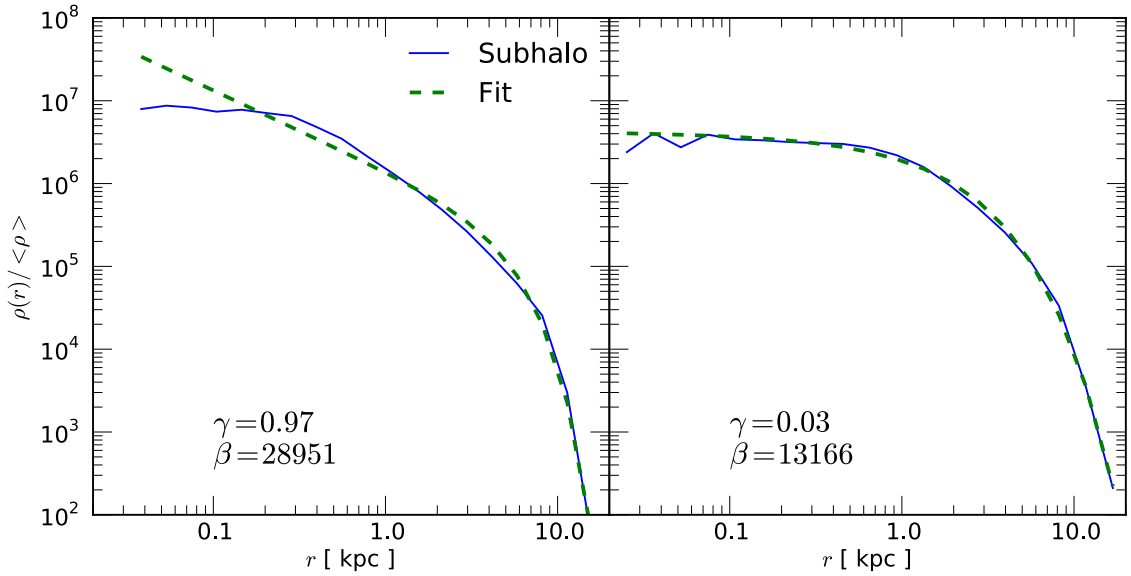

Figure 5.2: Spherically average density profile for the largest subhaloes in the Aq-A (left) and Aq-B (right) samples at the simulation output times nearest to their first inward crossing of $r_{\rm in}$ since $z = 1$. The solid blue line shows the profile of the actual subhalo, while the green dashed line is a multi-parameter fit. The values for the inner slope γ and the outer slope β as required by the fit are given in each case.

that the density profiles of many of the subhaloes in our samples are not well fitted by any simple analytical profile or even the multi-parameter (α, β, γ) density profile law (Zhao, 1996)

$$\rho(r) = \frac{\rho_s}{(r/r_s)^\gamma [1 + (r/r_s)^\alpha]^{(\beta-\gamma)/\alpha)}} \tag{5.2}$$

where γ determines the inner slope of the profile, β the outer slope, and α the sharpness of the transition between the inner and outer profile. Two examples of subhalo density profiles can be seen in Fig. 5.2 for the most massive subhaloes in each of the Aq-A and Aq-B samples. The profile is measured from the Aquarius simulation output nearest to their first inward crossing of the $r_{\rm in} = 50$ kpc boundary since $z = 1$. Both subhaloes are very flat in the centre, which may be due to limited resolution. They also both have a very rapid drop-off in the density at the outer edge. While the subhaloes can be fitted by the multi-parameter profile, it requires extreme values for the inner and outer slopes. For such extreme values it is impossible to construct an equilibrium subhalo realisation as they have unphysical distribution functions. The problem arises from assuming these subhaloes are in equilibrium. In the case of the Aq-B subhalo, it had already undergone

an earlier pericentric passage at $z \approx 1.2$, when the subhalo passed within ~ 18 kpc from the host halo centre and lost ~ 70 percent of its mass, and so had been radically changed from its original profile at accretion.

To avoid all these problems, we take advantage of the high resolution of the Aquarius simulations and extract the actual subhaloes directly from the simulations. This means we do not have to make any assumptions about the structure or profiles of the subhaloes but instead use actual cosmological subhaloes. The high resolution of the Aquarius simulations means that the subhaloes are known to be well converged, with their density profiles reliable down to ~ 250 pc (see Fig. 2.17). Previous work often chooses a particular subhalo profile and constructs models based on this. The problems with this are that to generate a subhalo realisation requires the assumption that the subhaloes are still in equilibrium, which is only true depending on when the subhaloes are introduced into the simulations at a large distance from the halo centre. The other problem is that the choice of profile immediately encodes assumptions about the concentrations and how bound the subhaloes are, properties which can have important implications for how long the subhaloes survive.

To extract subhaloes we use the particles identified by SUBFIND. These can be located in the outputs of the Aquarius simulation to extract a gravitationally bound subhalo. After scaling and rotation to the correct frame, we randomly subsample this set to define a bound object with the appropriate resolution and particle mass that can be placed directly into the disc galaxy simulation.

5.2.3 Simulations

All the simulations have been carried out using a modified version of GADGET-3. They are run as non-cosmological, isolated simulations using the disc galaxy model for initial conditions and are evolved for a period of 8.6 Gyr, finishing at $z = 0$. At the appropriate times the subhaloes are introduced into the simulation. In order to not artificially disturb the disc by suddenly placing the subhaloes in the simulation, we slowly grow an analytical potential over the preceding half gigayear, a period comparable to the dynamical time of the disc. At the time of entry the analytical potential is replaced with a live N-body model of the subhalo.

The origin of time in the simulations is taken to coincide with $z = 1$ of the Aquarius

simulations. The simulations run from $t = -1$ to $t = 7.6$ Gyr so that $t = 0$ and $t = 7.6$ Gyr corresponds to the Aquarius times $t = 5.97$ Gyr and $t = 13.6$ Gyr. Since some of the subhaloes enter the $r_{\rm in} = 50$ kpc boundary shortly after $z = 1$, we run the simulation for an extra gigayear at the start. This serves the dual purpose of allowing the initial conditions to relax to ensure they are in equilibrium and of having an initial period in which to fade in early subhaloes before they enter the simulation. We define the start of the simulation $t = 0$ to be after this period and measure the heating and other properties of the disc from this point onwards.

A Hernquist profile is used as the analytic potential to represent the subhaloes during the fade-in stage. The strength of the potential is increased by linearly increasing the mass of each subhalo up to its final value over a half gigayear period. The potential is set moving along a straight line with the velocity the subhalo will have at the point it is realised as a full N-body object. While a Hernquist profile is not always a good fit to the density profile of the actual subhaloes, it has the advantage of being very simple and being easily able to match their mass and size. When the subhaloes are actually introduced there will be some discontinuity in the potential, but substantially less than if they were simply suddenly placed into the simulations.

We introduce subhaloes into the disc galaxy model just as they are falling into the inner regions of the halo and about to interact with the galaxy. The simulations are stopped at each time a new subhalo enters the simulations. Additional particles belonging to the new subhalo are added into the snapshot output at the stop time, and this is used as the initial conditions to start the next stage of the simulation. As the Aquarius simulations have limited time outputs it is often the case that multiple subhaloes are found to cross the $r_{\rm in} = 50$ kpc in the same output. In these cases multiple subhaloes will be placed into the simulation at the same time. Once placed in the simulations as live N-body subhaloes, they are allowed to freely gravitationally interact with themselves and the other components of the simulation. The subhaloes may interact with the disc multiple times, but have usually been heavily stripped during the first passage. We leave the subhalo particles in the simulation to allows us to track their eventual fate and observe the final location of the material that originally comprised the subhaloes.

The mass of the particles contained in the subhaloes is set to be the same as the mass of the disc particles. After scaling, the extracted Aquarius subhaloes are randomly

sampled to a lower resolution for the level 1 and 2 simulations. Our level 3 simulation has a resolution above that of the scaled Aquarius simulations, so in this case we use all the subhalo particles without sampling and had to use a particle mass slightly larger than that of the disc particles. In addition to scaling the subhaloes' mass and position, the velocity is also scaled appropriately in order to ensure that the subhaloes enter the simulations on the same orbits they were on at the time they were extracted from the Aquarius simulations. We label our simulations by the prefix G, followed by a letter matching the Aquarius halo from which the population of subhaloes came, ending with a number to define the resolution, for example G-A-2.

5.2.4 Caveats

The two main limitations to our simulations are the lack of gas physics in our simulations and our use of a fixed mass halo. Not including gas physics and the associated phenomena of star formation, feedback and cooling in the simulations means that the disc does not grow in mass or size. It is likely that interactions with subhaloes would trigger bursts of star formation, creating new stars located in a thinner structure and resulting in a much more complex vertical distribution of stars and ages. Gas could also radiate away some of the energy from the interactions and reduce the damage to the disc (Quinn et al., 1993; Moster et al., 2010) and cool and settle to form a new thin disc. The growth of a new thin disc could further cause a substantial contraction in the thick disc (Villalobos et al., 2010).

We are also using a fixed mass dark matter halo and have neglected any cosmological evolution of the structure of the host halo or any accretion onto it. As seen in § 2.3.3, the Aquarius haloes grow in virial mass by a factor of ~ 1.6 between $z = 1$ and $z = 0$. However, $V_{\rm max}^2$, which is a better indication of growth in the central regions, changes very little over the same period. Other studies have also shown that the structure of dark haloes within the scale radius changes little at late times (Wechsler et al., 2002; Zhao et al., 2003; Romano-Diaz et al., 2006; Wang et al., 2011) and thus serves to justify our simplification of treating the halo as simple non-accreting.

5.3 Results

We start by examining how the subhaloes' evolution and orbits differ in the disc galaxy model simulations compared to how they behaved in the Aquarius simulations. All analysis of the disc is performed in the centre of mass rest frame of the disc. This removes any effects of the additional momentum that is added into the simulations when the subhaloes are introduced, which can cause the disc and halo to move away from the origin. Additionally, the disc is reoriented, through diagonalisation of its moment of inertia tensor, to lie on the x-y plane with the rotation axis parallel to the z-axis to remove any rotation that the subhaloes may have caused.

5.3.1 Subhalo Evolution

Focusing on four subhaloes, the largest two subhaloes each from the Aq-A and Aq-B populations, we compare how the same subhalo evolves in three different simulations. The evolution is best illustrated by the change in their SUBFIND masses and maximum circular velocities as a function of time, as shown in Fig. 5.3. The simulations were: the original Aquarius simulation from which they were taken; a simulation of just the dark matter halo of our galaxy model, without disc or bulge; and finally, a simulation with the complete galaxy model including a disc and bulge. Considering the evolution of subhaloes in the dark matter only halo of the standardised galaxy model, without disc or bulge, allows us to gauge exactly how much the difference from the Aquarius simulations is due to changing the host halo potential and how much is due to the addition of a disc.

The evolution in the Aquarius simulations and the dark matter halo only simulations are fairly similar. In both cases the subhaloes show a comparable mass loss history and survive for the same lengths of time; those still present at the end of the simulation have very similar final masses. The final maximum circular velocity does not match quite so well. The maximum circular velocity is a property of the internal structure of the subhalo that tends to remain constant as the subhaloes orbit within their host halo and only changes as the subhaloes pass pericentre and are tidally shocked. The rapid decreases in Fig. 5.3 can therefore be used to compare times of pericentre passages. It can be seen that the subhaloes have the same number of pericentric passages in both

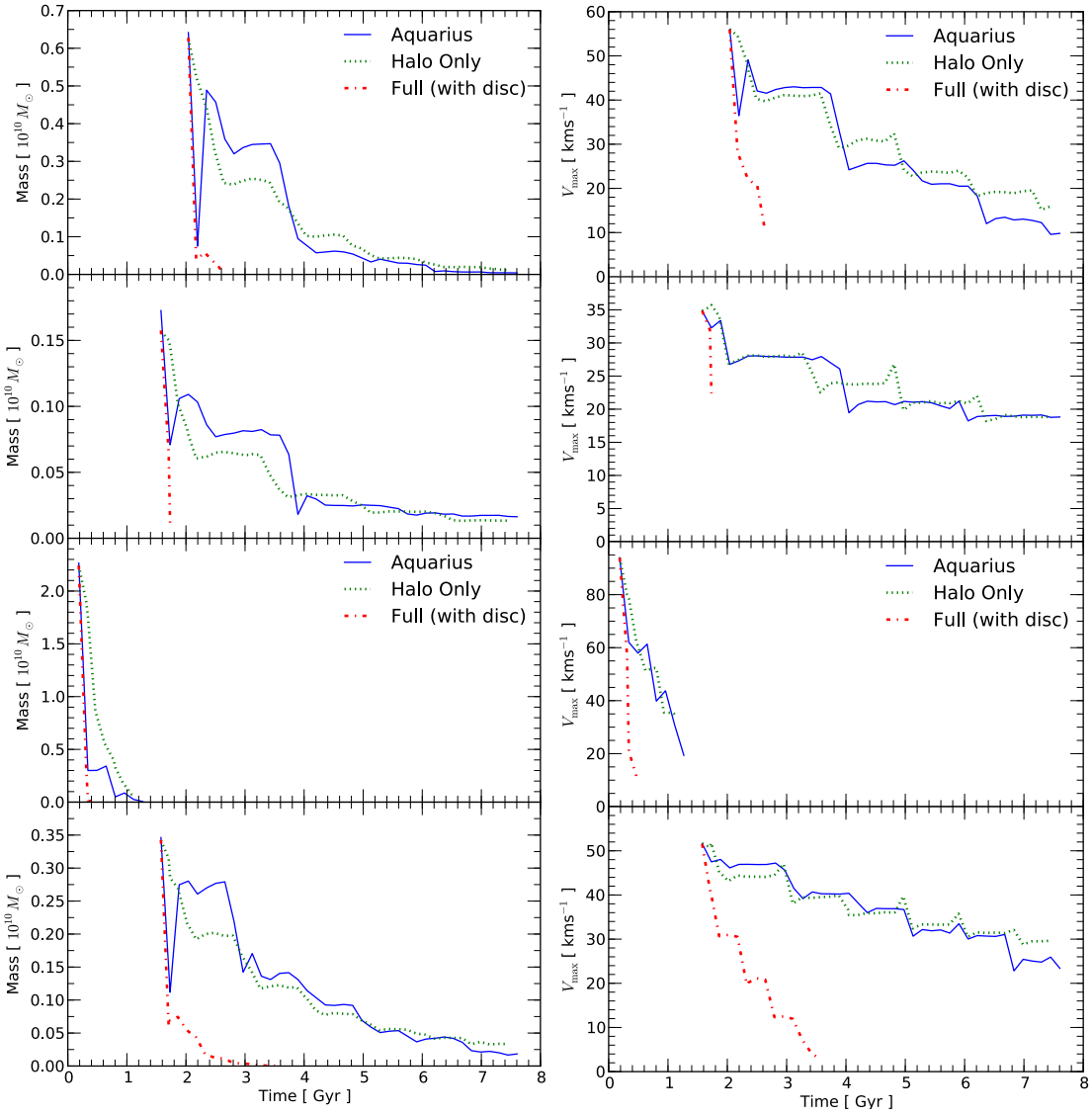

Figure 5.3: A comparison of the evolution of the largest two subhaloes in the Aq-A and Aq-B samples. *Left panel:* the SUBFIND mass. *Right panel:* the maximum circular velocity. The solid line follows the subhaloes' history in the original Aquarius simulations. The dotted line is the behaviour of the extracted subhalo placed into a dark matter halo only model simulation, while the dash-dotted line stands for the subhalo in the full galaxy model simulation including the bulge and disc.

cases, at approximately the same times. Only in the second subhalo is there a notable difference, with the passages in the Aquarius simulation occurring later.

An exact match in evolution is not expected, as while our galaxy model has been constructed to broadly resemble the Aquarius haloes in many aspects, it is still considerably different in many others. In particular, the model is static, it is not growing in mass, and in the halo only simulations it is spherically symmetric, none of which is true for cosmological Aquarius haloes. As shown in chapter 3, even when using the HEX technique to try and approximate a halo it is impossible to achieve identical evolution for subhaloes. We therefore conclude that the similar evolution in the two cases provides confirmation that our galaxy model is a reasonable basis for simulating the interactions of the Aquarius subhaloes with a galactic disc.

In the full simulations the subhaloes are introduced into our complete galaxy model that includes a halo, bulge and disc. There is a huge difference in the fate of the subhaloes. In the Aquarius simulations and the halo only simulations, three out of four of the subhaloes survived until the end, though with only a small fraction of their initial mass. In the full galaxy model, none of the four selected subhaloes survive for any significant time, with two of them being destroyed immediately. It is not clear if this is the result of additional mass deepening the potential well and therefore bringing subhaloes closer to the centre, where they will experience greater tidal stripping, or if the disc itself shocks the subhaloes so that they are more easily disrupted, as proposed in D'Onghia et al. (2010). Whatever the mechanism, it is clear that the presence of a galaxy is important in understanding subhalo evolution. In reality this rapid destruction may be partly counteracted if the subhaloes contain baryons, even hosting dwarf galaxies. Parry et al. (2011) look at the effects baryons have on subhaloes. They compare one of the dark matter only simulations of an Aquarius halo to a full hydrodynamic simulation of the same halo and find that the condensation of baryons has a relatively minor effect on the structure of the subhaloes and that there is no consistent trend for baryons to increase or decrease the central density of the dark matter. We therefore do not think that the lack of baryons in subhaloes is a problem for our calculation of disc heating.

The third subhalo, the most massive subhalo in the Aq-B sample as well as the most massive overall, is particularly interesting. It is the same subhalo that was discussed earlier, which had undergone a previous pericentric passage at $z \approx 1.2$, when the subhalo

passed within ~ 18 kpc from the host halo centre and lost ~ 70 percent of its mass. This subhalo is on a near radial orbit that decays rapidly. When initially introduced into the simulation, the subhalo is already very diffuse and only weakly bound. As it enters our simulation it is still in the process of being disrupted from its earlier pericentric passage, explaining its weakly bound state. Its subsequent radial orbit then takes it closer to the centre of the parent halo than the other subhaloes reached, where it makes several more pericentric passages in quick succession, experiences huge levels of tidal stripping and is completely disrupted during the third passage.

5.3.2 Disc Impacts

We now consider where and when in the five simulations the subhaloes impact the disc. In order to reconstruct the orbits of the subhaloes, the same technique of interpolating their paths between outputs is used as in the previous chapter. The disc impacts can be seen in Fig. 5.4. This plot is a direct analogue of Fig. 4.5, which displayed the locations where the subhaloes intersected with a hypothetical disc plane in the Aquarius simulations. It is therefore possible to get an indication of how the subhalo orbits were changed by placing them into a model with a central galaxy. The differences arise partly from the use of an NFW halo potential, but are primarily due to the presence of the disc.

The bombardment history is notably different. There is still a clear correspondence between the largest of the impacts in the two figures. In samples A-D the largest impact still occurs at the same time, but with a lower mass in the galaxy model and closer to the centre. These impacts correspond to the first passage of the subhaloes through the disc, at which point there has not been time for the orbits to significantly diverge between the Aquarius orbits and those in the disc simulations. However, even at this early time the subhaloes are less massive, reflecting the shorter lifetime of subhaloes when a galaxy is added. The reduced subhalo lifetimes are also responsible for the lack of late impacts on the discs. Few subhaloes survive to make a second impact on the disc, and if they do they no longer have appreciable mass by that time.

The impact of the most massive subhalo in the Aq-B sample is substantially smaller. As we have discussed this is because it is only weakly bound when it enters the simulation, making it particularly prone to disruption. However, having checked we find that the stripped material still moves with the subhalo and passes through the disc, so that

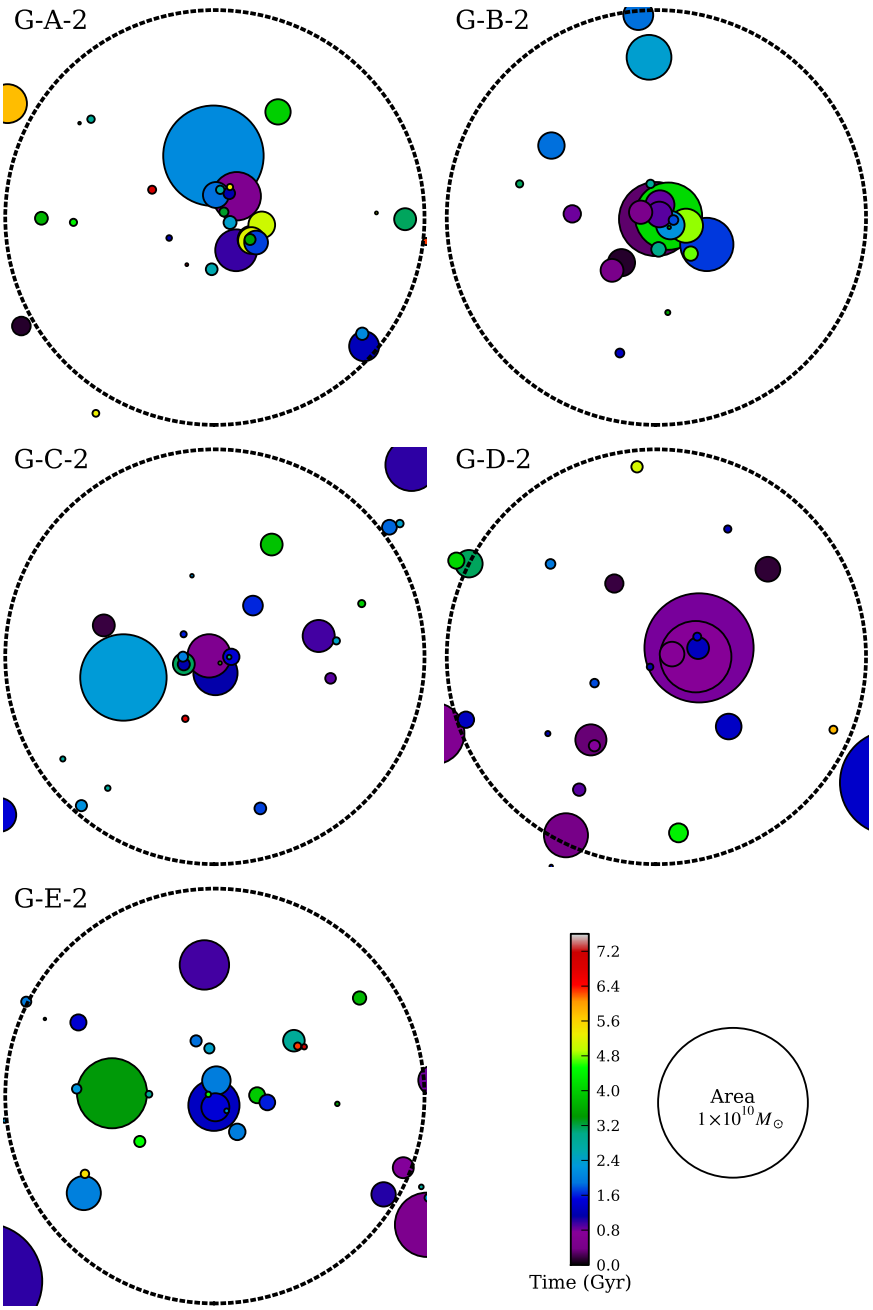

Figure 5.4: The locations of the subhalo impacts on the disc in the galaxy simulations. The circles mark the point of intersection on the disc. The colour of the circles represents the time of intersection and the area the mass estimated from its SUBFIND mass. The large dashed circle marks the 20 kpc radius defined to be the boundary of the disc. In order to calculate the exact point of intersection, the orbit of the subhaloes between outputs is reconstructed through interpolation.

Simulation	$\Delta z_{\rm rms}$ [pc]	$\Delta z_{\rm rms}$ [%]
G-A-1	-11	-2
G-A-2	2	0.5
G-A-3	28	9
G-B-1	107	21
G-B-2	128	33
G-B-3	142	44

Table 5.1: The change between the initial and final rms disc thickness for two sets of subhaloes, simulated at three resolutions.

this interaction ends up being a lot more damaging than is suggested by Fig. 5.4. The other notable difference is that the impacts tend to be closer to the centre of the disk. This is not the result of using a different halo potential but is due to the extra mass of the disc and bulge deepening the potential well and reducing the pericentric distances. In addition, as discussed at length for the Benson model, the disc applies dynamical friction to the subhaloes, causing their orbits to decay more rapidly.

5.3.3 Convergence

Before looking at the heating in all five haloes, we start by studying how well the results converge as the resolution of the simulations is increased for two of the subhalo samples, G-A and G-B. Each of these has been simulated at three resolutions. The standard level 2 resolution; one with five times the number of particles; and one with one fifth the number of particles. Convergence is assessed by comparing the change in the vertical thickness of the disc in each case. The results are plotted in Fig. 5.5 and the final thicknesses listed in Table 5.1. There is very little change in the thickness of the disc in the G-A set of simulations above that of numerical heating. At times in both the level 1 and the level 2 G-A simulations, the thickness of the disc in the simulations including subhaloes is thinner than the baseline disc only simulation. Rather than implying that the subhaloes are cooling the disc, it is more likely that it is simply a case of the subhalo heating altering the rate of numerical heating. Neither the level 1 nor the level 2 simulations have sufficient resolution to be able to resolve any subhalo heating. We are able to conclude only that subhaloes have very little effect on the disc, but cannot accurately

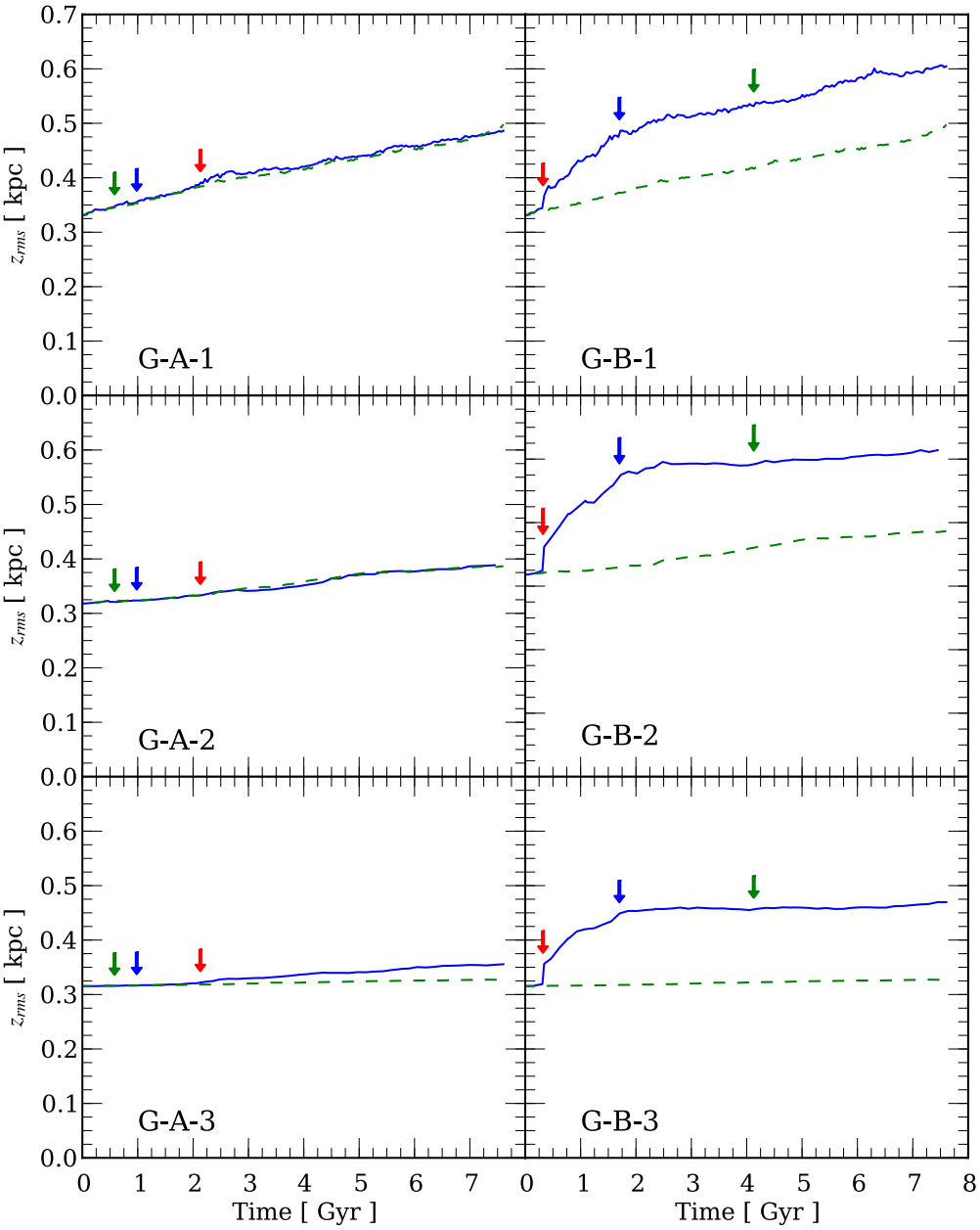

Figure 5.5: The change in the vertical thickness of the disc for the A and B samples of subhaloes, each simulated at three resolutions. The top panels are the lowest level 1 simulations, the middle panels are the standard level 2 resolution simulations, and the bottom panels the five times higher level 3 resolution. The green dashed lines show the numerical heating that occurs in the disc only simulations without subhaloes, and the solid blue line represents the simulations where subhaloes are included. The arrows mark the time of the three largest subhalo impacts in each simulations. Red is the largest and blue the smallest of the three.

quantify the exact amount. It is only for the level 3 simulation that heating above the noise is clearly discernible.

There is much greater heating in the G-B simulations, and at all three levels there is a clear signal of disc heating. The majority of the extra heating from subhaloes happens in the first two gigayears, after which the thickness of the disc remains fairly constant, except in G-B-1, where it continues to grow at a rate that can be entirely attributed to numerical heating. The final outcome is that there is twice the increase in the thickness of the disc in the G-B-3 simulation as in the G-B-1 simulation. This is presumably due to a reduction in the numerical heating in the level 1 simulation when subhaloes are included, rather than there being greater subhalo heating in the level 3 simulation. The G-A simulations suffer the same problem, with the G-A-1 having a decrease in disc thickness relative to the final disc only simulation thickness. Therefore, it is clear that taking the heating to be the difference between the final vertical thickness with subhaloes, to the simulations without, is too simplistic and for that reason the level 1 simulations have insufficient resolution to measure subhalo disc heating.

The level 2 simulations also suffer large amounts of numerical heating and find lower disc heating than the level 3 simulations. Only the level 3 simulations have a low enough level of numerical heating to render the artificial increase unimportant and allow precise measurements of the change in the vertical disc thickness. Ideally, all five cases would have been run at the high resolution, unfortunately restrictions on computational resources prevented this. In the rest of the work we quote the results of the G-A and G-B level 3 simulations, and for the other three haloes the results from the level 2 simulations. The level 2 simulations are sufficient to broadly classify the amount of subhalo heating but not to precisely measure it.

Our level 3 simulations are of considerably higher resolution than most of the previous work that has investigated subhalo disc heating (Benson et al., 2004; Villalobos and Helmi, 2008; Kazantzidis et al., 2008; Read et al., 2008; Kazantzidis et al., 2009; Purcell et al., 2009), but only half the resolution of those used in Dubinski et al. (2008). The level 2 simulations are approximately equal to those of Kazantzidis et al. (2008); Read et al. (2008); Kazantzidis et al. (2009); Purcell et al. (2009), and the level 1 simulations to those of Benson et al. (2004); Villalobos and Helmi (2008). Since it is only in our highest level 3 simulations that numerical heating is negligible, this raises questions about the

Simulation	ΔT_z [$10^{10}\mathrm{M}_\odot\mathrm{km}^2\mathrm{s}^{-2}$]	Δz_{rms} [pc]
G-A-3	99.1 (3%)	28 (9%)
G-B-3	504.1 (17%)	142 (44%)
G-C-2	3.1 (0.1%)	6 (2%)
G-D-2	104.6 (3%)	24 (6%)
G-E-2	17.1 (1%)	6 (2%)

Table 5.2: The increase in the vertical kinetic energy and the thickness of the discs when bombarded by the subhalo samples. The changes are given in terms of the absolute increases and as a percentage of the initial energy and thickness (values in parentheses).

conclusions of these previous studies.

5.3.4 Heating

We start by gauging the disc heating in terms of its change in thickness and vertical kinetic energy. These can both be increased either by interactions with subhaloes or through a redistribution of energy from motion in the disc plane into vertical motion. The overall vertical root mean squared thickness of the discs as a function of time for each of the five simulations can be seen in Fig. 5.6, and the vertical kinetic energy in Fig. 5.7. The discs in the simulations G-C-2 and G-E-2 show no significant increase in the disc thickness or vertical kinetic energy above that from numerical heating. The disc in G-A-3 shows a small change that was not evident in the lower resolution versions. G-C-2 and G-E-2 do not have sufficient resolution for it to be discernible whether there is little or no heating. Only in simulations G-B-3 and G-D-2 can it be confidently concluded that the discs have been affected by the interactions with the subhaloes, with the greatest change in the thickness seen for G-B-3.

The G-B-3 simulation experiences a large increase in thickness beginning at 0.5 Gyrs. This is triggered by the impact of the massive subhalo. At this time there is a sudden and rapid increase in the thickness from 0.32 kpc to 0.36 kpc. Over the next 2 Gyrs there continues to be a slower, steady increase that finally tails off at a thickness of 0.47 kpc. A potential explanation for the continuing heating after the impact is that the impact

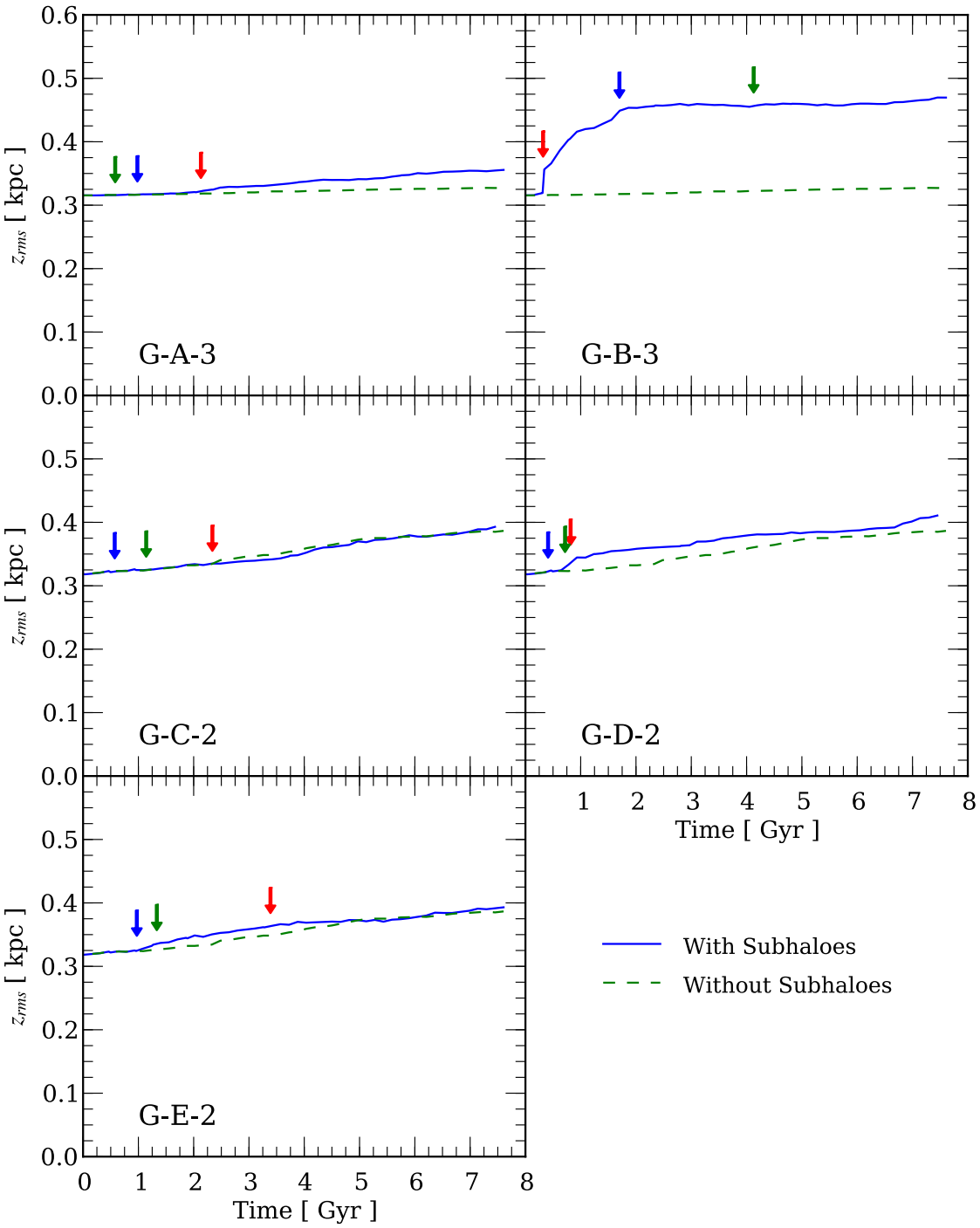

Figure 5.6: The root mean squared vertical thickness of discs as a function of time. The dashed green line shows the increase in thickness that occurs from numerical heating when no subhaloes are present. The solid blue line is the thickness with subhaloes. The arrows mark the time of the three largest subhalo impacts in each simulation. Red is the largest and blue the smallest of the three.

was massive enough to excite spiral structure throughout the whole disc. This structure slowly dies away over the following gigayear. The next two largest impact events are nowhere near as massive and do not seem to have a notable effect on the disc. It is clear from Fig. 5.6 that while increases in the disc thickness are clearly related to impact events, many of the impact events have no noticeable effect on the disc. It is only the very few large impacts that are important.

The initial vertical kinetic energy of the disc is $T_z = 2.9 \times 10^{13} \mathrm{M}_\odot \mathrm{km}^2 \mathrm{s}^{-2}$. The evolution of the vertical kinetic energy is shown in Fig. 5.7. It closely reflects the evolution of the thickness. However, the inner regions of the disc contribute more to the energy than to the thickness, as not only is the density greater towards the centre but the velocity dispersion has to be larger to maintain the same thickness. Subhaloes are more efficient at heating the outer regions of discs where the self gravity is less. As the disc self gravity is approximately proportional to the surface density, for the exponential disc under consideration, material is thus less tightly bound the further it is located from the centre. While this outer region might thicken, the total vertical kinetic energy will hardly change.

In Fig. 5.8 we look at the changes in the velocity dispersion of the stellar disc. The radial and azimuthal velocity dispersions tend to change sharply during an impact event and remain stable otherwise. The vertical velocity dispersion changes on the impacts but, like the thickness, also continues to increase for some time afterwards. In addition, the velocity dispersions in the plane show greater increases than the vertical velocity dispersions. For impacts normal to the disc this can be understood in terms of the impulsive approximation. As the subhalo passes through the disc, stars in the disc first receive a vertical impulse in one direction and then the other, whereas the horizontal impulses are applied in the same direction throughout the entire encounter. The integrated impulses in the plane are therefore greater than vertical ones, and the radial and azimuthal motions of the stars are perturbed more. While the impulsive approximation is not completely valid for subhalo encounters, as the velocity of the subhaloes is usually only about twice that of the disc circular velocity, the explanation still holds.

The age-velocity dispersion relation of the local neighbourhood is that older stars have larger velocity dispersions. Since the discs in our simulations only contain a single population of particles, it is impossible to measure any sort of age relation. Instead, look-

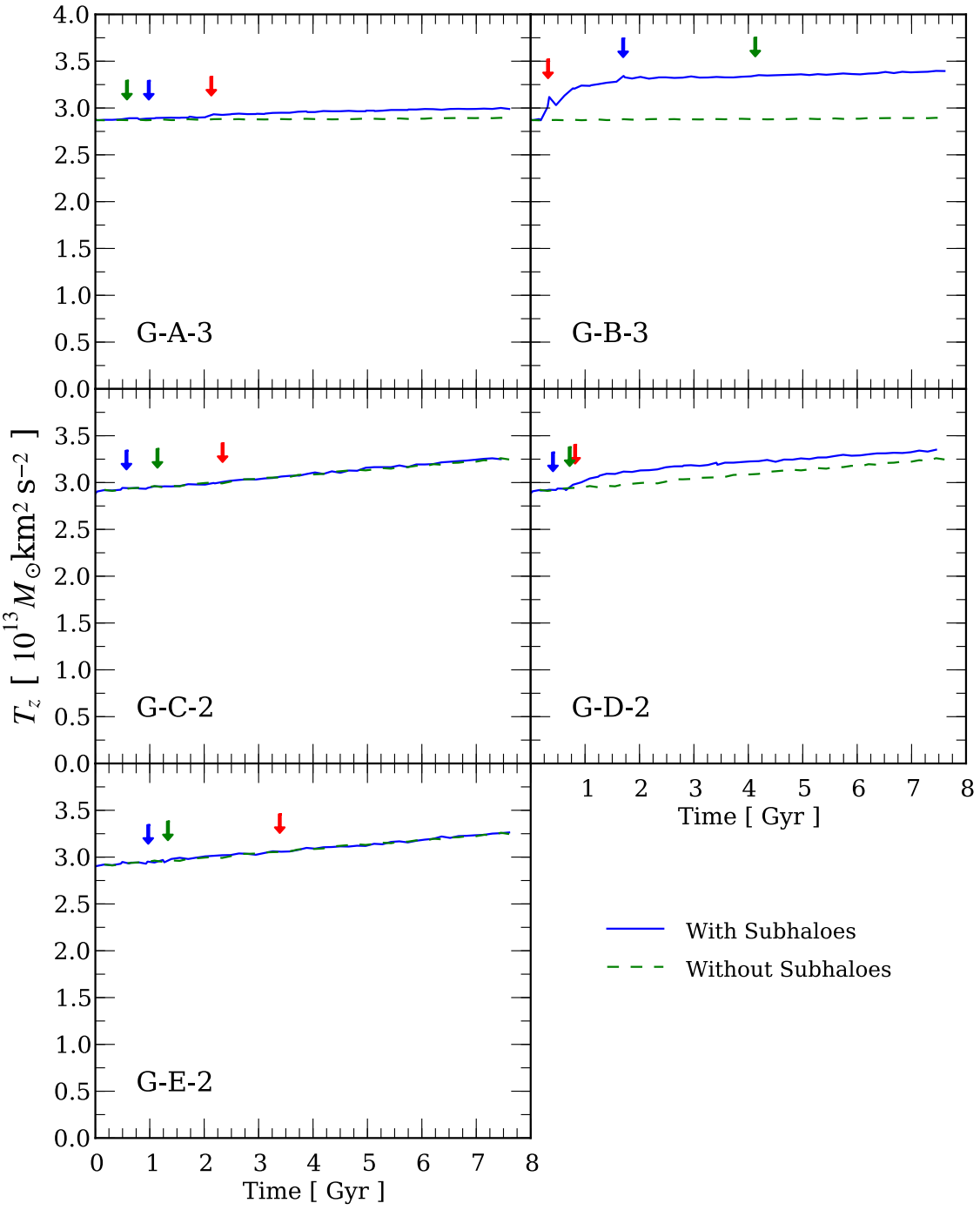

Figure 5.7: The evolution of the vertical kinetic energy of the discs when they are bombarded by the subhalo samples. The dashed green line shows the energy increase that occurs from numerical heating when no subhaloes are present. The solid blue line is the kinetic energy with subhaloes. The arrows mark the time of the three largest subhalo impacts in each simulations. Red is the largest and blue the smallest of the three.

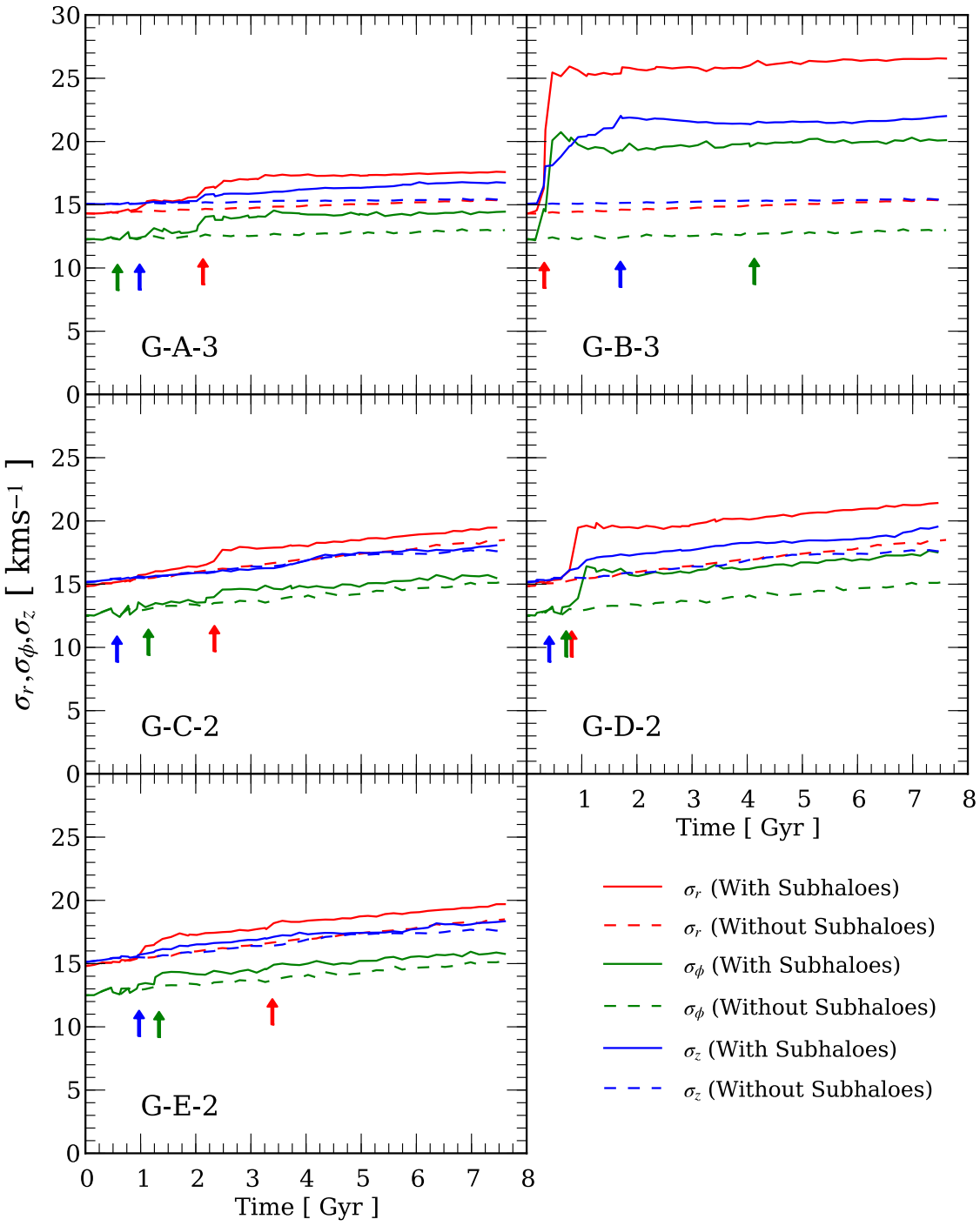

Figure 5.8: The evolution of the velocity dispersion at the 8 kpc radius when it is bombarded by the subhalo samples. The dashed lines shows how the velocity dispersions in the three principle directions increase when no subhaloes are present. The solid lines represent the change with subhaloes. The arrows mark the time of the three largest subhalo impacts as in previous plots.

ing at how the velocities of the particles increase with time is the closest possible comparison. The two are not totally equivalent, since it is possible under certain scenarios to reproduce the relation through a series of sudden heating events. However, these would require a frequent successive series of large encounters, which is not observed in our simulations. Instead we see that our five discs experience a few major, rapid increases in velocity dispersion, a type of heating not consistent with the age-velocity dispersion relation. It therefore seems that late-time subhalo encounters are not the cause of the age-velocity dispersion relation.

It is clear that subhalo encounters do heat the discs vertically and increase their thickness, but not enough in any of the Aquarius haloes to account for the formation of thick discs or, for three of the haloes, even for the observed heating in thin discs. The heating that does occur happens near the beginning of the simulations and is generated by one or two impact events. Therefore, it is likely that at even earlier times, when massive subhaloes were more numerous, subhalo heating would have been greater and could provide sufficient heating to create thick discs. It would only require one or two massive subhaloes to pass through the disc close to the centre. We are unable to confirm this hypothesis from this work, but the heating we observe is not inconsistent with such a scenario. Our results do demonstrate that there will be no late time heating of discs by substructures, suggesting that subhaloes would not prove to be a problem for the subsequent formation and survival of later thin discs.

5.3.5 Warping and Flaring

Up to this point we have focused on the global changes to the disc properties in response to subhalo interactions. We now briefly consider local changes, as the disc does not necessarily respond uniformly over its whole surface. It has already been observed from Fig. 5.6 that the vertical thickness of the discs in our five simulations is increased by subhalo interactions. Fig. 5.9 is a comparison of the final and initial vertical thickness of the disc as a function of radius and reveals that these increases occur non-uniformly, with the outer regions showing a greater change than the inner regions. Three of the discs, G-A-3, G-C-2 and G-E-2, have absolutely no change in their profiles in the inner 5 kpc, the other two have slight increases which tail off towards the centre.

As previously stated, the disc self gravity decreases outwards with the surface den-

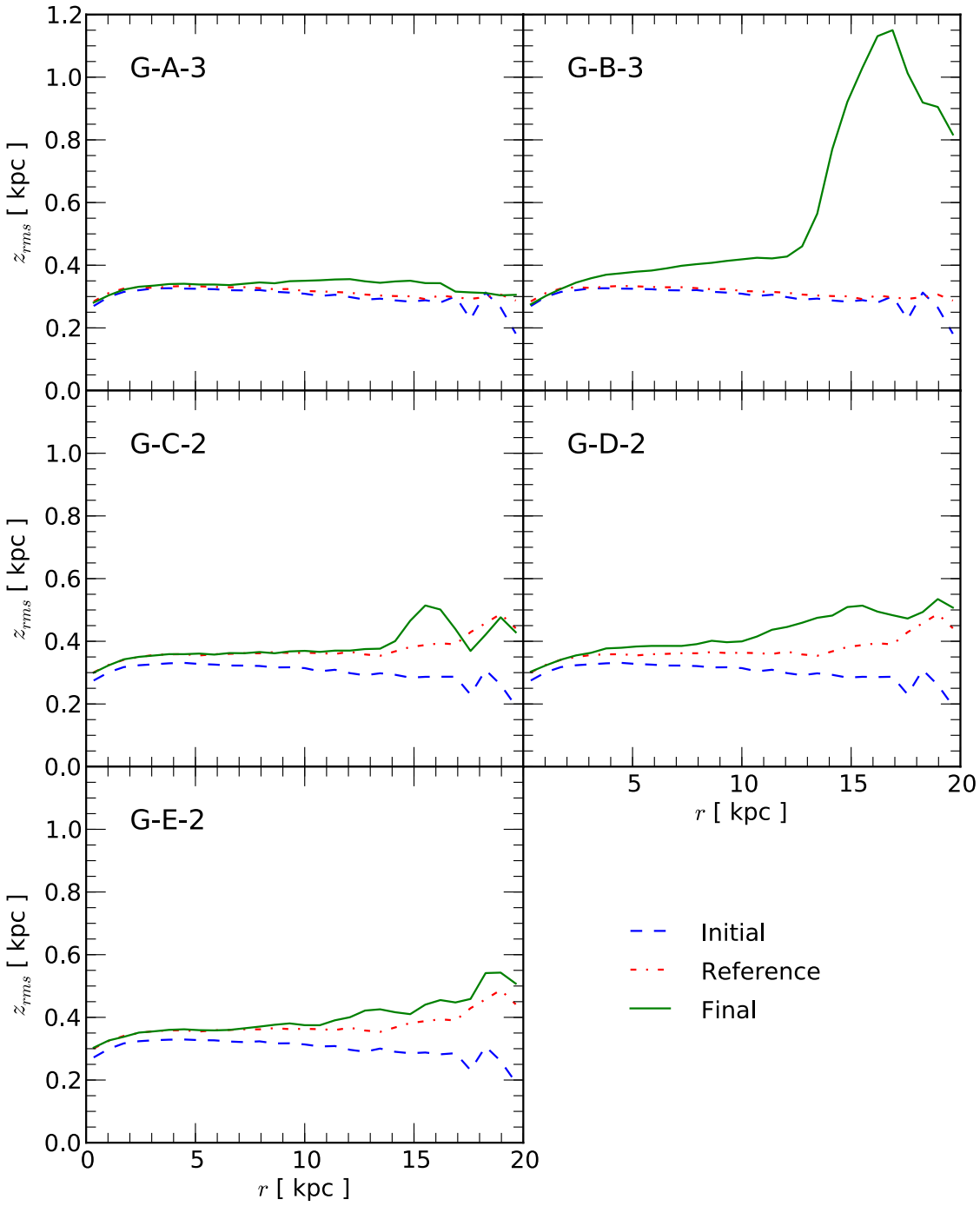

Figure 5.9: The root mean squared thickness of discs as a function of radius. For each simulation the blue dashed line shows the profile of the initial disc thickness. The red dash-dotted line is the disc profile at the end without subhaloes. The solid green line is the final disc thickness when the discs have been bombarded by the different subhalo populations

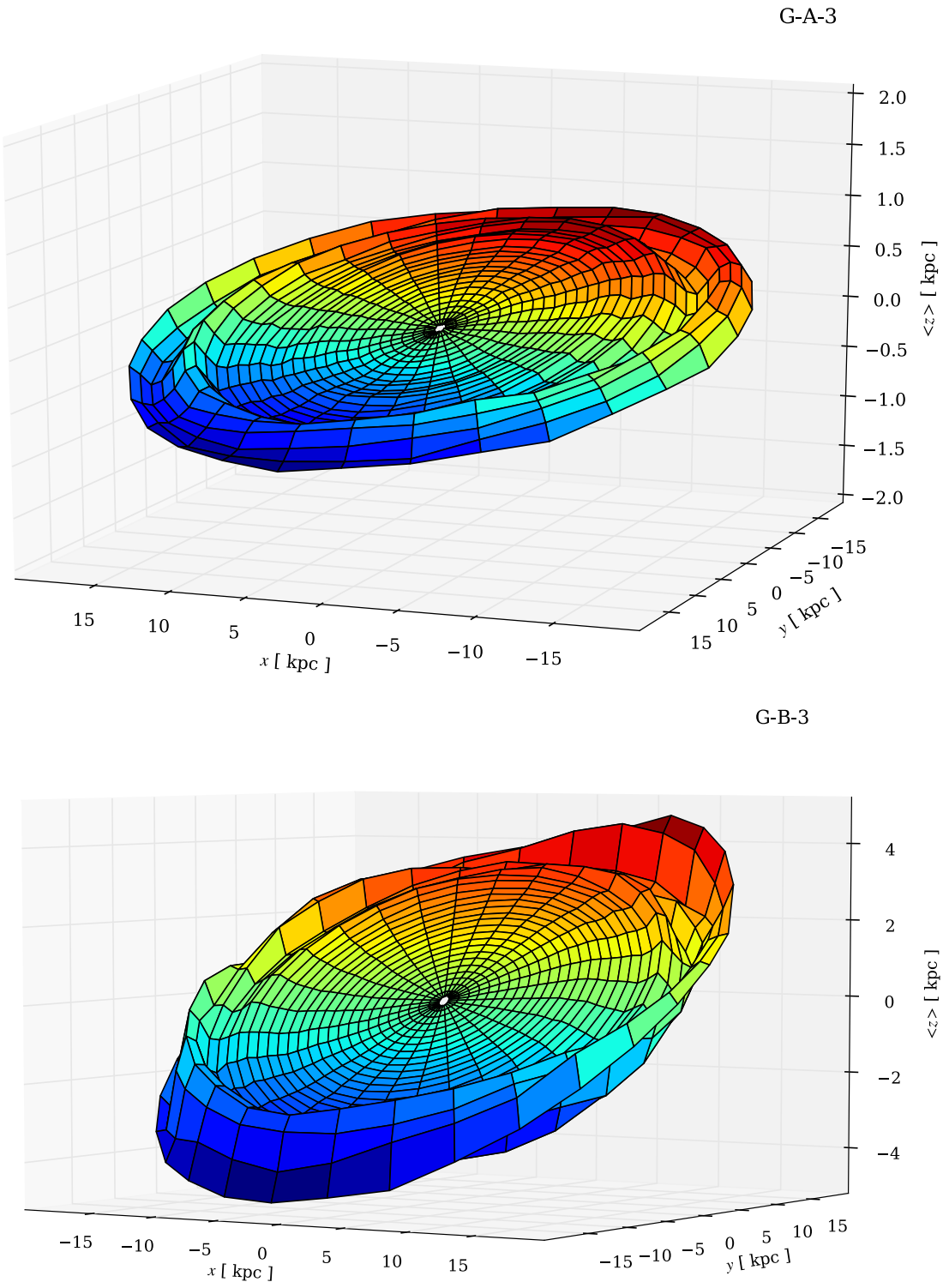

Figure 5.10: Mean height of the disc surface above the mid-plane of its original orientation. *Top panel:* the G-A-3 disc. *Bottom panel:* the G-B-3 disc. The colours emphasise the displacement from the mid-plane, with red representing displacements above the mid-plane and blue below. Note that the vertical scale in the lower plot spans twice the range of that in the upper plot.

sity, so the edges are more responsive to perturbations from subhaloes. Beyond 15 kpc the surface density is less than one percent of that at the centre and the disc surface is not strongly self-bound. It is at these distances from the centre that we see features in the radial profiles of Fig. 5.9. The most notable is the massive bump in the disc of G-B-3, suggesting that the edge of the disc is flared. To a lesser extent similar flares are present in G-C-2 and G-D-2. To understand the origin of these bumps we look at the two high resolution simulations in greater detail. Fig. 5.10 plots how the mean vertical displacement varies over the surface and reveals a host of interesting morphological features at the edges of the discs. In all previous plots we have worked in a frame orientated perpendicular to the disc by diagonalising the moment of inertia tensor; however, in Fig. 5.10 we remain in the initial frame of the disc. In both cases the entire disc has been tilted away from initial orientation, with the tilt of G-B-3 much greater than that of G-A-3.

In both discs there is clear spiral structure in the outer 15 kpc and the tilt does not match the tilt of the inner regions resulting in a warp. In the case of G-A-3 the outer edges are tilted less than the inner disc, while for G-B-3, for which the warp is less obvious, the spiral features in the outer parts tend to be displaced in the direction of a greater tilt. The features in G-A-3 are very subtle and do not show up the radial thickness profile, while for G-B-3 the high amplitude spiral waves are the reason for the flare in its radial profile. Examination of the other simulations finds that their discs all contain similar features, with strengths lying intermediate between the two extremes. The reason for the formation of these spirals and warps is not obvious; it is certainly related to the low surface density. It is likely that as the overall disc is tilted by the subhalo interactions, the inner regions rotate more as a rigid body than the outer regions, where the self gravity is lower. In addition, the stability of the disc may be lower at the edges, making it more prone to formation of transient spiral structure.

5.4 Applying the Benson Model

Finally, the Benson et al. (2004) semi-analytical model of disc heating that formed the topic of the previous chapter has been applied to the five disc simulations. The model estimates disc heating based on the energy lost from the subhalo as it passes through the disc due to dynamical friction. As we discussed, the original simulations used to

Halo	ΔT_z [$10^{10}\mathrm{M}_\odot\mathrm{km}^2\mathrm{s}^{-2}$]	ΔH_z [pc]
G-A-3	21.1 (1%)	3 (1%)
G-B-3	57.6 (3%)	9 (2%)
G-C-2	15.9 (1%)	2 (1%)
G-D-2	113.3 (5%)	17 (4%)
G-E-2	21.5 (1%)	3 (1%)

Table 5.3: The increase in the vertical kinetic energy and the thickness of the discs when bombarded by the subhaloes as predicted by the Benson model for the galaxy model simulations. The changes are given in terms of the absolute increases and as a percentage of the initial energy and thickness (values in parentheses).

demonstrate the success of the model were in fact too low resolution, approximately equal to our level 1 simulations, to actually resolve disc heating, and there were issues with the original implementation that led it to overestimate the heating. Therefore, we apply our new implementation of the Benson model to our set of N-body simulations in whose result we have high confidence. This serves the dual purpose of allowing us to test the validity of the model and enabling us to compare the difference in heating predicted from the same sets of subhaloes that were evolved with and without a disc. The final changes as predicted by the Benson model in the vertical kinetic energy and disc thickness are listed in Table 5.3 and the evolution of the vertical kinetic energy plotted in Fig. 5.11.

For the subhalo orbits and properties measured in the galaxy model simulation, the Benson model predicts less heating than actually occurs. The low resolution simulations G-C-2 – G-E-2, where the results can only be measured to within a few percent, are not a concern. The more problematic issue is that for the G-B-3 disc the model calculates an increase in energy almost a factor of ten smaller than is seen in the simulation. In fact, the biggest increase is now seen in the G-D-2 disc. A comparison of the heating in the simulations and that predicted by the Benson model in chapter 4, where it was applied to the subhalo orbits as they were in the Aquarius simulations, has better agreement, especially for the change in the disc thickness. The reason that the Benson model does not work as well on the actual data from the galaxy model simulations is due to the

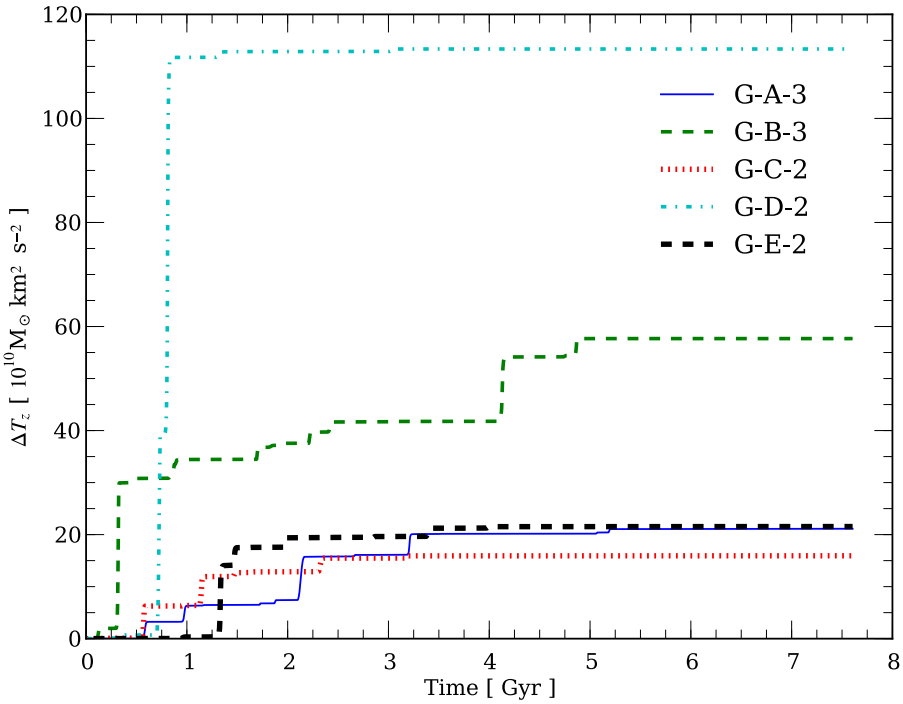

Figure 5.11: The increase in the vertical kinetic energy of a disc predicted by the Benson model for the galaxy model simulations.

reduction in masses of the subhaloes as they interact with the disc. The smaller masses lead the model to underestimate the effects of the impacts. We see a recurrence of the problem that the SUBFIND mass is not a good guide to the effective mass of a subhalo as it passes through the disc and may have a lot of stripped material that is not bound to it, but is still associated with it.

In an attempt to compensate for the underestimation of the mass we have tried using the mass at impact as the mass of the subhalo at its last apocentre before the passage. These masses are much larger, as they include all the material before the subhaloes have undergone any of the tidal stripping experienced on their pericentric passages. However, with this modification the model then hugely overestimated the heating, with the G-B-3 simulation predicting an increase in vertical kinetic energy of over 200 percent, compared to the 17 percent increase that the disc actually gained. We believe that even after modifying the mass there remains the more fundamental problem of the Benson model being too sensitive to the exact location of the impacts. For impacts close to the centre any small change in position leads to a massively different value for the dynam-

ical friction force. This is the problem we discussed in the last chapter, namely that the assumption that dynamical friction can be calculated as if the subhalo were passing through a homogeneous sea of particles is not valid in this case. The properties of the disc change drastically over the scale of the subhaloes. It has to be concluded that the Benson model is not a good guide to predicting subhalo heating. In real interactions such as we simulated there are too many variables that cannot be accurately measured or approximated in an analytical calculation.

It is nevertheless interesting to make the comparison of the change in the heating predicted by the Benson model for the subhalo properties based on the orbits and evolution they had in the Aquarius simulation, and the properties from the disc simulations. Contrasting Fig. 4.8 and Fig. 5.11 it can be noted that the energy increases occur at earlier times in the disc simulations; there is no late time heating, and that early increase in energy in the Aq-D/G-D case is greater in the disc simulation. These differences can again be explained by the shorter lifetime of subhaloes when a disc is present and the focusing effect of the galaxy brings the major impacts closer to the disc centre.

5.5 Conclusions

Our N-body simulations of the interactions between subhaloes extracted from the Aquarius simulations and stellar discs have demonstrated that subhaloes can have substantial effects on the structure of discs. In three out of five of the simulations the effect was minimal, but in the other two considerable heating was seen, with both the vertical thickness and the velocity dispersions in all three directions increased during the interactions. In each of the five haloes a single event was responsible for the majority of the heating, with the most dramatic changes occurring in G-B, when a massive but weakly bound subhalo passed through the disc close to the its centre.

The subhaloes heated the discs in both the vertical and horizontal directions as measured by the change in the velocity dispersions at 8 kpc. In conjunction with this the thickness and vertical kinetic energy of the discs was increased. However, the heating occurred only in short periods during the interactions and not in the continuous manner that would be required to reproduce the age-velocity dispersion relation. This eliminates subhaloes as a possible mechanism for generating the age-velocity dispersion relation.

The short, early heating is more consistent with that needed to form thick discs. While the subhaloes in our samples were insufficient to create discs thick enough to match observed thick discs, it is likely that at earlier times, when massive subhaloes are more numerous, even greater amounts of heating should be expected.

The change in the global disc properties, the thickness and vertical kinetic energy, could only be accurately resolved in our highest resolution level 3 simulations, where the numerical heating was negligible. These simulations contained 5×10^6 disc particles with masses of $8 \times 10^3 \mathrm{M}_\odot$. In the level 1 resolutions, the increase in the vertical thickness of the disc due to numerical heating was far greater in many cases than that expected from the subhaloes, and swamped any signal. The level 2 simulations still showed significant numerical heating, but were of sufficient resolution to broadly classify the amount of subhalo heating.

Compared to previous work, the subhaloes in our simulations are considerably less massive. We therefore do not see such dramatic changes in our discs as those studies which have looked at encounters between subhaloes with masses equal to or greater than the disc (Villalobos and Helmi, 2008; Purcell et al., 2009). Our work is more directly comparable to Read et al. (2008) and Kazantzidis et al. (2008, 2009) who also measured subhalo abundance from cosmological haloes. However, they both found a greater number of massive subhaloes and used these to bombard their discs. The subhalo abundance in the central regions of the Aquarius haloes is much lower, our discs therefore experience very few significant interactions, and only two out of our five haloes show notable heating. We therefore agree with the general consensus that subhaloes can heat discs, but from our sample conclude this is only important at early times and is not significant for every halo.

In addition to simply heating the discs, the subhalo interactions tilted the orientations of the discs and were responsible for the formation of several morphological features in the outer regions. These included flaring, warping and the generation of spiral waves and are similar to those seen in Kazantzidis et al. (2008). The inner regions of the discs were more robust to the encounters and the very central region, protected by the bulge, showed little or no change. Interactions between subhaloes and discs are obviously complicated events that have multiple effects on discs, and even if they do not directly disturb the disc, subhaloes can trigger internal secular evolution.

As well as the subhaloes having an effect on the disc, the disc had a considerable effect on the subhaloes. The additional mass of the galaxy focused the points of impact towards the centre of the disc, but more importantly caused the subhaloes to lose mass more rapidly and so drastically reduced their lifetimes. This meant that each subhalo only made one appreciable passage through the disc.

Applying the Benson et al. (2004) semi-analytical model of disc heating to our simulations found that it failed to estimate the correct changes in disc energies. It must be concluded that the model unfortunately does not provide a good method to estimate subhalo disc heating. The problem is partly due to the difficulty of estimating the correct subhalo mass, but more so to the simplistic assumptions it makes in order to model the dynamical friction.

Chapter 6 | *Conclusions*

6.1 Discussion

The ΛCDM model of galaxy formation has been incredibly successful at predicting and explaining the large scale structure of the universe, so much so that it has become the generally accepted cosmological paradigm. However, on small scales, those of galaxies and below, there remain several challenges for ΛCDM. Unfortunately it is here that the coupling between baryons and dark matter is the most complicated making it difficult to be sure which aspects are due to problems with the dark matter model and which are due to a lack of understanding of the baryonic physics. In this thesis we have focused on one of these problems, namely that of the gravitational interactions of subhaloes with the main halo and its central galaxy. This involves understanding how subhaloes evolve in the tidal field of their host haloes, how they interact with the centre galaxy and what are the visible signatures they leave behind.

N-body simulations have become highly developed and are now the primary tools for understanding the non-linear growth and structure of haloes. In order to probe down to the smallest scales and accurately resolve substructure, very high resolution simulations are required. The Aquarius haloes are the latest generation of simulations of single Milky Way mass haloes with unprecedented resolution and excellent convergence between multiple resolution simulations of the same halo. In chapter 2 we explored the properties of these haloes. The density profiles have been shown to be converged all the way down to the Power et al. (2003) convergence radii, which for the level 2 resolution haloes are within 500 pc of the centre. The central regions are better fitted by an Einasto profile rather than the standard NFW profile.

The ability to reliably probe to these small distances allows us to study the other internal properties of the haloes; one such property is the shape. We have demonstrated that the shape of different resolution simulations of the same haloes agrees well and

we have established a convergence criterion for how near to the centre the shape can be trusted. The haloes tend to be prolate near the centre and become more spherical towards the virial radius. A comparison with a larger selection of similar but lower resolution haloes from the MSII simulations has shown that the Aquarius haloes are fairly typical in most characteristics. They have a diverse range of properties that span the distributions of mass, concentration and spin, yet no one halo is an extreme in all aspects.

The Aquarius simulations show excellent convergence of not just the main haloes but also their subhaloes. Many of the individual subhaloes can be matched between different numerical resolutions of the same halo. This allows detailed convergence studies of the subhalo density profiles, which show that inside their tidal truncation radii, subhaloes can be well fitted by NFW or Einasto profiles and that they can be trusted down to ~ 250 pc. This level of detail and resolution for low mass substructure makes the Aquarius haloes an ideal sample for studying the behaviour of dark matter on small scales.

Unfortunately, the outputs of N-body simulations form huge datasets that can be slow and difficult to process. Often the detailed information in the outputs is not required and there is only interest in the overall structure and evolution of a halo. Analytical profiles are usually used to approximate a halo potential, and while simplistic, have the disadvantages of being spherical and static, and including none of the cosmological evolution real haloes undergo. Instead, in chapter 3, we have developed a new technique, using a basis function expansion to create a time-evolving density/potential approximation of the late growth of simulated N-body dark matter haloes. We demonstrated how the potential of a halo from the Aquarius Project can be accurately represented by a small number of basis functions, and showed that the halo expansion (HEX) method provides a way to replay simulations. The level of accuracy of the technique as well as some of its limitations were explored and it was found that the number of terms included in the expansion must be sufficient to resolve the large-scale distribution and shape of the halo, but beyond this, additional terms give little further improvement.

Particle and subhalo orbits can be integrated in this realistic, time-varying halo potential approximation, at much lower computational cost than the original simulation, with high fidelity for many individual orbits, and a good match to the distributions of orbital energy and angular momentum. Statistically, the evolution of structural sub-

halo properties, such as mass, half-mass radius and characteristic circular velocity, are very well reproduced in the halo expansion approximation over several gigayears. The method represents a significant improvement over commonly used techniques based on static analytical descriptions of the halo potential.

The HEX technique has allowed us to look at the orbits of subhaloes and follow their evolution in the tidal field of the main halo. It was found that their mass stripping primarily depends only on the radial component of the potential and not the angular part, so that the shape of the halo is unimportant. This is relevant for any work that assumes a profile, since using the wrong analytical halo profile will completely change the subhalo evolution. The HEX does not reliably reproduce exact orbits of the simulation, so is not the best way to reconstruct particular subhalo orbits. Therefore, its usefulness for the second part of this thesis proved to be limited. It is more suited for many other problems where it is potentially a very powerful tool. Some of these are discussed in the next subsection on future directions.

In the second half of the thesis we focused on the gravitational interactions between substructure and stellar discs. Subhaloes have been suggested as one of the mechanisms, in addition to others such as molecular clouds and spiral waves, that could be the cause of the observed age-velocity dispersion in the stars around the sun. Subhalo interactions with discs have also been proposed as a way to explain the formation of thick discs. In order to know the frequency and parameters of the disc-subhalo interactions we used the Aquarius haloes to study the abundance of subhaloes passing through the central 20 kpc region of five of the haloes. In the period from $z = 1$ to $z = 0$ there were very few massive subhaloes ($\sim 10^{10}\mathrm{M}_{\odot}$) in any of our five haloes, just one or two in most cases and with maximum masses that varied by a factor ~ 4 between the haloes. Therefore, we find that there would be very few late time impacts on a disc in the Aquarius haloes.

In chapter 4, we have tested the Benson et al. (2004) semi-analytical model to estimate the heating of a disc that subhaloes in the Aquarius simulation could generate. A critical examination of the model revealed some errors in the original implementation that leads it to overestimate the heating. We created a new implementation and found that it predicts a factor of $\sim 2 - 4$ less heating than the original implementation. As well as the problems in the code, there are also questions about the validity of the model. Benson et al. (2004) used a set of test simulations to calibrate the model. However, as

evidenced by work in chapter 5, these simulations are too low resolution to be able to disentangle the subhalo heating from the artificial numerical heating. Since our new implementation differs from the original and the Benson test simulations are insufficient resolution to properly evaluate the model, we applied it to our own set of simulations of subhalo-disc encounters to more conclusively assess its validity. The model was found not to accurately predict the heating. It must be concluded that the Benson model does not sufficiently capture the complexity of the interactions to be able to predict the heating effect of subhaloes on discs. The model's greatest flaw is that it approximates the dynamical friction force on the subhaloes based on the properties of the disc at a single point. This makes the model too sensitive to the location of the subhalo impacts on the disc, particularly for impacts close to the centre.

To address the problem of disc heating by subhaloes, in chapter 5, the same sets of subhaloes extracted from the Aquarius simulations were placed into high resolution N-body simulations including a disc galaxy and evolved for 8 Gyr. This allowed a direct measurement of the effect the subhaloes had on the disc. It was found that in two of the haloes no significant heating occurred; in haloes Aq-A and Aq-D there were small increases in the vertical kinetic energy and disc thickness; and in only one of the simulations, that containing the Aq-B subhaloes, was there a significant effect on the disc. The vertical kinetic energy was increased by 17 percent and the thickness by 44 percent.

The subhalo-disc simulations were run at three resolutions. In the lowest level, a resolution comparable to that used by Benson et al. (2004), due to the high level of numerical heating, it was impossible to tell how much extra heating the subhaloes contributed. In the intermediate, level 2 simulations, the artificial heating was slightly reduced, but still too high to accurately measure the subhalo heating. The simulations do have sufficient resolution to judge the overall effect of the subhaloes, but not to quantify the result. It was only in our highest resolution simulations that the exact change in the disc properties could be confidently measured. Unfortunately, none of the results from the different levels agreed, making it difficult to know if we have reached convergence. However, the noise in the high resolution simulations is negligible, so we are confident that increasing the resolution further would have little effect on the results.

Compared to previous simulations of disc-subhalo encounters, we find much lower heating of our discs. The main reason for this is that the subhaloes used to heat our

discs are a lot less massive than those considered by others (Villalobos and Helmi, 2008; Read et al., 2008; Kazantzidis et al., 2008, 2009; Purcell et al., 2009). We agree with the consensus that sufficiently massive subhaloes will have a significant effect, but differ in the number of such subhaloes that can expected. The populations of subhaloes came directly from the cosmological Aquarius haloes. There are some indications that the Aquarius haloes might be slightly quieter than the average. As discussed in chapter 2, Boylan-Kolchin et al. (2010) find that four of the Aquarius haloes are within the quietest ~ 15 percent of all similar mass haloes in terms of their most massive central merger since $z = 2$. However, since we have only considered late time interactions, those between $z = 1$ and $z = 0$, it is not obvious that the results of earlier times are relevant. The abundance of the Aq-B halo, shown by Boylan-Kolchin et al. (2010) to be more typical, is similar to that of the Aq-D halo even though Aq-D is meant to be one of the quiet haloes.

The type of heating that we observed in our simulations is not consistent with that needed to reproduce the age-velocity dispersion relation seen in the Milky Way. Older stars are found to have greater velocity dispersions in all three directions in the solar neighbourhood, with the variation being continuous with age. The heating in our simulations is sudden and brief, with the majority occurring as the subhaloes pass through the disc. It therefore seems that subhaloes are not good candidates to explain this relation. Subhalo bombardment of a disc could, however, be responsible for the formation of thick discs. All heating in our simulations occurred near the beginning. At earlier times, more massive subhaloes are expected to be more numerous, therefore at times before $z = 1$, it is plausible that sufficient substructure could have impacted the disc to cause even greater heating. At late times, not enough subhaloes survive to affect a disc. This is further reinforced by our finding that discs destroy subhaloes, thus further depleting the abundance in the central regions at later times.

6.2 Future Directions

The HEX technique is a powerful tool whose full potential has not yet been explored. While it was not ideally suited for the problem of disc heating, there are several other challenges to which we plan to apply it. The technique excels at problems that involve the evolution of objects in a realistic potentials, when reproducing the exact evolution

of a pre-existing object is not required. As we have shown, it reproduces the overall evolution of the population of subhaloes. It would therefore allow us to place generic subhaloes into the simulations and follow their development. The computational efforts can be focused on the subhaloes and much higher resolution objects can be tracked. This allows high mass subhaloes to be followed for much longer and for their eventual fate to be determined, or lower mass subhaloes could be placed in the simulation in order to test the mass function of substructure down to limits lower than have been previously resolved in simulations. Alternatively, rather than looking at the substructures, the fate of the material that is tidally stripped from them and forms streams can be tracked.

The other strand of work we intend to pursue is to further utilise our disc simulations. A large amount of computational effect has been invested into our disc-subhalo simulations and they still have huge untapped potential. The simulations are some of the highest resolution examples available of disc-subhalo encounters. We plan to run the other three haloes Aq-C – E at level 3 to complete the set. With five simulations there are several obvious features for further analysis. Two extensions that would be simple to look at are the radial migration of particles in the disc and the evolution of the eccentricity of disc stars.

Bird et al. (2011) looked at the radial migration of stars in the simulations of Kazantzidis et al. (2008). They find that subhalo perturbations can drive particles to migrate outwards and that this appears to be a distinct mechanism for inducing radial migration, in addition to migration induced by bars and spiral structure. We plan to examine if there is similar migration in our simulations, and to see if the effect depends on the resolution. The other point of interest is to look at the change in the orbital eccentricities of the disc particles after the subhalo impacts. This has been suggested as a way of discriminating between different thick disc formation scenarios. Sales et al. (2009) compared the final distribution of eccentricity in one of the Villalobos and Helmi (2008) simulations to several other thick disc formation scenarios. This involved a massive subhalo-disc interaction. It would be interesting to see if the distributions of eccentricity in our simulations of less dramatic interactions are consistent with their prediction that there should be a high eccentricity accreted component and lower eccentricity in-situ component.

Appendix A

Generating Halo Realizations

A.1 Introduction

An isolated, equilibrium N-body realization of a spherical halo can be created for a given profile through Monte Carlo sampling of its distribution function (DF). Unfortunately, finding the phase-space distribution functions is generally difficult to accomplish, and the problem cannot usually be solved analytically. There are only very few simple profiles, including the Plummer sphere, the Hernquist and the Jaff profiles, that have analytical answers; usually the DF has to be solved numerically.

Rather than finding the DF, an alternative method frequently used is based on the local Maxwellian approximation. This method involves approximating the velocity distribution at a given point in space by a multivariate Gaussian. However, it has been shown that this technique fails when used for creating high-resolution initial conditions of haloes. Near the centre velocity profiles often become strongly non-Gaussian and models built using the local Maxwellian approximation are found to be far from equilibrium at the centre and to rapidly relax away from their initial form.

Kazantzidis et al. (2004b) devise an algorithm for creating realisations using the phase-space DF for a general form of spherical density profiles. Models constructed using this method are claimed to be in equilibrium and not to suffer the same problems as those from the Maxwellian approach. We have implemented their algorithm and employ it to create N-body realisations of haloes. The method is briefly outlined below, along with some tests of the equilibrium of the resulting haloes.

A.2 Method

A.2.1 The Density Profile

The two parameter formula

$$\rho(r) = \frac{\rho_s}{(r/r_s)^\gamma [1 + (r/r_s)^\alpha]^{(\beta-\gamma)/\alpha}} \tag{A.1}$$

can be used to describe a large family of density profiles, including popular ones such as the Hernquist profile $(\alpha, \beta, \gamma) = (1, 4, 1)$ and the NFW profile $(\alpha, \beta, \gamma) = (1, 3, 1)$. ρ_s sets the characteristic inner density and r_s the scale radius. γ controls the inner slope, β the outer slope and α the sharpness of the transition between the two. For $\beta \leq 3$ the cumulative mass profile diverges as $r \to \infty$, so the profile must be truncated at some large distance $r > r_{vir}$. A sharp truncation would lead to unphysical models so Kazantzidis et al. (2004b) use an exponential cutoff for $r > r_{vir}$, as suggested in Springel and White (1999). This cutoff has the form

$$\rho(r) = \frac{\rho_{\rm s}}{c^\gamma (1 + c^\alpha)^{(\beta-\gamma)/\alpha}} \left(\frac{r}{r_{\rm vir}}\right)^\epsilon \exp\left(-\frac{r - r_{\rm vir}}{r_{\rm decay}}\right), \tag{A.2}$$

where r_{decay} is the scale on which the density falls away. $c \equiv r_{vir}/r_s$ is the concentration parameter and ϵ is set as

$$\epsilon = \frac{-\gamma - \beta c^\alpha}{1 + c^\alpha} + \frac{r_{\rm vir}}{r_{\rm decay}}, \tag{A.3}$$

to ensure a smooth transition between the two sections of the profile.

A.2.2 Solving the Distribution Function

The distribution function is the solution to the collisionless Boltzmann equation and describes the phase space density of a halo. For the purpose of sampling it can be considered as the probability of a particle occupying a particular volume in phase space. In general the collisionless Boltzmann equation cannot be solved, since it involves seven independent variables. However, in the static equilibrium case the Jeans theorem (Binney and Tremaine, 1987; Lynden-Bell, 1962) shows that the solution depends on the phase-space coordinates only through the integrals of the motion, and that for spherical state systems the DF can be expressed as a function $f(\mathcal{E}, \boldsymbol{L})$, where $\mathcal{E}$ is the binding energy per unit mass and $\boldsymbol{L}$ the angular momentum vector per unit mass.

In Kazantzidis et al. (2004b) they restrict their attention to DFs of the form $f = f(Q)$ where

$$Q \equiv \mathcal{E} - \frac{L^2}{2r_a^2}. \tag{A.4}$$

These are known as Osipkov-Merritt models (Osipkov, 1979; Merritt, 1985b,a) and with the additional constraint $f(Q) = 0$ for $Q \leq 0$, are a special class of non-rotating spherical halo models. They have a velocity dispersion of the form

$$\beta(r) \equiv 1 - \frac{\sigma_\theta^2}{\sigma_r^2} = \frac{r^2}{r^2 + r_{\rm a}^2}. \tag{A.5}$$

where r_a is known as the anisotropy radius. Inside r_a, $\beta \to 0$ and the velocity dispersion is nearly isotropic, while outside r_a it becomes increasingly more radially anisotropic. The DF is then given as

$$f(Q) = \frac{1}{\sqrt{8}\pi^2}\left[\int_0^Q \frac{d^2\rho_Q}{d\psi^2}\frac{d\psi}{\sqrt{Q-\psi}} + \frac{1}{\sqrt{Q}}\left(\frac{d\rho_Q}{d\psi}\right)_{\psi=0}\right], \tag{A.6}$$

where $\rho_Q(r) \equiv \rho(r)(1 + r^2/r_{\rm a}^2)$, and $\psi(r) = -\Phi(r)$ is the relative gravitational potential. For any reasonable density profile the second term vanishes and will therefore be ignored from now on.

Restricting attention to DFs of this form and the above two parameter density profile, the integrand of Eq A.6 can be rewritten in a form that can finally be numerically integrated. The first factor in the integrand can be changed to a derivative in r by the chain rule

$$\frac{d^2\rho_Q}{d\psi^2} = \frac{d^2\rho_Q}{dr^2}\left(\frac{d\psi}{dr}\right)^{-2} - \frac{d\rho_Q}{dr}\left(\frac{d\psi}{dr}\right)^{-3}\frac{d^2\psi}{dr^2} \tag{A.7}$$

with

$$\frac{d\rho_Q}{dr} = \frac{d\rho}{dr}\left(1 + \frac{r^2}{r_a^2}\right) + \frac{2r}{r_a^2}\rho \tag{A.8}$$

and

$$\frac{d^2\rho_Q}{dr^2} = \frac{d^2\rho}{dr^2}\left(1 + \frac{r^2}{r_a^2}\right) + \frac{4r}{r_a^2}\frac{d\rho}{dr} + \frac{2}{r_a^2}\rho. \tag{A.9}$$

The derivatives of the relative potential ψ can be found from Poisson's equation, and written as

$$\frac{d\psi}{dr} = -\frac{GM(<r)}{r^2} \tag{A.10}$$

and

$$\frac{d^2\psi}{dr^2} = -4\pi G\rho - \frac{2}{r}\frac{d\psi}{dr} \tag{A.11}$$

where the mass enclosed within r is

$$M(<r) = \int_0^r 4\pi r^2 \rho dr \tag{A.12}$$

The relative potential ψ can partially be solved by integration by parts, but the second term has to be numerically integrated

$$\psi = \frac{GM(<r)}{r} - \int_\infty^r 4\pi G r \rho dr \tag{A.13}$$

Finally, the derivatives of the density profile for $r \leq r_{vir}$ are

$$\frac{d\rho}{dr} = -\frac{\rho_s}{r_s(r/r_s)^\gamma[1+(r/r_s)^\alpha]^{(\beta-\gamma)/\alpha}}\left[\frac{\gamma}{(r/r_s)} + \frac{\beta-\gamma}{(r/r_s)^{1-\alpha}[1+(r/r_s)^\alpha]}\right] \tag{A.14}$$

$$\frac{d^2\rho}{dr^2} = \frac{\rho_s}{r_s(r/r_s)^\gamma[1+(r/r_s)^\alpha]^{(\beta-\gamma)/\alpha}}\left[\frac{\gamma(\gamma+1)}{(r/r_s)^2} + \frac{(\beta-\gamma)(2\gamma-\alpha+1)}{(r/r_s)^{2-\alpha}[1+(r/r_s)^\alpha]} + \frac{(\beta-\gamma)(\beta-\gamma+\alpha)}{(r/r_s)^{2(1-\alpha)}[1+(r/r_s)^\alpha]^2}\right] \tag{A.15}$$

and for $r > r_{vir}$

$$\frac{d\rho}{dr} = \frac{\rho_s}{c^\gamma(1+c^\alpha)^{(\beta-\gamma)/\alpha}}\left(\frac{r}{r_{vir}}\right)^\epsilon\left[\frac{\epsilon}{r} - \frac{1}{r_{decay}}\right]\exp\left(-\frac{r-r_{vir}}{r_{decay}}\right) \tag{A.16}$$

$$\frac{d^2\rho}{dr^2} = \frac{\rho_s}{c^\gamma(1+c^\alpha)^{(\beta-\gamma)/\alpha}}\left(\frac{r}{r_{vir}}\right)^\epsilon\left[\frac{\epsilon(\epsilon-1)}{r^2} - \frac{2\epsilon}{r_{decay}r} + \frac{1}{r_{decay}^2}\right]\exp\left(-\frac{r-r_{vir}}{r_{decay}}\right) \tag{A.17}$$

This finally achieves an expression in terms of r, $M(r)$, $\psi(r)$ and $d\psi/dr$ that can be numerically integrated. However, the DF Eq A.6 has an integrable singularity at $\psi = Q$. This is best dealt with by changing variable to $\psi = Q\sin^2 x$. The integral then becomes

$$f(Q) = \frac{2\sqrt{Q}}{\sqrt{8}\pi^2}\int_0^{\pi/2}\frac{d^2\rho_Q}{d\psi^2}\sin x dx \tag{A.18}$$

The factor $d^2\rho_Q/d\psi^2$ still remains as a function of r, so during the numerical integration, at each x point evaluated it is necessary to find the corresponding r. Unfortunately this cannot be done analytically, but instead both r and ψ can be tabulated on a grid and then linearly interpolated from ψ to r as required. Similarly, in order to reduce computational time, the other qualities that can only be solved by numerical integration, $M(r)$, $\psi(r)$ and $d\psi/dr$, are tabulated and interpolated as needed. The grid points are chosen to be uniformly spaced in $\log r$ from $r_{min} = 10^{-6}r_s$ to $r_{max} = 10^5 r_s$ for $\beta > 3$ and $r_{max} = r_{vir} + 10^3 r_{decay}$ for $\beta \leq 3$. It has been found that 10^4 points are sufficiently

closely spaced to give an accuracy of better than 10^{-5} in the potential when tested for the Hernquist profile.

Having a fixed r_{max} and r_{min} where the potential is calculated, imposes a ψ_{min} and ψ_{max}. This does not prove to be a problem for either of the limits. ψ_{max} is only required to calculate $f(Q)$ for the largest values of Q. These correspond to particles very near the centre of the potential, within r_{min}, which are also at rest. This is a negligible volume in phase space. Similarly, the ψ_{min} limit affects the lower limit of the integral of the DF. Instead of integrating from zero, we can now only integrate from ψ_{min}. The integral of $f(Q)$ is slightly underestimated; however, only for Q values very close to ψ_{min} is this significant and noticeable. Particles with velocity very near to the escape velocity may be slightly undersampled, but again this is a very small region of phase space.

Evaluating the DF for each value of Q is an expensive operation, instead $f(Q)$ is tabulated at 10^4 points equally spaced in $\log Q$. Linear interpolation in $\log Q$ is used to find $\log f(Q)$. Logarithmic space is employed as the DF is smoother there, allowing more accurate interpolation. It is most important that high accuracy is achieved nearer Q_{max} as $f(Q)$ is most rapidly changing here. There must be sufficient points in this region for the interpolation, otherwise generated halos are not in equilibrium at their centre and rapidly relax away from their initial state. A comparison with the exact analytic DF of the Hernquist model (Hernquist, 1990) obtains an accuracy of better than 10^{-5}, the same level as was achieved in the original paper.

A.2.3 Sampling the Distribution Function

After obtaining the DF it is rejection sampled to create a halo realization. This is a two-step process: first the density distribution is sampled to choose the particle positions, and subsequently the full DF used to choose an appropriate velocity at each position.

The density distribution can be sampled in two ways: either by choosing points at random or by deforming a lattice. The first method involves randomly selecting a mass between zero and M_{max} and then solving for the radius at which this mass is enclosed. A direction is then chosen at random and the particle placed at the calculated radius. By using the cumulative mass function one automatically includes both the density distribution and the density of states at each radius. Each particle is given a mass of M_{total}/n, where n is the number of sample particles.

The alternative method involves initially placing the sample particles uniformly on a three-dimensional lattice. $6n/\pi$ particles are placed in a cubic box and any that lie outside the unit sphere are discarded. This results in approximately n samples equally spaced in the three orthogonal directions. For each lattice particle the fraction of the particles within the sphere bounded by that particle is proportional to the fraction of the total mass within the sphere. Each particle radius can then be scaled to the profile radius within which the same mass is enclosed. This second method has the advantage of resulting in a distribution with a much lower Poisson noise.

For each particle the potential of the particle at its position sets the range that Q can take from zero to $Q_{max} = \psi$. This limits the magnitude of the velocity this particle can take to between zero and $v_{esc} = \sqrt{2\psi}$. We can understand this when it is considered that the halo is in equilibrium so can contain no particles with velocities greater than the escape velocity. Velocities within an ellipsoid with axes lengths v_{esc} in the radial direction and $v_{esc}/\sqrt{(1+(r/r_a)^2)}$ in the tangential direction are randomly chosen. Selecting velocities only within this range automatically ensures the correct velocity dispersion. Finally the Q value of this particle can be calculated and rejection sampled. If $f(Q) > x f_{max}(Q)$, where x is a random number in the interval $[0, 1)$, the velocity is rejected. If rejected, a new velocity is selected and tested. This process is repeated until all particles have been assigned acceptable velocities.

A.3 Tests

Our implementation of the Kazantzidis et al. (2004b) algorithm has been tested by generating the initial conditions for two different halo models. These were then simulated in isolation for 3 Gyrs and checked for any evolution away from their initial state. The first model that was used contained $995,297$ particles, based on a Hernquist profile with a scale radius of 30 kpc, a mass of $10^{12} M_{\odot}$ and an anisotropy radius of 40 kpc. GADGET-3 was used to perform the simulations and a fixed inter-particle softening length of 1 kpc was employed. The left panels in Fig A.1 show the results of this test. The top panel is the spherically averaged radial density profile. It can be clearly seen that outside of the softening length the halo shows no change in its density profile. At radii smaller than the softening length within 1 Gyr, the density profile relaxes to a flatter profile which is

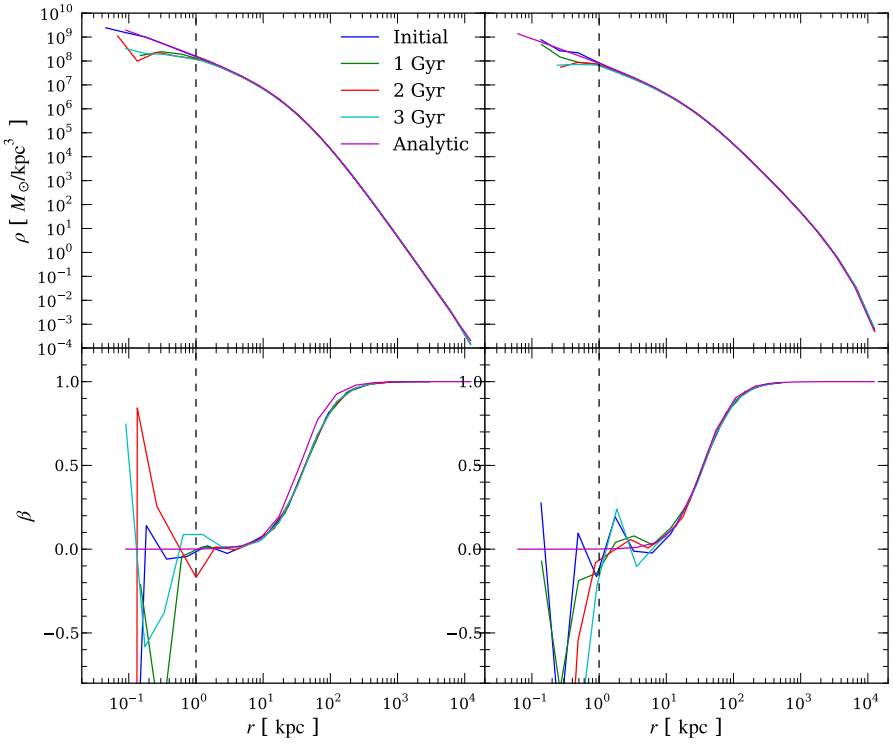

Figure A.1: *Top Left:* Radial density profile of a halo set up to initially follow a Hernquist profile and then evolved in isolation for 3 Gyrs. *Bottom Left:* The evolution of the velocity anisotropy of the Hernquist halo. *Top Right:* Radial density profile of a halo initially following an NFW profile. *Bottom Right:* Velocity anisotropy of NFW model. The dashed line marks the softening length used in the simulations.

then maintained; however, numerical convergence is not expected in this region (Power et al., 2003). The velocity anisotropy is also stable over the period of the simulations, but shows larger noise near the centre, which is present even in the initial conditions out to 4 kpc.

Secondly, we tested the initial conditions of a halo based on the NFW profile with a scale radius of 25 kpc, virial radius 250 kpc, virial mass of $10^{12} M_{\odot}$ and an anisotropy radius of 35 kpc. The right panels of Fig A.1 shows the results. Since an NFW profile has $\beta = 3$ and consequently has infinite mass, it is necessary to use an exponential cut-off at large radii. However, it was found that choosing too small decay radius caused an overly sudden truncation, resulting in a negative DF. The form of the current choice of the density cutoff is discontinuous in the second derivative. In order to smooth out this discontinuity and obtain a physically meaningful DF, r_{decay} was set to 2.5 Mpc. An

alternative cutoff function which is continuous at the virial radius in both first and second derivatives might be less problematic. Increasing the decay radius achieved a stable halo.

Bibliography

Abadi, M. G., Navarro, J. F., Fardal, M., Babul, A., and Steinmetz, M.: 2010, MNRAS **407**, 435

Abadi, M. G., Navarro, J. F., Steinmetz, M., and Eke, V. R.: 2003, ApJ **597**, 21

Abramowitz, M. and Stegun, I. A.: 1964, *Handbook of Mathematical Functions with Formulas, Graphs, and Mathematical Tables*, Chapt. 22, Dover, New York, ninth dover printing, tenth gpo printing edition

Adams, F. C. and Bloch, A. M.: 2005, ApJ **629**, 204

Adelman-McCarthy, J. K., Agüeros, M. A., Allam, S. S., Allende Prieto, C., Anderson, K. S. J., Anderson, S. F., Annis, J., Bahcall, N. A., Bailer-Jones, C. A. L., Baldry, I. K., Barentine, J. C., Bassett, B. A., Becker, A. C., Beers, T. C., Bell, E. F., Berlind, A. A., Bernardi, M., Blanton, M. R., Bochanski, J. J., Boroski, W. N., Brinchmann, J., Brinkmann, J., Brunner, R. J., Budavári, T., Carliles, S., Carr, M. A., Castander, F. J., Cinabro, D., Cool, R. J., Covey, K. R., Csabai, I., Cunha, C. E., Davenport, J. R. A., Dilday, B., Doi, M., Eisenstein, D. J., Evans, M. L., Fan, X., Finkbeiner, D. P., Friedman, S. D., Frieman, J. A., Fukugita, M., Gänsicke, B. T., Gates, E., Gillespie, B., Glazebrook, K., Gray, J., Grebel, E. K., Gunn, J. E., Gurbani, V. K., Hall, P. B., Harding, P., Harvanek, M., Hawley, S. L., Hayes, J., Heckman, T. M., Hendry, J. S., Hindsley, R. B., Hirata, C. M., Hogan, C. J., Hogg, D. W., Hyde, J. B., Ichikawa, S.-i., Ivezić, Ž., Jester, S., Johnson, J. A., Jorgensen, A. M., Jurić, M., Kent, S. M., Kessler, R., Kleinman, S. J., Knapp, G. R., Kron, R. G., Krzesinski, J., Kuropatkin, N., Lamb, D. Q., Lampeitl, H., Lebedeva, S., Lee, Y. S., Leger, R. F., Lépine, S., Lima, M., Lin, H., Long, D. C., Loomis, C. P., Loveday, J., Lupton, R. H., Malanushenko, O., Malanushenko, V., Mandelbaum, R., Margon, B., Marriner, J. P., Martínez-Delgado, D., Matsubara, T., McGehee, P. M., McKay, T. A.,

Meiksin, A., Morrison, H. L., Munn, J. A., Nakajima, R., Neilsen, Jr., E. H., Newberg, H. J., Nichol, R. C., Nicinski, T., Nieto-Santisteban, M., Nitta, A., Okamura, S., Owen, R., Oyaizu, H., Padmanabhan, N., Pan, K., Park, C., Peoples, Jr., J., Pier, J. R., Pope, A. C., Purger, N., Raddick, M. J., Re Fiorentin, P., Richards, G. T., Richmond, M. W., Riess, A. G., Rix, H.-W., Rockosi, C. M., Sako, M., Schlegel, D. J., Schneider, D. P., Schreiber, M. R., Schwope, A. D., Seljak, U., Sesar, B., Sheldon, E., Shimasaku, K., Sivarani, T., Smith, J. A., Snedden, S. A., Steinmetz, M., Strauss, M. A., SubbaRao, M., Suto, Y., Szalay, A. S., Szapudi, I., Szkody, P., Tegmark, M., Thakar, A. R., Tremonti, C. A., Tucker, D. L., Uomoto, A., Vanden Berk, D. E., Vandenberg, J., Vidrih, S., Vogeley, M. S., Voges, W., Vogt, N. P., Wadadekar, Y., Weinberg, D. H., West, A. A., White, S. D. M., Wilhite, B. C., Yanny, B., Yocum, D. R., York, D. G., Zehavi, I., and Zucker, D. B.: 2008, ApJS **175**, 297

Alard, C.: 2000, *ArXiv Astrophysics e-prints*

Allen, S. W., Schmidt, R. W., Fabian, A. C., and Ebeling, H.: 2003, MNRAS **342**, 287

Allgood, B., Flores, R. A., Primack, J. R., Kravtsov, A. V., Wechsler, R. H., Faltenbacher, A., and Bullock, J. S.: 2006, MNRAS **367**, 1781

Altay, G., Colberg, J. M., and Croft, R. A. C.: 2006, MNRAS **370**, 1422

Angulo, R. E., Lacey, C. G., Baugh, C. M., and Frenk, C. S.: 2009, MNRAS **399**, 983

Angulo, R. E. and White, S. D. M.: 2010, MNRAS **401**, 1796

Aragón-Calvo, M. A., van de Weygaert, R., Jones, B. J. T., and van der Hulst, J. M.: 2007, ApJ **655**, L5

Ardi, E., Tsuchiya, T., and Burkert, A.: 2003, ApJ **596**, 204

Aubert, D. and Pichon, C.: 2007, MNRAS **374**, 877

Aubert, D., Pichon, C., and Colombi, S.: 2004, MNRAS **352**, 376

Aumer, M. and Binney, J. J.: 2009, MNRAS **397**, 1286

Babcock, H. W.: 1939, *Lick Observatory Bulletin* **19**, 41

Bailin, J. and Steinmetz, M.: 2004, ApJ **616**, 27

Bailin, J. and Steinmetz, M.: 2005, ApJ **627**, 647

Barbanis, B. and Woltjer, L.: 1967, ApJ **150**, 461

Barnes, J. and Hut, P.: 1986, Nature **324**, 446

Battaglia, G., Helmi, A., Morrison, H., Harding, P., Olszewski, E. W., Mateo, M., Freeman, K. C., Norris, J., and Shectman, S. A.: 2005, MNRAS **364**, 433

Belokurov, V., Zucker, D. B., Evans, N. W., Gilmore, G., Vidrih, S., Bramich, D. M., Newberg, H. J., Wyse, R. F. G., Irwin, M. J., Fellhauer, M., Hewett, P. C., Walton, N. A., Wilkinson, M. I., Cole, N., Yanny, B., Rockosi, C. M., Beers, T. C., Bell, E. F., Brinkmann, J., Ivezić, Ž., and Lupton, R.: 2006, ApJ **642**, L137

Belokurov, V., Zucker, D. B., Evans, N. W., Kleyna, J. T., Koposov, S., Hodgkin, S. T., Irwin, M. J., Gilmore, G., Wilkinson, M. I., Fellhauer, M., Bramich, D. M., Hewett, P. C., Vidrih, S., De Jong, J. T. A., Smith, J. A., Rix, H.-W., Bell, E. F., Wyse, R. F. G., Newberg, H. J., Mayeur, P. A., Yanny, B., Rockosi, C. M., Gnedin, O. Y., Schneider, D. P., Beers, T. C., Barentine, J. C., Brewington, H., Brinkmann, J., Harvanek, M., Kleinman, S. J., Krzesinski, J., Long, D., Nitta, A., and Snedden, S. A.: 2007, ApJ **654**, 897

Bensby, T., Zenn, A. R., Oey, M. S., and Feltzing, S.: 2007, ApJ **663**, L13

Benson, A. J., Lacey, C. G., Baugh, C. M., Cole, S., and Frenk, C. S.: 2002, MNRAS **333**, 156

Benson, A. J., Lacey, C. G., Frenk, C. S., Baugh, C. M., and Cole, S.: 2004, MNRAS **351**, 1215

Bett, P., Eke, V., Frenk, C. S., Jenkins, A., Helly, J., and Navarro, J.: 2007, MNRAS **376**, 215

Bett, P., Eke, V., Frenk, C. S., Jenkins, A., and Okamoto, T.: 2010, MNRAS **404**, 1137

Bett, P. E.: 2011, *ArXiv e-prints*

Binney, J.: 1977, MNRAS **181**, 735

Binney, J. and Tremaine, S.: 1987, *Galactic Dynamics*, Princeton University Press, 1st edition

Binney, J. and Tremaine, S.: 2008, *Galactic Dynamics: Second Edition*, Princeton University Press

Bird, J. C., Kazantzidis, S., and Weinberg, D. H.: 2011, *ArXiv e-prints*

Bosma, A.: 1978, *Ph.D. thesis*, PhD Thesis, Groningen Univ., (1978)

Bournaud, F., Elmegreen, B. G., and Martig, M.: 2009, ApJ **707**, L1

Boylan-Kolchin, M., Bullock, J. S., and Kaplinghat, M.: 2011, MNRAS **415**, L40

Boylan-Kolchin, M., Ma, C., and Quataert, E.: 2008, MNRAS **383**, 93

Boylan-Kolchin, M., Springel, V., White, S. D. M., and Jenkins, A.: 2010, MNRAS **406**, 896

Boylan-Kolchin, M., Springel, V., White, S. D. M., Jenkins, A., and Lemson, G.: 2009, MNRAS **398**, 1150

Brook, C. B., Kawata, D., Gibson, B. K., and Freeman, K. C.: 2004, ApJ **612**, 894

Brooks, A.: 2010, in L. M. Stanford, J. D. Green, L. Hao, & Y. Mao (ed.), *New Horizons in Astronomy: Frank N. Bash Symposium 2009*, Vol. 432 of *Astronomical Society of the Pacific Conference Series*, pp 17–+

Brown, W. R., Geller, M. J., Kenyon, S. J., and Diaferio, A.: 2010, AJ **139**, 59

Bryan, G. L. and Norman, M. L.: 1998, ApJ **495**, 80

Bryan, S. E. and Cress, C. M.: 2007, MNRAS **380**, 657

Bullock, J. S., Dekel, A., Kolatt, T. S., Kravtsov, A. V., Klypin, A. A., Porciani, C., and Primack, J. R.: 2001, ApJ **555**, 240

Bullock, J. S. and Johnston, K. V.: 2005, ApJ **635**, 931

Burkert, A.: 2009, in S. Jogee, I. Marinova, L. Hao, & G. A. Blanc (ed.), *Galaxy Evolution: Emerging Insights and Future Challenges*, Vol. 419 of *Astronomical Society of the Pacific Conference Series*, pp 3–+

Burstein, D.: 1979, ApJ **234**, 829

Carlberg, R. G.: 1987, ApJ **322**, 59

Carlberg, R. G. and Hartwick, F. D. A.: 1989, ApJ **345**, 196

Carollo, D., Beers, T. C., Chiba, M., Norris, J. E., Freeman, K. C., Lee, Y. S., Ivezić, Ž., Rockosi, C. M., and Yanny, B.: 2010, ApJ **712**, 692

Chandrasekhar, S.: 1943, ApJ **97**, 255

Chen, B., Stoughton, C., Smith, J. A., Uomoto, A., Pier, J. R., Yanny, B., Ivezić, Ž., York, D. G., Anderson, J. E., Annis, J., Brinkmann, J., Csabai, I., Fukugita, M., Hindsley, R., Lupton, R., Munn, J. A., and the SDSS Collaboration: 2001, ApJ **553**, 184

Chiba, M. and Beers, T. C.: 2000, AJ **119**, 2843

Choi, J., Weinberg, M. D., and Katz, N.: 2009, MNRAS **400**, 1247

Clutton-Brock, M.: 1972, Ap&SS **16**, 101

Clutton-Brock, M.: 1973, Ap&SS **23**, 55

Colberg, J. M., White, S. D. M., Jenkins, A., and Pearce, F. R.: 1999, MNRAS **308**, 593

Cole, S. and Lacey, C.: 1996, MNRAS **281**, 716

Colless, M., Dalton, G., Maddox, S., Sutherland, W., Norberg, P., Cole, S., Bland-Hawthorn, J., Bridges, T., Cannon, R., Collins, C., Couch, W., Cross, N., Deeley, K., De Propris, R., Driver, S. P., Efstathiou, G., Ellis, R. S., Frenk, C. S., Glazebrook, K., Jackson, C., Lahav, O., Lewis, I., Lumsden, S., Madgwick, D., Peacock, J. A., Peterson, B. A., Price, I., Seaborne, M., and Taylor, K.: 2001, MNRAS **328**, 1039

Couchman, H. M. P.: 1991, ApJ **368**, L23

Dalcanton, J. J. and Bernstein, R. A.: 2002, AJ **124**, 1328

Davis, M., Efstathiou, G., Frenk, C. S., and White, S. D. M.: 1985, ApJ **292**, 371

De Simone, R., Wu, X., and Tremaine, S.: 2004, MNRAS **350**, 627

Debattista, V. P., Moore, B., Quinn, T., Kazantzidis, S., Maas, R., Mayer, L., Read, J., and Stadel, J.: 2008, ApJ **681**, 1076

Dehnen, W., McLaughlin, D. E., and Sachania, J.: 2006, MNRAS **369**, 1688

Diemand, J., Kuhlen, M., Madau, P., Zemp, M., Moore, B., Potter, D., and Stadel, J.: 2008, Nature **454**, 735

Diemand, J., Moore, B., Stadel, J., and Kazantzidis, S.: 2004, MNRAS **348**, 977

D'Onghia, E., Springel, V., Hernquist, L., and Keres, D.: 2010, ApJ **709**, 1138

Dubinski, J.: 1992, ApJ **401**, 441

Dubinski, J. and Carlberg, R. G.: 1991, ApJ **378**, 496

Dubinski, J., Gauthier, J.-R., Widrow, L., and Nickerson, S.: 2008, in J. G. Funes & E. M. Corsini (ed.), *Formation and Evolution of Galaxy Disks*, Vol. 396 of *Astronomical Society of the Pacific Conference Series*, pp 321–+

Edvardsson, B., Andersen, J., Gustafsson, B., Lambert, D. L., Nissen, P. E., and Tomkin, J.: 1993, A&A **275**, 101

Efstathiou, G., Davis, M., White, S. D. M., and Frenk, C. S.: 1985, ApJS **57**, 241

Einasto, J.: 1965, *Trudy Inst. Astrofiz. Alma-Ata* **51**, 87

Eke, V. R., Cole, S., and Frenk, C. S.: 1996, MNRAS **282**, 263

Elmegreen, B. G. and Elmegreen, D. M.: 2006, ApJ **650**, 644

Eyre, A. and Binney, J.: 2011, MNRAS **413**, 1852

Fall, S. M. and Efstathiou, G.: 1980, MNRAS **193**, 189

Faltenbacher, A., Allgood, B., Gottlöber, S., Yepes, G., and Hoffman, Y.: 2005, MNRAS **362**, 1099

Fellhauer, M., Belokurov, V., Evans, N. W., Wilkinson, M. I., Zucker, D. B., Gilmore, G., Irwin, M. J., Bramich, D. M., Vidrih, S., Wyse, R. F. G., Beers, T. C., and Brinkmann, J.: 2006, ApJ **651**, 167

Font, A. S., Navarro, J. F., Stadel, J., and Quinn, T.: 2001, ApJ **563**, L1

Franx, M., Illingworth, G., and de Zeeuw, T.: 1991, ApJ **383**, 112

Frenk, C. S., Evrard, A. E., White, S. D. M., and Summers, F. J.: 1996, ApJ **472**, 460

Frenk, C. S., White, S. D. M., Davis, M., and Efstathiou, G.: 1988, ApJ **327**, 507

Frenk, C. S., White, S. D. M., Efstathiou, G., and Davis, M.: 1985, Nature **317**, 595

Frieman, J. A., Turner, M. S., and Huterer, D.: 2008, ARA&A **46**, 385

Friese, V., Fuchs, B., and Wielen, R.: 1995, in P. C. van der Kruit & G. Gilmore (ed.), *Stellar Populations*, Vol. 164 of *IAU Symposium*, pp 414–+

Fuhrmann, K.: 2008, MNRAS **384**, 173

Fuhrmann, K.: 2011, MNRAS **414**, 2893

Galassi, M., Davies, J., Theiler, J., Gough, B., Jungman, G., Booth, M., and Rossi, F.: 2003, *Gnu Scientific Library: Reference Manual*, Network Theory Ltd.

Gao, L., Navarro, J. F., Cole, S., Frenk, C. S., White, S. D. M., Springel, V., Jenkins, A., and Neto, A. F.: 2008, MNRAS **387**, 536

Gao, L., White, S. D. M., Jenkins, A., Stoehr, F., and Springel, V.: 2004, MNRAS **355**, 819

Gavazzi, R., Treu, T., Rhodes, J. D., Koopmans, L. V. E., Bolton, A. S., Burles, S., Massey, R. J., and Moustakas, L. A.: 2007, ApJ **667**, 176

Ghigna, S., Moore, B., Governato, F., Lake, G., Quinn, T., and Stadel, J.: 1998, MNRAS **300**, 146

Gilmore, G. and Reid, N.: 1983, MNRAS **202**, 1025

Gilmore, G. and Wyse, R. F. G.: 1985, AJ **90**, 2015

Gnedin, O. Y., Brown, W. R., Geller, M. J., and Kenyon, S. J.: 2010, ApJ **720**, L108

Gnedin, O. Y., Kravtsov, A. V., Klypin, A. A., and Nagai, D.: 2004, ApJ **616**, 16

Governato, F., Willman, B., Mayer, L., Brooks, A., Stinson, G., Valenzuela, O., Wadsley, J., and Quinn, T.: 2007, MNRAS **374**, 1479

Green, A. M., Hofmann, S., and Schwarz, D. J.: 2004, MNRAS **353**, L23

Guth, A. H.: 1981, Phys. Rev. D **23**, 347

Hayashi, E., Navarro, J. F., and Springel, V.: 2007, MNRAS **377**, 50

Hayashi, E., Navarro, J. F., Taylor, J. E., Stadel, J., and Quinn, T.: 2003, ApJ **584**, 541

Helly, J. C., Cole, S., Frenk, C. S., Baugh, C. M., Benson, A., and Lacey, C.: 2003, MNRAS **338**, 903

Helmi, A.: 2004, ApJ **610**, L97

Hernquist, L.: 1990, ApJ **356**, 359

Hernquist, L. and Ostriker, J. P.: 1992, ApJ **386**, 375

Hockney, R. W. and Eastwood, J. W.: 1988, *Computer simulation using particles*, Taylor & Francis

Holmberg, J., Nordström, B., and Andersen, J.: 2007, A&A **475**, 519

Hopkins, P. F., Hernquist, L., Cox, T. J., Younger, J. D., and Besla, G.: 2008, ApJ **688**, 757

Huang, S. and Carlberg, R. G.: 1997, ApJ **480**, 503

Hubble, E.: 1929, *Proceedings of the National Academy of Science* **15**, 168

Ibata, R., Lewis, G. F., Irwin, M., Totten, E., and Quinn, T.: 2001, ApJ **551**, 294

Ida, S., Kokubo, E., and Makino, J.: 1993, MNRAS **263**, 875

Jenkins, A.: 1992, MNRAS **257**, 620

Jenkins, A. and Binney, J.: 1990, MNRAS **245**, 305

Jing, Y. P. and Suto, Y.: 2002, ApJ **574**, 538

Julian, W. H. and Toomre, A.: 1966, ApJ **146**, 810

Jurić, M., Ivezić, Ž., Brooks, A., Lupton, R. H., Schlegel, D., Finkbeiner, D., Padmanabhan, N., Bond, N., Sesar, B., Rockosi, C. M., Knapp, G. R., Gunn, J. E., Sumi, T., Schneider, D. P., Barentine, J. C., Brewington, H. J., Brinkmann, J., Fukugita, M., Harvanek, M., Kleinman, S. J., Krzesinski, J., Long, D., Neilsen, Jr., E. H., Nitta, A., Snedden, S. A., and York, D. G.: 2008, ApJ **673**, 864

Katz, N. and White, S. D. M.: 1993, ApJ **412**, 455

Kazantzidis, S., Abadi, M. G., and Navarro, J. F.: 2010, ApJ **720**, L62

Kazantzidis, S., Bullock, J. S., Zentner, A. R., Kravtsov, A. V., and Moustakas, L. A.: 2008, ApJ **688**, 254

Kazantzidis, S., Kravtsov, A. V., Zentner, A. R., Allgood, B., Nagai, D., and Moore, B.: 2004a, ApJ **611**, L73

Kazantzidis, S., Magorrian, J., and Moore, B.: 2004b, ApJ **601**, 37

Kazantzidis, S., Mayer, L., Mastropietro, C., Diemand, J., Stadel, J., and Moore, B.: 2004c, ApJ **608**, 663

Kazantzidis, S., Zentner, A. R., Kravtsov, A. V., Bullock, J. S., and Debattista, V. P.: 2009, ApJ **700**, 1896

Keres, D., Vogelsberger, M., Sijacki, D., Springel, V., and Hernquist, L.: 2011, *ArXiv e-prints*

Kessler, R., Becker, A. C., Cinabro, D., Vanderplas, J., Frieman, J. A., Marriner, J., Davis, T. M., Dilday, B., Holtzman, J., Jha, S. W., Lampeitl, H., Sako, M., Smith, M., Zheng, C., Nichol, R. C., Bassett, B., Bender, R., Depoy, D. L., Doi, M., Elson, E., Filippenko, A. V., Foley, R. J., Garnavich, P. M., Hopp, U., Ihara, Y., Ketzeback, W., Kollatschny, W., Konishi, K., Marshall, J. L., McMillan, R. J., Miknaitis, G., Morokuma, T., Mörtsell, E., Pan, K., Prieto, J. L., Richmond, M. W., Riess, A. G., Romani, R., Schneider, D. P., Sollerman, J., Takanashi, N., Tokita, K., van der Heyden, K., Wheeler, J. C., Yasuda, N., and York, D.: 2009, ApJS **185**, 32

King, I. R.: 1966, AJ **71**, 64

Klypin, A., Kravtsov, A. V., Valenzuela, O., and Prada, F.: 1999, ApJ **522**, 82

Klypin, A. A. and Shandarin, S. F.: 1983, MNRAS **204**, 891

Knebe, A., Knollmann, S. R., Muldrew, S. I., Pearce, F. R., Aragon-Calvo, M. A., Ascasibar, Y., Behroozi, P. S., Ceverino, D., Colombi, S., Diemand, J., Dolag, K., Falck, B. L., Fasel, P., Gardner, J., Gottlöber, S., Hsu, C.-H., Iannuzzi, F., Klypin, A., Lukić, Z., Maciejewski, M., McBride, C., Neyrinck, M. C., Planelles, S., Potter, D., Quilis, V., Rasera,

Y., Read, J. I., Ricker, P. M., Roy, F., Springel, V., Stadel, J., Stinson, G., Sutter, P. M., Turchaninov, V., Tweed, D., Yepes, G., and Zemp, M.: 2011, MNRAS **415**, 2293

Knop, R. A., Aldering, G., Amanullah, R., Astier, P., Blanc, G., Burns, M. S., Conley, A., Deustua, S. E., Doi, M., Ellis, R., Fabbro, S., Folatelli, G., Fruchter, A. S., Garavini, G., Garmond, S., Garton, K., Gibbons, R., Goldhaber, G., Goobar, A., Groom, D. E., Hardin, D., Hook, I., Howell, D. A., Kim, A. G., Lee, B. C., Lidman, C., Mendez, J., Nobili, S., Nugent, P. E., Pain, R., Panagia, N., Pennypacker, C. R., Perlmutter, S., Quimby, R., Raux, J., Regnault, N., Ruiz-Lapuente, P., Sainton, G., Schaefer, B., Schahmaneche, K., Smith, E., Spadafora, A. L., Stanishev, V., Sullivan, M., Walton, N. A., Wang, L., Wood-Vasey, W. M., and Yasuda, N.: 2003, ApJ **598**, 102

Kochanek, C. S.: 1996, ApJ **457**, 228

Komatsu, E., Smith, K. M., Dunkley, J., Bennett, C. L., Gold, B., Hinshaw, G., Jarosik, N., Larson, D., Nolta, M. R., Page, L., Spergel, D. N., Halpern, M., Hill, R. S., Kogut, A., Limon, M., Meyer, S. S., Odegard, N., Tucker, G. S., Weiland, J. L., Wollack, E., and Wright, E. L.: 2011, ApJS **192**, 18

Lacey, C. and Cole, S.: 1993, MNRAS **262**, 627

Lacey, C. G.: 1984, MNRAS **208**, 687

Lacey, C. G. and Ostriker, J. P.: 1985, ApJ **299**, 633

Larson, D., Dunkley, J., Hinshaw, G., Komatsu, E., Nolta, M. R., Bennett, C. L., Gold, B., Halpern, M., Hill, R. S., Jarosik, N., Kogut, A., Limon, M., Meyer, S. S., Odegard, N., Page, L., Smith, K. M., Spergel, D. N., Tucker, G. S., Weiland, J. L., Wollack, E., and Wright, E. L.: 2011, ApJS **192**, 16

Law, D. R., Johnston, K. V., and Majewski, S. R.: 2005, ApJ **619**, 807

Law, D. R., Majewski, S. R., and Johnston, K. V.: 2009, ApJ **703**, L67

Lewis, J. R. and Freeman, K. C.: 1989, AJ **97**, 139

Li, Y.-S., De Lucia, G., and Helmi, A.: 2010, MNRAS **401**, 2036

Li, Y.-S. and White, S. D. M.: 2008, MNRAS **384**, 1459

Libeskind, N. I., Knebe, A., Hoffman, Y., Gottlöber, S., Yepes, G., and Steinmetz, M.: 2011, MNRAS **411**, 1525

Lovell, M., Eke, V., Frenk, C., Gao, L., Jenkins, A., Theuns, T., Wang, J., Boyarsky, A., and Ruchayskiy, O.: 2011a, *ArXiv e-prints*

Lovell, M. R., Eke, V. R., Frenk, C. S., and Jenkins, A.: 2011b, MNRAS **413**, 3013

Lynden-Bell, D.: 1962, MNRAS **124**, 1

Lynden-Bell, D. and Kalnajs, A. J.: 1972, MNRAS **157**, 1

Macciò, A. V., Kang, X., Fontanot, F., Somerville, R. S., Koposov, S., and Monaco, P.: 2010, MNRAS **402**, 1995

Mantz, A., Allen, S. W., Rapetti, D., and Ebeling, H.: 2010, MNRAS **406**, 1759

Martin, N. F., Ibata, R. A., Irwin, M. J., Chapman, S., Lewis, G. F., Ferguson, A. M. N., Tanvir, N., and McConnachie, A. W.: 2006, MNRAS **371**, 1983

Martínez-Delgado, D., Gómez-Flechoso, M. Á., Aparicio, A., and Carrera, R.: 2004, ApJ **601**, 242

Mashchenko, S., Couchman, H. M. P., and Wadsley, J.: 2006, Nature **442**, 539

Mashchenko, S., Wadsley, J., and Couchman, H. M. P.: 2008, *Science* **319**, 174

Mayer, L., Governato, F., and Kaufmann, T.: 2008, *Advanced Science Letters* **1**, 7

McConnachie, A. W., Huxor, A., Martin, N. F., Irwin, M. J., Chapman, S. C., Fahlman, G., Ferguson, A. M. N., Ibata, R. A., Lewis, G. F., Richer, H., and Tanvir, N. R.: 2008, ApJ **688**, 1009

McMillan, P. J. and Dehnen, W.: 2007, MNRAS **378**, 541

Merritt, D.: 1985a, MNRAS **214**, 25P

Merritt, D.: 1985b, AJ **90**, 1027

Mihos, J. C., Walker, I. R., Hernquist, L., Mendes de Oliveira, C., and Bolte, M.: 1995, ApJ **447**, L87+

Minchev, I. and Quillen, A. C.: 2006, MNRAS **368**, 623

Mo, H. J., Mao, S., and White, S. D. M.: 1998, MNRAS **295**, 319

Momany, Y., Zaggia, S., Gilmore, G., Piotto, G., Carraro, G., Bedin, L. R., and de Angeli, F.: 2006, A&A **451**, 515

Moore, B.: 2000, in *Constructing the Universe with Clusters of Galaxies*

Moore, B., Ghigna, S., Governato, F., Lake, G., Quinn, T., Stadel, J., and Tozzi, P.: 1999a, ApJ **524**, L19

Moore, B., Quinn, T., Governato, F., Stadel, J., and Lake, G.: 1999b, MNRAS **310**, 1147

Morrison, H. L., Miller, E. D., Harding, P., Stinebring, D. R., and Boroson, T. A.: 1997, AJ **113**, 2061

Moster, B. P., Macciò, A. V., Somerville, R. S., Johansson, P. H., and Naab, T.: 2010, MNRAS **403**, 1009

Muldrew, S. I., Pearce, F. R., and Power, C.: 2011, MNRAS **410**, 2617

Natarajan, P. and Refregier, A.: 2000, ApJ **538**, L113

Navarro, J. F., Abadi, M. G., Venn, K. A., Freeman, K. C., and Anguiano, B.: 2011, MNRAS **412**, 1203

Navarro, J. F. and Benz, W.: 1991, ApJ **380**, 320

Navarro, J. F., Eke, V. R., and Frenk, C. S.: 1996a, MNRAS **283**, L72

Navarro, J. F., Frenk, C. S., and White, S. D. M.: 1994, MNRAS **267**, L1+

Navarro, J. F., Frenk, C. S., and White, S. D. M.: 1995, MNRAS **275**, 56

Navarro, J. F., Frenk, C. S., and White, S. D. M.: 1996b, ApJ **462**, 563

Navarro, J. F., Frenk, C. S., and White, S. D. M.: 1997, ApJ **490**, 493

Navarro, J. F., Hayashi, E., Power, C., Jenkins, A. R., Frenk, C. S., White, S. D. M., Springel, V., Stadel, J., and Quinn, T. R.: 2004, MNRAS **349**, 1039

Navarro, J. F., Ludlow, A., Springel, V., Wang, J., Vogelsberger, M., White, S. D. M., Jenkins, A., Frenk, C. S., and Helmi, A.: 2010, MNRAS **402**, 21

Navarro, J. F. and White, S. D. M.: 1994, MNRAS **267**, 401

Neto, A. F., Gao, L., Bett, P., Cole, S., Navarro, J. F., Frenk, C. S., White, S. D. M., Springel, V., and Jenkins, A.: 2007, MNRAS **381**, 1450

Newberg, H. J., Yanny, B., Rockosi, C., Grebel, E. K., Rix, H.-W., Brinkmann, J., Csabai, I., Hennessy, G., Hindsley, R. B., Ibata, R., Ivezić, Z., Lamb, D., Nash, E. T., Odenkirchen, M., Rave, H. A., Schneider, D. P., Smith, J. A., Stolte, A., and York, D. G.: 2002, ApJ **569**, 245

Nordström, B., Mayor, M., Andersen, J., Holmberg, J., Pont, F., Jørgensen, B. R., Olsen, E. H., Udry, S., and Mowlavi, N.: 2004, A&A **418**, 989

Osipkov, L. P.: 1979, *Soviet Astronomy Letters* **5**, 42

Ostriker, J. P. and Mark, J.: 1968, ApJ **151**, 1075

Parry, O. H., Eke, V. R., Frenk, C. S., and Okamoto, T.: 2011, *ArXiv e-prints*

Peñarrubia, J., Belokurov, V., Evans, N. W., Martínez-Delgado, D., Gilmore, G., Irwin, M., Niederste-Ostholt, M., and Zucker, D. B.: 2010, MNRAS **408**, L26

Peñarrubia, J. and Benson, A. J.: 2005, MNRAS **364**, 977

Peñarrubia, J., Benson, A. J., Martínez-Delgado, D., and Rix, H. W.: 2006, ApJ **645**, 240

Peñarrubia, J., Martínez-Delgado, D., Rix, H. W., Gómez-Flechoso, M. A., Munn, J., Newberg, H., Bell, E. F., Yanny, B., Zucker, D., and Grebel, E. K.: 2005, ApJ **626**, 128

Pontzen, A. and Governato, F.: 2011, *ArXiv e-prints*

Power, C., Navarro, J. F., Jenkins, A., Frenk, C. S., White, S. D. M., Springel, V., Stadel, J., and Quinn, T.: 2003, MNRAS **338**, 14

Profumo, S., Sigurdson, K., and Kamionkowski, M.: 2006, *Physical Review Letters* **97(3)**, 031301

Purcell, C. W., Kazantzidis, S., and Bullock, J. S.: 2009, ApJ **694**, L98

Quillen, A. C. and Garnett, D. R.: 2001, in J. G. Funes & E. M. Corsini (ed.), *Galaxy Disks and Disk Galaxies*, Vol. 230 of *Astronomical Society of the Pacific Conference Series*, pp 87–88

Quinn, P. J. and Goodman, J.: 1986, ApJ **309**, 472

Quinn, P. J., Hernquist, L., and Fullagar, D. P.: 1993, ApJ **403**, 74

Read, J. I., Lake, G., Agertz, O., and Debattista, V. P.: 2008, *ArXiv e-prints* 803

Reddy, B. E., Lambert, D. L., and Allende Prieto, C.: 2006, MNRAS **367**, 1329

Riess, A. G., Filippenko, A. V., Challis, P., Clocchiatti, A., Diercks, A., Garnavich, P. M., Gilliland, R. L., Hogan, C. J., Jha, S., Kirshner, R. P., Leibundgut, B., Phillips, M. M., Reiss, D., Schmidt, B. P., Schommer, R. A., Smith, R. C., Spyromilio, J., Stubbs, C., Suntzeff, N. B., and Tonry, J.: 1998, AJ **116**, 1009

Robin, A. C., Haywood, M., Creze, M., Ojha, D. K., and Bienayme, O.: 1996, A&A **305**, 125

Romano-Diaz, E., Faltenbacher, A., Jones, D., Heller, C., Hoffman, Y., and Shlosman, I.: 2006, ApJ **637**, L93

Saha, K., Tseng, Y.-H., and Taam, R. E.: 2010, ApJ **721**, 1878

Sakamoto, T., Chiba, M., and Beers, T. C.: 2003, A&A **397**, 899

Sales, L. V., Helmi, A., Abadi, M. G., Brook, C. B., Gómez, F. A., Roškar, R., Debattista, V. P., House, E., Steinmetz, M., and Villalobos, Á.: 2009, MNRAS **400**, L61

Sales, L. V., Navarro, J. F., Schaye, J., Dalla Vecchia, C., Springel, V., and Booth, C. M.: 2010, MNRAS **409**, 1541

Schönrich, R. and Binney, J.: 2009, MNRAS **396**, 203

Seabroke, G. M. and Gilmore, G.: 2007, MNRAS **380**, 1348

Sellwood, J. A. and Binney, J. J.: 2002, MNRAS **336**, 785

Sellwood, J. A. and Carlberg, R. G.: 1984, ApJ **282**, 61

Sellwood, J. A., Nelson, R. W., and Tremaine, S.: 1998, ApJ **506**, 590

Sofue, Y., Honma, M., and Omodaka, T.: 2009, PASJ **61**, 227

Soubiran, C., Bienaymé, O., and Siebert, A.: 2003, A&A **398**, 141

Spergel, D. N., Verde, L., Peiris, H. V., Komatsu, E., Nolta, M. R., Bennett, C. L., Halpern, M., Hinshaw, G., Jarosik, N., Kogut, A., Limon, M., Meyer, S. S., Page, L., Tucker, G. S., Weiland, J. L., Wollack, E., and Wright, E. L.: 2003, ApJS **148**, 175

Spitzer, Jr., L. and Schwarzschild, M.: 1951, ApJ **114**, 385

Spitzer, Jr., L. and Schwarzschild, M.: 1953, ApJ **118**, 106

Springel, V.: 2005, MNRAS **364**, 1105

Springel, V., Wang, J., Vogelsberger, M., Ludlow, A., Jenkins, A., Helmi, A., Navarro, J. F., Frenk, C. S., and White, S. D. M.: 2008, MNRAS **391**, 1685

Springel, V. and White, S. D. M.: 1999, MNRAS **307**, 162

Springel, V., White, S. D. M., and Hernquist, L.: 2004, in S. Ryder, D. Pisano, M. Walker, and K. Freeman (eds.), *Dark Matter in Galaxies*, Vol. 220 of *IAU Symposium*, p. 421

Springel, V., White, S. D. M., Jenkins, A., Frenk, C. S., Yoshida, N., Gao, L., Navarro, J., Thacker, R., Croton, D., Helly, J., Peacock, J. A., Cole, S., Thomas, P., Couchman, H., Evrard, A., Colberg, J., and Pearce, F.: 2005, Nature **435**, 629

Springel, V., White, S. D. M., Tormen, G., and Kauffmann, G.: 2001a, MNRAS **328**, 726

Springel, V., Yoshida, N., and White, S. D. M.: 2001b, *New Astronomy* **6**, 79

Stadel, J., Potter, D., Moore, B., Diemand, J., Madau, P., Zemp, M., Kuhlen, M., and Quilis, V.: 2009, MNRAS **398**, L21

Stewart, K. R., Bullock, J. S., Wechsler, R. H., Maller, A. H., and Zentner, A. R.: 2008, ApJ **683**, 597

Stinson, G., Seth, A., Katz, N., Wadsley, J., Governato, F., and Quinn, T.: 2006, MNRAS **373**, 1074

Stoehr, F., White, S. D. M., Springel, V., Tormen, G., and Yoshida, N.: 2003, MNRAS **345**, 1313

Strigari, L. E., Frenk, C. S., and White, S. D. M.: 2010, MNRAS **408**, 2364

Summers, F. J., Davis, M., and Evrard, A. E.: 1995, ApJ **454**, 1

Taylor, J. E. and Babul, A.: 2001, ApJ **559**, 716

Thacker, R. J. and Couchman, H. M. P.: 2001, ApJ **555**, L17

Tissera, P. B., White, S. D. M., Pedrosa, S., and Scannapieco, C.: 2010, MNRAS **406**, 922

Toomre, A.: 1964, ApJ **139**, 1217

Tormen, G.: 1997, MNRAS **290**, 411

Toth, G. and Ostriker, J. P.: 1992, ApJ **389**, 5

Treu, T. and Koopmans, L. V. E.: 2004, ApJ **611**, 739

Velazquez, H. and White, S. D. M.: 1999, MNRAS **304**, 254

Vera-Ciro, C. A., Sales, L. V., Helmi, A., Frenk, C. S., Navarro, J. F., Springel, V., Vogelsberger, M., and White, S. D. M.: 2011, *ArXiv e-prints*

Villalobos, Á. and Helmi, A.: 2008, *Monthly Notices of the Royal Astronomical Society* **391(4)**, 1806

Villalobos, Á., Kazantzidis, S., and Helmi, A.: 2010, ApJ **718**, 314

Walker, I. R., Mihos, J. C., and Hernquist, L.: 1996, ApJ **460**, 121

Walker, M. G., Mateo, M., Olszewski, E. W., Peñarrubia, J., Wyn Evans, N., and Gilmore, G.: 2009, ApJ **704**, 1274

Wang, J., Navarro, J. F., Frenk, C. S., White, S. D. M., Springel, V., Jenkins, A., Helmi, A., Ludlow, A., and Vogelsberger, M.: 2011, MNRAS **413**, 1373

Warren, M. S., Quinn, P. J., Salmon, J. K., and Zurek, W. H.: 1992, ApJ **399**, 405

Wechsler, R. H., Bullock, J. S., Primack, J. R., Kravtsov, A. V., and Dekel, A.: 2002, ApJ **568**, 52

Weinberg, M. D.: 1996, ApJ **470**, 715

Weinberg, M. D.: 1999, AJ **117**, 629

White, S.: 2000, in *KITP Program: Galaxy Formation and Evolution*

White, S. D. M.: 2009, in J. Andersen, J. Bland-Hawthorn, & B. Nordström (ed.), *IAU Symposium*, Vol. 254 of *IAU Symposium*, pp 19–20

White, S. D. M., Davis, M., and Frenk, C. S.: 1984, MNRAS **209**, 27P

White, S. D. M., Frenk, C. S., and Davis, M.: 1983, ApJ **274**, L1

White, S. D. M. and Rees, M. J.: 1978, MNRAS **183**, 341

Wielen, R.: 1977, A&A **60**, 263

Wilkinson, M. I. and Evans, N. W.: 1999, MNRAS **310**, 645

Wolf, J., Martinez, G. D., Bullock, J. S., Kaplinghat, M., Geha, M., Muñoz, R. R., Simon, J. D., and Avedo, F. F.: 2010, MNRAS **406**, 1220

Xue, X. X., Rix, H. W., Zhao, G., Re Fiorentin, P., Naab, T., Steinmetz, M., van den Bosch, F. C., Beers, T. C., Lee, Y. S., Bell, E. F., Rockosi, C., Yanny, B., Newberg, H., Wilhelm, R., Kang, X., Smith, M. C., and Schneider, D. P.: 2008, ApJ **684**, 1143

Yanny, B., Newberg, H. J., Grebel, E. K., Kent, S., Odenkirchen, M., Rockosi, C. M., Schlegel, D., Subbarao, M., Brinkmann, J., Fukugita, M., Ivezic, Ž., Lamb, D. Q., Schneider, D. P., and York, D. G.: 2003, ApJ **588**, 824

Yoachim, P. and Dalcanton, J. J.: 2006, AJ **131**, 226

Zentner, A. R. and Bullock, J. S.: 2003, ApJ **598**, 49

Zhao, D. H., Mo, H. J., Jing, Y. P., and Börner, G.: 2003, MNRAS **339**, 12

Zhao, H.: 1996, MNRAS **278**, 488

Zucker, D. B., Kniazev, A. Y., Bell, E. F., Martínez-Delgado, D., Grebel, E. K., Rix, H.-W., Rockosi, C. M., Holtzman, J. A., Walterbos, R. A. M., Annis, J., York, D. G., Ivezić, Ž., Brinkmann, J., Brewington, H., Harvanek, M., Hennessy, G., Kleinman, S. J., Krzesinski, J., Long, D., Newman, P. R., Nitta, A., and Snedden, S. A.: 2004, ApJ **612**, L121

Zwicky, F.: 1933, *Helvetica Physica Acta* **6**, 110